DOE Award # DE-SC0001531

Project Title
"SISGR-Fundamental Experimental and Theoretical Studies on a Novel Family of Oxide Catalyst Supports for Water Electrolysis"

Principal Investigator
Prashant N. Kumta

Date of the Report: September 10, 2014

Period: September 1, 2009-August 31, 2012

The present project is directed at conducting fundamental studies to identify and synthesize more economical, more durable nano-structured electro-catalyst supports. The project involves conducting both theoretical and experimental investigations. This report represents a compilation of all the work that was conducted during the entire three year period of the project. Results of the major technical accomplishments attained in both theory and experimental areas since September 2009 are summarized in the pages to follow.

FUNDAMENTAL STUDY OF NANOSTRUCTURED ELECTRO-CATALYSTS WITH REDUCED NOBLE METAL CONTENT FOR PEM BASED WATER ELECTROLYSIS

Identification and development of non-noble metal based electro-catalysts or electro-catalysts with significant reduction of expensive noble metal contents (*E.g.* IrO_2, Pt) with comparable electrochemical performance as the standard noble metal/metal oxide for proton exchange membrane (PEM) based water electrolysis would constitute a major breakthrough in the generation of hydrogen by water electrolysis. Accomplishing such a system would not only result reduction of the overall capital costs of PEM based water electrolyzers, but also help attain the targeted hydrogen production cost [< $ 3.0 / gallon gasoline equivalent (gge)] comparable to conventional liquid fuels.

In line with these goals, it was demonstrated that fluorine doped IrO_2 thin films and nanostructured high surface area powders display remarkably higher electrochemical activity, and comparable durability as pure IrO_2 electro-catalyst for the oxygen evolution reaction (OER) in PEM based water electrolysis. Furthermore, corrosion resistant SnO_2 and NbO_2 support has been doped with F and coupled with IrO_2 or RuO_2 for use as an OER electro-catalyst. A solid solution of SnO_2:F or NbO_2:F with only 20 - 30 mol.% IrO_2 or RuO_2 yielding a rutile structure in the form of thin films and bulk nanoparticles displays similar electrochemical activity and stability as pure IrO_2/RuO_2. This would lead to more than 70 mol.% reduction in the noble metal oxide content. Novel nanostructured ternary $(Ir,Sn,Nb)O_2$ thin films of different compositions

have also been studied. It has been shown that $(Ir_{0.40}Sn_{0.30}Nb_{0.30})O_2$ shows similar electrochemical activity and enhanced chemical robustness as compared to pure IrO_2. F doping of the ternary $(Ir,Sn,Nb)O_2$ catalyst helps in further decreasing the noble metal oxide content of the catalyst.

As a result, these reduced noble metal oxide catalyst systems would potentially be preferred as OER electro-catalysts for PEM electrolysis. The excellent performance of the catalysts coupled with its robustness would make them great candidates for contributing to significant reduction in the overall capital costs of PEM based water electrolyzers. This thesis provides a detailed fundamental study of the synthesis, materials, characterization, theoretical studies and detailed electrochemical response and potential mechanisms of these novel electro-catalysts for OER processes.

TABLE OF CONTENTS

LIST OF TABLES

LIST OF FIGURES

INTRODUCTION

1.1 HYDROGEN

Hydrogen, composed of a single proton and electron, comprises 90% of all matter of the universe. Its extreme buoyancy allows hydrogen to disperse rapidly in case of accidental release and will ultimately end up escaping the earth's atmosphere or coming down as water when combined with the oxygen in the air [1]. Hydrogen has been considered as an attractive alternative to fossil fuels over the past decade and is considered by many a harbinger to the hydrogen economy. Furthermore, as the most lightweight fuel it has the potential to provide clean, reliable, and affordable energy supply to meet the growing global energy demand [2-4]. However a major impediment towards commercialization has been the ability to economically generate clean and pure hydrogen combined with cost effective strategies for storage and distribution [4-8].

Currently, most of the hydrogen is produced from fossil fuels like coal, natural gas and oil. The current technology for generating hydrogen is quite advanced but remains to be optimized for large scale production in order to increase energy efficiency, and reduce environmental impact and costs. The most economical and frequently used process for manufacture of hydrogen is catalytic steam reforming of natural gas, which is mainly composed of methane. Possible improvements of the process are mainly focused on recovery of thermal

energy, process integration, and gas purification [9, 10]. Another widely used method for hydrogen production is by coal gasification. These technologies are mature, but further improvements are still considerable and it takes into account innovative membranes for air separation, progress in gasifier configuration, hot gas purification systems, new solvents and membrane reactors for hydrogen separation.

Gasification and biomass conversion is an emerging technology for producing hydrogen via natural gas or heavy fuel oil. But, it is a high temperature process with substantial electricity inputs. Hydrogen can also be produced from water through thermochemical cycles, photoelectrochemically *i.e.* direct thermal or catalytic splitting of water; and photobiologically using sunlight and photosynthetic microorganisms. These processes have very low efficiencies and have not been explored commercially [1, 9, 10].

Water electrolysis or reverse fuel cell operation is the conversion of electric energy into hydrogen. In its present state, the process is significantly more expensive than hydrogen production from fossil fuels and covers only a small share of the world production. But, this process yields very high purity hydrogen and is a benign and environmental friendly process [3, 5, 8, 11, 12].

1.2 HYDROGEN PRODUCTION TECHNOLOGIES

The main requirement for hydrogen production comprises feedstock and energy. In today's world, the logical feed stocks for hydrogen production are hydrocarbon fuels (C_xH_y) and water (H_2O). However, extraction of hydrogen from either hydrocarbons or water requires energy. The

energy required for production of hydrogen, though will always be greater than the amount of energy released by hydrogen utilization. Hydrogen is currently being produced industrially by fossil fuels like natural gas, oil and coal.

Hydrogen production technologies such as steam reforming, partial oxidation of hydrocarbons, and gasification are mature and widely used. But, they need to be optimized for large-scale production in order to better efficiency, environmental impact, and, capital and operating costs. For these processes to be sustainable in the long time run, they need to be coupled with capture and storage of CO_2 which is the main by-product of these processes. Development of solutions for economical and cost-effective CO_2 capture is very essential to have an environmental friendly process. The cheapest and frequently used process is the catalytic steam reforming of natural gas. There is a lot of ongoing work on the improvements of this process focusing on thermal energy recovery, process integration and gas purification [9, 13]. The potential for further improvements is very much critically needed to take into consideration development of innovative membranes for air separation, modifications in gasifier configuration, and the hot gas purification systems amongst many more. There is also need for synthesizing new diluents, materials and solvents along with membrane reactors for hydrogen separation.

Other technologies such as coal gasification would be interesting if they are integrated into combined cycles with CO_2 capture and storage. Processes such as autothermal reforming and partial oxidation of hydrocarbons are used for heavier hydrocarbons. Other less explored process includes thermal or catalytic cracking of methane, which converts methane in hydrogen and carbon, without CO_2 production; and solar steam reforming, that in turn use concentrated solar energy as the heat source for reforming.

Hydrogen can also be produced from biomass using different biological processes and thermochemical processes *viz.,* gasification and pyrolysis. The thermochemical processes are similar to that used for coal gasification. The biomass comprises of agricultural and forest residues, industrial and urban wastes, and organic waste materials. A lot of improvement is needed in order to increase output, efficiency and reliability, along with decreasing costs. Photobiological hydrogen production uses sunlight and photosynthetic microorganisms for splitting water. These techniques are still at laboratory scale and the conversion efficiencies are way too low for commercial use.

Also, photoelectrochemical systems have been explored wherein the electric energy generation from solar light and its utilization to produce hydrogen from water are combined *via* an electrolyzer. It uses semiconductor devices introduced in a solution, which converts solar energy to chemical energy. It is a very promising approach to produce hydrogen, but considerable research needs to be done on developing materials and engineering the process in order for these systems to be used for large scale production.

All the above mentioned technologies are thus either energy intensive, or in their nascent stages. All the currently used commercial or large scale hydrogen production processes do not give us ultra high purity (UHP) hydrogen, with their primary dependence on scarce fossil fuel reserves and need to combat with reducing the pollutants generated in the processes. This high energy intensity of production and storage of hydrogen increases the net energy use, owing to investment in efforts to reduce the greenhouse gas emissions. High quality hydrogen can only be produced effectively by electrochemical conversion of water to hydrogen and oxygen. Electricity induced splitting of water offers no pollution or toxic by-products if the electricity is generated *via* renewable energy sources like photovoltaics, wind turbines, geothermal and hydropower. We

can thus envision this as a very plausible and ecologically sustainable option for energy production if the efficiency of water electrolysis can be improved [14-17].

1.3 WATER ELECTROLYSIS

A promising approach to produce hydrogen is by electricity induced splitting of water using alkaline, neutral or polymer electrolyte membrane (PEM) based water electrolysis [2, 11, 15, 16, 18]. This involves passing an electric current through the water to split it into hydrogen and oxygen. Electrolysis is less efficient than a direct chemical path but it offers virtually no pollution or toxic byproducts if the electric current is generated using renewable energy *viz.*, wind, solar, geothermal and hydropower [3, 8, 12, 15, 16, 19-23].

The high capital costs of current electrolyzers arise as a result of the use of expensive noble metal based electro-catalysts like IrO_2, RuO_2, Pt; use of relatively small systems of comparatively low efficiencies, combined with the added costs of customized power electronics, and labor intensive fabrication [2, 7, 9, 12, 22, 24, 25]. The approach nevertheless, is potentially very lucrative since it offers virtually no green house gas emission or toxic byproducts particularly, if the electric current is generated using renewable energy or nuclear energy sources. Consequently, it would provide a plausible option if the efficiency were increased by the generation of highly efficient non-noble metal/metal oxide based electro-catalysts or identification of electro-catalysts with significant reduction of the expensive noble metal fraction [2, 12, 15, 16, 24, 26-28].

Rutile type noble metal oxides, IrO_2 and RuO_2 are well known and are typically accepted as the archetypical standards for oxygen evolution reaction (OER) anode electrode catalysts in PEM based water electrolysis. However, the anodic over-potential and the cell resistance in electrolysis contribute to a majority of the losses witnessed in catalytic performance. In addition, the electro-catalyst based on IrO_2 and RuO_2 undergo electrochemical or mechanical degradation under extreme and highly corrosive electrochemical environments prevalent in the acid assisted water electrolysis which reduce the performance with time and moreover, diminish the service life of the electrode during OER [24, 29-31]. Therefore, the design, synthesis and processing of non-precious metal/metal oxide catalysts for OER electrodes exhibiting high activity and durability under the highly aggressive chemical environments of water electrolysis would be of paramount importance in significantly decreasing the overall capital costs.

For PEM electrolysis cells, non-precious metal catalysts for electrodes with high activity and durability would decrease overall capital costs. However, it is unlikely that a non-noble metal catalyst will be identified for PEM system, but ways to decrease noble metal loading need to be identified. Decreasing the noble metal loading as well as improving the catalytic activity and durability could be achieved using novel synthesis techniques to generate high surface area nanostructured electro-catalysts, or improved low cost support structure (diluents) for electro-catalyst [29, 30, 32-36]. Strategies involving less expensive, more durable materials as supports or diluents for expensive electro-catalyst that are easier to manufacture would immensely help to lower the costs.

The schematic layout of a water electrolysis cell is shown in **Figure 1** [37]. Hydrogen is produced by supplying water to the anode decomposing into oxygen, protons, and electrons. The protons are transported through the proton conductive membrane to the cathode. The electrons

exit the cell via the external circuit, which supplies the driving force (i.e. cell potential) for the reaction. At the cathode the electrons and protons re-combine to yield hydrogen gas. The volume of hydrogen gas produced is therefore twice the amount of oxygen gas.

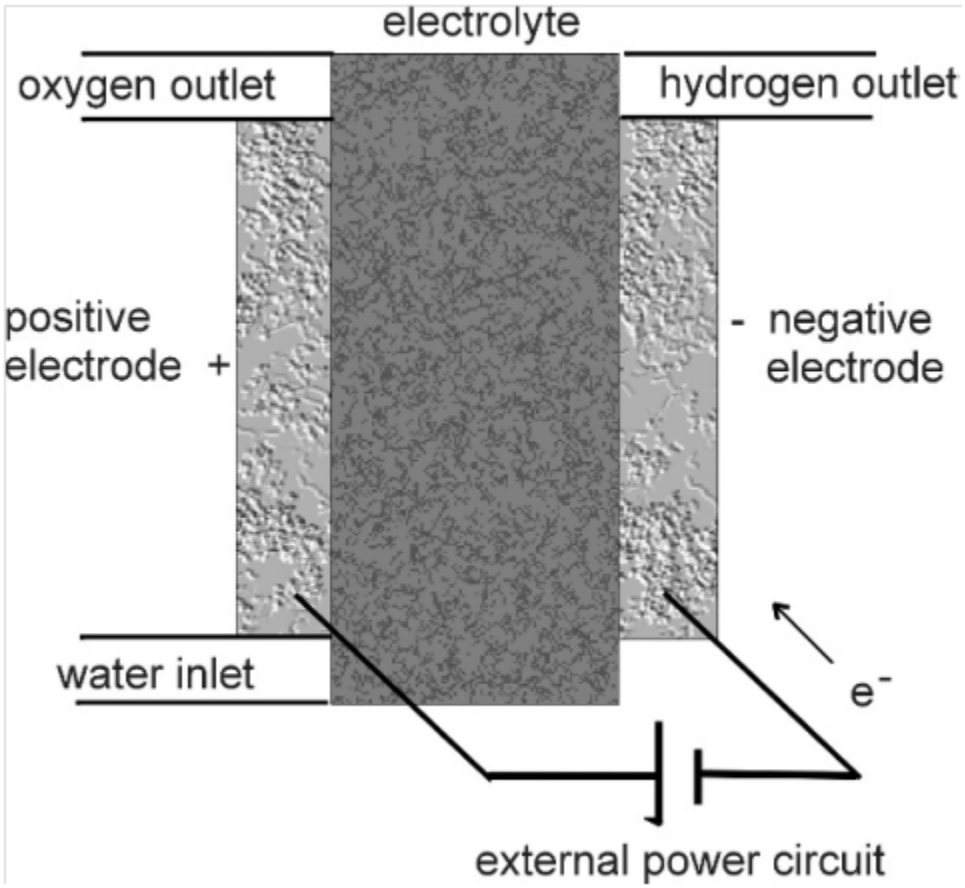

Figure 1. Schematic of a water electrolysis cell

2.0 BACKGROUND

2.1 TYPES OF ELECTROLYZERS

Three different types of electrolysis cells are proposed and they are classified into groups with respect to the electrolyte being used for the same. They are alkaline electrolysis cells, solid oxide electrolyzers and PEM based electrolysis. The overall electrolysis reaction is the sum of two electrochemical reactions (half-cell reactions) taking place at the electrodes. The anode is the electrode where oxidation of the reactants and/or intermediates occurs and cathode is where reduction reaction occurs.

2.1.1 Alkaline Electrolysis

Alkaline elctrolyzers is a mature technology wherein electrolysis reaction occurs in an alkaline solution of caustic potash solution at a concentration of 20 - 30 wt.% KOH between temperatures of 40°C and 90°C. The anode is typically made of nickel and the cathode of steel or stainless steel on which are coated the catalysts. The catalysts are often nickel based compounds with molybdenum on the cathode and mixed oxides of cobalt, nickel and/or lanthanum on the anode [3, 37-39]. The two electrodes are separated by a diaphragm which selectively allows the hydroxyl and water molecules to permeate through it, while restricting the mixing of the evolved

gases. The cell design can be of a tank type or a filter press type. The tank type uses monopolar electrodes fitted in a tank. This monopolar system offers a rugged system with a simple design and construction, but only at the expense of large power consumption. The filter press type uses hundreds of bipolar electrodes stacked together. The reactions taking place at each electrode are given below:

Anode (oxidation): $2OH^-_{(aq)} \rightarrow H_2O_{(l)} + 2e^- + 0.5O_{2\,(g)}$

Cathode (reduction): $2H_2O_{(l)} + 2e^- \rightarrow 2OH^-_{(aq)} + H_{2\,(g)}$

Overall Reaction: $H_2O_{(l)} \rightarrow H_{2\,(g)} + 0.5O_{2\,(g)}$

The major disadvantage of this system is that it uses a highly caustic electrolyte and is unable to produce hydrogen at high pressures. This results in addition of an external compressor, leading to added costs and complexity in the system. The alkaline electrolzer systems have a very low partial load range, limited current density and less efficiency (~ 30 - 35%) [40, 41]. The product gases cross-diffuse through the membrane causing a decrease in the efficiency, since the oxygen gets catalyzed back to water on the cathode side with the evolving hydrogen. The limiting maximum achievable current density is due to the massive ohmic losses across the electrolyte and the membrane. Gas purity is also compromised due to traces of electrolyte which need to be scrubbed. All these factors lead to a very bulky stack design configuration [3, 17, 39].

2.1.2 Solid Oxide Electrolysis

Solid oxide electrolyzer cells (SOEC) operate at high temperatures in the range of 700°C to 1000°C. At these temperatures, water in its vapor state *i.e.* steam is split into hydrogen and oxygen. The heat provides a lot of energy for this endothermic reaction which is favored with

increase in temperature, and hence the electrical energy needed for decomposition of water at such high temperatures is very less [17, 42]. The SOECs have a solid ionic conducting electrolyte, mostly yttria stabilized zirconia which has very good mechanical strength and oxygen ion conductivity at high temperatures. The cathode is usually based on nickel due to its high electrochemical activity. Ceramics with very high active surface are also employed in order to maximize transport of steam and gas. The anodes are usually mixed oxides possessing a perovskite structure such as strontium doped lanthanum manganite ($La_{0.6}Sr_{0.4}MnO_3$) [43, 44]. A tubular or a planar cell design can be employed for these systems. The planar cell design is usually selected as it offers higher power densities, although its sealing is very demanding [43]. The reactions taking place at each electrode are given below:

Anode (oxidation): $2O^{2-}{}_{(g)} \rightarrow O_{2\,(g)} + 4e^-$

Cathode (reduction): $2H_2O_{\,(g)} + 4e^- \rightarrow 2H_{2\,(g)} + 2O^{2-}{}_{(g)}$

Overall Reaction: $2H_2O_{\,(g)} \rightarrow 2H_{2\,(g)} + O_{2\,(g)}$

There are several issues affecting SOEC which include long start-up and shut-down time for the system, bulky system design along with sealing issues; thermal expansion and chemical instability due to the high temperatures used. There is a need for research and development of novel, facile and reduced cost, highly durable materials for SOECs. The durability and endurance of the electrodes is also very poor due to increase in electrical resistance and delamination of the oxygen electrode. Optimization of the material structure and detailed understanding of the electrochemistry and degradation mechanisms is required for large scale production of hydrogen by solid oxide electrolysis [42, 45].

2.1.3 PEM based Water Electrolysis

Polymer Electrolyte Membrane or Proton Exchange Membrane (PEM) based electrolyzer cells employ a solid polymer electrolyte, wherein a solid sulfonated polystyrene membrane (Nafion) is used as an electrolyte. This membrane has a very high protonic conductivity and low crossover rates. Since the electrolyte is a membrane, it is immobilized in the cell and will not lead to any leaching of the same [42, 46]. The PEM electrolyzer system has very compact stack design and can withstand very high pressures. High current densities can be achieved due to very less resistance of the thin polymer electrolyte membrane, and ultra high purity (UHP) hydrogen is produced due to low crossover rates. The high pressure operation helps in delivering the hydrogen at high pressure, thus reducing the energy requirement to compress and store the hydrogen. The widely used electrodes at the anode are iridium oxide (IrO_2) and/or ruthenium oxide (RuO_2) on a titanium support; and platinum on the cathode side [17, 47]. **Figure 2** shows the basic operation of a PEM electrolzer cell. The reactions taking place at each electrode are given below:

Anode (oxidation): $2H_2O_{(l)} \rightarrow O_{2\,(g)} + 4H^+_{(aq)} + 4e^-$

Cathode (reduction): $4H^+ + 4e^- \rightarrow 2H_{2\,(g)}$

Overall Reaction: $2H_2O_{(l)} \rightarrow 2H_{2\,(g)} + O_{2\,(g)}$

Due to the high voltage (> 1.5 V) and harsh acidic conditions in PEM based water electrolysis, the components have to be robust and highly corrosion resistant, especially at the oxygen evolution electrode. Carbon based materials cannot be used such as in PEM fuel cells since they undergo corrosion above 1 V. Hence, titanium and stainless steel supports are used at the anode as supports for the catalysts albeit with no electrochemical activity [47, 48]. The

electrolyte is also corrosive and this requires usage of expensive metal components in the cell design. The noble metal based electro-catalysts used at the electrodes are thus very expensive (Pt, IrO_2, RuO_2) and are still not very durable [39, 49]. More research is therefore required to synthesize cost effective catalysts which are more electrochemically active and robust in the acidic conditions to achieve the maximum power density. This method of hydrogen production can be envisioned for the creation of a novel hydrogen societyin the future, wherein hydrogen (energy carrier) is incorporated in an idealized energy cycle. Here, electricity from renewable energy sources would be the only input used to split water and the only output would be electric power.

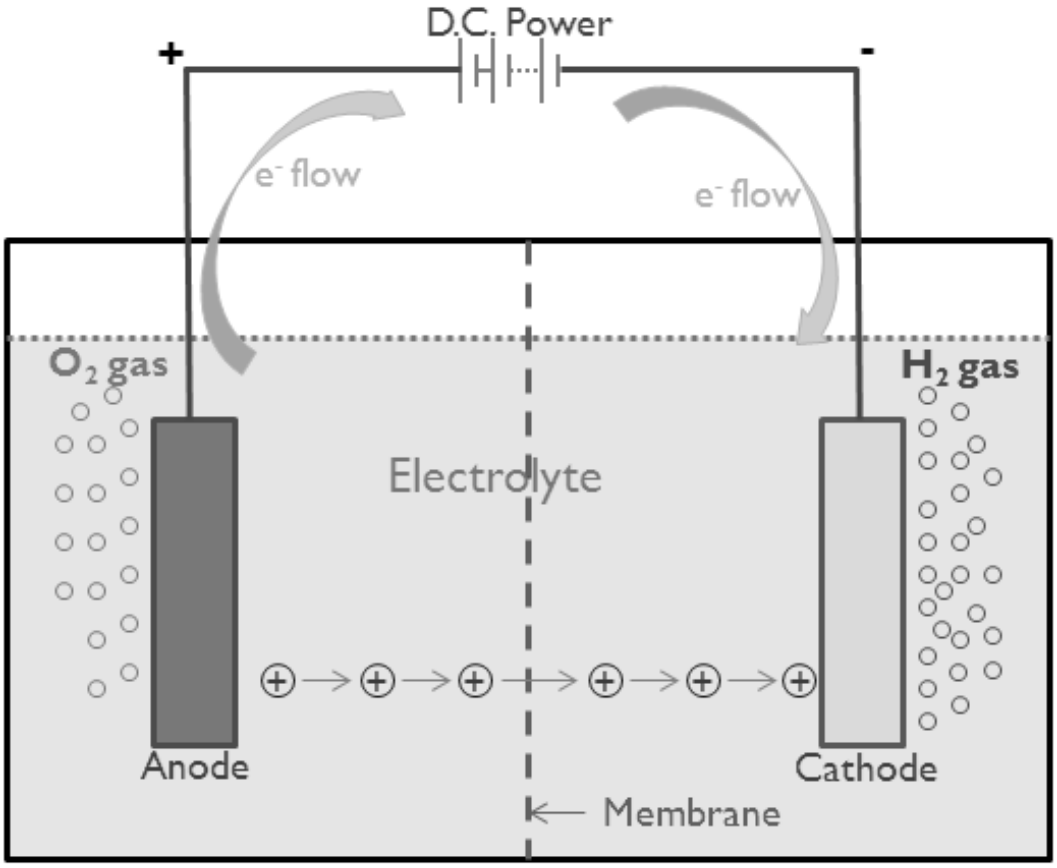

Figure 2. PEM electrolysis schematic diagram

2.2 FUNDAMENTALS

2.2.1 Thermodynamics and Kinetics

The energy required splitting one mole of water into hydrogen and oxygen corresponds to the enthalpy of formation of one mole of water. A part of this enthalpy of the reaction (ΔH_f) can be applied as thermal energy. The Gibbs free energy (ΔG_f) is the minimum amount of the enthalpy of the reaction that needs to be applied *via* electrical energy. From the electrochemists' point of view, the minimum reversible cell voltage needed to be applied can be expressed by the equation $V_r = \Delta G_f / nF$, where 'n' is the number of electrons per mole of product *i.e.* 2 in the case of water electrolysis, and F is the Faraday constant (96485 C/mol). At the standard conditions of temperature and pressure *i.e.* T = 25°C and P = 1 atm, $\Delta G_f \sim 237$ kJ/mol, $\Delta H_f \sim 285$ kJ/mol, and thus, $V_r \sim 1.23$ V. This potential corresponds to the standard reversible cell potential with respect to liquid water electrolysis [15, 42, 50].

The total energy required for splitting water can be supplied by a combination of electricity and heat. If heat cannot be incorporated in the system, the minimum cell voltage becomes related to the enthalpy of the reaction and this is defined as the thermo-neutral voltage. It can be expressed by the equation $V_{th} = \Delta H_f / nF$. At the standard conditions for temperature

and pressure, V_{th} ~ 1.48 V. This demonstrates the reason higher temperatures are more advantageous for water electrolysis from a thermodynamic view point [38, 50].

The cell voltage of an operating electrolysis cell is higher than the thermodynamic ideal cell voltage. The total applied voltage or the real cell voltage can be described as the potential necessary to enhance the electron transfer. The real cell voltage is the sum of the ideal thermodynamic cell voltage (~1.23 V) along with the voltage drop caused due to ohmic resistance (iR) at a particular current density 'i'; the iR drop due to solution, electrode and membrane resistance; and the overpotentials at the cathode and the anode. The overpotentials at the cathode and anode are caused due to irreversible processes occurring at the electrode-electrolyte interface which is termed as the activation overpotential (kinetic limitation). This overpotential is dependent on the rate of exchange of electrons at the electrochemical interface under reversible conditions and on the reaction pathway or mechanism. The electro-catalysts used at the cathode and anode help increase the rate of the reaction at their respective electrodes.

The Tafel equation can be obtained from the Butler-Volmer equation when the reaction is driven infinitely in one specific direction *i.e.* either anodic or cathodic. The anodic Tafel equation is given below:

$\eta = (RT/\alpha F) \ln (i/i_0)$, where 'η' is the overpotential, 'R' is the universal gas constant, 'T' is the temperature (K), 'α' is the transfer co-efficient (0.5) and expresses the activation barrier of the electrochemical reaction, 'i' is the current density, and 'i_0' is the exchange current density. The Tafel slope from this equation is used to determine the reaction kinetics, and is very useful since the slopes are independent of the electrode surface area [51-53].

2.2.2 Reaction Mechanism

The calculated Tafel slope would give an indication of the reaction mechanism. In PEM based water electrolysis, water splitting occurs in the acidic media. Under the harsh acidic conditions, the interactions between hydrogen and the metal cathode is very weak. Thus, hydrogen evolution is much faster at the cathode as compared to oxygen evolution at the anode. The hydrogen evolution reaction is thus expectedly not considered to be the rate determining step [54-56]. The anodic reaction mechanism as reported in literature [53, 55] is given below, wherein the * represents an active site on the metal oxide surface:

$$2H_2O \rightarrow HO^{*} + H_2O + H^{+} + e^{-}$$

$$\rightarrow O^{*} + H_2O + 2H^{+} + 2e^{-}$$

$$\rightarrow HOO^{*} + 3H^{+} + 3e^{-}$$

$$\rightarrow O_2 + 4H^{+} + 4e^{-}$$

The Tafel slope would help determine the limiting step and thus confirm the number of electrons transferred in the course of electrolysis whilst using a particular electro-catalyst. The third reaction is thus the rate determining step of this mechanism and it has been proved theoretically and experimentally in literature [54, 55, 57-59].

3.0 GOALS AND OBJECTIVES

3.1 MOTIVATION

First row transition metal oxides such as AB_2O_4 type spinels (*E.g.* $NiCo_2O_4$, Co_3O_4), ABO_3 perovskites (*E.g.* $LaNiO_3$, $LaCoO_3$) or $A_{1-x}A'_xB_yB'_{1-y}O_3$ perovskite (*E.g.* $Ba_{0.5}Sr_{0.5}Co_{0.8}Fe_{0.2}O_{3-\delta}$) have been identified as cost effective alternatives in alkaline water electrolysis to IrO_2 as anodes in PEM electrolysis. However, although promising, the overall electrochemical response relative to state of the art IrO_2 electro-catalyst indicated the need for further work [2, 3, 27, 28]. Similarly, Nocera *et al.* [18, 26] reported phosphate based catalysts functioning at neutral pH.

In recent years however, it has been reported that PEM based water electrolysis systems offer several advantages over traditional alkaline and neutral pH based water electrolysis technologies. They include higher energy efficiency, greater production rates, increased product purity, use of much less corrosive electrolyte, and offering a more compact design thus rendering PEM electrolysis a simple, sustainable, and cost-effective technology for generating, compressing, and storing hydrogen [15, 16, 24, 31, 32, 37]. In addition, PEM electrolysis can be designed to electrochemically generate hydrogen at pressures of 200 psi or greater, thus eliminating the need for highly expensive mechanical compression which is required for conventional alkaline water electrolysis [16, 37]. Identification of non-precious metal catalysts or catalysts with substantially reduced noble metal contents exhibiting no reduction in

electrochemical activity compared to the noble metal oxide would hence constitute a major breakthrough in PEM based water electrolysis.

3.2 ELECTRO-CATALYST SYSTEMS

In PEM based water electrolysis, rutile type noble metal oxides, IrO_2 and RuO_2, have been identified and considered as gold standards for the oxygen electrode anode electro-catalyst [29-31, 33, 35, 36, 60-62]. Chen *et al.* [63, 64] examined potential oxide supports for oxygen electrode in PEM fuel cells: ebonex (primarily composed of Ti_4O_7), phase pure microcrystalline Ti_4O_7 and $Ti_{0.9}Nb_{0.1}O_2$. However, there is gradual loss of current associated with these supports due to the electrochemical instability of ebonex and Ti_4O_7 at oxygen evolution conditions above 1.6V in 1N H_2SO_4. In the search for electro-catalysts for PEM based water electrolysis, many less expensive and highly corrosion resistant metal oxides such as tin oxide (SnO_2), niobium oxide (Nb_2O_5), tantalum oxide (Ta_2O_5) or titanium oxide (TiO_2) have been explored as excellent alternative anode candidates to currently used expensive IrO_2 or RuO_2 electro-catalysts. Unfortunately, the above mentioned non-noble metal oxides show no catalytic activity for the oxygen evolution reaction in PEM based water electrolysis and furthermore, these systems also exhibit very poor electronic conductivity.

It has been reported that mixed oxides obtained by the addition of cheaper, economical oxides as supports such as SnO_2, Ta_2O_5, Nb_2O_5, TiO_2 with the noble metal oxide electro-catalyst, IrO_2 and/or RuO_2 (*E.g.* IrO_2 - SnO_2, RuO_2 - SnO_2, IrO_2 - Ta_2O_5, IrO_2 - SnO_2 - Nb_2O_5 *etc.*) [24, 29-32, 35, 36, 48, 57, 58, 60, 65-74] would reduce the cost of the noble metal loading by

maintaining the catalytic activity and electronic conductivity similar to the pure noble metal oxide, while also improving the overall corrosion characteristics of noble metal oxide electro-catalysts. However, such *mixed oxides* mixtures result in a decrease in active surface area and electrical conductivity with increase in the less economical non-conductive metal oxide content, and as a result no beneficial effect on the electrochemical performance is perceived with the addition of less expensive oxides beyond a threshold limit (*E.g.* above 50 at.%) [24, 29-32, 36, 48, 65-68, 74].

For instance, IrO_2 + Ta_2O_5 with the composition of 70 at.% IrO_2 has been identified as the best combination in binary oxide system in the presently commercial application owing to their good electroctalytic activities and high stability [30, 48, 68, 74]. However, the electrochemical properties IrO_2+Ta_2O_5 drastically degrade below 50 at.% Ta_2O_5. Therefore, the search for high performance alternative non-noble metal based electro-catalysts or electro-catalysts with significant reduction in noble metal content with comparable activity and durability as the pure noble metal oxides is thus a very pertinent and active area of research with potentially tremendous pay off.

Nb_2O_5 has also been identified as a promising candidate to substitute Ta_2O_5 since it presents similar properties and is cheaper than Ta_2O_5. However, only few studies have been performed based on IrO_2 + Nb_2O_5 as an anode for PEM based water electrolysis [71-73]. On the other hand, IrO_2 - SnO_2 mixtures have been extensively investigated with respect to oxygen evolution in acid environment due to the similarity between the two oxide structures [29, 32, 66]. In the case of IrO_2 + SnO_2 mixed electrodes synthesized by thermal decomposition of the corresponding metal salts on Ti plate, De Pauli *et al.* [29, 66] have reported a noticeable surface enrichment of IrO_2 accompanied by an increase of the surface charge of the mixed oxide in

comparison with the pure oxides and as a result a significant reduction of noble metal loadings has been reported. On the other hand, Marshall *et al.* [31, 32, 60] have reported a decrease in active surface area and electrical conductivity of $(Ir_xSn_{1-x})O_2$ solid solution with increase in SnO_2 content, and as a result no beneficial effect on electrochemical performance has been noticed with addition of SnO_2 to IrO_2 as an anode for PEM water electrolysis.

3.3 PROPOSED NOVEL STRATEGY

In order to develop a cost effective non-noble metal oxide as an electro-catalyst for PEM electrolysis, a two pronged prudent experimental and theoretical approach is required and reported herein to explore different OER electro-catalyst systems for PEM based water electrolysis. The catalyst systems should demonstrate excellent electronic conductivity, high electro-catalytic activity, high specific surface area, and excellent stability at pH ~ 0 and potential of ~ 1.5 V. A key aspect proposed is the generation of a solid solution of the parent noble metal oxide namely, the rutile structure containing varying amounts of the non-noble transition metal or Group IV oxide. By creation of such a solid solution, the inherent noble as well as chemically resistant structural characteristics of the parent, rutile noble metal oxide is maintained while also altering the electronic structure to mimic the parent noble metal oxide as evidenced by the calculation of the Fermi energy level and the corresponding shift in the d band center brought about by the solid solution and the doping of F, the lightweight anion but with remarkable ability to alter the electronic conductivity without compromising the chemical

stability and the electrochemical activity. Accordingly, work has been conducted in the following systems proposed as under.

3.3.1 Fluorine doped IrO_2

Work has been carried out to identify a novel dopant/alloying element for the noble metal oxide electro-catalyst (*E.g.* IrO_2 or RuO_2) in order to improve the catalytic activity compared to pure noble metal oxide electro-catalyst without compromising the corrosion stability of the electro-catalyst. Theoretical studies by *ab initio* calculations have shown fluorine to be a great candidate for a dopant in water electrolysis [55, 56]. Fluorine has been used as a dopant with IrO_2 as the anode electro-catalyst, denoted as IrO_2:F, with 0 to 30 wt.% F doping. IrO_2:F has been synthesized in the form of thin films and nanostructured electro-catalysts. Detailed kinetic studies have also been performed on the same for fundamental understanding of the electrochemical behavior. It shows the viability of F as a potential dopant and also has the potential to be a promising OER anode electro-catalyst that shows significant improvement of catalytic activity as compared to pure IrO_2 [34, 55].

3.3.2 Binary SnO_2 based electro-catalysts

High performance OER electro-catalysts have been synthesized based on highly corrosion resistant and electrically conductive F doped SnO_2. The F doped SnO_2 (SnO_2:F) with different F concentration has been extensively studied as transparent conducting oxide for solar cells, heat mirrors *etc* [75-77]. Due to the improved electronic conductivity of F doped SnO_2 with respect to

pure SnO_2 [78, 79], it would be an attractive alternative to other non-noble metal oxides for PEM based water electrolysis. It is well known that SnO_2:F is electrochemically inactive as an anode for PEM electrolysis IrO_2 or RuO_2 has been added in small amounts to SnO_2:F to synthesize a homogeneous solid solution. The electrochemical performance of the OER electrode consisting of a nanocrystalline solid solution of SnO_2:F and IrO_2 or RuO_2, denoted as $(Ir,Sn)O_2$:F or $(Ru,Sn)O_2$ respectively, was synthesized in the form of thin films and bulk nanomaterials of different compositions ranging from zero noble metal oxide incorporation to pure noble metal oxide.

Reduction in 70 - 80 at.% of the noble metal oxide is achieved when coupled with SnO_2:F. These reduced noble metal electro-catalysts show comparable electrochemical performance to pure IrO_2 / RuO_2. An important aspect is the generation of the nanocrystalline single phase solid solution of $(Ir,Sn)O_2$:F which expectedly displays a more favorable microstructure than the two phase mixtures (*E.g.* $IrO_2 + SnO_2$) with each particle representing the solid solution composition thereby acting as a catalyst unlike the local IrO_2 site alone serving as a catalyst for the two phase mixtures previously reported in the literature [29-32, 35, 67]. As a result, the stability of the catalysts is also not compromised, and it portends to be a potential electro-catalyst for PEM electrolysis with substantial reduction in overall costs [57, 58].

3.3.3 Binary Nb_2O_5 based electro-catalysts

This study demonstrates a novel anode electro-catalyst for PEM water electrolysis based on highly corrosion resistant niobium oxide. Nb_2O_5 is known for its applications in metallurgy for production of robust materials with extreme hardness, electrochromic coatings, and

nanocrystalline solar cells [80, 81]. Niobium oxide has previously been studied as a support along with IrO_2 and/or RuO_2 as a thin film on titanium substrate for water electrolysis [71-73, 82]. But, the electrochemical properties, catalytic activity and stability degrade when the noble metal oxide content is reduced below ~50 at.%. In this approach, F doped Nb_2O_5 was used in order to improve the electrical conductivity of iridium oxide. The single phase solid solution of $(Ir,Nb)O_2$:F has been synthesized in the nanopowder form by a two step sol-gel approach. This yields a favorable microstructure and results in ~ 75 at.% decrease in the IrO_2 content. The stability of the catalysts is superior to the commercially available IrO_2.

3.3.4 Ternary metal oxide electro-catalysts

A novel support has been identified for the electro-catalysts has been shown to not only decrease the precious metal loading without compromising the electrochemical activity of the noble metal oxide electro-catalyst, but also improves the corrosion stability for the OER. In this study, IrO_2 has been used as anode electro-catalyst due to its higher corrosion resistance in the PEM electrolysis condition compared to RuO_2, though it shows slightly lower electrochemical activity than RuO_2 [30, 83]. On the grounds of the very promising performances shown by both $(Ir,Sn)O_2$ and $(Ir,Nb)O_2$ as an anode electro-catalyst, investigation has been carried out on the synthesis and characterization of composite ternary Ir-Sn-Nb oxide systems.

In this direction, a single phase solid solution of IrO_2, SnO_2 and NbO_2 of compositions $(Ir_{1-2x}Sn_xNb_x)O_2$ with x ranging from 0 to 0.50, denoted as $(Ir,Sn,Nb)O_2$, has been synthesized by thermal decomposition of a mixture of metal salt precursors on Ti foil as a thin film OER catalyst for PEM electrolysis. For better understanding of the electrochemical activity, long term

stability of the (Ir,Sn,Nb)O_2 electro-catalyst has also been carried out to complement the present experimental study. Reduction in ~ 60 at.% IrO_2 gives similar electrochemical performance and much enhanced chemical robustness (durability) than pure IrO_2 [24]. This is due to the stronger Nb-O bonds as compared to the Ir-O bonds incorporated in the IrO_2 lattice structure.

As F helped in increasing the activity of the (Ir,Sn)O_2 and (Ir,Nb)O_2 electro-catalysts leading to much enhanced performance, the novel ternary oxide electro-catalyst has been doped with fluorine in order to improve the catalytic activity in order to further decrease the amount of IrO_2. Correspondingly, F doped (Sn,Nb)O_2 has been used as a support with the noble metal oxide as the catalyst for anode oxidation in PEM based water electrolysis [59]. This novel catalyst system of F doped Ir-Sn-Nb oxide, denoted as (Ir,Sn,Nb)O_2:F, helps increase the electro-catalytic activity and improve the durability of the electro-catalyst with further reduction in IrO_2 content.

4.0 EXPERIMENTAL DETAILS

4.1 THIN FILM ELECTRO-CATALYST PREPARATION

4.1.1 F doped IrO_2

Iridium tetrachloride [$IrCl_4$, 99.5%, Alfa Aesar] and ammonium fluoride [NH_4F, Alfa Aesar] were used as the sources for Ir oxide and F, respectively. Stock solution corresponding to $IrCl_4$ of desired compositions was dissolved in absolute ethanol inside an atmosphere controlled glove box (MBraun Unilab Work station) to prevent any undesired side reaction. On the other hand, NH_4F was dissolved in ethanol-deionised (DI) water mixture (5:1 volume ratio). The stock solutions $IrCl_4$ and NH_4F of desired compositions ($NH_4F/IrCl_4$: 0.04, 0.085, 0.14, 0.19 and 0.33) are then mixed together to synthesize IrO_2: x wt.% F electro-catalyst with x = 0, 5, 10, 15, 20 and 30, respectively. The resulting solution was then spin coated on pretreated titanium substrates (99.99%, 0.005 in thick, Alfa Aesar) of ~ 1 cm^2 areas (Specialty coating Systems Inc, Model P6712) with rotating speed of 500 rpm for 10 sec. Prior to coating, the Ti substrate was sand blasted and then etched in boiling HCl (30 wt.%) for 30 minutes in order to ensure maximum adhesion of the coating. The HCl treated Ti foil was washed with purified water by the Milli-Q system and dried at 130^{o}C before coating. The thin film precursors deposited on the pretreated titanium substrate were dried at 60°C for 2 hours. Following this, they were thermally treated to

400°C for 4 hours in air to decompose the precursors and, as a result IrO_2:F films of different compositions are generated on the Ti foils. The loading of the IrO_2:F deposited on the Ti foil is ~ 0.3 mg/cm^2 irrespective of the different compositions.

4.1.2 Binary F doped (Ir,Sn)O_2

Iridium tetrachloride [$IrCl_4$, 99.5%, Alfa Aesar], tin (II) chloride dihydrate [$SnCl_2$. $2H_2O$, 98%, Alfa Aesar] and ammonium fluoride [NH_4F, 98%, Alfa Aesar] were used as the sources for Ir, Sn and F, respectively. Stock solution corresponding to $IrCl_4$ and $SnCl_2.2H_2O$ of the desired compositions were dissolved in absolute ethanol inside an atmosphere controlled glove box and NH_4F was dissolved in ethanol-DI water mixture (5:1 volume ratio). The stock solutions $IrCl_4$, $SnCl_2.2H_2O$ and NH_4F of composition $(Ir_ySn_{1-y})O_2$: x wt.% F, where y ranges from 0 to 1 and x = 0, 5, 10 and 15 are then mixed together to synthesize (Ir,Sn)O_2:F electro-catalyst. The resulting solution was then spin coated on the pretreated titanium substrates (99.99%, 0.005 in thick, Alfa Aesar) of ~ 1 cm^2 areas (Specialty coating Systems Inc, Model P6712) with rotating speed of 500 rpm for 10 sec. Prior to coating, the Ti substrate was sand blasted and then etched in boiling HCl (30 wt.%) for 30 minutes in order to ensure maximum adhesion of the coating. The HCl treated Ti foil was washed with purified water by the Milli-Q system and dried at 130^{o}C before coating. The thin film precursors deposited on the pretreated titanium substrate were dried at 60°C for 2 hours. Following this drying, they were thermally treated at 400°C for 4 hours in air to decompose the precursors and, as a result gives the (Ir,Sn)O_2:F films of different compositions are generated on the Ti foils with the loading being ~ 0.3 mg/cm^2 irrespective of the different compositions.

4.1.3 Binary F doped $(Ru,Sn)O_2$

Ruthenium trichloride [$RuCl_3$, 99.9%, Alfa Aesar], tin (II) chloride dihydrate [$SnCl_2.2H_2O$, 98%, Alfa Aesar] and ammonium fluoride [NH_4F, 98%, Alfa Aesar] were used as the sources for Ru, Sn and F, respectively. Stock solution corresponding to $RuCl_3$ and $SnCl_2.2H_2O$ of the desired compositions were dissolved in absolute ethanol inside an atmosphere controlled glove box and NH_4F was dissolved in ethanol-DI water mixture (5:1 volume ratio). The stock solutions $RuCl_3$, $SnCl_2.2H_2O$ and NH_4F of composition $(Ru_ySn_{1-y})O_2$: x wt.% F, where y ranges from 0 to 1 and x = 0, 5, 10 and 15 are then mixed together to synthesize $(Ru,Sn)O_2$:F electro-catalyst. The resulting solution was then spin coated on the pretreated titanium substrates (99.99%, 0.005 in thick, Alfa Aesar) of ~ 1 cm^2 areas (Specialty coating Systems Inc, Model P6712) with rotating speed of 500 rpm for 10 sec. Prior to coating, the Ti substrate was sand blasted and then etched in boiling HCl (30 wt.%) for 30 minutes in order to ensure maximum adhesion of the coating. The HCl treated Ti foil was washed with purified water by the Milli-Q system and dried at 130^oC before coating. The thin film precursors deposited on the pretreated titanium substrate were dried at 60°C for 2 hours. Following this drying, they were thermally treated at 400°C for 4 hours in air to decompose the precursors and, consequently generate $(Ru,Sn)O_2$:F film of different compositions are generated on the Ti foils. The loading of the $(Ru,Sn)O_2$:F deposited on the Ti foil is ~ 0.3 mg/cm^2 irrespective of the different compositions.

4.1.4 Ternary (Ir,Sn,Nb)O_2

Figure 3 shows the molar ratio of Ir:Sn:Nb compositions chosen to investigate as an anode electo-catalyst for PEM based water electrolysis. Iridium tetrachloride [$IrCl_4$, 99.5%, Alfa Aesar], tin (II) chloride dihydrate [$SnCl_2$. $2H_2O$, 98%, Alfa Aesar] and niobium chloride [$NbCl_5$, 99.95%, Alfa Aesar] were used as the sources for Ir, Sn and Nb, respectively. Stock solution corresponding to $IrCl_4$, $SnCl_2.2H_2O$ and $NbCl_5$ of desired compositions were dissolved in absolute ethanol inside the glove box to prevent any undesired side reaction. The stock solutions $IrCl_4$, $SnCl_2.2H_2O$ and $NbCl_5$ of composition $(Ir_{1-2x}Sn_xNb_x)O_2$, where x ranges from 0 to 1 are then mixed together to synthesize (Ir,Sn,Nb)O_2 electro-catalyst. The resulting solution was then spin coated on pretreated titanium substrates (99.99%, 0.005 in thick, Alfa Aesar) of ~ 1 cm^2 areas (Specialty coating Systems Inc, Model P6712) with rotating speed of 500 rpm for 10 sec. Prior to coating, Ti substrate was sand blasted and then etched in boiling HCl (30 wt.%) for 30 min in order to ensure a maximum adhesion of the coating. The HCl treated Ti foil was washed with purified water by the Milli-Q system and dried at 130^oC before coating. The thin film precursors deposited on the pretreated titanium substrate were dried at 60°C for 2 hours. Following this, they were thermally treated to 400°C for 4 hours in air to decompose the metal precursor and, as a result (Ir,Sn,Nb)O_2 film of different compositions is formed on the Ti foil. The loading of (Ir,Sn,Nb)O_2 deposited on the Ti foil is ~ 0.3 mg/cm^2 irrespective of compositions.

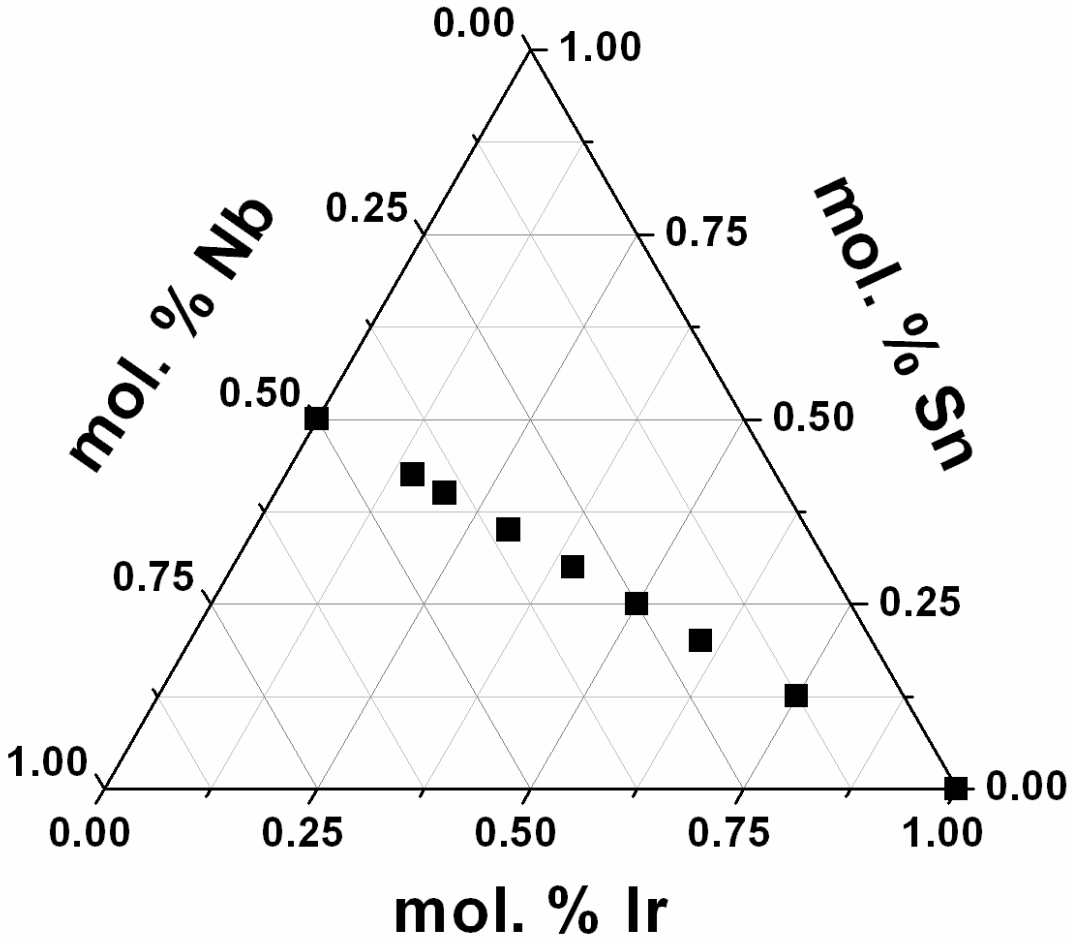

Figure 3. Molar ratio of (Ir,Sn,Nb)O_2 chosen to investigate as an anode electro-catalyst in PEM water electrolysis

4.1.5 Ternary F doped (Ir,Sn,Nb)O_2

Iridium tetrachloride [$IrCl_4$, 99.5%, Alfa Aesar], tin (II) chloride dihydrate [$SnCl_2$. $2H_2O$, 98%, Alfa Aesar], niobium chloride [$NbCl_5$, 99.95%, Alfa Aesar] and ammonium fluoride [NH_4F,

98%, Alfa Aesar] were used as the sources for Ir, Sn, Nb and F, respectively. Stock solution corresponding to $IrCl_4$, $SnCl_2.2H_2O$ and $NbCl_5$ of desired compositions were dissolved in absolute ethanol inside the glove box to prevent any undesired side reaction. NH_4F was dissolved in ethanol-DI water mixture (5:1 volume ratio). The stock solutions $IrCl_4$, $SnCl_2.2H_2O$, $NbCl_5$ and NH_4F of composition $(Ir_{0.3}Sn_{0.35}Nb_{0.35})O_2$: x wt.% F, where x = 0, 5, 10, 15 and 20 are then mixed together to synthesize $(Ir,Sn,Nb)O_2$:F electro-catalyst. The resulting solution was then spin coated on pretreated titanium substrates (99.99%, 0.005 in thick, Alfa Aesar) of ~ 1 cm^2 areas (Specialty coating Systems Inc, Model P6712) with rotating speed of 500 rpm for 10 sec. Prior to coating, Ti substrate was sand blasted and then etched in boiling HCl (30 wt.%) for 30 min in order to ensure a maximum adhesion of the coating. The HCl treated Ti foil was washed with purified water by the Milli-Q system and dried at 130^oC before coating. The thin film precursors deposited on the pretreated titanium substrate were dried at 60°C for 2 hours. Following this, they were thermally treated to 400°C for 4 hours in air to decompose the metal precursors and, as a result $(Ir,Sn,Nb)O_2$:F film of different compositions is generated on the Ti foil with the loading being ~ 0.3 mg/cm^2 irrespective of the different compositions.

4.2 NANOPARTICULATE CATALYST SYNTHESIS

4.2.1 F doped IrO_2

Iridium tetrachloride [$IrCl_4$, 99.5%, Alfa Aesar], and ammonium fluoride [NH_4F, 98%, Alfa Aesar] were used as the precursor sources for Ir and F, respectively. IrO_2:F was synthesized

using the modified Adams fusion method, first reported by Adams *et al.* [84] and used by other researchers as well [67, 85]. The precursors were taken in stoichiometric amounts and completely dissolved in D.I. water by the Milli-Q system [18.2 MΩ.cm deionized water; Milli-Q Academic, Millipore]. They were then mixed with excess of sodium nitrate [$NaNO_3$, 99%, Alfa Aesar] dissolved in D.I. water. The resulting mixture was homogenized by stirring vigorously for 2 hours and the water is then carefully evaporated at 60°C. The mixture is then introduced into a furnace wherein it is heated to 500°C at a ramp rate of 50 K/min, and then held at 500°C for 1 hour. The salt mixture is then washed multiple times with D.I. water in order to remove all the excess salt. The resulting powder is then dried in an oven at 60°C for 24 hours to form the IrO_2:x wt.% F electro-catalyst, where x ranges from 0 to 20.

4.2.2 Binary F doped (Ir,Sn)O_2

Iridium tetrachloride [$IrCl_4$, 99.5%, Alfa Aesar], tin (II) chloride hydrate [$SnCl_2$. xH_2O, 99.995%, Alfa Aesar] and ammonium fluoride [NH_4F, 98%, Alfa Aesar] were used as the precursor sources for Ir, Sn and F, respectively. For synthesizing SnO_2:F, a mixed-surfactant template route has been employed as reported previously in literature [86]. A mixed cationic surfactant Cetyl trimethylammonium bromide [CTAB, 95%, Aldrich] is used for preparing undoped and fluorine doped SnO_2. CTAB is dissolved completely in D.I. water by the Milli-Q system [18.2 MΩ.cm deionized water, Milli-Q Academic, Millipore] to which a solution of 6 wt.% ammonium hydroxide (Fisher Scientific) is added. After homogenizing this mixture, a solution of tin chloride hydrate dissolved in D.I. water is introduced that gave a white slurry. For preparing SnO_2:F, NH_4F dissolved in D.I. water is also introduced after the addition of

$SnCl_2.xH_2O$. The resulting solution is vigorously stirred for 4 hours. It is then aged at room temperature for 48 hours. The precipitate obtained after filtration is thoroughly washed with D.I. water. It is then dried in an oven at 50°C followed by heat treatment in air at 300°C which resulted into SnO_2:F. For the preparation of (Ir,Sn)O_2:F, $IrCl_4$ was dissolved in ethanol along with the appropriate amount of the as-prepared SnO_2 or SnO_2:F. The solution was then dried in an alumina crucible in an oven at 60°C for 3 hours. This crucible was then subjected to heat treatment in air at 400°C for 4 hours in order to form $(Ir_xSn_{1-x})O_2$: y wt.% F, where x ranges from 0.2 to 0.8 and y = 0 and 10.

4.2.3 Binary F doped (Ir,Nb)O_2

Iridium tetrachloride [$IrCl_4$, 99.5%, Alfa Aesar], niobium (V) chloride [$NbCl_5$, 99.95%, Alfa Aesar] and trifluoroacetic acid [CF_3COOH, 99%, Alfa Aesar] were used as the sources or precursors for Ir, Nb and F, respectively. For preparing undoped and fluorine doped niobium oxide, a procedure similar to the sol-gel method previously reported in literature is used [87]. $NbCl_5$ powder was dissolved in absolute ethanol (200 proof, Fisher Scientific) inside an atmosphere controlled glove box (MBraun Unilab Work station) to prevent any undesired side reaction which yielded a clear yellow solution. Preparation of 10 wt.% F doped Nb_2O_5 was carried out using trifluoroacetic acid dissolved in ethanol followed by mixing with $NbCl_5$ solution. This solution was then added to 0.3 M ammonium hydroxide solution. The mixture is then washed with D.I. water multiple times and a white precipitate is obtained. The precipitate is taken in a round bottom flask which is kept under ice. 6 wt.% hydrogen peroxide is then dispersed in to the precipitate and the mixture is stirred for *c.a.* 15 minutes in ice until a

transparent yellow sol is obtained. This sol is then allowed to gel in a sealed round bottom flask at 75°C for 24 hours. The gel is then dried at 75°C for 48 hours to form amorphous 10 wt.% F doped Nb_2O_5 or undoped Nb_2O_5. The preparation of F doped $(Ir,Nb)O_2$ was performed by dissolving $IrCl_4$ in ethanol along with the appropriate amount of the as-prepared Nb_2O_5 or Nb_2O_5:F. This solution was then dried in a crucible in an oven at 60°C for 3 hours and subsequent heat treatment in air at 400°C for 4 hours in order to form $(Ir_xNb_{1-x})O_2$: y wt.% F, where x ranges from 0.2 to 0.8 and y = 0 and 10.

4.3 PHYSICAL AND CHEMICAL CHARACTERIZATION

4.3.1 X-ray Characterization

In order to perform qualitative phase analysis, all the synthesized materials were characterized by X-ray diffraction (XRD) using Philips XPERT PRO system employing CuK_α (λ = 0.15406 nm) radiation with operating voltage and current at 45kV and 40mA, respectively. The XRD peak profile of the thin films of different compositions was analyzed using Pseudo-Voigt function to determine the Lorentzian and Gaussian contribution of the peak. The integral breadth of the Lorentzian contribution, determined from peak profile analysis using single line approximation method after eliminating the instrumental broadening and lattice strain contribution, is used in the Scherrer formula to calculate the effective crystallite size [88].

4.3.2 Specific surface area Determination

The specific surface area of the nanopowders synthesized as anode electro-catalysts for PEM water electrolysis was analyzed using the common nitrogen adsorption / desorption method pioneered by Brunauer-Emmett-Teller, commonly referred to as BET technique. Each sample was first vacuum degassed, weighed (Denver Instruments SI403), and then tested using a Micromeritics ASAP 2020. Multipoint BET surface areas are reported for all synthesized powders.

4.3.3 Thermogravimetric Analysis

In order to understand the phase formation and decomposition temperature, thermogravimetric and differential thermal analysis (TGA-DTA) has been conducted on the fluorine doped nanostructured powders using a TGA-DTA machine (Netzsch STA 409PC/4/H/Luxx TG-DTA). The TGA-DTA analysis was carried out employing a heating rate of 10°C/min from room temperature up to 700°C in air. A small quantity of the material was loaded into an alumina crucible and placed into the Netzsch STA 409PC/4/H/Luxx TG-DTA instrument. A protective ultra high purity (UHP) argon gas flow of 40 ml/min and a carrier gas flow *i.e.* air of 25 ml/min was used. The gas flows were allowed to stabilize for ~ 30 minutes before the materials are tested.

4.3.4 Microstructure Analysis

To investigate the microstructure of the thin film electrodes, scanning electron microscopy (SEM) and transmission electron microscopy (TEM) was conducted. Quantitative elemental analysis and distribution of elements (x-ray mapping) was investigated using the energy dispersive X-ray spectroscopy (EDX) analyzer integrated into the SEM machine. Philips XL-30FEG equipped with an EDX detector system comprised of an ultrathin beryllium window and Si(Li) detector operating at 20 kV was employed for the secondary electron (SE) image, elemental and x-ray mapping analyses.

JEOL 4000EX operating at 400 kV was employed for conducting TEM analysis to evaluate the particle size and the structure. High resolution transmission electron microscopy (HRTEM) analysis was conducted on the samples using JEOL JEM - 2100F to further investigate the morphology. For the thin films, the particles are obtained by mechanically abrading the powders from top of the several micron thick films synthesized by spin coating techniques. The TEM analysis samples are prepared by dispersing the catalyst in ~ 5 ml of ethanol and ultrasonicating for 10 minutes. A Formvar carbon coated 300 mesh Cu grid (Electron Microscopy Sciences) was placed on a piece of filter paper on which the ultrasonicated solution was pipetted.

4.3.5 X-ray Photoelectron Spectroscopy

X-ray photoelectron spectroscopy (XPS) was done on selected electro-catalysts in order to determine the electronic states of the elements that exist in the alloy. The catalysts analyzed by

XPS used a Physical Electronics (PHI) model 32-096 X-ray source control and a 22-040 power supply interfaced to a model 04-548 X-ray source with an Omni Focus III spherical capacitance analyzer (SCA). The system is routinely operated within the pressure range of 10^{-8} to 10^{-9} Torr (1.3×10^{-6} to 1.3×10^{-7} Pa). The system was calibrated in accordance with the manufacturer's procedures utilizing the photoemission lines E_b of Cu $2p_{3/2}$ (932.7 eV), E_b of Au $4f_{7/2}$ (84 eV) and E_b of Ag $3d_{5/2}$ (368.3 eV) for a magnesium anode. All the reported intensities are experimentally determined peak areas divided by the instrumental sensitivity factors. Charge correction was obtained by referencing the adventitious C 1s peak to 284.8 eV.

4.4 ELECTROCHEMICAL CHARACTERIZATION

4.4.1 Set-up

Electrochemical characterization was conducted on all the synthesized electro-catalysts using a five port jacketed reaction cell (Ace Glass Inc.) in which was assembled a 3-electrode test system as shown in **Figure 4**. The testing was executed using a VersaSTAT 3 (Princeton Applied Research). A solution of 1 N sulfuric acid was used as the electrolyte which also served as the fuel. The solution is kept at a constant temperature of 40°C using a Fisher Scientific 3006S Isotemp Refrigerator Circulator. The reference electrode was a XR 200 mercury/mercurous sulfate electrode [Hg/Hg_2SO_4, Radiometer Analytical] which has a potential of ~ +0.654 V with respect to the Standard Hydrogen Electrode (SHE / NHE). Platinum foil (Alfa Aesar, 0.25 mm thick, 99.95%) was used as the counter electrode.

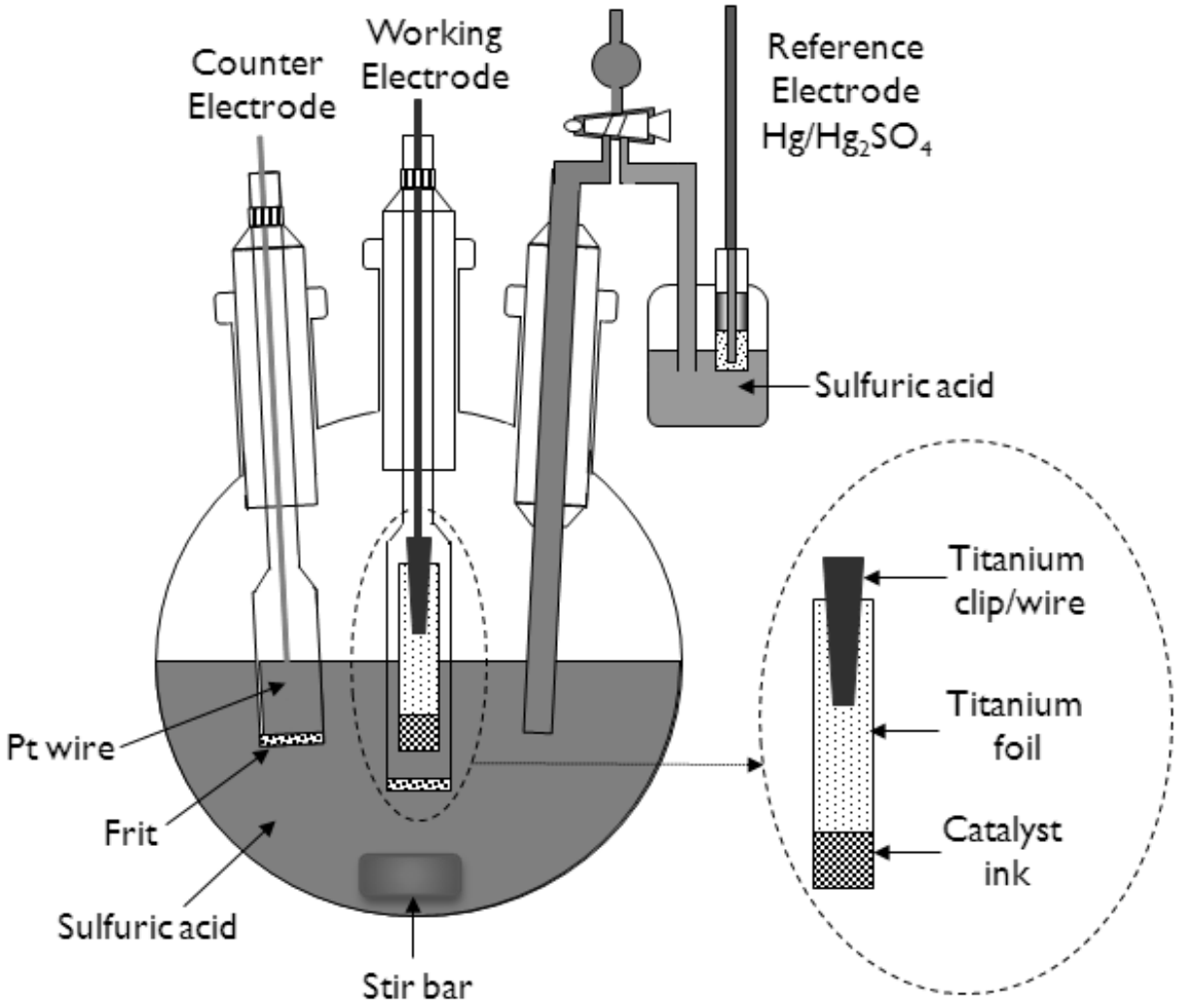

Figure 4. Three electrode cell set-up for electrochemical testing

The thin films of IrO_2:F, $(Ir,Sn)O_2$:F, $(Ru,Sn)O_2$:F, $(Ir,Sn,Nb)O_2$ and $(Ir,Sn,Nb)O_2$:F of different compositions coated on the Ti foil were used as the working electrode with an exposed surface area ~ 1 cm^2 with a total loading of ~ 0.3 mg/cm^2 for each system.

For the nanoparticulate electro-catalysts, the working electrodes were prepared by uniformly spreading the catalyst ink on porous titanium foil [50 % porosity, Accumet Materials

Co.] on an area of ~ 1 cm^2. The catalyst ink consisted of 85 wt.% catalyst and 15 wt.% Nafion 117 solution [5 wt.% solution in lower aliphatic alcohols, Sigma-Aldrich]. The total loading on the Ti foil for all the electro-catalyst compositions was ~ 0.3 mg/cm^2.

4.4.2 Polarization Testing

A current - voltage scan is conducted by cycling between 0 to 2 V (*vs.* NHE) at 10 mV/s for multiple cycles and the current response is measured. Once complete, polarization curves are recorded by stepping the voltage from open circuit potential (OCP) to 2V (*vs.* NHE) while measuring the current response. This difference between the two tests is that the polarization test contains information about the onset potential of the system which can prove valuable in understanding the viability of the anode electro-catalysts.

4.4.3 Electrochemical Impedance Spectroscopy (EIS)

Electrochemical Impedance Spectroscopy (EIS) has been used to determine the solution resistance, electrode resistance and the polarization resistance of the electro-catalyst using a suitable circuit model such as $R_s(R_eQ_1)(R_{ct}Q_{dl})$, where R_s is the solution resistance, R_e is the electrode resistance, R_{ct} is the polarization / charge transfer resistance, Q_1 is the constant phase element (CPE) and Q_{dl} includes both the double layer capacitance (C_{DL}) and pseudocapacitance (C_{PC}) [48, 52, 85]. The ohmic resistance (R_Ω) has been be used to perform the ohmic loss (iR_Ω) correction, whereas the polarization resistance (R_{ct}) has been used to understand the electrochemical activity of the electro-catalyst. The uncorrected polarization curve and the non-

linear Tafel plot encounter a large amount of ohmic / solution resistance (R_s) which is determined from the EIS plot at high frequencies. This helps us in preparing the linear Tafel plots and the iR corrected polarization curves. The plots after correcting for the ohmic loss help us in evaluating the inherent electro-catalytic property of the electrodes. The Tafel plot after iR correction is given by the following equation:

$$\eta = b \log i + a$$

Here 'η' is the overpotential, 'b' is the Tafel slope, 'i' is the current density and 'a' determines the exchange current density. The corresponding Tafel slope (b) is used to determine the reaction kinetics [51, 52]. Electrochemical impedance spectroscopy has been carried out in the frequency range of 100 mHz - 100 kHz using the electrochemical work station (VersaSTAT 3, Princeton Applied Research). Impedance data has been modeled by using the ZView software from Scribner Associates.

4.4.4 Kinetic Studies

Rotating disk electrode (RDE) experiments have been carried out on select electro-catalysts in order to obtain information about the kinetics and mechanism of the electrochemical reaction. It helps confirm the number of electrons getting transferred in the OER and calculate the apparent activation energy of the reaction. The RDE tests were performed in a three electrode system, using the same reference electrode and counter electrode as described before. A titanium disk insert [5 mm OD, 4 mm thick, mirror polish; Pine Research Instrumentation] was used for the working electrode. The catalyst ink was deposited on the Ti disk and dried in an ethanol saturated environment overnight. The disk was then heated to 130°C for 2 hours.

A multiple small potential step measurement has been used for all RDE measurements, first used by Chu *et al.* [89]. Potential steps of 5 mV are given starting from open circuit potential and current is recorded at every potential for 16 seconds. The last value of the current is taken into consideration for accurate analysis *i.e.* there is a decay time of 15 seconds in order to ensure that the electrode double layer charging current and the adsorption current is negligible [89]. The RDE experiments have been done by varying speeds from 500 rpm to 2000 rpm. The Koutecky - Levich plot, widely used for RDE studies [89-91], is represented by the following equations which involve the kinetic current (i_k) and Levich current (i_L), as given below:

$$i^{-1} = i_k^{-1} + i_L^{-1}$$

$$i_k = k\ n\ A\ F\ C$$

$$i_L = 0.62\ n\ F\ A\ D^{2/3}\ \omega^{1/2}\ \upsilon^{-1/6}\ C$$

Here, 'i' is the current (A), 'k' is the kinetic rate constant of the reaction (cm/s), 'n' is the electron transfer number, 'A' is the electrode area (0.19625 cm^2), 'F' is the Faraday constant (96485 As/mol), 'C' is the concentration of reactive species (1.3 x 10^{-6} mol/cm^3), 'D' is the diffusion coefficient (1.7 x 10^{-5} cm^2/s), 'ω' is the rotation rate (radians/s), and 'υ' is the viscosity (0.01 cm^2/s) [91-95]. The slope of the Koutecky - Levich plot *i.e.* i^{-1} *vs.* $\omega^{-1/2}$ helps determine the number of electrons (n) transferred in the reaction and the intercept gives the kinetic rate constant (k) of the reaction.

The influence of temperature on the OER has been studied for selected anode catalysts in order to calculate the apparent activation energy (E_a). In the RDE setup, a high rotation speed of 1500 rpm was used and multiple small potential step measurement as mentioned before was carried out in the temperature range of 25°C - 70°C. The Arrhenius relation is given below:

$$i = k_0 \exp(-E_a/RT)$$

Here, 'k_0' is the pre-exponential factor, 'E_a' is the apparent activation energy (J/mol), 'R' is the universal gas constant (8.314 J/mol K), and 'T' is the temperature (K). A plot of ln i *vs.* T^{-1} *i.e.* the Arrhenius plot would help in determination of the apparent energy of activation [96-99].

4.4.5 Chronoamperometry

In order to study the long term structural stability or chemical robustness of the synthesized electro-catalysts, chronoamperometry (CA) *i.e.* current signal as a function of time has been conducted for the anode catalysts. Testing of the electrodes was performed for 12 - 48 hours using 1 N H_2SO_4 as the electrolyte (fuel) at 40°C under a constant voltage of ~ 1.65 V (*vs*. NHE) without iR correction.

Elemental analysis of the media collected after the stability testing (CA) was performed by inductively coupled plasma optical emission spectroscopy (ICP-OES, iCAP 6500 duo Thermo Fisher) in order to determine the amount of iridium, ruthenium, tin and/or niobium leached in the solution. Standards for getting the calibration lines were procured from Sigma Aldrich. They were then diluted with the stock solution used for CA tests *i.e.* 1 N sulfuric acid.

4.4.6 Single full cell test Analysis

The catalyst ink for the anode and cathode consisted of 85 wt.% catalyst and 15 wt.% Nafion 117 solution (5 wt.% solution in lower aliphatic alcohols, Sigma-Aldrich). For the single cell testing, a membrane electrode assembly was fabricated by using a Nafion 115 membrane sandwiched between the two gas diffusion electrodes coated with the catalyst ink. The cathode catalyst used

for the single cell test was Platinum black (Sigma Aldrich) supported on a Teflon treated carbon paper (Electrochem Inc.). The anode materials were the best lectro-catalyst composition powders synthesized *i.e.* IrO_2:10 wt.% F, $(Ir_{0.3}Sn_{0.7})O_2$:10 wt.% F and $(Ir_{0.25}Nb_{0.75})O_2$:10 wt.% F which were also compared with pure IrO_2 (undoped). The backing layer used on the anode side was titanium felt (60% porosity, Electrochem Inc.). The Nafion 115 membrane was pretreated first with a 3 wt.% hydrogen peroxide solution to its boiling point in order to oxidize any organic impurities. Subsequently, it was boiled in D.I. water followed by immersion in a boiling 1 N sulfuric acid solution to eliminate any metallic impurities. Finally, it is treated multiple times in D.I water to remove any traces of remnant acid. This membrane is then stored in D.I. water to avoid dehydration. The membrane electrode assembly (MEA) was then fabricated by placing the two nafion impregnated electrodes (anode and cathode) on both sides of the pretreated nafion membrane. This assembly was then hot-pressed in a 25T hydraulic lamination hot press with dual temperature controller (MTI Corporation) at a temperature of 125°C. The pressure applied was approximately 40 atm for ~ 30 seconds to ensure good contact between the electrodes and the membrane. This 5 layer MEA is then used in the single cell testing.

The 5 layer MEA prepared was then sandwiched between two Teflon gaskets of 5 mils thickness. The area of the electrodes and the hole in the gaskets was a square area of 5 cm^2. This assembly is then placed in Proton's test cell and the tests were conducted at Proton OnSite (Wallingford, CT). All the samples were heat soaked by flowing 65°C water throughout the cell for 1 hour prior to testing. The polarization curve was taken at 50°C by ramping up the current, stepping in 1 minute intervals of 100 mA/cm^2. The polarization curve is then run back down at 1 minute intervals. The polarization curves were then run back up and down at 1 minute intervals until the forward and reverse scans basically overlaid each other.

5.0 RESULTS AND DISCUSSION

5.1 THIN FILMS

5.1.1 F doped IrO_2

5.1.1.1 Structural Analysis

Figure 5 shows the XRD patterns of thin film IrO_2:F with 10, 20 and 30 wt.% F synthesized by thermal decomposition of homogeneous mixture of $IrCl_4$ and NH_4F ethanol-DI water solution coated on Ti foil at 400°C for 4 hours. The XRD patterns of IrO_2:F of different compositions, shows a rutile type tetragonal structure similar to pure IrO_2, which suggests the formation of complete solid solution between IrO_2 and F without any undesirable phase formation (*E.g.* IrF_3). The lattice parameter (a ~ 0.4547 nm, c ~ 0.3136 nm) and molar volume of IrO_2:F (~ 19.53 ± 0.04 cm^3/mol) of different compositions, calculated using least square refinement techniques, is comparable with pure IrO_2 (~ 19.64 ± 0.04 cm^3/mol) [24] which suggest that F^- substitution for O^{-2} has no significant effect on the molar volume of IrO_2:F. This may be largely due to the fact that the ionic radius of O^{-2} (125pm) is comparable with F^{-1} (120pm). The effective crystallite size of IrO_2:F, calculated using the Scherrer formula from the integral breadth of the Lorentzian contribution determined from peak profile analysis using single line approximation method after

eliminating the instrumental broadening and lattice strain contribution [88], is in the range of ~ 4 - 6 nm irrespective of compositions indicating the nanocrystalline nature of the catalyst.

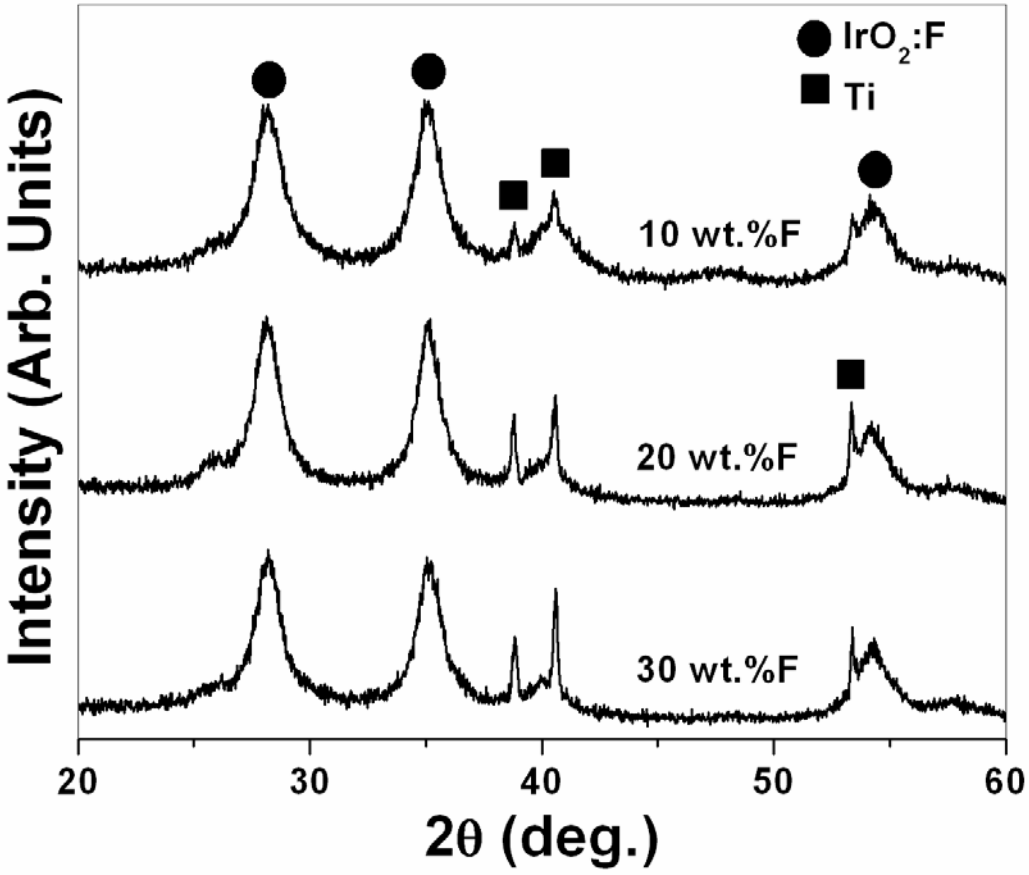

Figure 5. XRD patterns of thin film IrO2:F with 10, 20 and 30 wt.% F coated on Ti foil

The presence of elemental Ir and O in the IrO_2:F film of different compositions has also been confirmed using energy dispersive X-ray spectroscopy analysis (EDX) attached to the SEM. However, the presence of F could not be detected in the EDX analysis. Suitable spectroscopic techniques, such as wavelength dispersive x-ray florescence and Rutherford

backscattering, needs to be used for accurate determination of F in the F-doped IrO_2 [100]. It must be mentioned here that the real F content in IrO_2:F thin film will be different than the staring composition due to expected loss of F (high volatility) during thermal decomposition of the starting precursors at 400°C [100]. The SEM image along with EDX of the IrO_2:F film with 10 wt.% F, shown in **Figure 6**, indicates the presence of Ir and O, and the characteristic sintered "mud-crack" type morphology of IrO_2:F film coated on the Ti foil typically seen for chemically derived thin films.

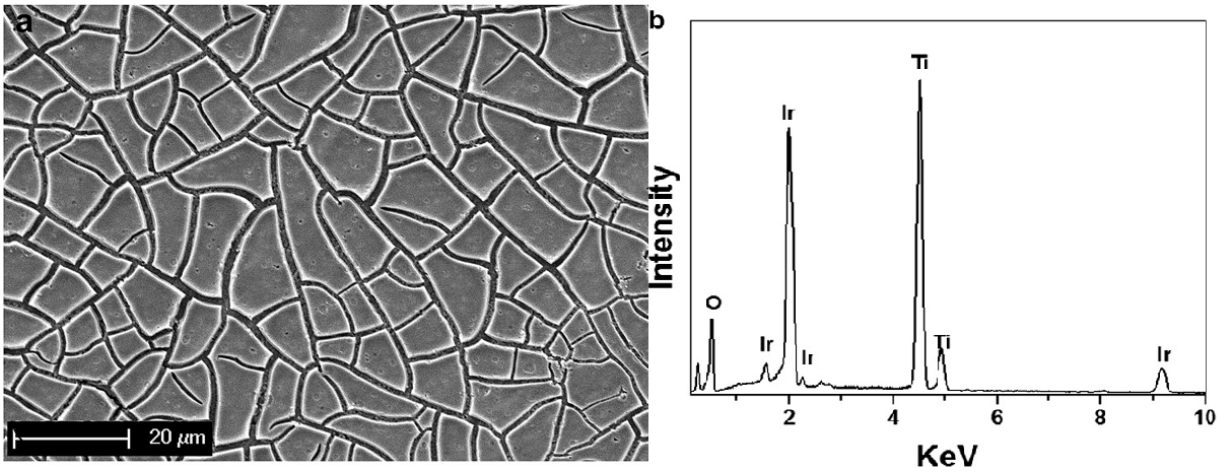

Figure 6. The SEM micrograph (a) along with EDAX (b) of IrO2:F film with 10wt.% F

5.1.1.2 Electrochemical Testing

The electrochemical activity of nanocrystalline thin film of IrO_2:F of different F compositions has been studied as a suitable oxygen evolution anode electro-catalyst for PEM based water electrolysis. The polarization curve of pure IrO_2 and IrO_2:F film of different F compositions, conducted in the presence of 1 N H_2SO_4 solution at 40^oC with a scan rate of 1 mV/sec, shown in

Figure 7, clearly indicates that the oxygen evolution reaction (water splitting) occurs at a potential of ~ 1.43 V *vs.* NHE irrespective of the varying F compositions. The polarization curve of IrO_2:F of different F compositions, shows that the electrochemical activity of IrO_2:F increases with increasing F content up to ~ 20 wt.% F.

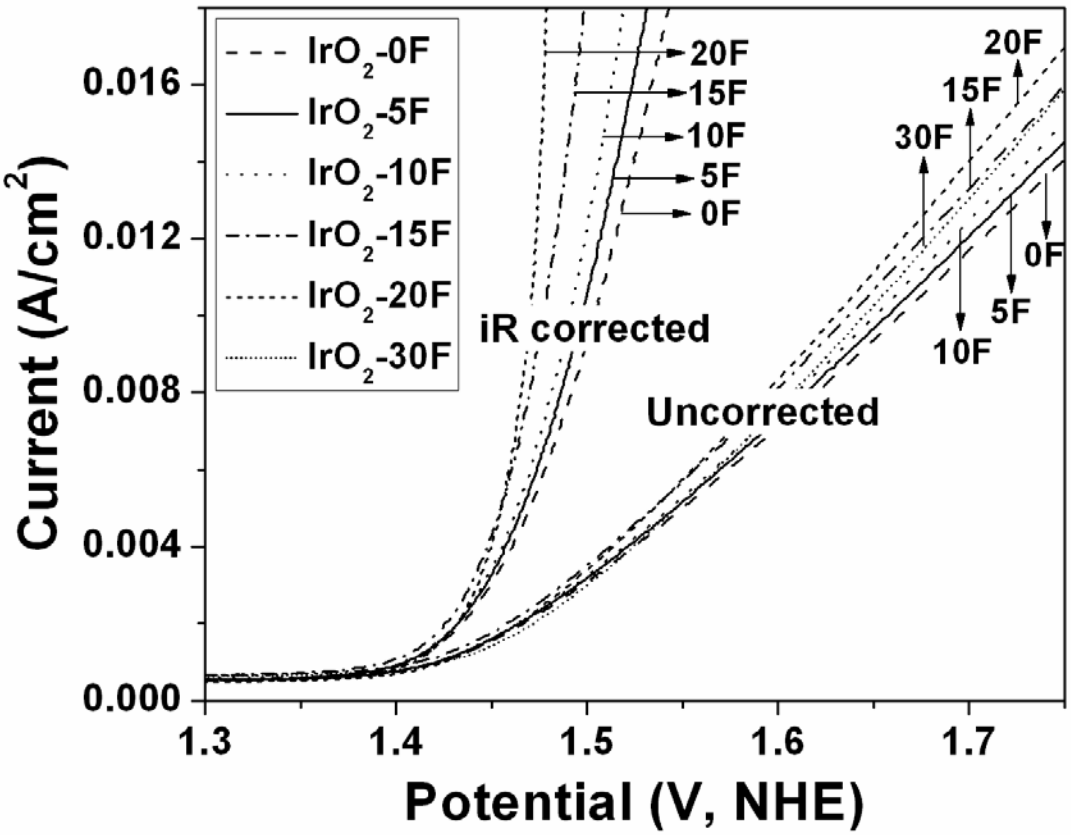

Figure 7. The polarization curve with iR correction of IrO_2:F films conducted in the presence of 1 N H_2SO_4 solution at 40°C with a scan rate of 1 mV/sec

It must be mentioned here that the present results also include the ohmic loss (iR loss) in the polarization curve which is known to arise mainly due to the solution resistance. In the present study, the solution resistance has been determined from electrochemical impedance spectroscopy to be approximately, ~ 16 Ωcm^2. The current density at ~ 1.65 V (*vs.* NHE) of IrO_2:F for different F compositions with a total loading ~ 0.3 mg/cm^2, plotted and shown in **Figure 8**, indicates that the current density of IrO_2:F increases up to 20 wt.% F beyond which there is a decrease in the current density suggesting a reduction in the electrochemical activity. The IrO_2:F with 20 wt.% F shows a current density of ~ 0.01116 ± 0.0001 A/cm^2 which is ~ 19 % higher to that of pure IrO_2 (~ 0.0094 A/cm^2) at ~ 1.65 V. On the other hand, it has been noticed that the current density decreases with increase in F content above 20 wt.% F.

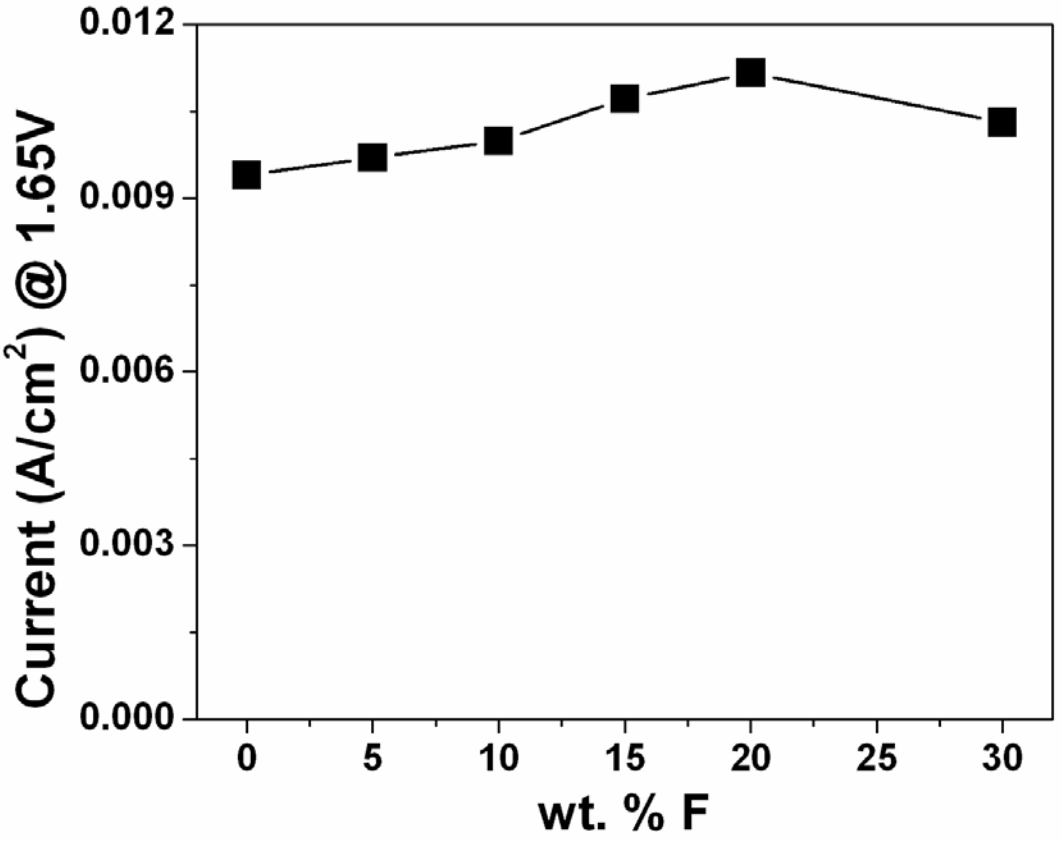

Figure 8. The variation of current density at ~ 1.65 V (*vs.* NHE) with F content of the doped IrO_2:F anode electro-catalyst

In order to study the corrosion and structural stability of anode electro-catalyst IrO_2:F in 1 N H_2SO_4, chronoamperometry (CA) test is conducted for 24 hours at 40^oC at a constant voltage of 1.65 V. The CA curves, obtained at a constant voltage of ~ 1.65 V, of IrO_2:F with 5, 10 and 20 wt.% F along with pure IrO_2, are shown in **Figure 9**. The IrO_2:F electrodes categorically show higher initial current with increase in F content due to their higher oxygen evolution activity as demonstrated in the polarization curves (**Figure 7**). The CA curve shows a marked decay of

current (10 % of the initial value) for all electrodes in the initial 1 hour which may arise either due to significant dissolution of the irregular coatings located at the edge of the mud cracks or diffusion controlled reaction [30]. A steady decay of current (13 % after 24 hours in comparison with the 1 hour value) has been noticed after 1 hour of initial period for IrO_2:F and pure IrO_2 which suggests that IrO_2:F (up to 20 wt.% F) has similar structural stability compared to pure IrO_2 [34].

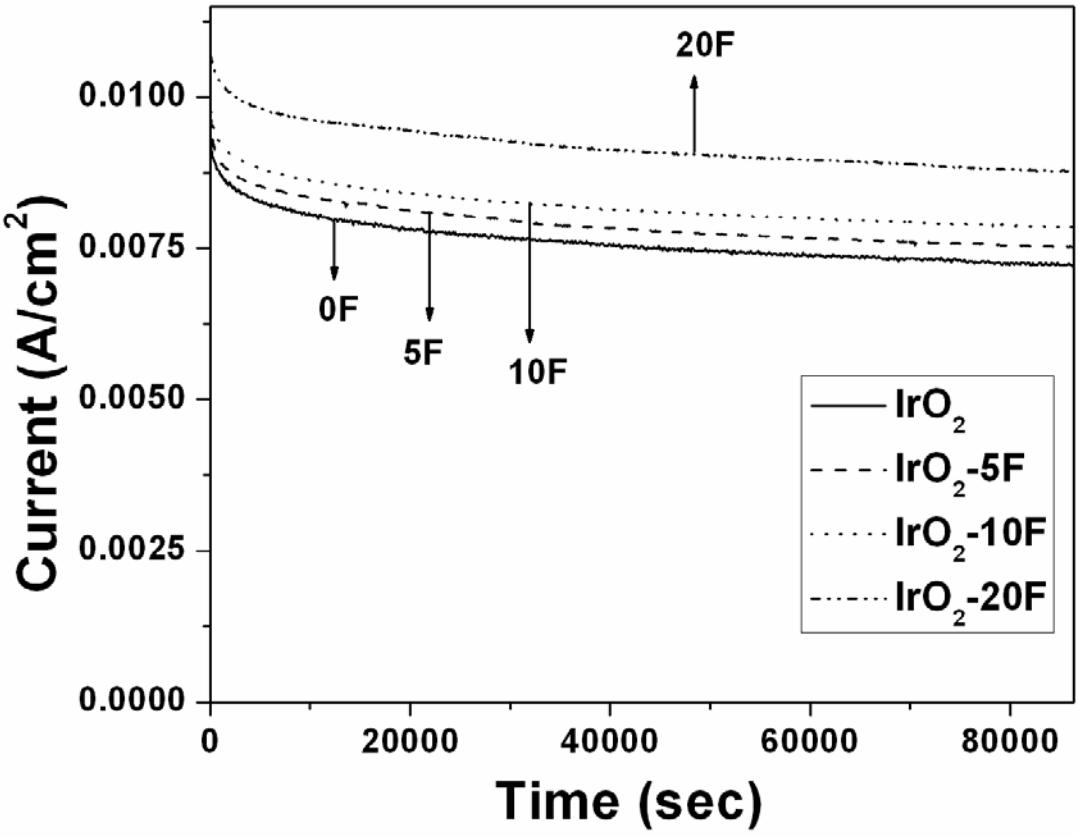

Figure 9. Variation of current *vs.* time in the accelerated life test of IrO_2:F performed in a 1 N H_2SO_4 solution under ~ 1.65 V at 40°C

However, the ICP results, conducted in the H_2SO_4 electrolyte solution collected after 24 hours of CA measurement, show no presence of Ir up to 20 wt.% F doping which suggests that the steady decay of current of IrO_2:F during CA measurement may arise due to loss of fuel rather than the dissolution of IrO_2 electro-catalyst. In the present experimental condition, it has been noticed that ~ 9 ml fuel has been lost after 24 hours of CA measurement for the F doped IrO_2 due to the high OER activity. The present study therefore successfully identifies IrO_2:F as a promising anode electro-catalyst with the ability to significantly improve the electro-catalytic performance and electrochemical stability. The IrO_2:F anode electro-catalysts can therefore be expected to exhibit significant reduction in capital cost of PEM based water electrolyzers due to the significant improvement in the electrochemical activity and stability.

5.1.2 Binary F doped $(Ir,Sn)O_2$

5.1.2.1 Structural Analysis

The XRD patterns, shown in **Figure 10**, of $(Ir,Sn)O_2$: x wt.% F thin film of optimal composition corresponding to 20 mol.% IrO_2 - 80 mol.% SnO_2 (x=0) deposited on the pretreated Ti foil. It shows peaks corresponding to single phase rutile type tetragonal structure suggesting the formation of a single phase homogeneous solid solution of IrO_2 and SnO_2 [$(Ir,Sn)O_2$] without indicating any undesirable phase separation (*E.g.* IrO_2 + SnO_2). The compositions we study will be denoted as $(Ir,Sn)O_2$:F henceforth.

The molar volume of $(Ir,Sn)O_2$, calculated using the least square refinement technique, is ~ 21.20 ± 0.05 cm^3/mol, which is in good agreement with the expected value determined by considering the change of molar volume of SnO_2 (21.66 cm^3/mol) and IrO_2 (19.22 cm^3/mol)

solid solution following the Vegard's law further confirming formation of the solid solution. The effective crystallite size of $(Ir,Sn)O_2$, calculated using the Scherrer formula from the integral breadth of the Lorentzian contribution determined from peak profile analysis employing the single line approximation method after eliminating the instrumental broadening and lattice strain contribution [88], is in the range of ~ 5 - 7 nm confirming the nanocrystalline nature of the Ir containing Sn oxide solid solution. In order to improve the electrical conductivity of the $(Ir,Sn)O_2$, fluorine has been introduced into the structure to substitute for oxygen at nominal compositions of 5, 10 and 15 wt.% F. The XRD patterns of the $(Ir_{0.2}Sn_{0.8})O_2$:F solid solution corresponding to the different compositions, shown in **Figure 10**, confirms the retention of the tetragonal structure similar to the parent $(Ir,Sn)O_2$. The calculated molar volume of $(Ir,Sn)O_2$:F (~ 21.20 ± 0.05 cm^3/mol) is comparable with undoped $(Ir,Sn)O_2$ which suggests that F^- doping on O^{-2} sites has no significant effect on the molar volume of $(Ir,Sn)O_2$:F. This may be due to the comparable ionic radius of O^{-2} (125 pm) with F^{-1} (120 pm). The calculated effective crystallite size of $(Ir,Sn)O_2$:F is also in the range of ~ 4 - 7 nm which is comparable with $(Ir,Sn)O_2$ suggesting that F^- doping has no significant effect on the refinement of crystallite size of $(Ir,Sn)O_2$.

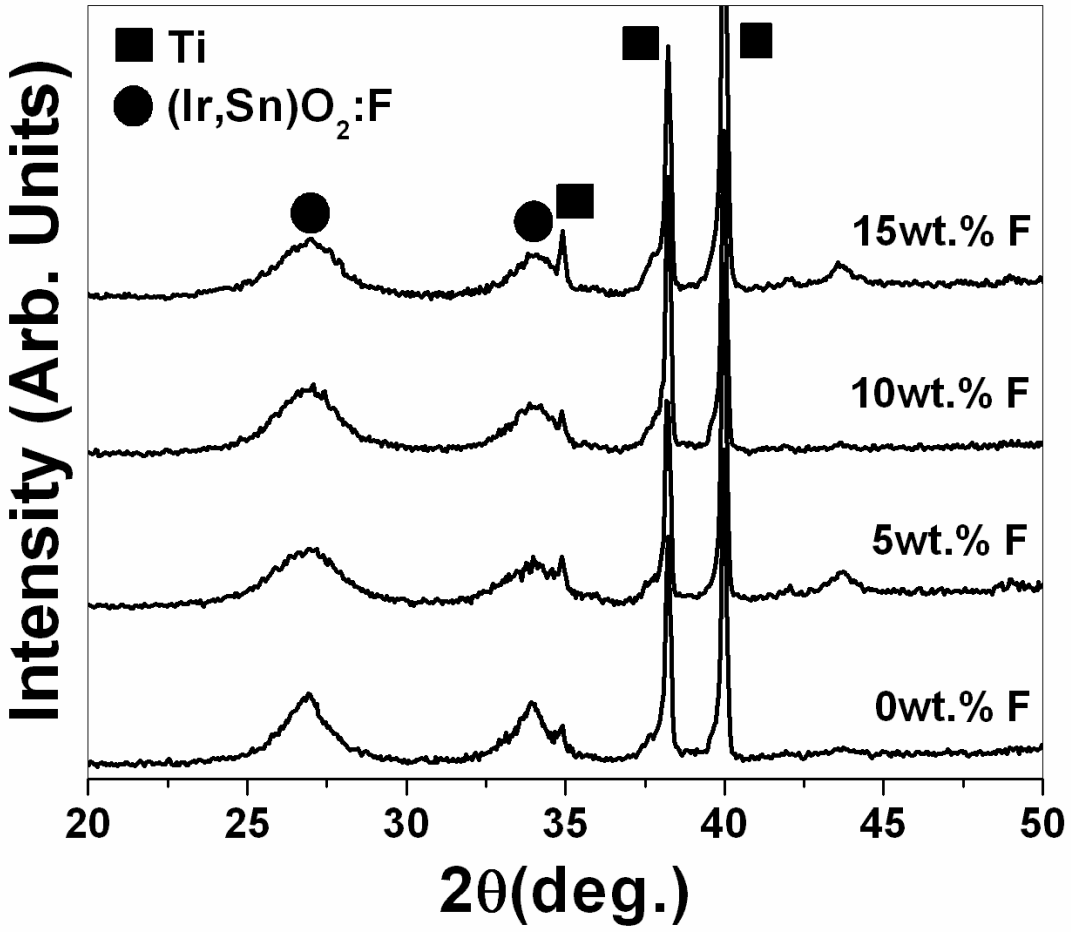

Figure 10. XRD patterns of $(Ir_{0.20}Sn_{0.80})O_2$:F of different compositions coated on Ti foil

The presence of elemental Ir, Sn and O in the (Ir,Sn)O2:F film of different compositions has been confirmed using energy dispersive X-ray spectroscopy analysis (EDX) configured to the SEM. However, the presence of F could not be detected in the EDX analysis as outlined in **Section 5.1.1.1**. The SEM image along with x-ray mapping and EDX of the $(Ir,Sn)O_2$:F film containing 10 wt.% F, shown in **Figure 11**, indicates the presence of the characteristic "mud-crack" type morphology of the representative composition of $(Ir,Sn)O_2$:F film coated on the Ti

foil. Elemental x-ray maps of Ir, Sn and O testify that Ir and Sn are homogeneously distributed within the (Ir,Sn)O_2:F particles without being segregated on any specific site. Quantitative elemental composition analysis of the (Ir,Sn)O_2:F films obtained by EDX further shows that the measured elemental compositions of Ir and Sn are close to the nominal composition. The bright field TEM image of (Ir,Sn)O_2:F particles collected from the representative film composition containing 10 wt.% F depicted in **Figure 12** confirms the nanometer sized (~ 10 - 15 nm) state of the fine particles.

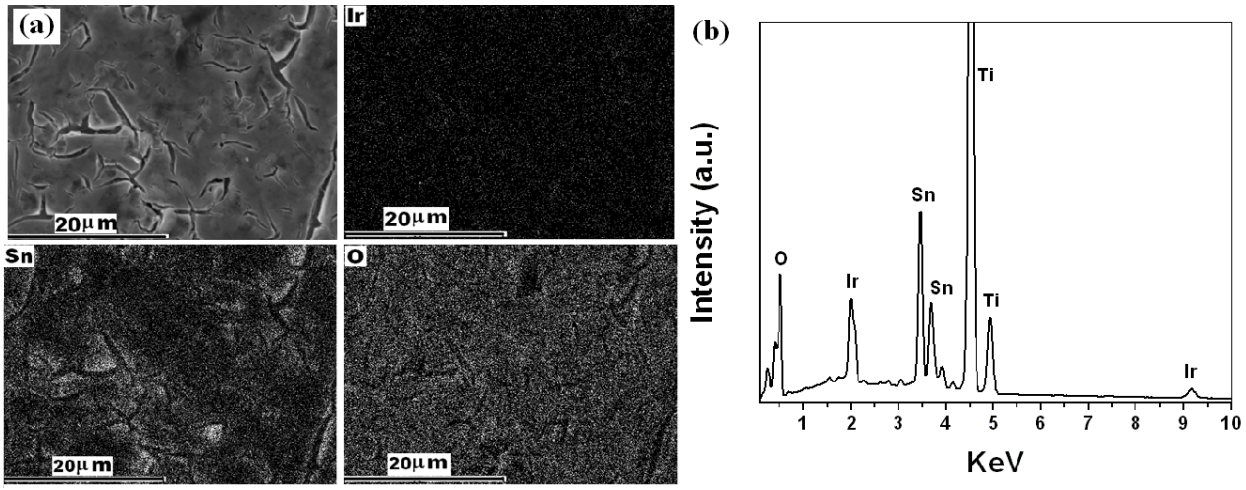

Figure 11. The SEM micrograph along with x-ray mapping of Ir, Sn and O (a), and EDAX (b) of $(Ir_{0.20}Sn_{0.80})O_2$:F film

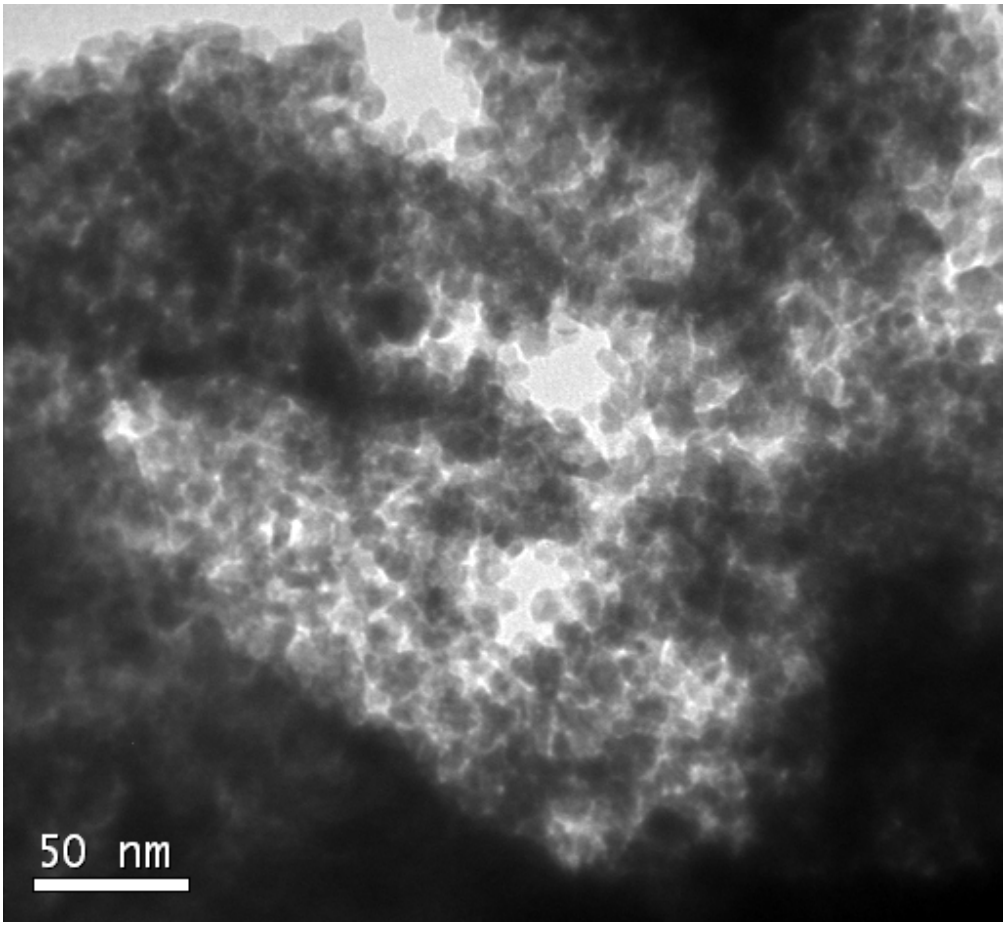

Figure 12. The bright field TEM image $(Ir_{0.2}Sn_{0.8})O_2$:10F film shows the presence of fine particles in the nanometer range (~ 10 - 15 nm)

5.1.2.2 Electrochemical Testing

In the present study, the linear polarization curve and non-linear Tafel plot are most often encountered due to ohmic resistance contribution which mainly arises due to solution resistance of the electrolyte (R_s), oxide film electrode resistance (R_e) and accumulation of oxygen bubble covering the electrode surface during water electrolysis at higher current density (R_{bub}) [51, 52]. In order to evaluate the inherent electrochemical property / electrode kinetics of the studied

electro-catalysts, the polarization curve of different samples, conducted in the presence of 1 N H_2SO_4 solution at 40^oC with a scan rate of 1 mV/sec, is therefore plotted after accounting for total ohmic loss (iR_Ω) correction. The value of R_s and R_e of different samples, tabulated in **Table 1**, is obtained from electrochemical impedance spectroscopy (EIS) measurement at different potential with respect to NHE at 40^oC. The impedance parameters are obtained by fitting the experimental data as shown in **Figure 13** using ZView software from Scribner Associtates utilizing the circuit model $R_s(R_eQ_1)(R_{ct}Q_{dl})$, where R_s is the solution resistance, R_e is the electrode resistance, R_{ct} is the charge transfer resistance, Q_1 is the constant phase element and Q_{dl} includes contributions from both the double layer capacitance and pseudocapacitance [48, 85].

Table 1. Impedance parameters and Tafel slope of IrO_2 and $(Ir,Sn)O_2$:F thin film

Composition	R_s (Ω cm^2)	R_e (Ω cm^2)	R_{ct} (Ω cm^2)	Tafel slope (b)
IrO_2	13.8	1	6	60
$(Ir_{0.8}Sn_{0.2})O_2$	12.1	2.7	15	76
$(Ir_{0.8}Sn_{0.2})O_2$:5F	13.1	1.8	10	70
$(Ir_{0.8}Sn_{0.2})O_2$:10F	13.3	1	6.7	62

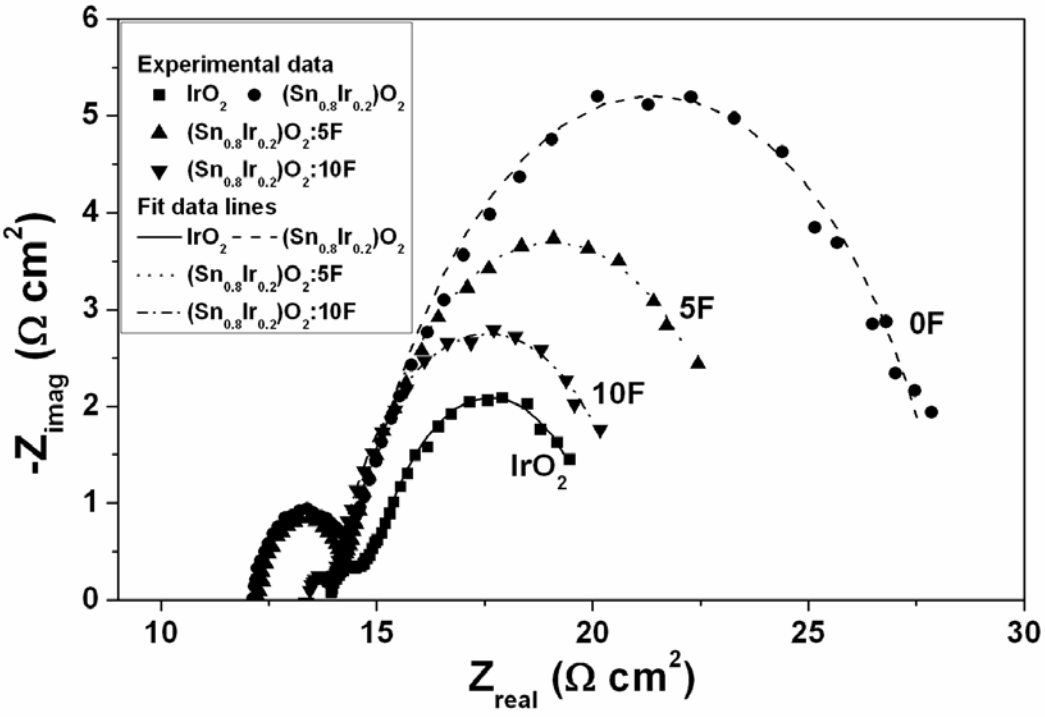

Figure 13. The EIS plot obtained at 1.6 V at 40°C in the presence of 1 N H_2SO_4 solution in the frequency range of 100 mHz - 100 kHz

As shown in **Table 1**, the value of R_e of (Ir,Sn)O_2:F decreases with increase of F content in the parent (Ir,Sn)O_2 lattice which may arise due to increase in electronic conductivity of (Ir,Sn)O_2:F with increase in F content. The (Ir,Sn)O_2:F with 10 wt.% F shows almost identical electrode resistance (R_e ~ 1 Ωcm^2) with pure IrO_2 which suggest that both possess identical electronic conductivity. It can also be noticed that the solution resistance and electrode resistance of IrO_2 and $(Ir_{0.2}Sn_{0.8})O_2$:F is unchanged with change of potential as seen in **Figure 14**, respectively. The low frequency EIS plot of pure IrO_2 and (Ir,Sn)O_2:F shows a well formed semicircle related to OER and also shows that the diameter of the low frequency semicircle,

which should be a measure of the polarization resistance (R_{ct}); and thereby the catalytic activity of the electrode, decreases with increase of F content. The above results suggest that the electrochemical activity of (Ir,Sn)O_2:F increases with increase in F content as the polarization resistance value becomes similar to that of pure IrO_2.

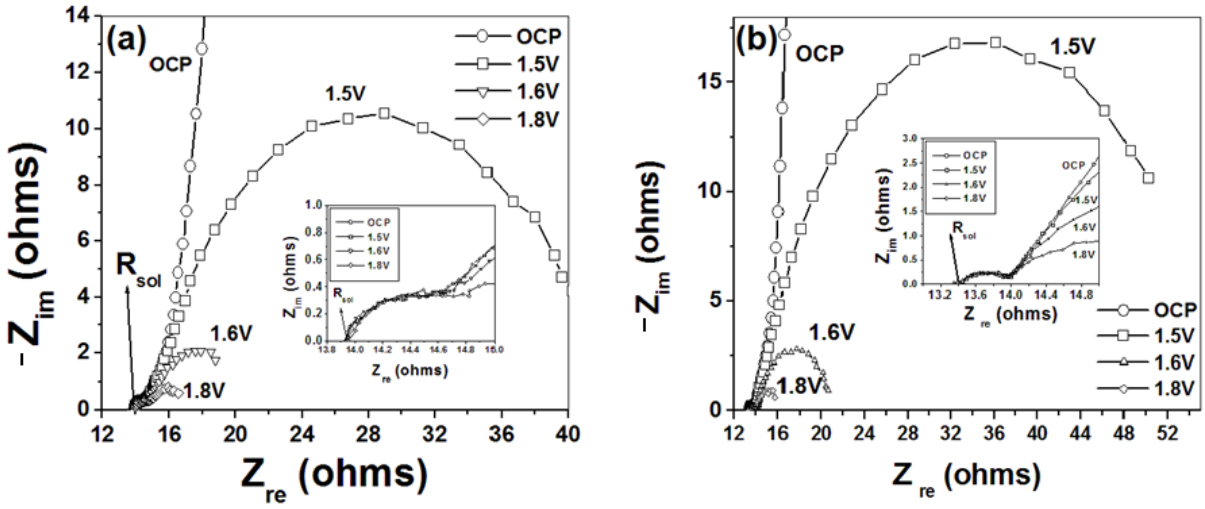

Figure 14. The EIS plot obtained at open circuit potential and different voltages for pure IrO_2 (a), and (Ir,Sn)O_2:10F (b) in the frequency range of 100 mHz - 100 kHz

The polarization curve of pure SnO_2:F and IrO_2 film, before and after ohmic resistance correction ($iR_\Omega = iR_{sol}+iR_e$) without considering the bubble resistance, conducted in the presence of 1 N H_2SO_4 solution at 40^oC with a scan rate of 1 mV/sec, is shown in **Figure 15**. Nanocrystalline pure IrO_2 clearly indicates the occurrence of the water splitting reaction at a potential of ~ 1.43V *vs.* NHE. The current density at ~ 1.55 V after iR_Ω correction (*vs.* NHE) is ~ 0.014 ± 0.001 A/cm^2 at 40^oC with a total loading ~ 0.3 mg/cm^2 of IrO_2. The Tafel slope of pure IrO_2, calculated from iR corrected Tafel plot, is ~ 60 mV/decade, which corresponds to the two electron pathway reaction assuming a transfer coefficient of ~ 0.5 [30, 48, 53, 101].

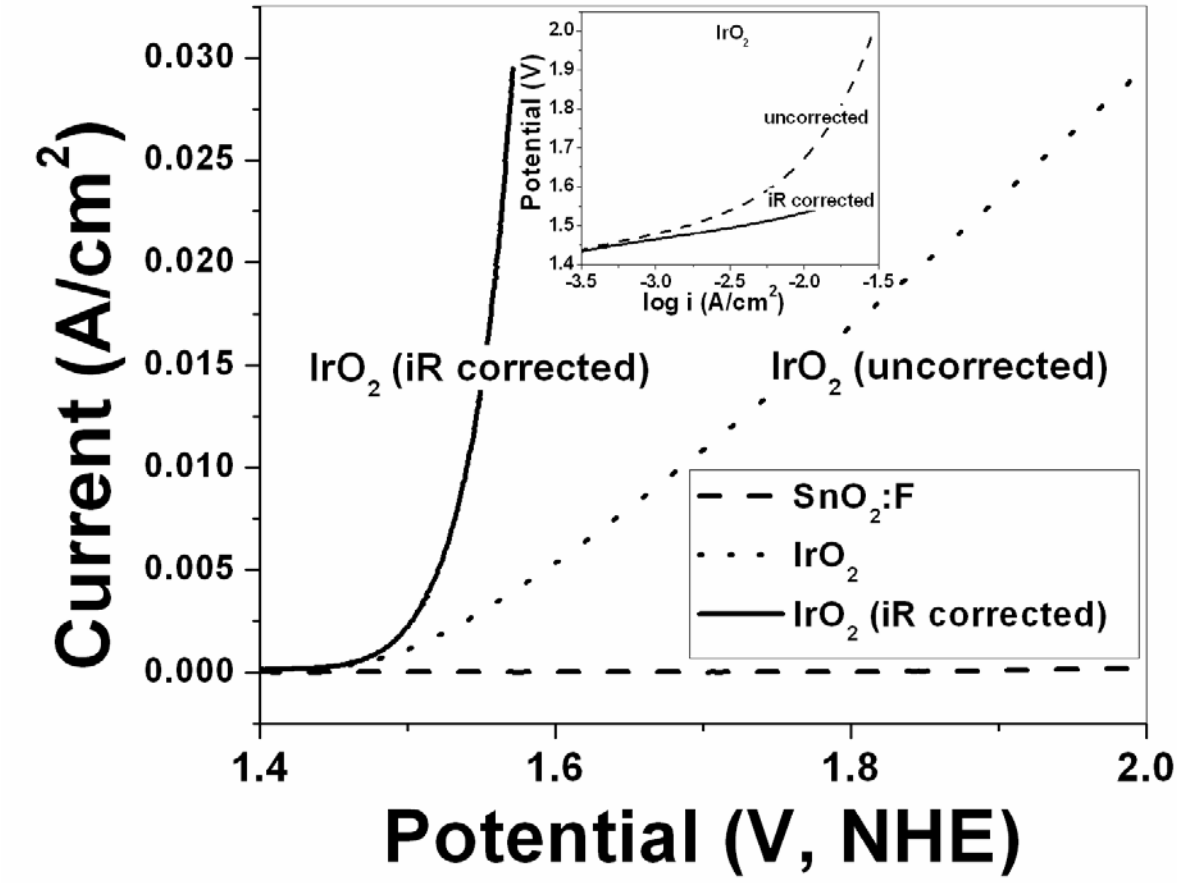

Figure 15. The polarization curve of pure IrO_2 and SnO_2:10F film before and after iR correction, and the inset shows the Tafel plot of pure IrO_2 before and after iR correction

The polarization curve for (Ir,Sn)O_2:F films before and after iR correction corresponding to the different compositions of F, plotted in **Figure 16**, also shows that water splitting (oxygen evolution reaction) occurs at the potential of ~1.43 V (*vs.* NHE) irrespective of the composition which is identical to that of pure IrO_2. Furthermore, the current density at ~ 1.55 V (*vs.* NHE) after iR correction for undoped (Ir,Sn)O_2 solid solution (0 F) with an identical total loading ~ 0.3

mg/cm^2 is ~ 0.0042 ± 0.0001 A/cm^2 at 40^{o}C which is almost three times lower than pure IrO_2. However, the current density of (Ir,Sn)O_2:F increases with increase in F content. In fact, (Ir,Sn)O_2:F containing 10 wt.% F shows a current density of ~ 0.014 ± 0.001 A/cm^2 at ~ 1.55 V (*vs.* NHE) which is comparable to that of pure IrO_2.

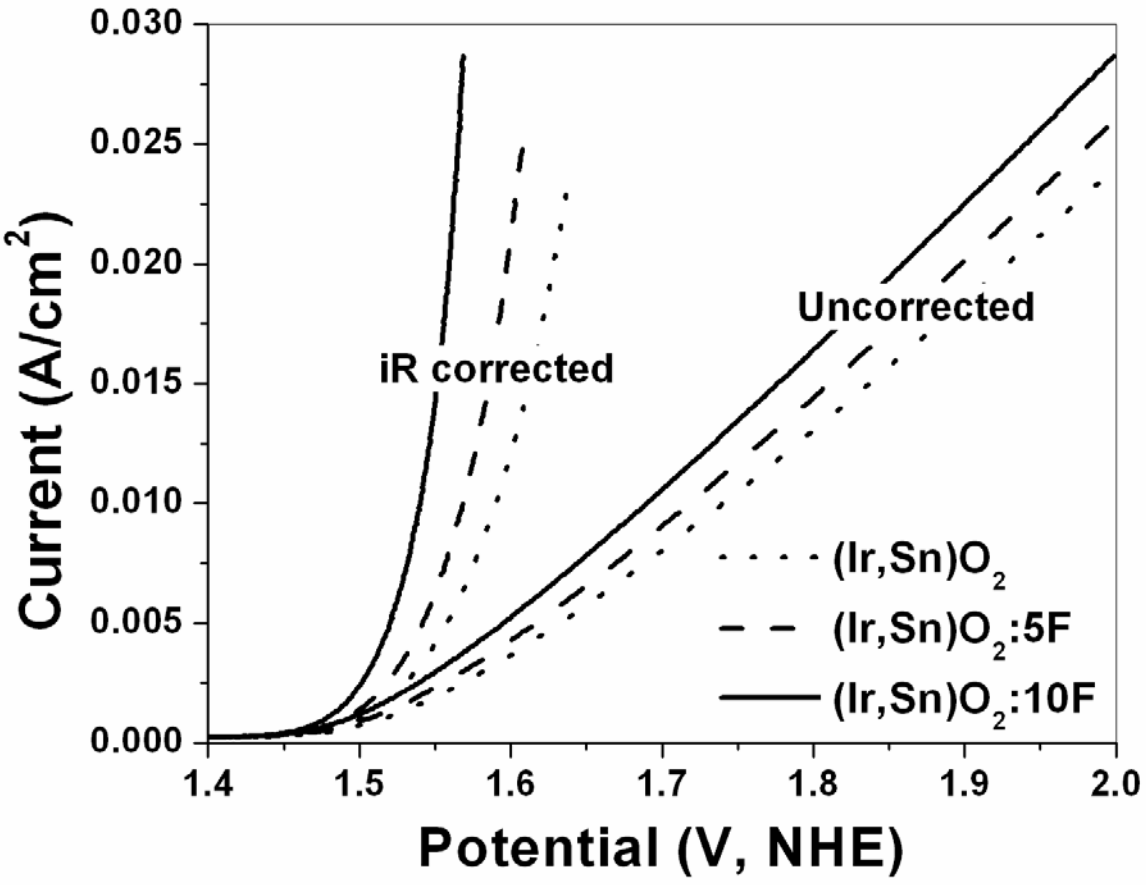

Figure 16. The polarization curve of (Ir,Sn)O_2:F film conducted in the presence of 1 N H_2SO_4 solution at 40°C with a scan rate of 1 mV/sec before and after iR correction.

On the other hand, it has also been observed that the current density decreases with increase in F content above 10 wt.% F as shown in **Figure 17**. The Tafel slope of (Ir,Sn)O_2:F with 0, 5, and 10 wt.% F (**Table 1**), calculated from the corresponding Tafel plots shown in **Figure 18**, is 76, 70 and 62 mV/decade respectively, which suggests that the electrochemical activity of (Ir,Sn)O_2:F increases with increase in F content and corresponding decrease of Tafel slope with increase in F. Moreover, the Tafel slope value of ($Ir_{0.2}Sn_{0.8}$)O_2:10F is similar to that of pure IrO_2 (inset of **Figure 15**). These results clearly suggest that (Ir,Sn)O_2:F with 10 wt.% F, exhibits similar electrochemical activity as that of pure IrO_2, and is indeed a promising candidate as anode electro-catalyst for PEM based water electrolysis.

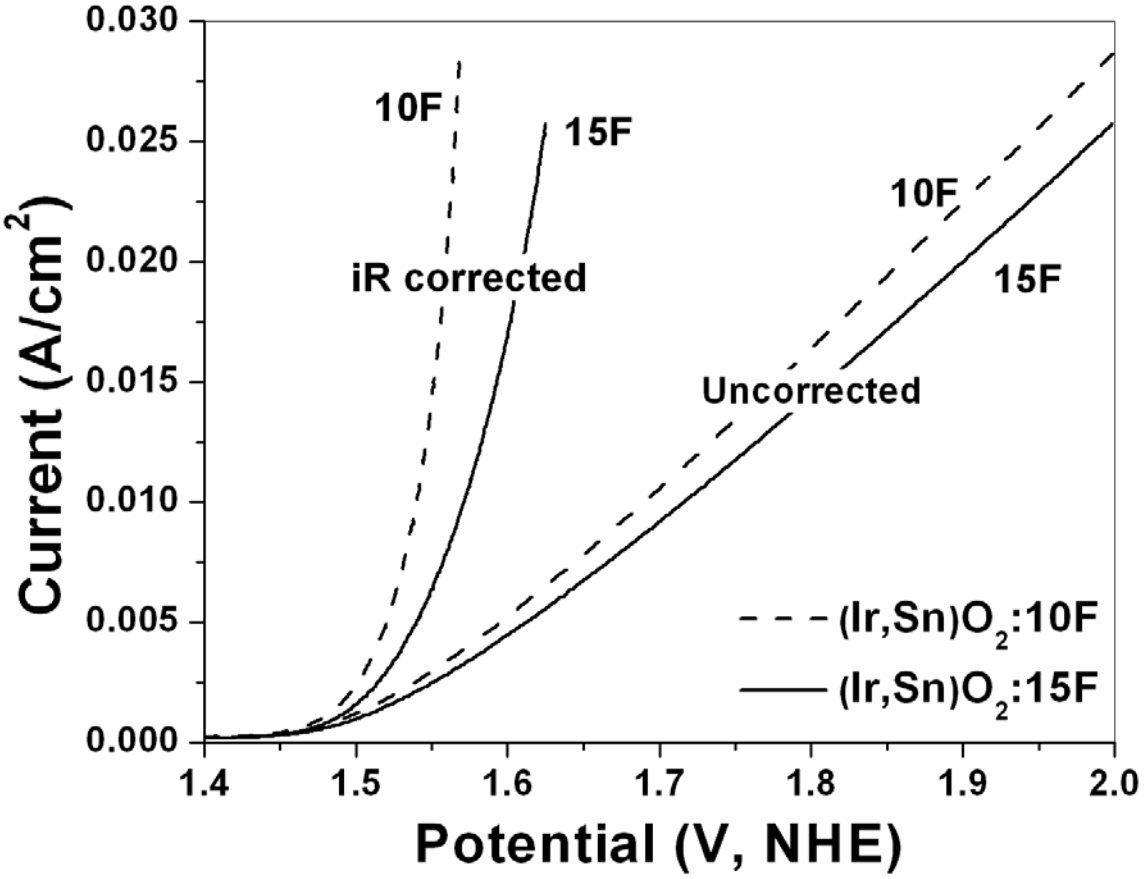

Figure 17. The polarization curve for high F doping of (Ir,Sn)O_2:F film conducted in the presence of 1 N H_2SO_4 solution at 40°C before and after iR correction

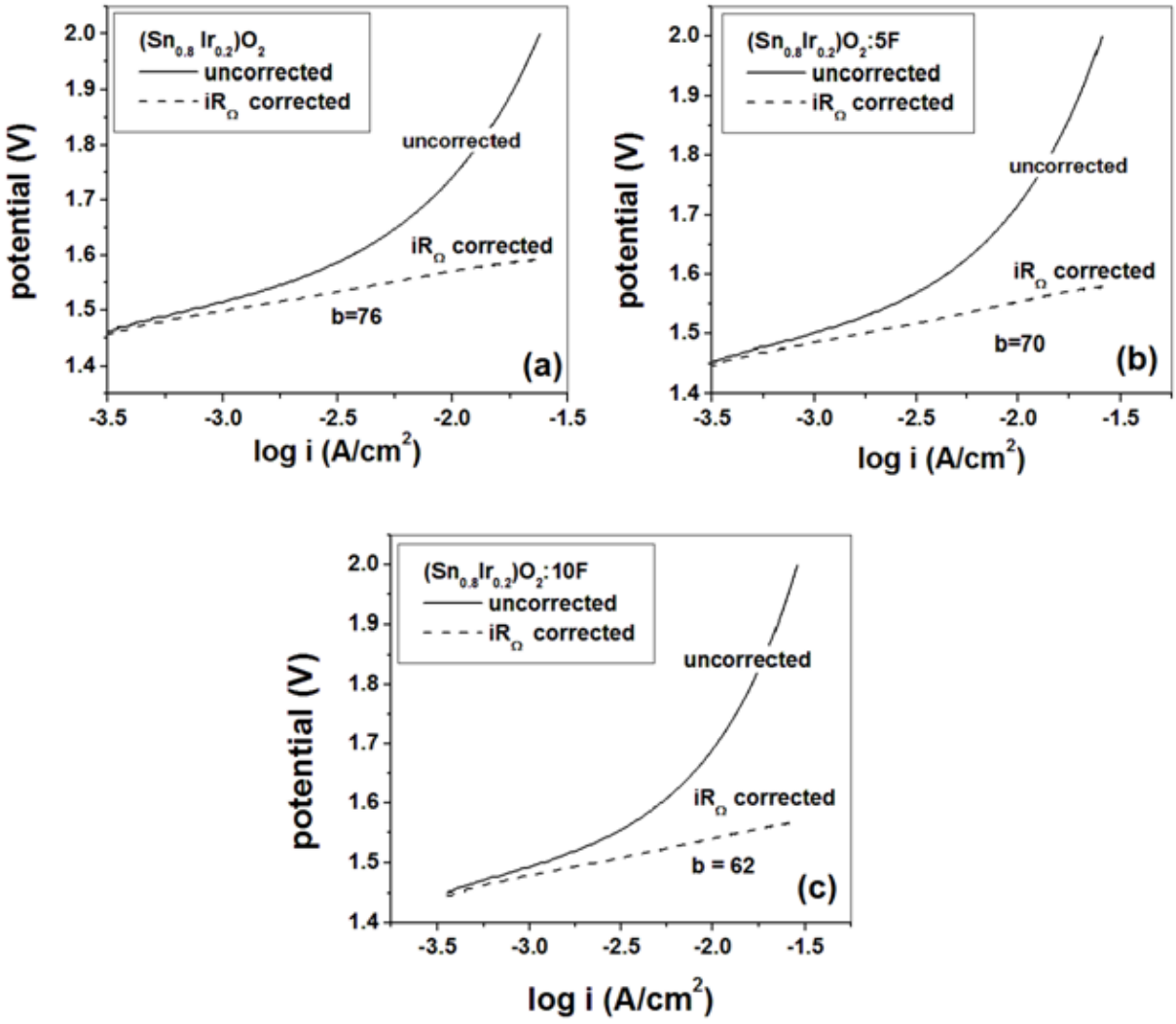

Figure 18. The Tafel plot of $(Ir_{0.2}Sn_{0.8})O_2$ (a), $(Ir_{0.2}Sn_{0.8})O_2$:5F (b), and $(Ir_{0.2}Sn_{0.8})O_2$:10F (c), before and after iR correction, showing the Tafel slope

Multiple small potential step voltammetry was performed for the rotating disk electrode studies in order to study the fundamental kinetics and calculate the apparent activation energy of the OER. The catalyst ink coated Ti disk insert was rotated at speeds varying from 500 rpm to 2000 rpm. **Figure 19** shows the Koutecky - Levich plot *i.e.* i^{-1} *vs.* $\omega^{-1/2}$ for the most optimum

electro-catalyst composition of $(Ir_{0.2}Sn_{0.8})O_2$:10 wt.% F. The current values at different rotation speeds have been plotted at three potentials of 1.55 V, 1.65 V and 1.75 V (*vs.* NHE) without iR correction. The potentials are not iR corrected since the tests have been conducted in-situ (*via* multiple small potential step voltammetry) from which the RDE results are reported directly. This dynamic testing process does not allow accounting for the iR drop from the solution resistance. These RDE plots at different potentials give parallel straight lines of similar nature; and the current increases with increase in voltage as expected, causing a decrease in the value of i^{-1}. This trend is thus consistent with the results obtained from the polarization curves (**Figure 16**). From the slope of the graphs, the number of electrons transferred (n) is determined as explained in **Section 4.4.4**. The average value of 'n' determined at the three voltages for the $(Ir_{0.2}Sn_{0.8})O_2$:10F electro-catalyst is ~ 1.81. The kinetic rate constant (k) of an electrochemical reaction not only varies with the applied potential, but is also dependent on many other factors *viz.*, temperature, electrode surface structure, composition of the catalyst, surface adsorption and reaction intermediates [95, 96, 102, 103]. The range of 'k' is in between 0.055 and 0.075 cm/s. The RDE tests and the Koutecky - Levich plot confirm the two electron pathway mechanism for the OER in PEM electrolysis for all our explored catalyst compositions. This further elucidates the high electrochemical activity and the close to ideal Tafel slope of the 10 wt.% F doped $(Ir,Sn)O_2$, portending it to be a preferred OER electro-catalyst composition for PEM electrolyzer cells.

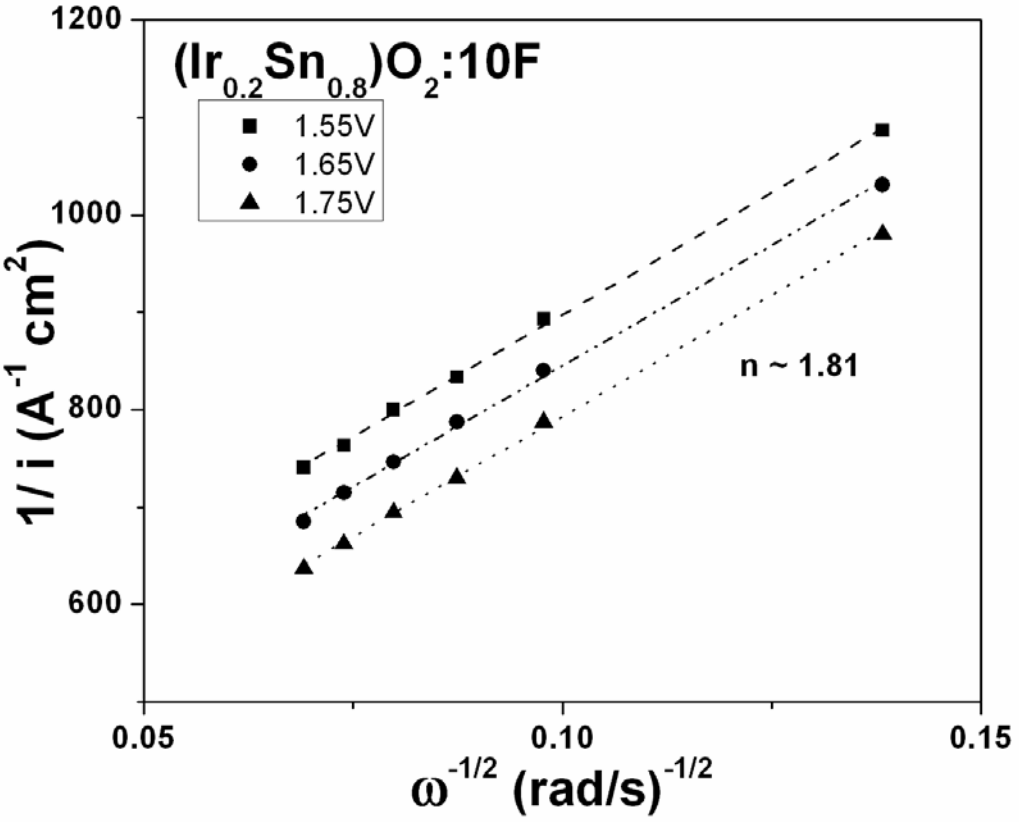

Figure 19. Koutecky - Levich plot in PEM based water electrolysis at 1.55 V, 1.65 V and 1.75 V (*vs.* NHE) in 1 N H_2SO_4 at 25°C for $(Ir_{0.2}Sn_{0.8})O_2$:10 wt.% F

The influence of temperature on the OER was studied in order to calculate apparent activation energy from the Arrhenius relationship as explained before in **Section 4.4.4**. The Arrhenius plots *i.e.* ln i *vs.* T^{-1} for $(Ir_{0.2}Sn_{0.8})O_2$:10 wt.% F is shown in **Figure 20**. The temperature was varied between 25 - 70°C and data points in these graphs have been plotted at three different potentials of 1.55 V, 1.65 V and 1.75 V (*vs.* NHE) as used before. The slope of these lines was averaged in order to calculate the E_a which is ~ 25.2 ± 1.5 kJ/mol. This E_a value is lesser and in the range of values reported for the OER by other researchers [97, 98, 104-107].

The E_a value for all the electrodes being similar to the powder catalysts (undoped and F doped IrO_2) as shown in **Section 5.2.2.2** suggests that the OER on the electrodes proceeds *via* the same reaction mechanism [97, 108]. The reaction mechanism has been previously reported by Nørskov *et al.* and in our earlier publication [53-55]. This four step reaction mechanism occurring during PEM based water electrolysis is described in **Section 2.2.2**.

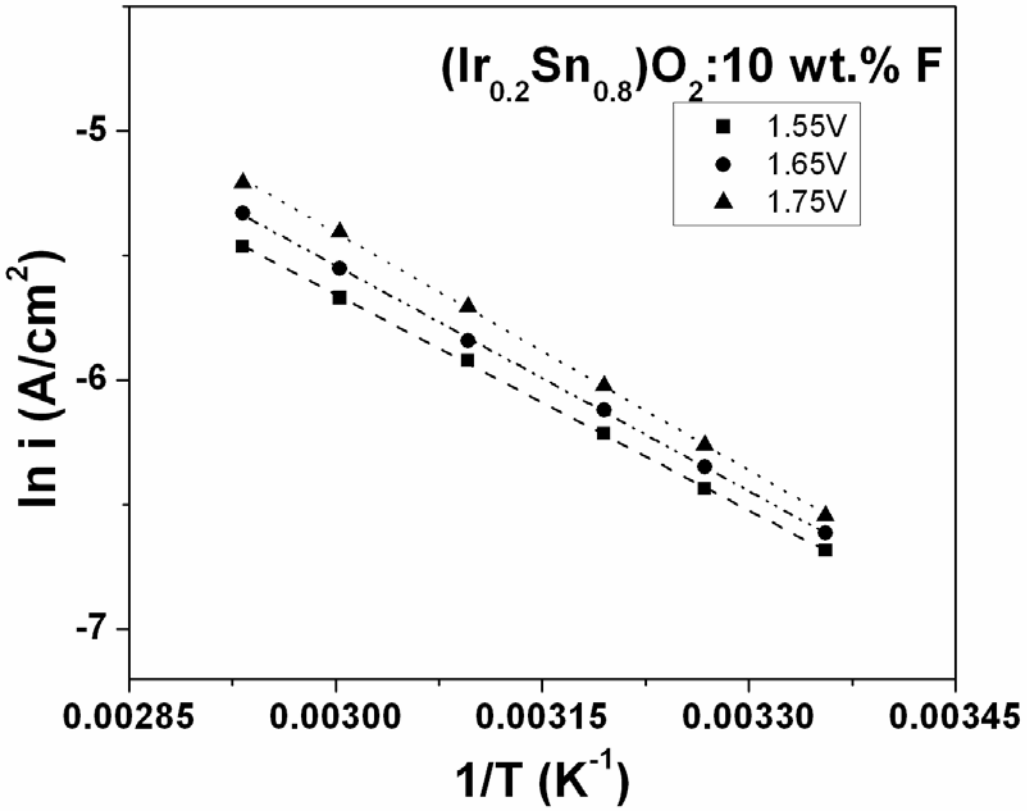

Figure 20. Arrhenius plot for $(Ir_{0.2}Sn_{0.8})O_2$:10 wt.% F at 1.55 V, 1.65 V and 1.75 V (*vs.* NHE) over a temperature range of 25°C to 70°C

In order to study the electrochemical stability of the anode electro-catalyst (Ir,Sn)O_2:F in 1N H_2SO_4, CA test is conducted for 12 hours at 40^oC at a constant voltage. The CA curves, obtained at a constant voltage of ~ 1.65 V (*vs.* NHE), of (Ir,Sn)O_2:10 wt.% F combined with that of pure IrO_2 are shown in **Figure 21**. The CA curve clearly shows a marked decay of current (13 % of the initial value) for both electrodes in the initial 30 minutes. A steady state of current ~ 0.006 A/cm^2 has also been achieved however after 1 hour of the initial period for (Ir,Sn)O_2:F and pure IrO_2 over the test run. This indicates similar structural stability of (Ir,Sn)O_2:F compared to IrO_2. The ICP results, conducted in the H_2SO_4 electrolyte solution collected after CA measurement, show no presence of Ir up to 10 wt.% F suggesting that the steady decrease of current during CA measurement may arise due to loss of fuel rather than dissolution of IrO_2 electro-catalyst [57].

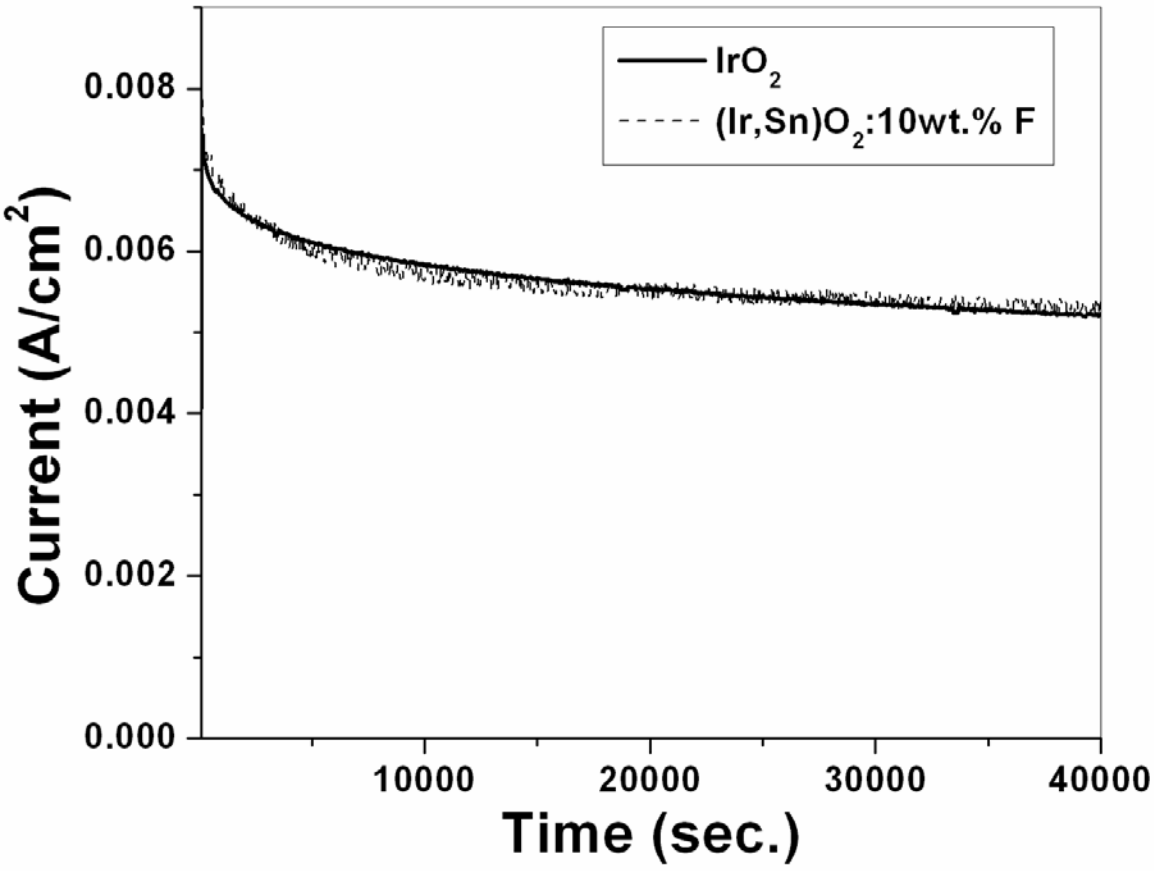

Figure 21. Variation of current *vs.* time in the accelerated life test of pure IrO_2 and $(Ir_{0.2}Sn_{0.8})O_2$:10F performed in a 1 N H_2SO_4 solution under ~ 1.65 V at 40°C

After the conclusion of the CA test, the IrO_2 and the $(Ir_{0.2}Sn_{0.8})O_2$:10 wt.% F thin film electrodes were subject to polarization testing as seen in **Figure 22** in order to determine the activity of the electrodes after long term structural stability tests. The Tafel plots from these polarization curves (post CA measurement) after iR correction are shown in **Figure 23** and **Figure 24**. A Tafel slope of ~ 77 mV/decade and ~ 82 mV/decade was obtained for pure IrO_2 thin film and $(Ir,Sn)O_2$:10 wt.% F respectively. This is slightly higher but still close and

comparable to the values obtained from the polarization tests conducted before CA (**Figure 15** and **Figure 18**). This test further demonstrates the robustness of the electro-catalysts.

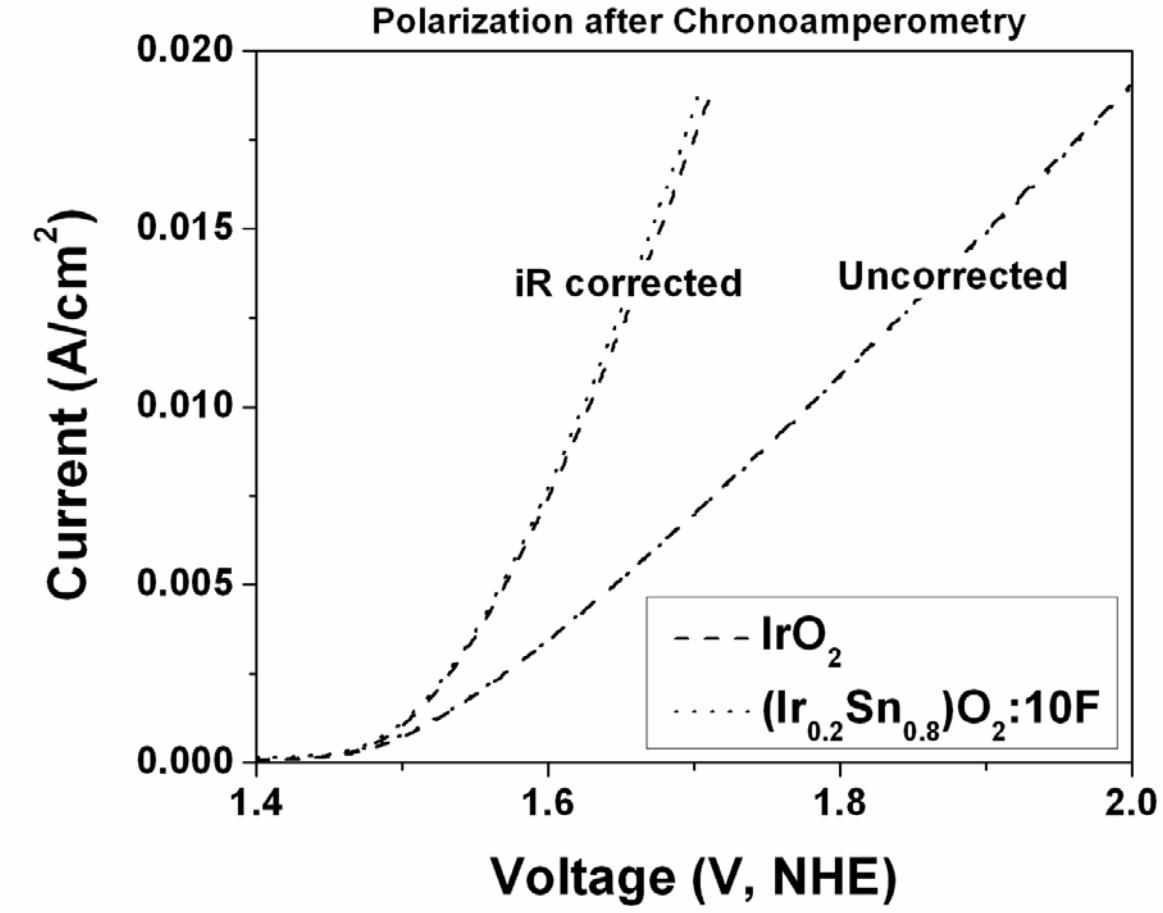

Figure 22. Polarization curve of IrO_2 and (Ir,Sn)O_2:10 wt.% F thin film after the CA test

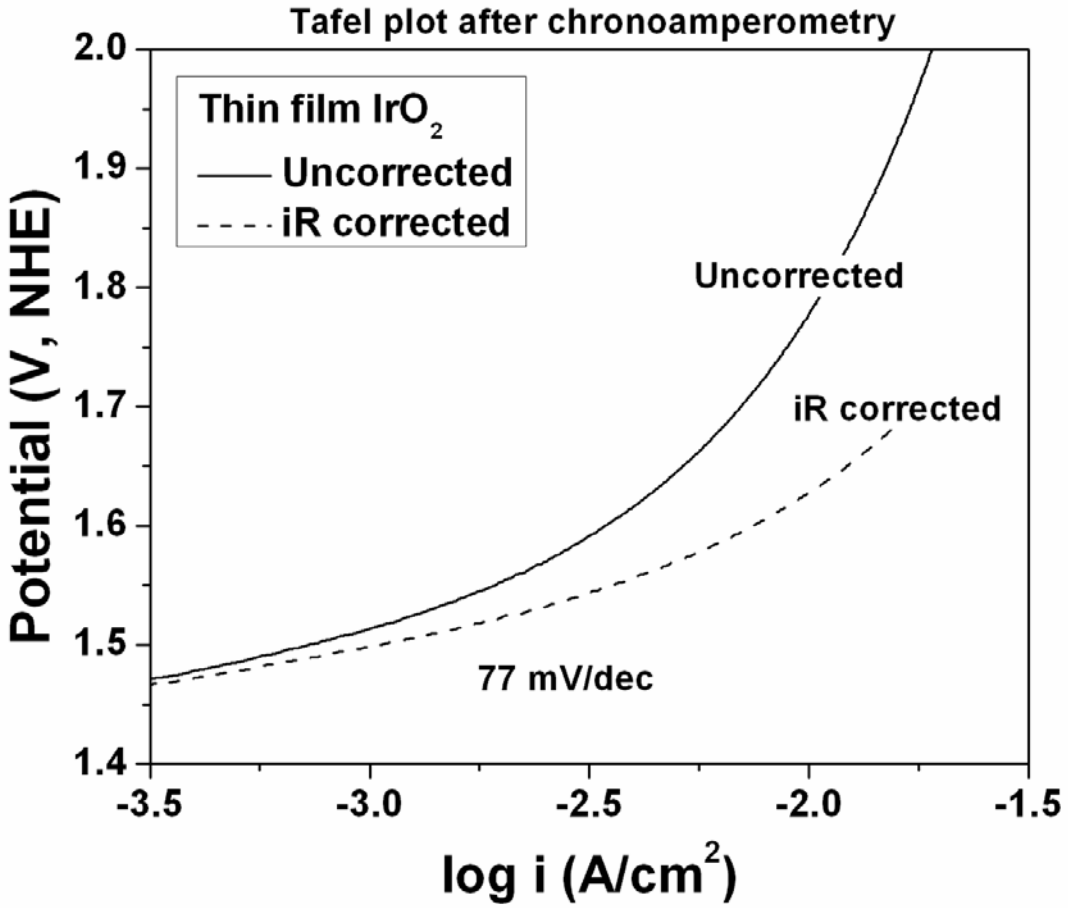

Figure 23. The Tafel plot of pure IrO_2 after the CA test

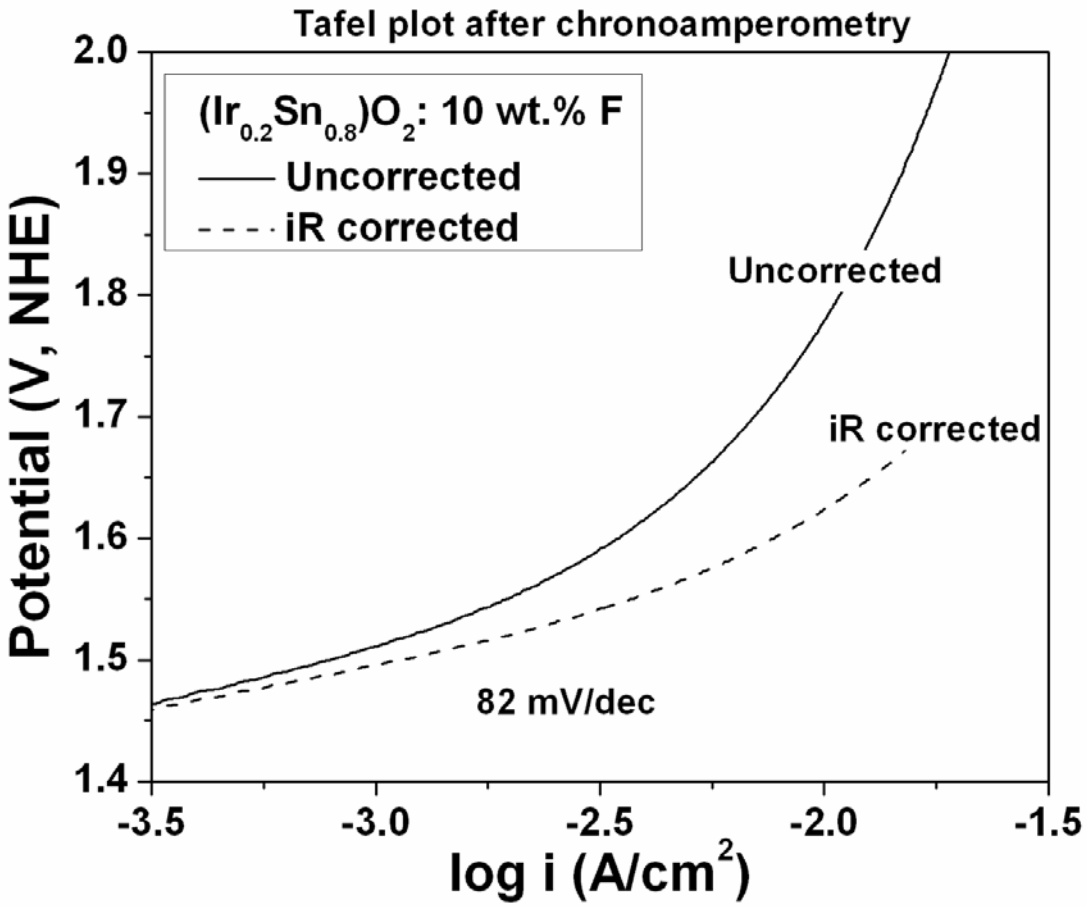

Figure 24. The Tafel plot of (Ir,Sn)O_2:10 wt.% F thin film after the CA test

The present experimental study thus successfully demonstrates that F doped $(Ir_{0.20}Sn_{0.80})O_2$, synthesized as a thin film on Ti foil, shows an improve in electrochemical performance with the addition of F suggesting that this system is indeed a promising OER electro-catalyst for PEM based water electrolysis. Identification of such non-noble metal based catalysts or electro-catalysts with significant reduction of expensive noble metal contents (*E.g.* IrO_2, Pt) with comparable or higher electrochemical performance as the standard noble metal/oxide for PEM based water electrolysis would result in reduction in the overall capital

costs of PEM based water electrolyzers, and therefore, attainment of the targeted hydrogen production cost (< $ 3.0 / gge delivered) comparable to conventional liquid fuels.

5.1.3 Binary F doped $(Ru,Sn)O_2$

5.1.3.1 Structural Analysis

Figure 25 shows the XRD patterns of thin films of RuO_2 and SnO_2 synthesized by thermal decomposition of $RuCl_3$ and $SnCl_2.2H_2O$ ethanol solution, respectively, coated on Ti foil following heat treatment at 400°C for 4 hours. The XRD patterns of the RuO_2 and SnO_2 thin film show tetragonal structure as expected. The XRD patterns of the most optimized electro-catalyst composition having only 20 at.% RuO_2 *i.e.* $(Ru_{0.2}Sn_{0.8})O_2$:F with different F compositions (0, 5, 10, 15 wt.%), shown in **Figure 26**, also show the peaks corresponding to tetragonal structure which suggest the formation of complete solid solution without any undesirable phase separation (*E.g.* $SnO_2 + RuO_2$). Formation of metastable solid solution between RuO_2 and SnO_2 as well as in the other oxide systems such as RuO_2, SbO_2, and SnO_2 has been reported by other researchers [32, 109, 110]. However, it should be noted that $(Ru,Sn)O_2$:15 wt.% F shows an extra peak for SnO_2 which indicates that excess F substitution leads to phase separation. The calculated effective crystallite size for all of the $(Ru,Sn)O_2$:F films is in the range of ~ 5 - 10 nm which is comparable with $(Ru,Sn)O_2$ suggesting that F^- doping has no significant effect on the refinement of crystallite size of $(Ru,Sn)O_2$.

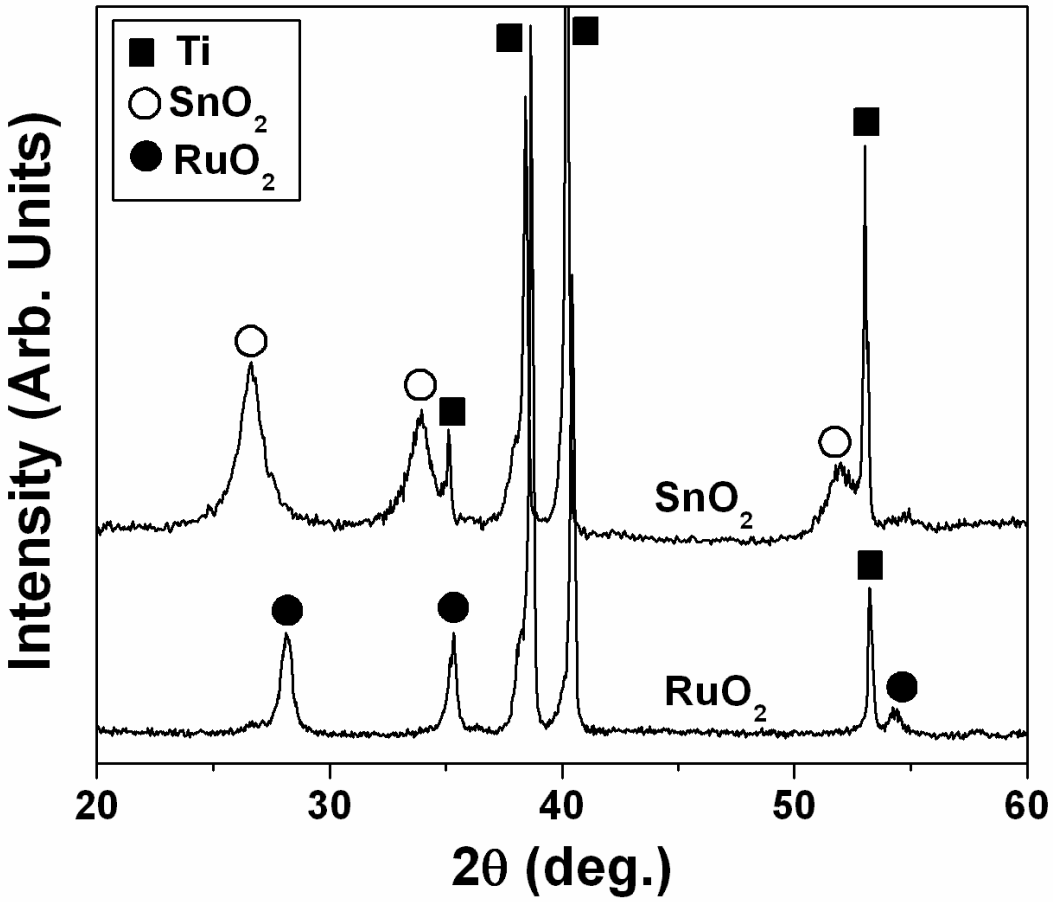

Figure 25. XRD patterns of thin film RuO_2 and SnO_2 coated on a Ti foil

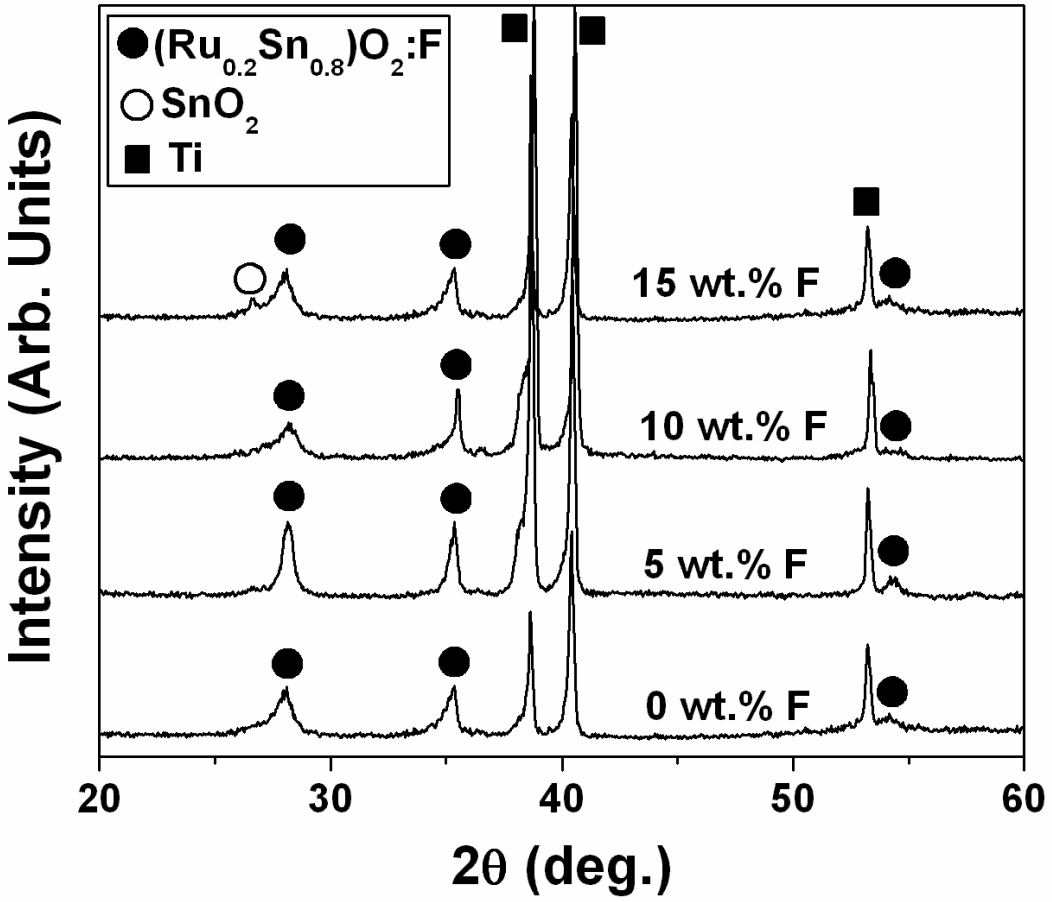

Figure 26. XRD patterns of thin film $(Ru_{0.2}Sn_{0.8})O_2$:F for different F compositions coated on Ti foil

The presence of The presence of elemental Ru, Sn and O in the (Ru,Sn)O_2:F film of different compositions has been confirmed using energy dispersive x-ray analysis (EDX) configured to the SEM, although as expected, the presence of F could not be detected. The SEM image along with elemental x-ray mapping, shown in **Figure 27**, is for a representative (Ru,Sn)O_2:F film containing 10 wt.% F. It indicates the presence of the characteristic "mud-crack" morphology of the (Ru,Sn)O_2:F film coated on Ti foil, and also validates the presence of

Ru, Sn and O which are homogeneously distributed within the $(Sn,Ru)O_2$:F particles (see the elemental dot maps in **Figure 27**) without being segregated on any specific site or on any particular region of the particle.

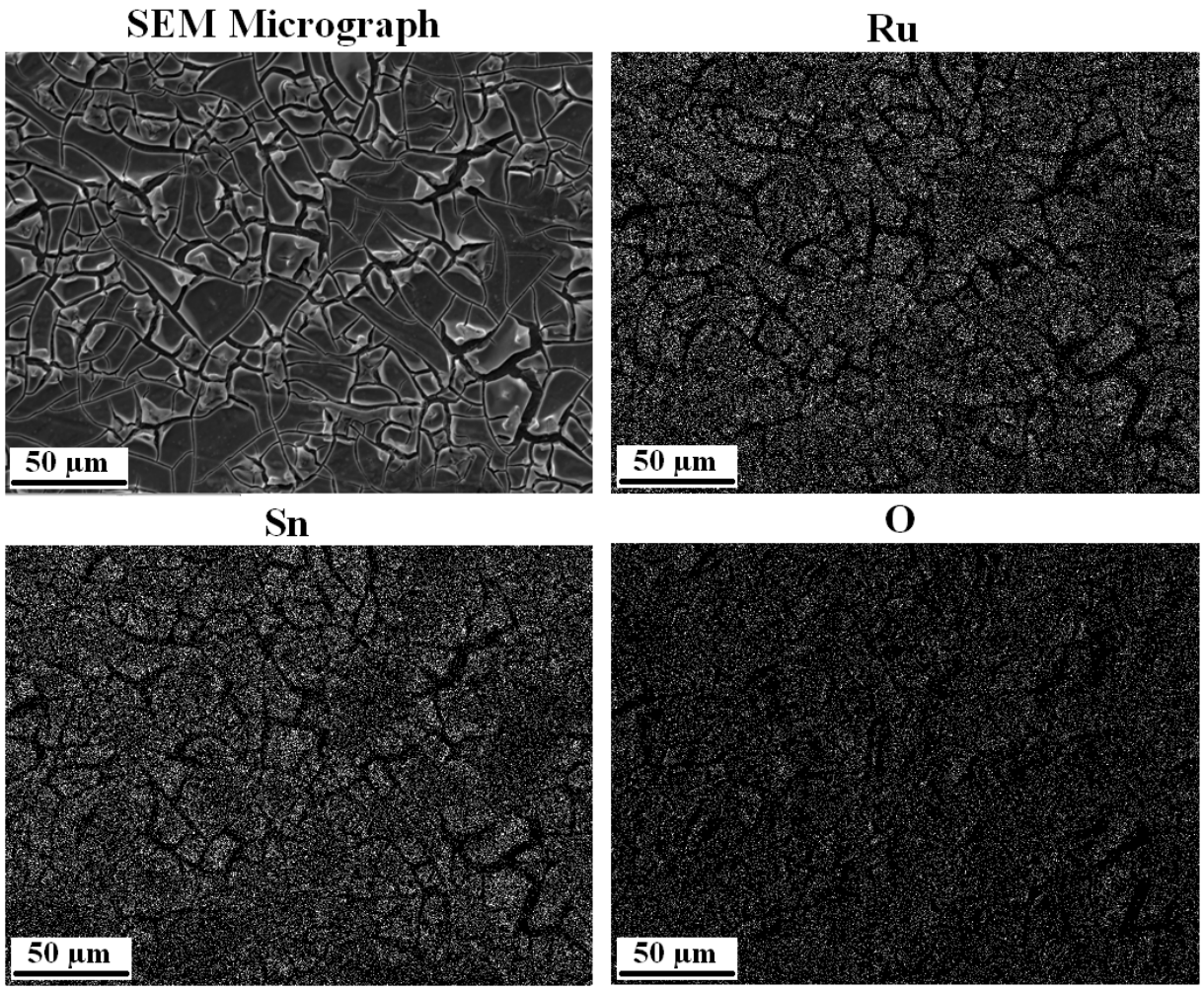

Figure 27. The SEM micrograph along with x-ray mapping of Ru, Sn and O

Figure 28 shows the quantitative analysis of the elemental composition of the representative $(Ru,Sn)O_2$:10F films obtained by EDX (a) and the TEM image (b). The EDX shows that the measured elemental composition of Sn and Ru which is 77.4 at.% and 22.6 at.%

respectively are expectedly close to the nominal composition. Elemental composition of the other electro-catalysts was also measured by EDX and was found to be similar to the nominal composition. The bright field TEM image of $(Ru,Sn)O_2$:F particles as seen in **Figure 28** (b), collected from the $(Ru,Sn)O_2$:10 wt.% F film confirms nanostructured fine particles of ~ 10 - 15 nm corresponding to the $(Ru,Sn)O_2$:F solid solution.

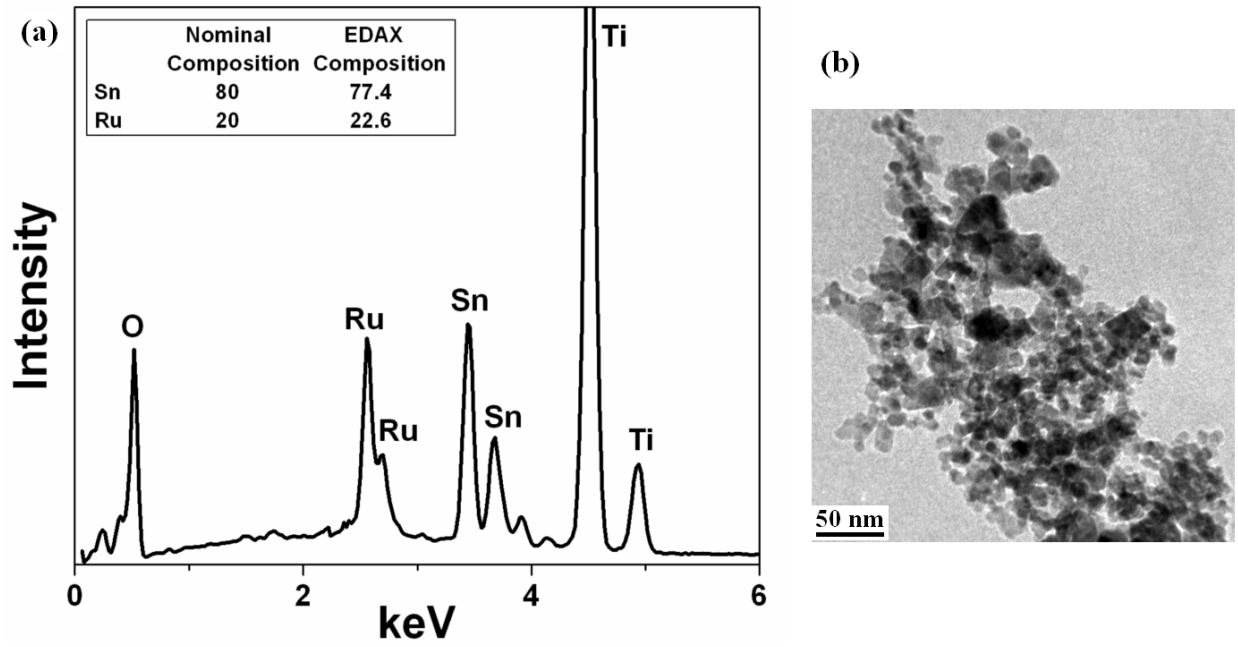

Figure 28. The EDX (a), and TEM imaging (b) of $(Ru,Sn)O_2$:10F thin film

5.1.3.2 Electrochemical Testing

The electrochemical activity of RuO_2 and $(Ru,Sn)O_2$:F thin films of different composition has been studied as an OER anode electro-catalyst for PEM based water electrolysis. It should be noted that the linear polarization curve and non-linear Tafel plots are typically most often encountered due to a large contribution of ohmic resistance (R_Ω) which mainly arises due to the

solution resistance of the electrolyte (solution resistance, R_s), the oxide film electrode resistance (R_e) and the accumulation of oxygen gas bubble covering the electrode surface during water electrolysis occurring at higher current densities (bubble resistance, R_{bub}) [83, 111]. These contributions were also observed in the present study. In order to evaluate the inherent electrochemical property or the electrode kinetics of the electro-catalyst studied herein, the polarization curve of different samples, conducted in the presence of 1 N H_2SO_4 solution at 40°C with a scan rate of 1mV/sec, is plotted after appropriately correcting for the total ohmic loss (iR_Ω). The total ohmic loss (iR_Ω) is the sum value of the solution resistance (R_s) and the electrode resistance (R_e). The value of R_s and R_e, respectively of the different samples, tabulated in **Table 2**, is obtained from electrochemical impedance spectroscopy (EIS) measurements conducted at different potentials with respect to NHE at 40^{o}C.

Table 2. Impedance parameters and Tafel slope of RuO_2 and (Ru,Sn)O_2:F

Composition	R_s (Ωcm^2)	R_e (Ωcm^2)	R_{ct} (Ωcm^2)	Tafel slope (b)
RuO_2	13.5	1.1	3.10	77
$(Ru_{0.2}Sn_{0.8})O_2$	12.3	3.2	4.96	76
$(Ru_{0.2}Sn_{0.8})O_2$:5F	10.6	2.0	4.65	67
$(Ru_{0.2}Sn_{0.8})O_2$:10F	12.3	1.5	4.17	65

Figure 29 shows the electrochemical impedance plot of RuO_2 and (Sn,Ru)O_2:F obtained at 1.6 V, the typical voltage selected for evaluating the optimal performance of the catalyst at

40°C in the presence of 1 N H_2SO_4 solution in the frequency range of 100 mHz - 100kHz. The impedance parameters (**Table 2**) is obtained by fitting the experimental data using the ZView software from Scribner Associates with a circuit model $R_s(R_eQ_1)(R_{ct}Q_{dl})$, where R_s is the solution resistance, R_e is the electrode resistance, R_{ct} is the charge transfer resistance, Q_1 is the constant phase element (CPE) and Q_{dl} includes contributions from both the double layer capacitance and pseudo-capacitance, respectively [65, 67]. R_s is the resistance encountered at high frequencies due to charge transfer in the solution. R_e is the resistance faced in the circuit due to electron transfer from the electrode to the current collector (*i.e.* our coated Ti foil substrate). It has been observed that the solution resistance (R_s) and the electrode resistance (R_e) of RuO_2 and $(Ru,Sn)O_2$:F for the different F containing compositions is unchanged with change in potential. As shown in **Table 2**, the value of the electrode resistance (R_e) of $(Ru,Sn)O_2$:F decreases with increase in F content in the parent $(Ru,Sn)O_2$ lattice which may arise due to the improved electronic conductivity of $(Ru,Sn)O_2$:F with increase in F. Consequently, $(Ru,Sn)O_2$:F with 10 wt.% F exhibits almost identical electrode resistance (R_e ~ 1.5 Ωcm^2) as pure RuO_2 (R_e ~ 1.1 Ωcm^2) suggesting the identical electronic conductivity of both systems. The low frequency EIS plot of pure RuO_2 and $(Ru,Sn)O_2$:F (**Figure 29**) shows a well formed semicircle related to OER and also indicates that the diameter of the low frequency semicircle typically a measure of the polarization resistance (R_{ct}) decreases with increase in F. The above results therefore clearly suggests that the electrochemical activity of $(Ru_{0.2}Sn_{0.8})O_2$:F increases with increase in F and moreover, the polarization resistance (R_{ct}) value of $(Ru_{0.2}Sn_{0.8})O_2$:10F is similar (~ 4.2 Ωcm^2) to that of pure RuO_2 (~ 3.1 Ωcm^2) which further indicates that both systems will likely exhibit almost equivalent electro-catalytic activity as detailed below.

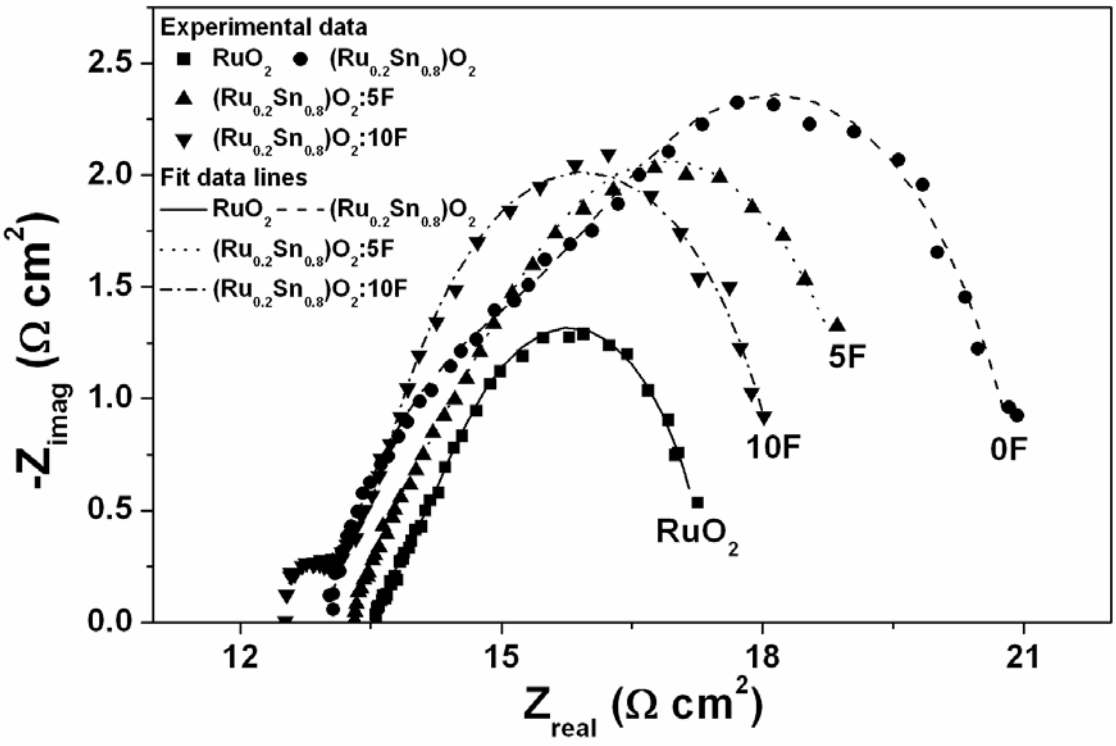

Figure 29. The EIS plot of (Ru,Sn)O_2:F and RuO_2 obtained at 1.6 V in the presence of 1 N H_2SO_4 solution in the frequency range of 100 mHz - 100 kHz

The polarization curve of pure SnO_2:F and RuO_2 film, before and after ohmic resistance correction ($iR_\Omega = iR_s + iR_e$) without considering the bubble resistance, conducted in the presence of 1 N H_2SO_4 solution at 40°C with a scan rate of 1 mV/sec, is shown in **Figure 30**. The polarization curve of SnO_2:F as expected shows no catalytic activity at all for water electrolysis. On the other hand, nano-crystalline, undoped and pure RuO_2 clearly indicates the occurrence of the water splitting or OER at a potential of ~ 1.42 V *vs.* NHE. The current density at ~ 1.55 V (*vs.* NHE), a voltage selected to evaluate the electrochemical activity for water electrolysis

obtained from iR_Ω corrected plot is ~ 0.0176 ± 0.001 A/cm^2 at 40^{o}C with a total loading ~ 0.3 mg/cm^2 of RuO_2. The polarization curve for the various (Ru,Sn)O_2:F film compositions containing different amounts of F before and after iR_Ω correction, plotted in **Figure 31** also shows that water splitting occurs at the potential of ~1.42 V (*vs.* NHE) irrespective of the composition which is identical to that of pure RuO_2. Furthermore, the current density at ~ 1.55 V (*vs.* NHE) obtained from iR_Ω corrected plot for undoped (Ru,Sn)O_2 solid solution (0 F) with an identical total loading of ~ 0.3 mg/cm^2 is ~ 0.009 ± 0.0001 A/cm^2 at 40°C which is almost 50 % of that of pure RuO_2. However, the current density of (Ru,Sn)O_2:F increases with increase in F content. In fact, (Ru,Sn)O_2:F containing 10 wt.% F has a current density at ~ 1.55 V (*vs.* NHE) of ~ 0.0175 ± 0.001 A/cm^2 which is comparable with that of pure RuO_2. However, the trend does not continue with increase in F content and it can be seen that the current density unfortunately decreases with continued increase in F content above 10 wt.% F as seen in **Figure 32**. (Ru,Sn)O_2:15 wt.% F has lesser catalytic activity, and this could potentially arise due to the phase separation of SnO_2 from (Ru,Sn)O_2:F as observed in the XRD pattern (**Figure 26**). **Figure 33** shows the variation of current density for all undoped compositions of binary (Ru,Sn)O_2 and F doped $(Ru_{0.2}Sn_{0.8})O_2$ at a potential of ~ 1.75 V (*vs.* NHE) from all the polarization tests.

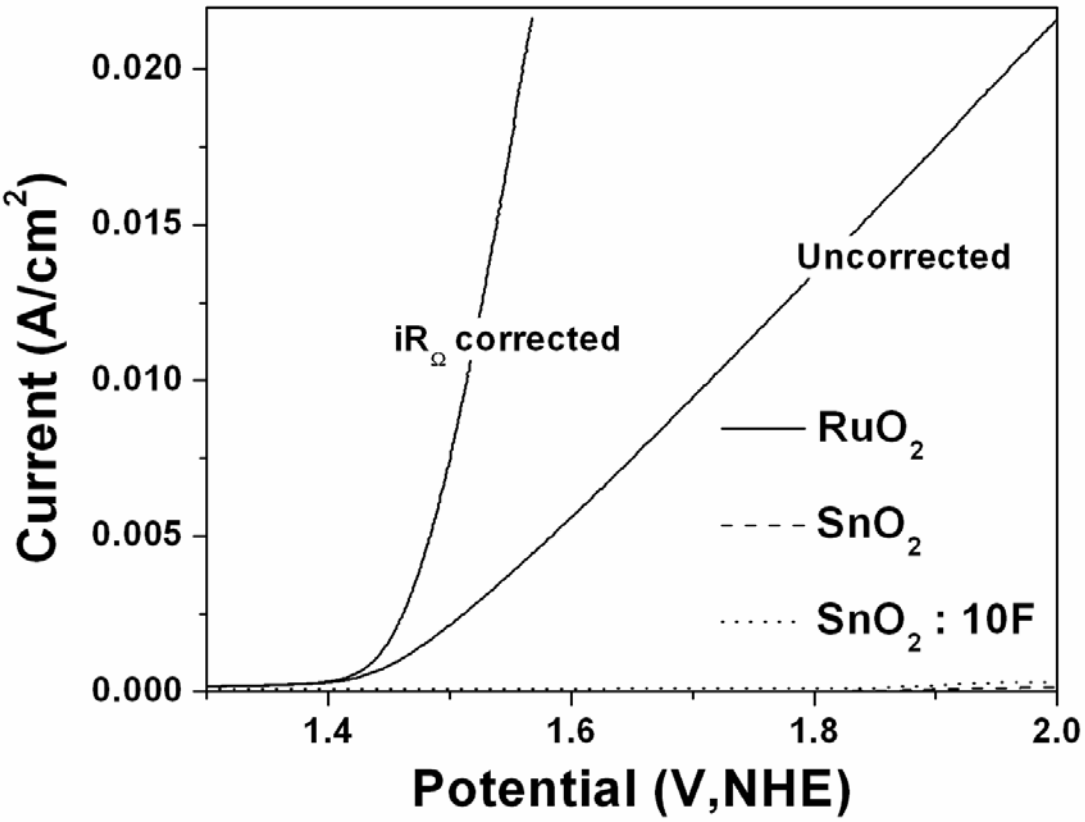

Figure 30. The polarization curve of pure RuO_2, SnO_2 and SnO_2:10F film conducted in the presence of 1 N H_2SO_4 solution at 40°C with a scan rate of 1mV/sec

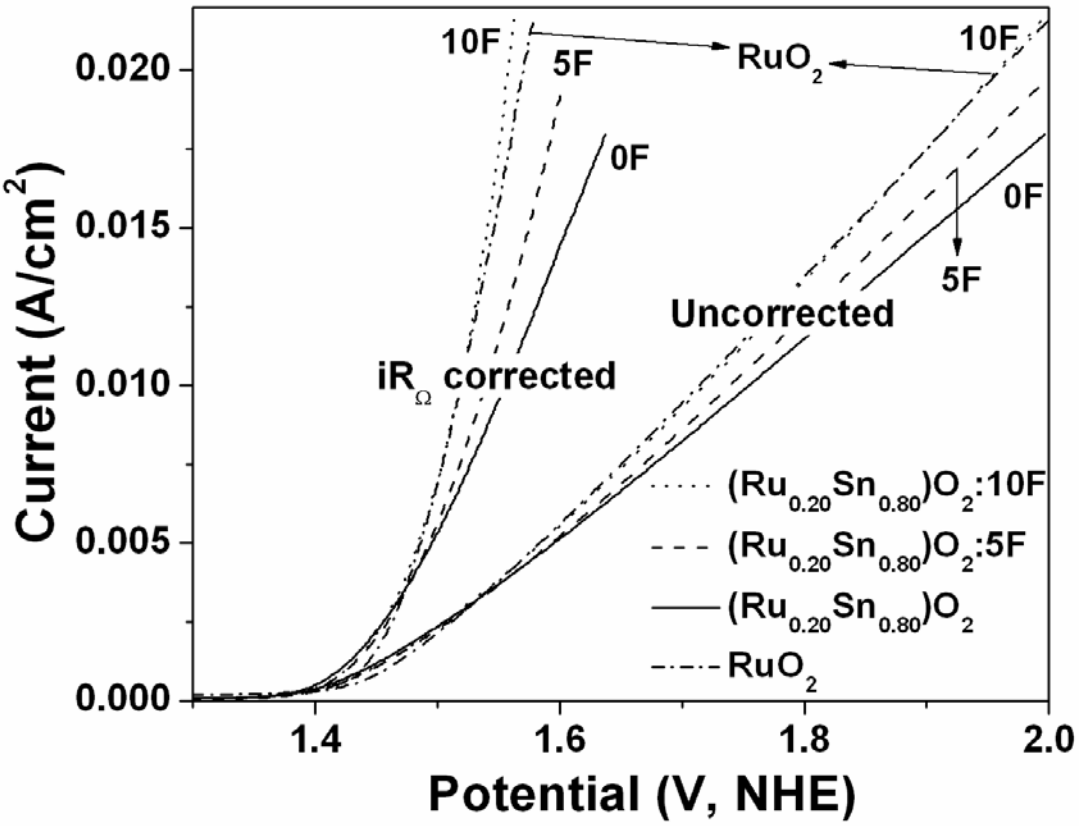

Figure 31. The polarization curve of $(Ru,Sn)O_2$:F film of different F compositions conducted in 1 N H_2SO_4 at 40°C with a scan rate of 1mV/sec before and after iR correction

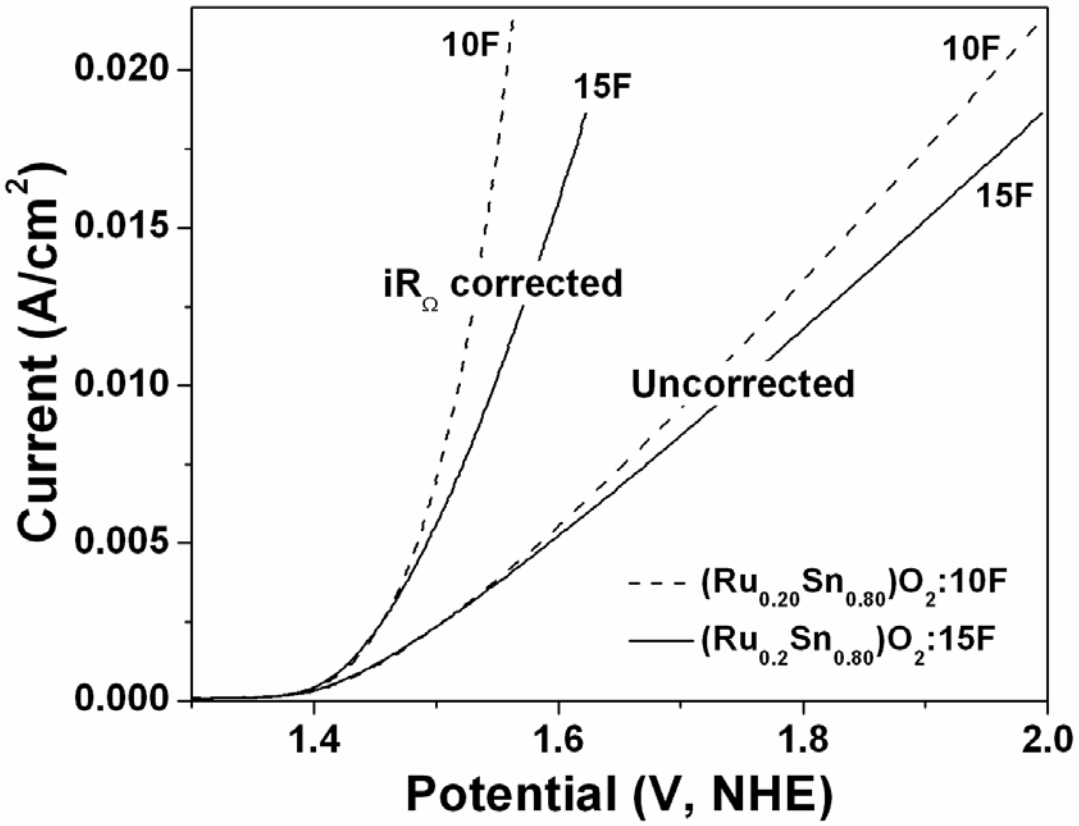

Figure 32. The polarization curve for high F doping of (Ru,Sn)O_2:F film conducted in 1 N H_2SO_4 solution at 40°C before and after iR correction with a scan rate of 1mV/sec

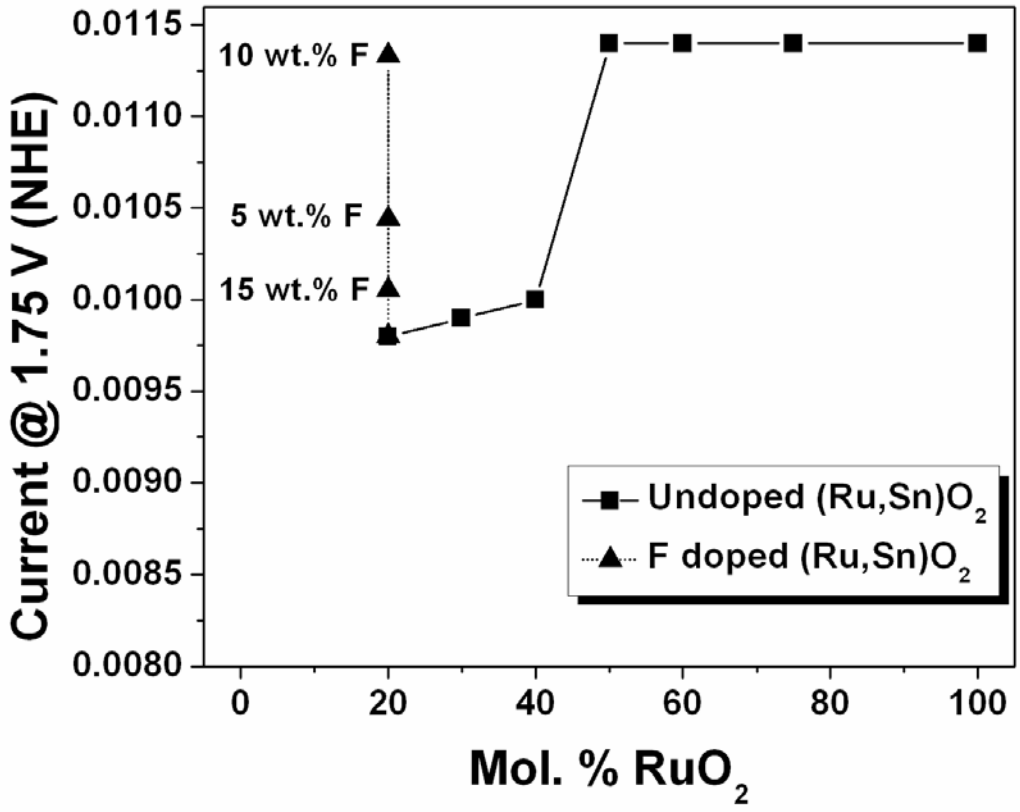

Figure 33. Variation of current density at ~ 1.75V (*vs.* NHE) with compositions of undoped and F doped (Ru,Sn)O_2 anode electro-catalyst

Figure 34, **Figure 35**, **Figure 36** and **Figure 37** shows the Tafel plots of pure RuO_2, (Ru,Sn)O_2, (Ru,Sn)O_2:5 wt.% F, and (Ru,Sn)O_2:10 wt.% F respectively. The Tafel slopes of RuO_2 and $(Ru_{0.2}Sn_{0.8})O_2$:F with 0, 5 and 10 wt.% F calculated from the corresponding iR_Ω corrected Tafel plots, are 77, 76, 67 and 65 mV/decade, respectively. This suggests that the electrochemical activity of (Ru,Sn)O_2:F increases with increase in F with the corresponding decrease in the Tafel slope for increasing F content reaching an optimal value for

$(Ru_{0.2}Sn_{0.8})O_2$:10F thus exhibiting comparable electrochemical activity to that of pure RuO_2. These results therefore clearly suggest that (Ru,Sn)O_2:F containing 10wt% F nominal composition is indeed a promising candidate as an OER anode electro-catalyst for PEM based water electrolysis. It should be noted that although the exact amount of F incorporated in the structure cannot be detected using EDAX analysis, it is nevertheless clear that with increasing amount of F there is significant increase in the electrochemical activity reaching an optimal value for the nominal composition of the oxide containing 10 wt.% F.

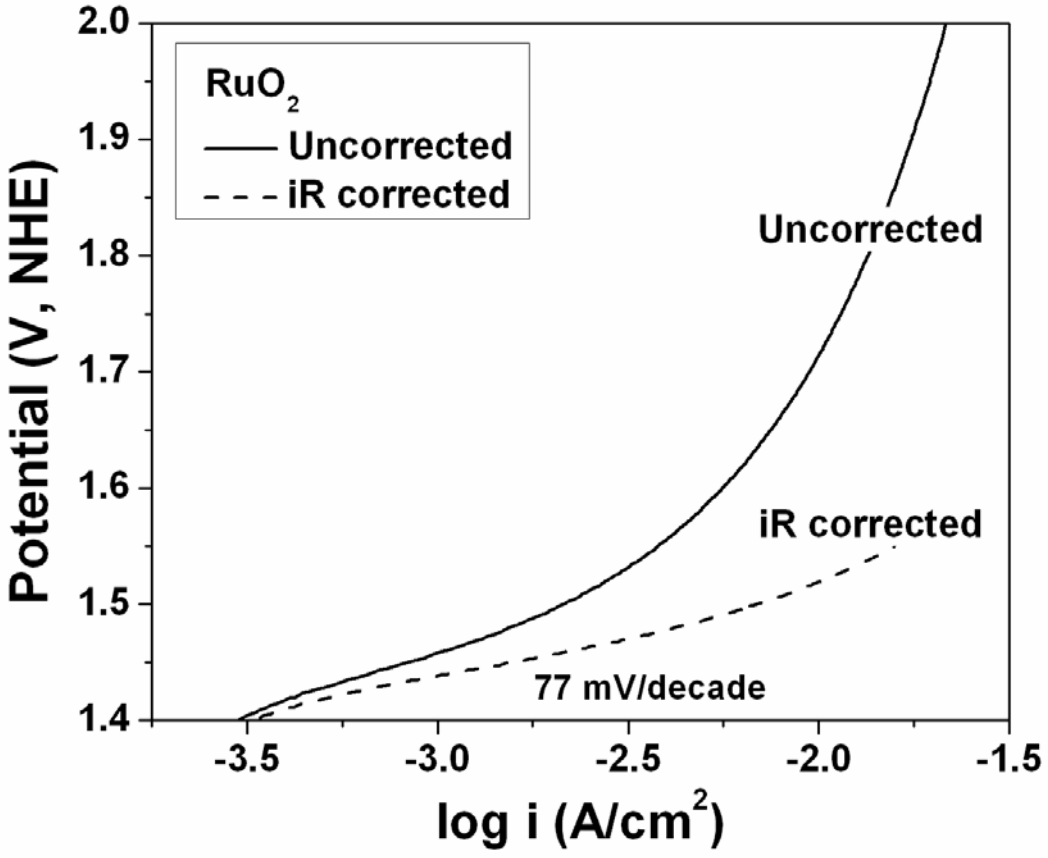

Figure 34. The Tafel plot of pure RuO_2 before and after iR correction

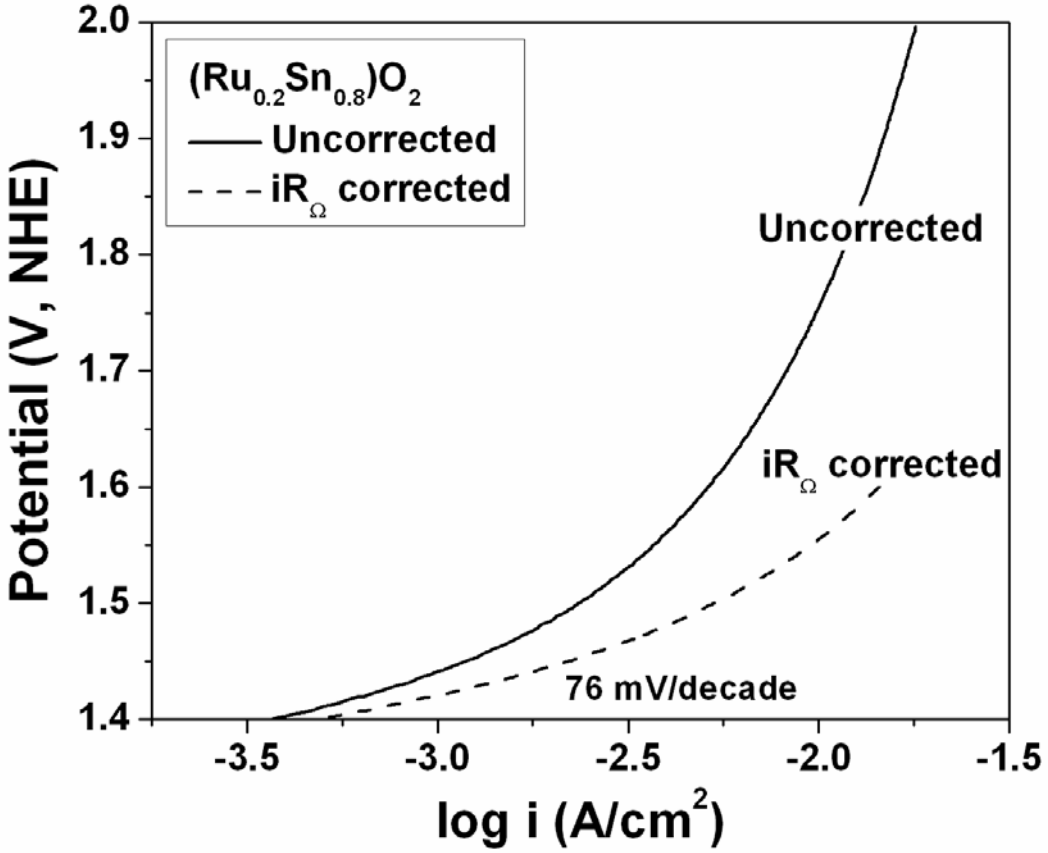

Figure 35. The Tafel plot of $Ru_{0.2}Sn_{0.8})O_2$ before and after iR correction

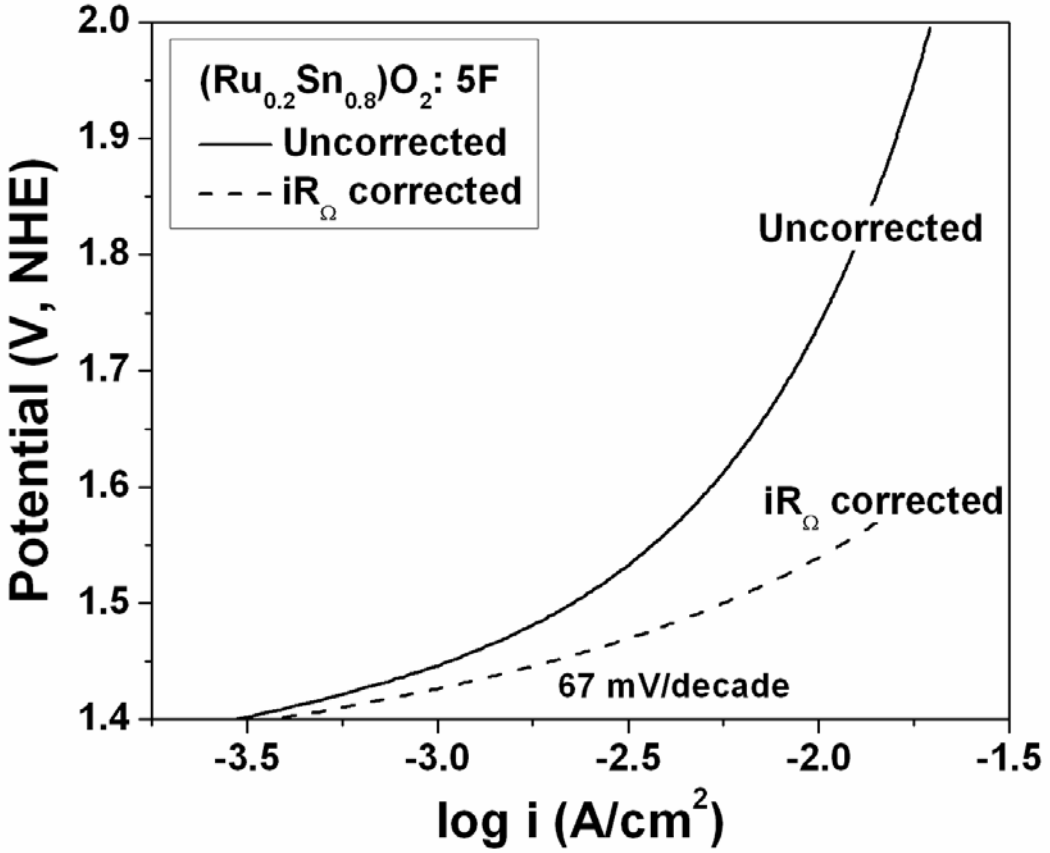

Figure 36. The Tafel plot of $(Ru_{0.2}Sn_{0.8})O_2$:5 wt.% F before and after iR correction

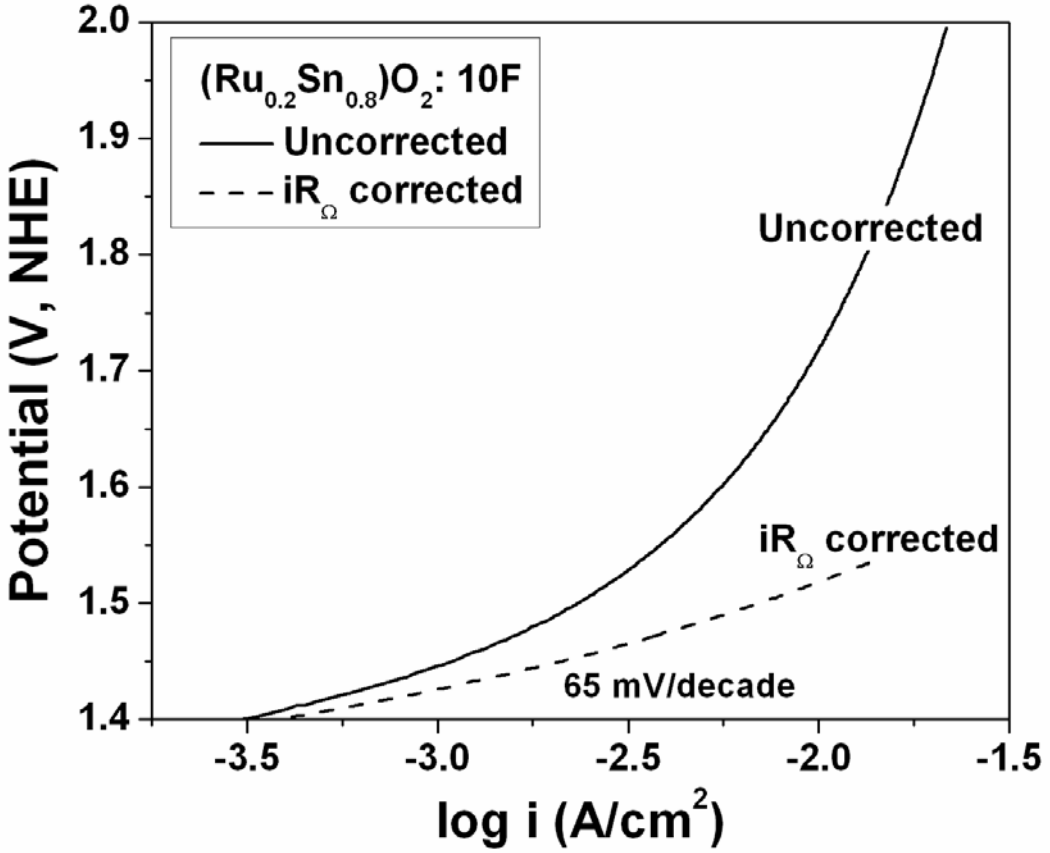

Figure 37. The Tafel plot of $(Ru_{0.2}Sn_{0.8})O_2$:10 wt.% F before and after iR correction

In order to study the electrochemical stability (durability) of the anode electro-catalyst $(Ru,Sn)O_2$:F in 1 N H_2SO_4 during OER, CA test is conducted for 12 hours at 40°C at a constant voltage of ~ 1.5 V (after iR_Ω correction), a standard accepted potential for estimating electrochemical activity. Hence, this was also selected as the potential for determining the current density for assessing the degradation or loss of activity of the catalyst as a function of time in CA studies. The CA curves, obtained at a ~ 1.5 V, for $(Ru,Sn)O_2$:F combined with that of pure RuO_2 are shown in **Figure 38**. The CA curve clearly shows a decrease in current (after iR_Ω

correction) with time which may be due to either dissolution of the irregular coating located at the edge of the mud cracks [30], diffusion controlled reaction or evaporation induced loss of electrolyte. A steady decrease in current has been noticed after 2 hours of the initial period for both (Ru,Sn)O_2:10 wt.% F and pure RuO_2 which suggests that ($Ru_{0.2}Sn_{0.8}$)O_2:10F has similar structural stability compared to pure RuO_2.

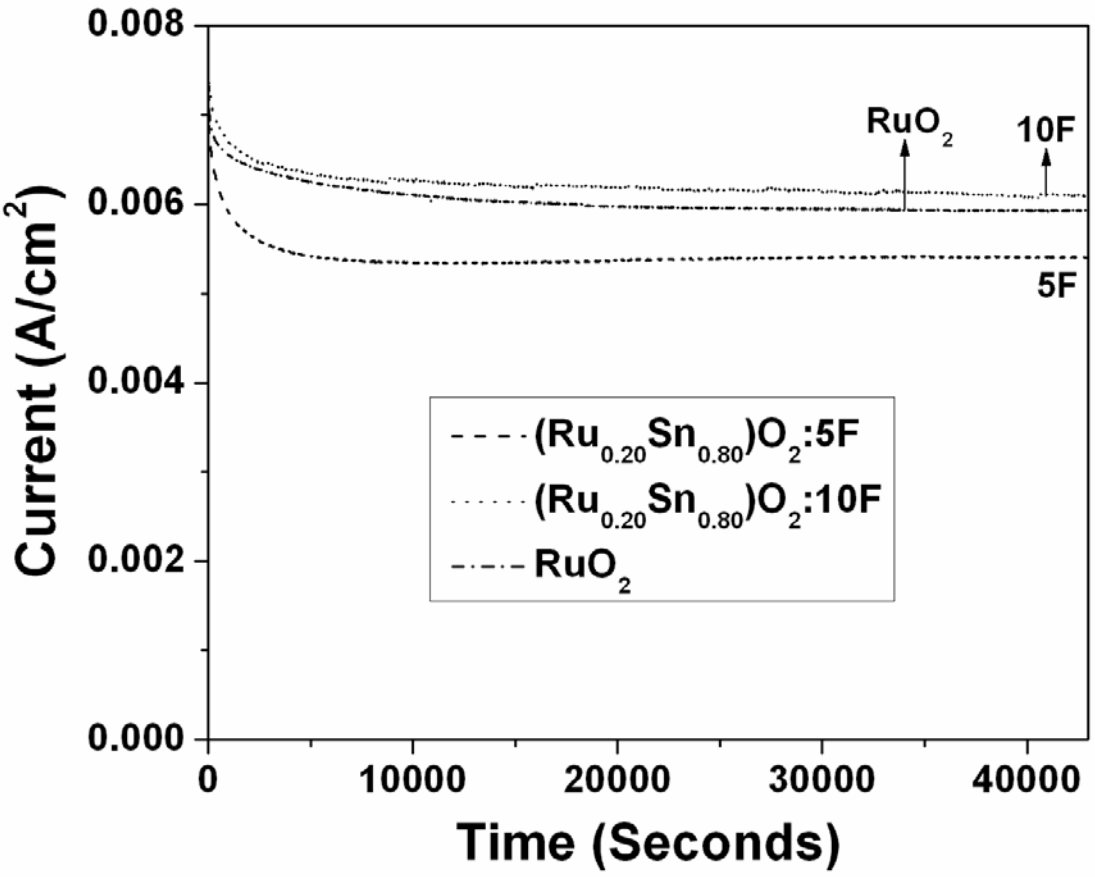

Figure 38. The variation of current *vs.* time in the durability test of pure RuO_2 and (Ru,Sn)O_2:F performed in a 1 N H_2SO_4 solution under ~ 1.5 V at 40°C

However, the ICP analysis conducted on the 1 N H_2SO_4 electrolyte solution collected after 12 hours of CA measurement, shows no presence of Ru up to 10 wt.% F which suggest that the steady decrease in current for RuO_2 and $(Ru_{0.2}Sn_{0.8})O_2$:10F during the CA measurement may arise due to loss of fuel rather than dissolution of the Ru from the electro-catalyst present on the surface of the electrode. However, it has been noticed from ICP analysis that Sn is leached in minute amounts in the solution. $(Ru_{0.2}Sn_{0.8})O_2$:F with 0, 5 and 10 wt.% F solutions after 12 hours of CA have 0.253 ppm, 0.227 ppm and 0.202 ppm of Sn respectively.

After the conclusion of the CA test, the RuO_2 and the $(Ru_{0.2}Sn_{0.8})O_2$:10 wt.% F thin film electrodes were subject to polarization testing as seen in **Figure 39** in order to determine the activity of the electrodes after long term structural stability tests. The Tafel plots from these polarization curves (post CA measurement) after iR correction are shown in **Figure 40** and **Figure 41**. A Tafel slope of ~ 92 mV/decade and ~ 94 mV/decade was obtained for pure RuO_2 thin film and $(Ru,Sn)O_2$:10 wt.% F respectively. This is slightly higher but still close and comparable to the values obtained from the polarization tests conducted before CA (**Figure 34** and **Figure 37**). This test further demonstrates the robustness of the electro-catalysts.

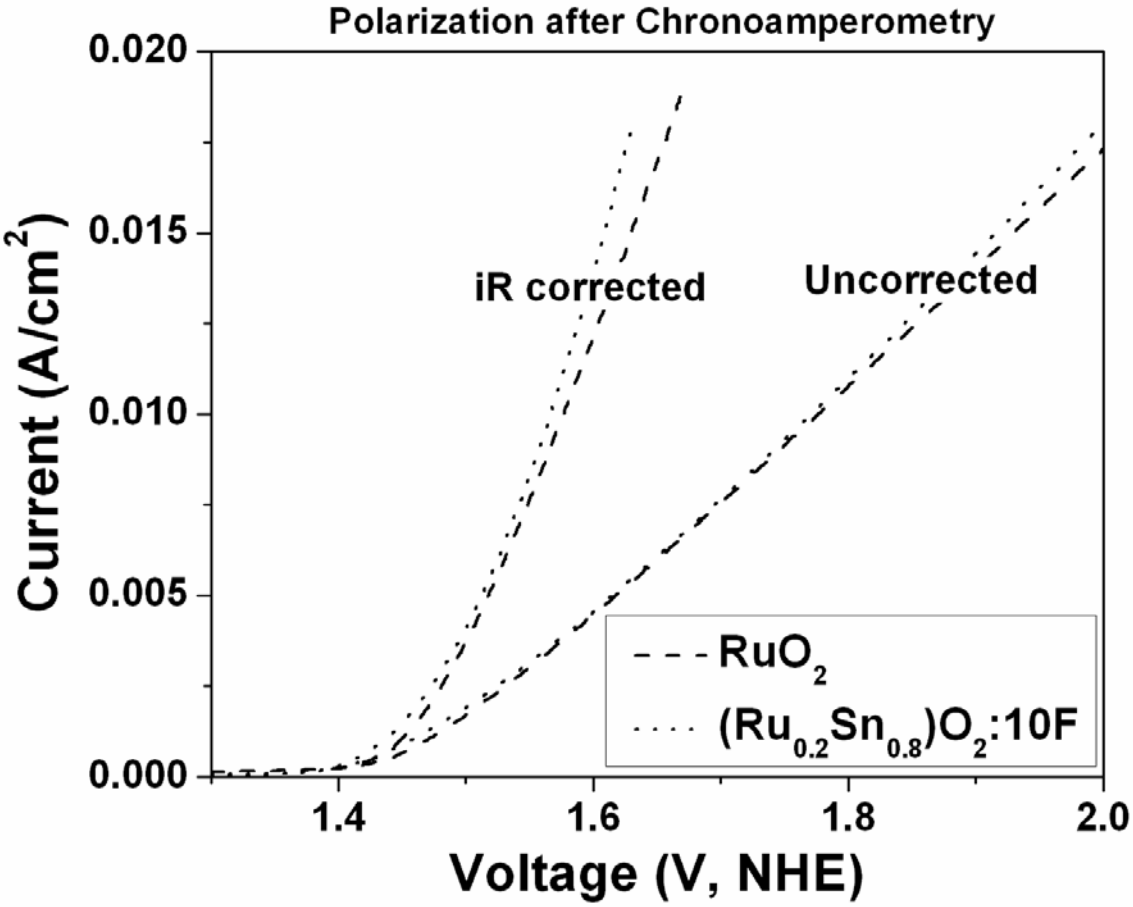

Figure 39. Polarization curve of RuO_2 and (Ru,Sn)O_2:10 wt.% F thin film after the CA test

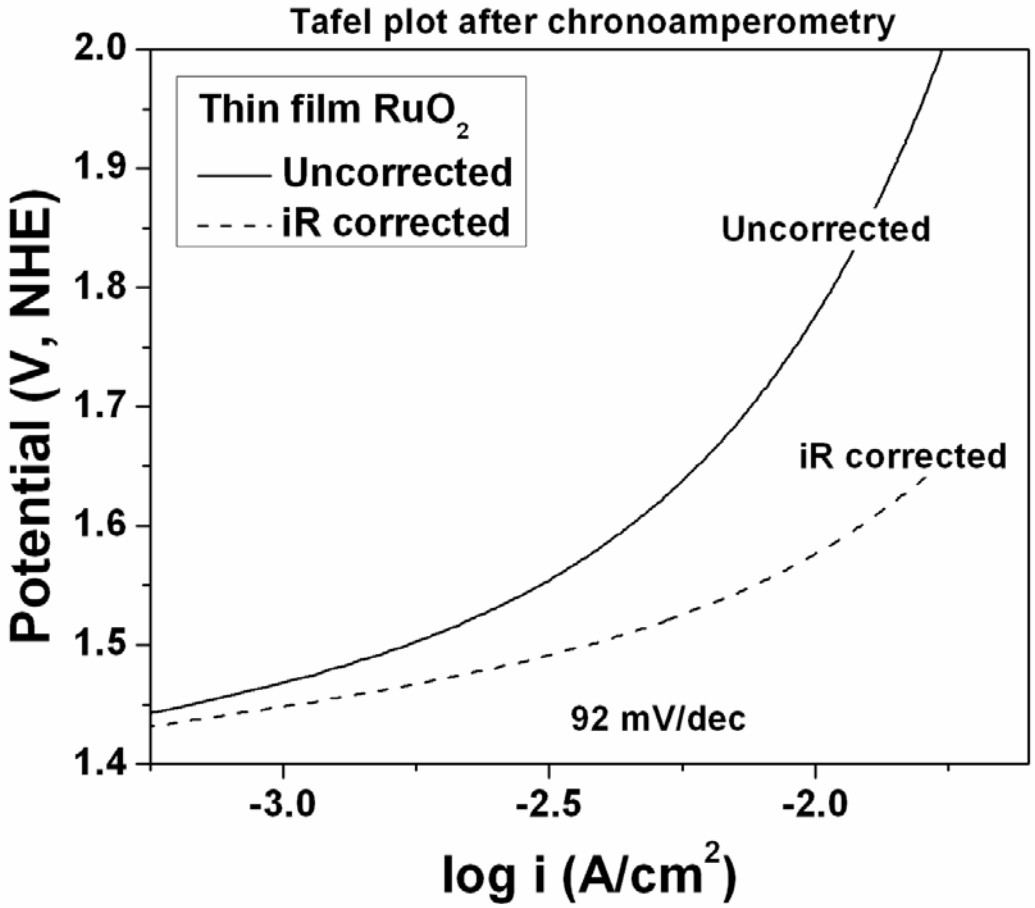

Figure 40. The Tafel plot of RuO_2 thin film after the CA test

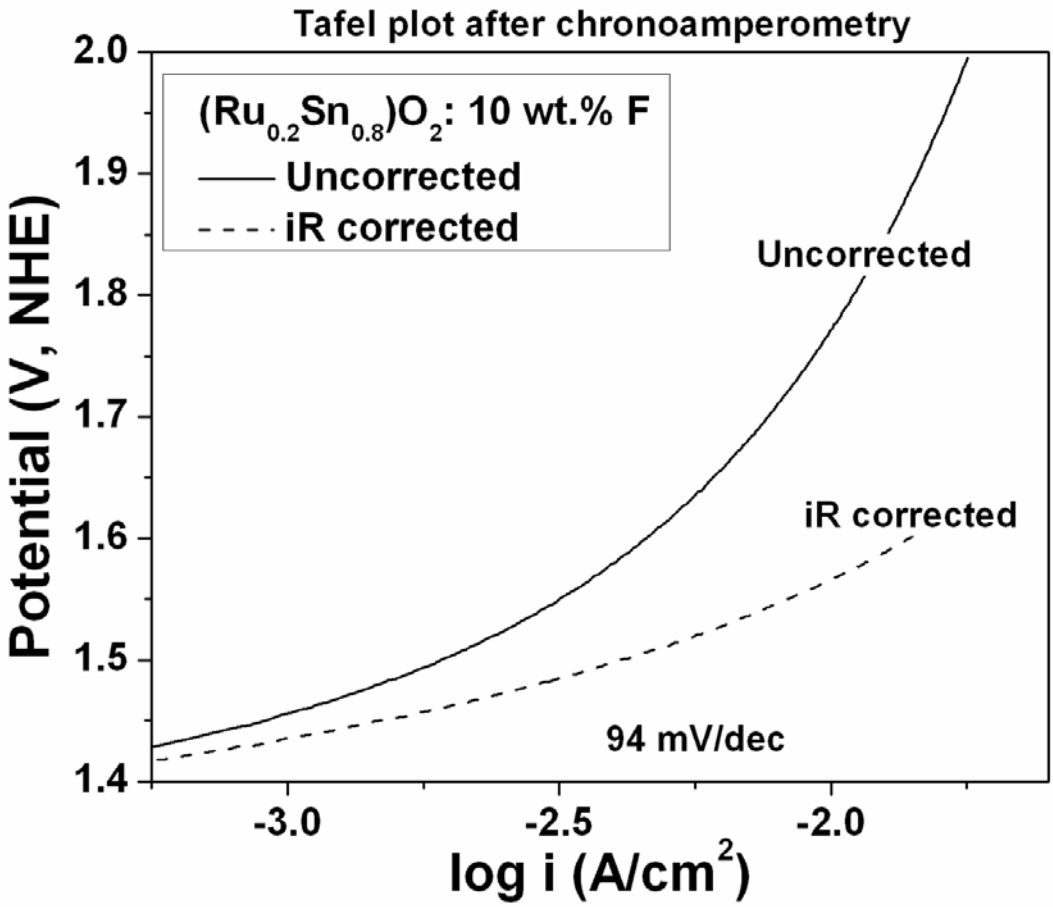

Figure 41. The Tafel plot of (Ru,Sn)O_2:10 wt.% F thin film after the CA test

This experimental study successfully demonstrates that F doped ($Ru_{0.20}Sn_{0.80}$)O_2 is a promising OER electro-catalyst for PEM based water electrolysis. The electrochemical performance including the current density, polarization resistance, Tafel slope and stability / durability at an optimal composition of 10 wt.% F matches that of pure RuO_2. As a result, we conclude that ($Ru_{0.20}Sn_{0.80}$)O_2:10 wt.% F is potentially a preferred oxygen evolution electro-catalyst composition for water electrolysis resulting in ~ 80 % reduction in the noble metal oxide

content. This system and the composition can thus be considered to portend a significant reduction in the overall capital cost of PEM based water electrolyzers.

5.1.4 Ternary (Ir,Sn,Nb)O_2

5.1.4.1 Structural Analysis

Figure 42 shows the XRD patterns of thin film pure IrO_2 and SnO_2 synthesized by thermal decomposition of $IrCl_4$ and $SnCl_2.2H_2O$ ethanol solution, respectively, coated on Ti foil at 400°C for 4 hours. It also shows the XRD patterns of representative composition $(Sn_{0.5}Nb_{0.5})O_2$ synthesized by thermal decomposition of homogeneous mixture $SnCl_2.2H_2O$ and $NbCl_5$ ethanol solution with Sn:Nb molar ratio 1:1 coated on Ti foil at 400°C for 4 hours. The XRD patterns of IrO_2 and SnO_2 show tetragonal structure as expected. The XRD pattern of $(Sn_{0.5}Nb_{0.5})O_2$ also shows tetragonal structure similar to tetragonal SnO_2 structure without any detectable peaks of orthorhombic or monoclinic Nb_2O_5 which suggest Nb_2O_5 forms a solid solution with SnO_2 [(Sn,Nb)O_2]. Formation of solid solution of Nb_2O_5 with SnO_2, synthesized by Pechni process, has also been reported in literature [60, 112].

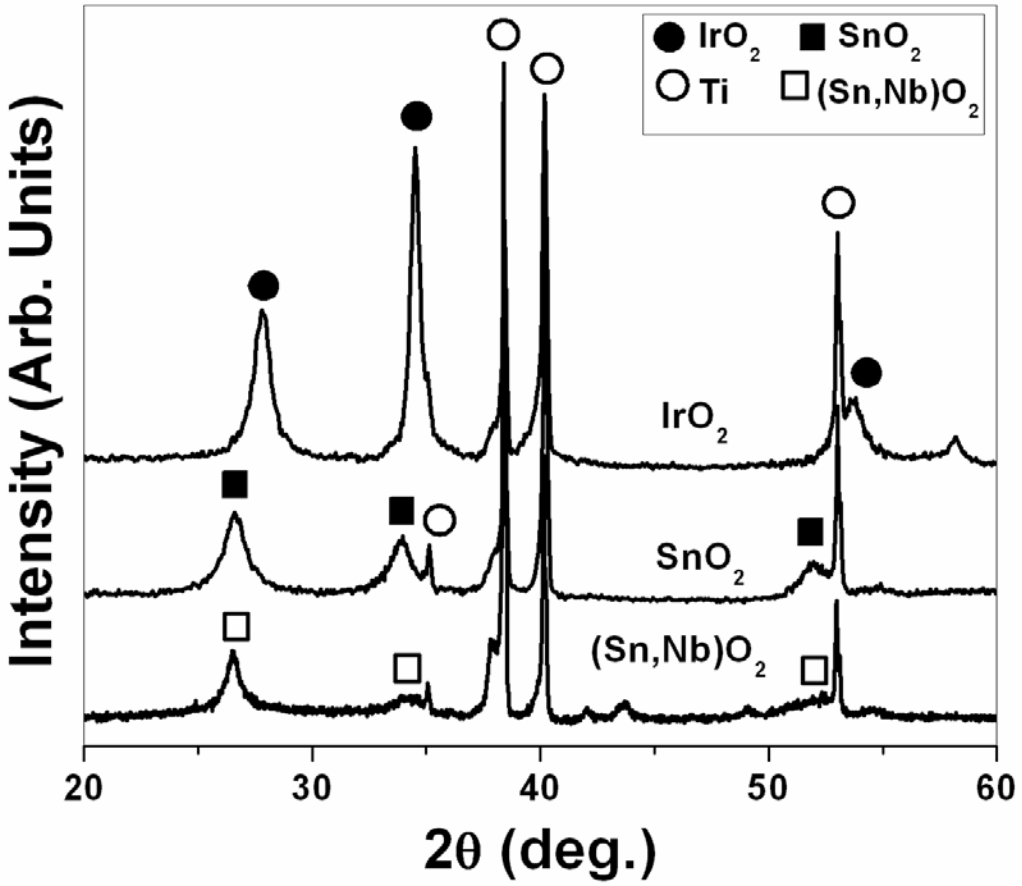

Figure 42. XRD patterns of thin film IrO_2, SnO_2 and $(Sn_{0.50}Nb_{0.50})O_2$ coated on Ti foil

The lattice parameter (nm) as well as molar volumes, calculated using least square refinement techniques, of thin film IrO_2, SnO_2 and $(Sn_{0.5}Nb_{0.5})O_2$ are shown in **Table 3**. The lattice parameter and the molar volume of $(Sn,Nb)O_2$ is very close to pure SnO_2 due to the ionic radius of Sn^{+4} (69 pm) being comparable with Nb^{+4} (68 pm) as well as the molar volume of SnO_2 (21.65 cm^3/mol) and NbO_2 (21.17 cm^3/mol) being close to each other in the bulk state. It also shows the effective crystallite sizes, calculated using Pseudo - Voigt function of single line approximation method, of thin film IrO_2, SnO_2 and $(Sn_{0.5}Nb_{0.5})O_2$. The thin film IrO_2, SnO_2 and

$(Sn_{0.5}Nb_{0.5})O_2$ are nanocrystalline in nature (below 20 nm). It must be mentioned here that the molar volume of nanocrystalline (~14 nm) IrO_2 is higher (~ 2 %) than the corresponding bulk state volume (~ 19.22 cm^3/mol) which suggests that IrO_2 exhibits lattice softening with refinement of crystallite size (CS) as also reported for other systems [113].

Table 3. Lattice parameter, molar volumes and crystallite size of $(Ir,Sn,Nb)O_2$ compositions

Composition	a=b (nm)	c (nm)	V_m (cm^3/mol)	CS (nm)
IrO_2	0.4537	0.3169	19.64	14
SnO_2	0.4736	0.3188	21.53	10
$(Sn_{0.5}Nb_{0.5})O_2$	0.4751	0.3149	21.40	8
$(Ir_{0.75}Sn_{0.125}Nb_{0.125})O_2$	0.4565	0.3414	19.74	8.5
$(Ir_{0.6}Sn_{0.2}Nb_{0.2})O_2$	0.4578	0.3416	19.83	8.4
$(Ir_{0.5}Sn_{0.25}Nb_{0.25})O_2$	0.4589	0.3139	19.90	9
$(Ir_{0.4}Sn_{0.3}Nb_{0.3})O_2$	0.4599	0.3132	19.96	9
$(Ir_{0.3}Sn_{0.35}Nb_{0.35})O_2$	0.4608	0.3131	20.02	3.7
$(Ir_{0.20}Sn_{0.40}Nb_{0.40})O_2$				3.3
$(Ir_{0.15}Sn_{0.425}Nb_{0.425})O_2$				3

On the other hand, the XRD patterns of ternary IrO_2-SnO_2-NbO_2 system of different compositions synthesized by thermal decomposition of homogeneous mixture of $IrCl_4$, $SnCl_2.2H_2O$ and $NbCl_5$ ethanol solution coated on Ti foil are shown in **Figure 43** and **Figure 44**. The XRD patterns of different compositions show the peaks corresponding to tetragonal structure which suggest the formation of complete solid solutions between IrO_2, SnO_2 and NbO_2 [$(Ir,Sn.Nb)O_2$]. Formation of metastable solid solution between IrO_2 and SnO_2 ($Ir_{1-x}Sn_xO_2$) as well as in the other systems such as IrO_2 - SbO_2 - SnO_2 and SnO_2 - IrO_2 - Ta_2O_5 has been reported by other researchers [32, 57, 60, 63, 65]. The lattice parameters and molar volume, calculated using least square refinement techniques, of $(Ir,Sn,Nb)O_2$ of different compositions are tabulated in **Table 3**.

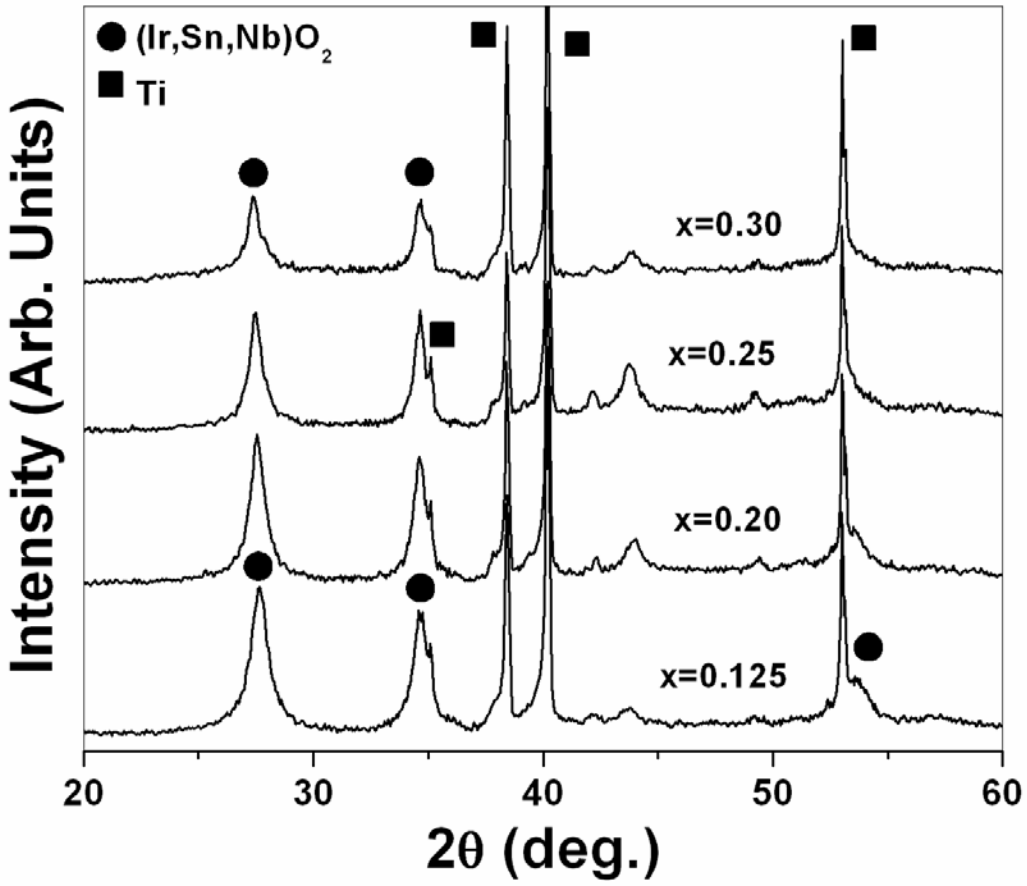

Figure 43. XRD patterns of $(Ir_{1-2x}Sn_xNb_x)O_2$ with x = 0.125, 0.20, 0.25, 0.30 coated on a Ti foil

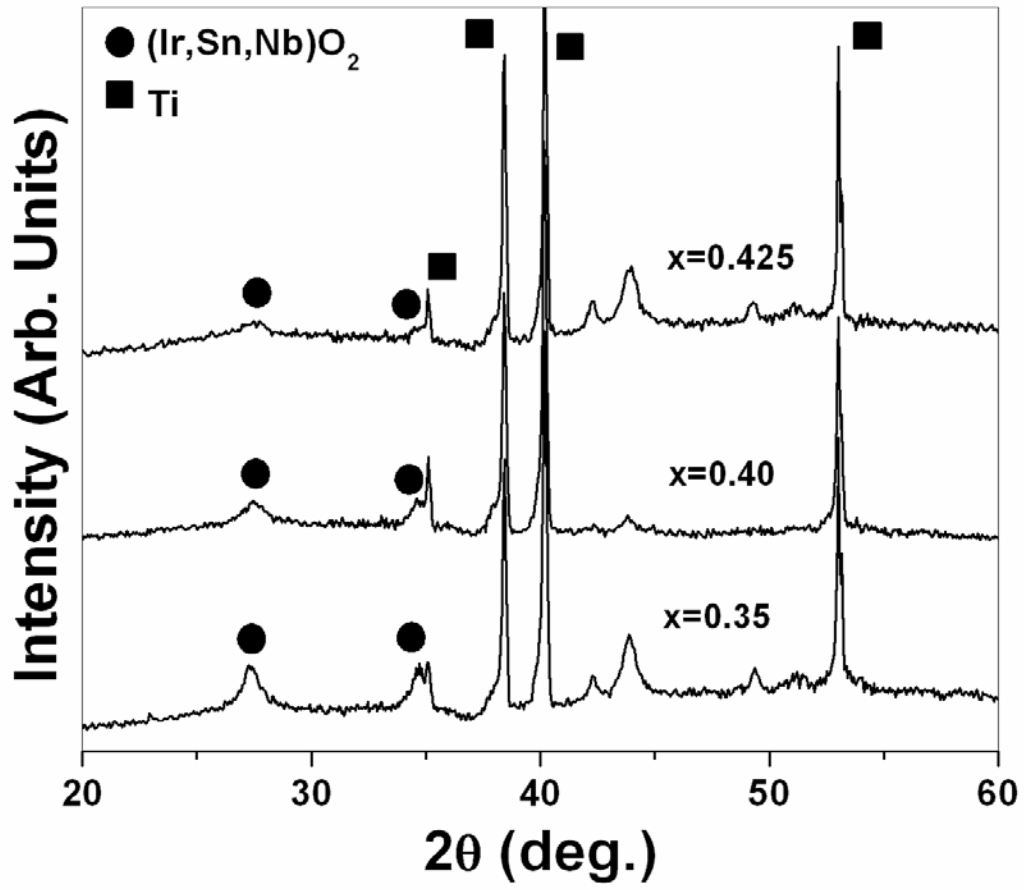

Figure 44. XRD patterns of $(Ir_{1-2x}Sn_xNb_x)O_2$ with x = 0.35, 0.40 and 0.425 coated on Ti foil

The lattice parameter and molar volume of $(Ir_{0.20}Sn_{0.40}Nb_{0.40})O_2$ (x = 0.40) and $(Ir_{0.15}Sn_{0.425}Nb_{0.425})O_2$ (x = 0.425) has not been reported because the XRD peak position not accurately detectable due to low intensity and large broadening of the XRD peaks (**Figure 44**). The crystallite size remains almost same (~ 8 - 9 nm) up to x = 0.30 (40 mol%. IrO_2), with a sudden decrease in crystallite size (~ 3 nm) observed at x = 0.35 (30 mol.% IrO_2). This result clearly suggests that $(Ir,Sn,Nb)O_2$ with higher percentage of $(Sn,Nb)O_2$ exhibit smaller crystallite size than IrO_2 rich composition. De Pauli *et al.* [29, 66] also suggested that high surface charge,

proportional to the active surface concentration, of SnO_2 rich IrO_2+SnO_2 system could arise due to increase in surface area with the addition of SnO_2.

The presence of elemental Ir, Sn and Nb in the (Ir,Sn,Nb)O_2 film of different compositions has been confirmed using energy dispersive X-ray spectroscopy analysis (EDX) attached to the SEM. The SEM image along with EDX of the $(Ir_{1-2x}Sn_xNb_x)O_2$ film of composition x = 0.40 $[(Ir_{0.2}Sn_{0.4}Nb_{0.4})O_2]$ and x = 0.125 $[(Ir_{0.75}Sn_{0.125}Nb_{0.125})O_2]$, shown in **Figure 45** and **Figure 46**, respectively; indicates the presence of "mud-cracked" morphology of (Ir,Sn,Nb)O_2 film coated on the pretreated Ti foil. However, it must be mentioned here that the coating morphology of the (Ir,Sn,Nb)O_2 electro-catalyst, synthesized by thermal decompositions of the homogeneous mixtures of the metal precursors on pretreated Ti foil, is affected by the composition. The coatings obtained with higher IrO_2 concentration (**Figure 46**) appear less cracked compared to lower IrO_2 containing composition (**Figure 45**). The high magnification SEM image of x = 0.125 shows the presence of fine particles in the nanometer range (~ 10 - 15 nm) which is comparable with the calculated crystallite size from the XRD pattern. Quantitative analysis of the elemental composition of (Ir,Sn,Nb)O_2 films obtained by EDX, as presented in **Figure 47** and **Table 4**, shows that the measured elemental contents are close to the nominal composition.

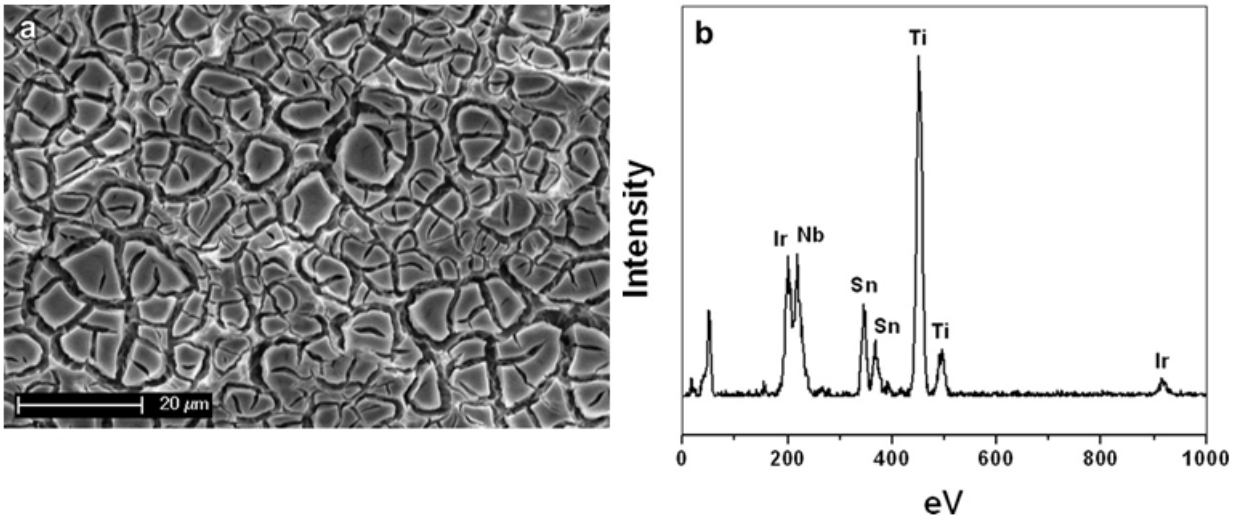

Figure 45. The SEM micrograph (a), and EDAX spectra (b) of $(Ir_{0.2}Sn_{0.4}Nb_{0.4})O_2$ film

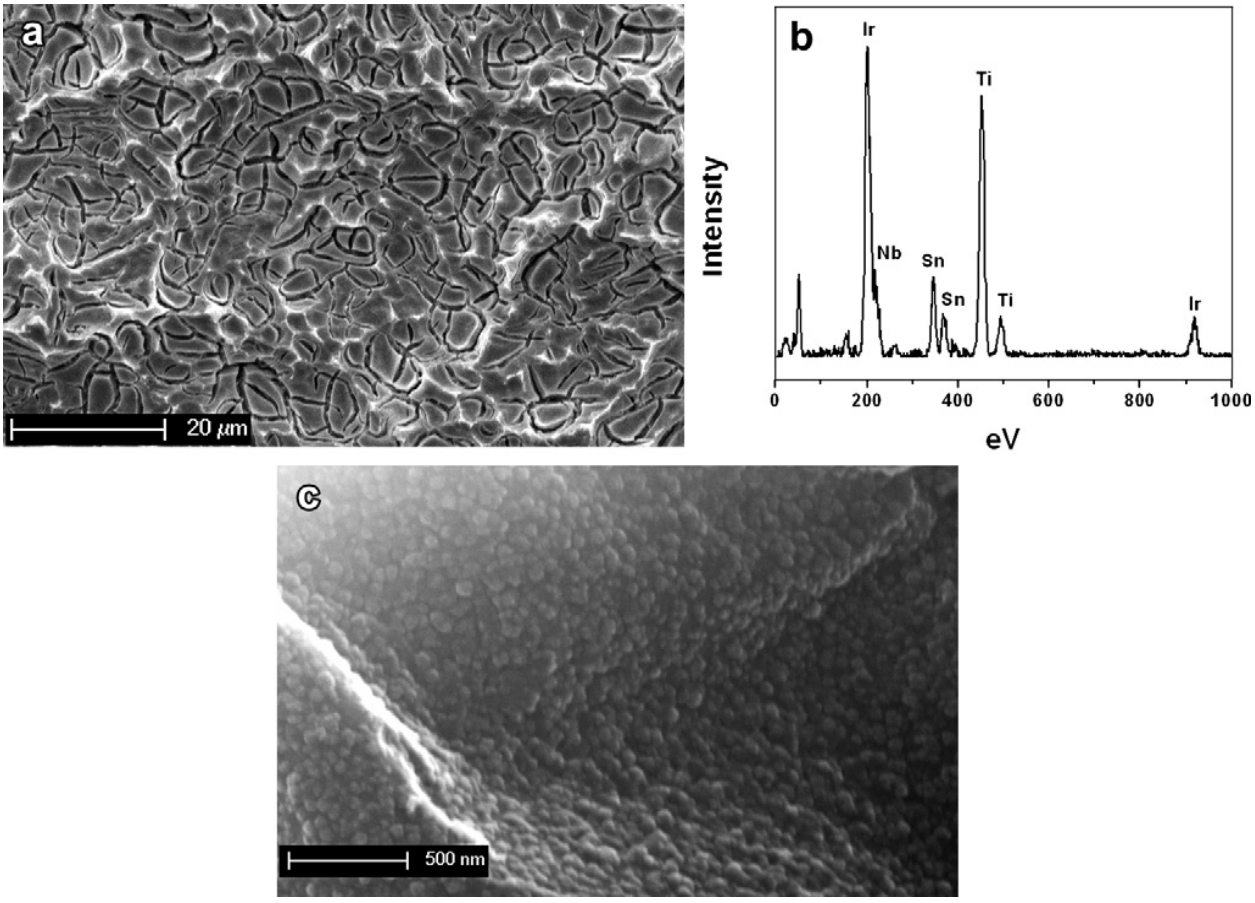

Figure 46. The SEM micrograph (a), EDAX (b), and high magnification SEM image (c) of $(Ir_{0.75}Sn_{0.125}Nb_{0.125})O_2$ film showing the presence of fine nano-particles.

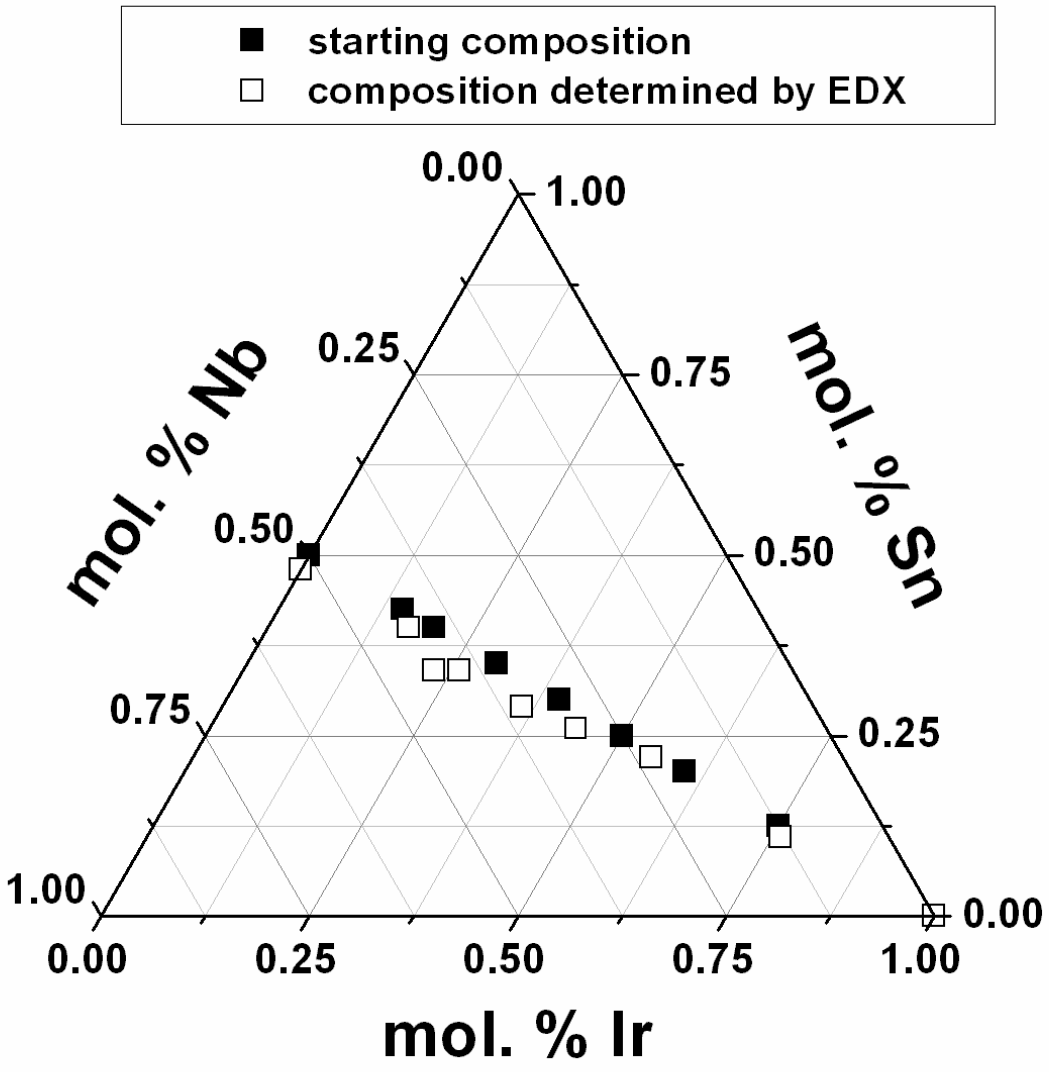

Figure 47. The nominal and EDAX determined molar ratio of (Ir,Sn,Nb)O_2 anode electro-catalyst for PEM based water electrolysis

Table 4. Starting compositions compared to compositions determined by EDX analysis for $(Ir,Sn,Nb)O_2$

Nominal Composition (at. %)			EDX composition (at. %)		
Ir	**Sn**	**Nb**	**Ir**	**Sn**	**Nb**
	50	50		48	52
75	12.5	12.5	76	11	13
60	20	20	55	22	23
50	25	25	44	26	30
40	30	30	36	29	35
30	35	35	26	34	40
20	40	40	23	34	43
15	42.5	42.5	17	40	43

In order to determine the valence state of Ir, Sn, Nb and O in the IrO_2 and SnO_2 as well as ternary $(Ir,Sn,Nb)O_2$ systems, the XPS studies of the thin film have been performed. The XPS spectra of Ir 4f peaks of pure IrO_2 and $(Ir,Sn,Nb)O_2$ thin film of different compositions are shown in **Figure 48**. The XPS spectra of Ir corresponding to pure IrO_2 and $(Ir,Sn,Nb)O_2$ shows the presence of Ir $4f_{5/2}$ and Ir $4f_{7/2}$ doublet. The binding energy of Ir $4f_{5/2}$ and Ir $4f_{7/2}$ of pure IrO_2

and (Ir,Nb,Sn)O_2 is ~ 65.0 eV and ~ 62.0 eV, respectively; and the O1s peak is centered at ~ 530 eV, as shown in **Figure 49** which is consistent with the values of bulk IrO_2. On the other hand, the XPS spectra of Sn corresponding to pure SnO_2 and (Ir,Sn,Nb)O_2 thin film of different compositions is shown in **Figure 50**. The XPS spectra of Sn 3d shows the peak separation of Sn $3d_{5/2}$ and Sn $3d_{3/2}$ for pure SnO_2 as well as (Ir,Sn,Nb)O_2 with a binding energy of ~ 487 eV and ~ 495 eV, respectively; and O1s line centered at ~ 530 eV (**Figure 49**) which is consistent with stoichiometric SnO_2. The XPS spectra of Nb in $(Ir_{1-2x}Sn_xNb_x)O_2$ thin film of compositions x = 0.30 to x = 0.425, shown in **Figure 51**, shows the peak separation of Nb $3d_{5/2}$ and Nb $3d_{3/2}$ with a binding energy of ~ 207 eV and ~ 210 eV, respectively; which corresponds to NbO_x.

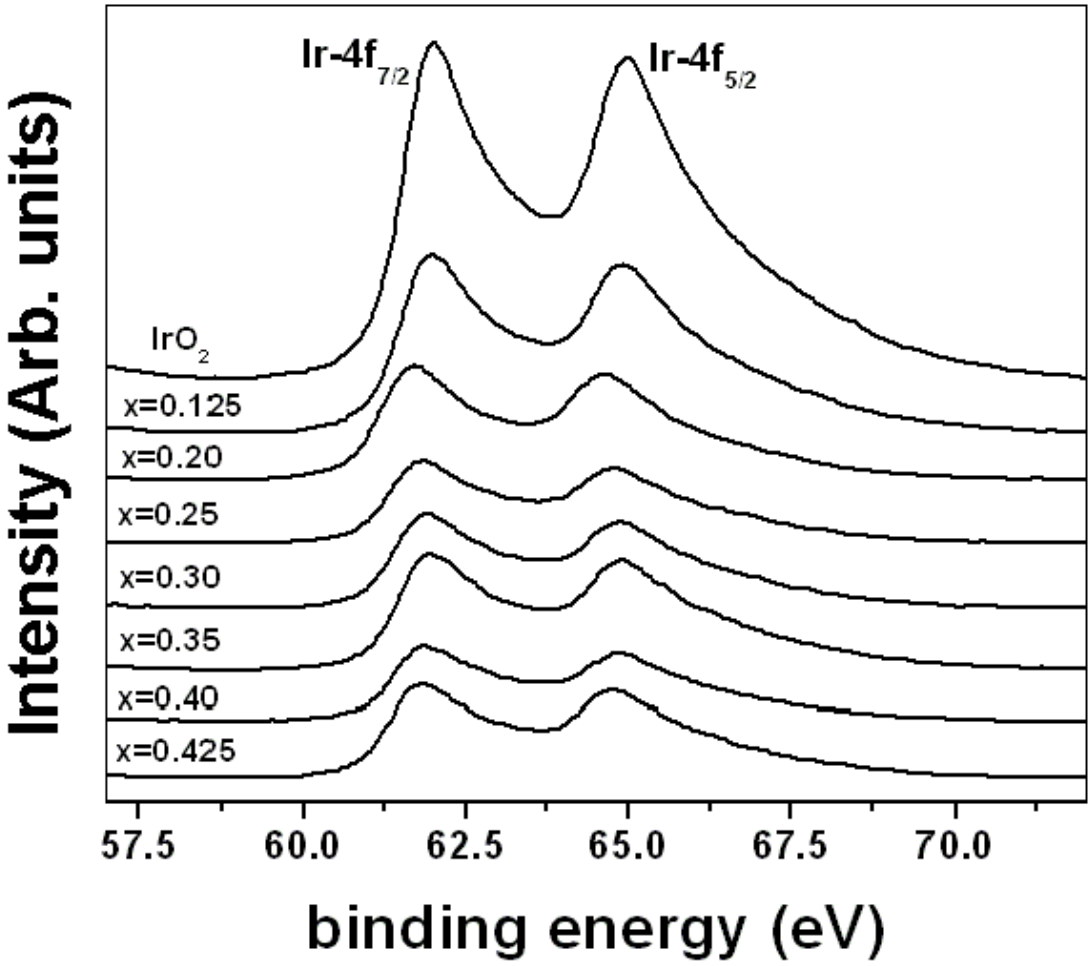

Figure 48. The XPS spectra of Ir $4f_{7/2}$ and $4f_{5/2}$ doublet of pure IrO_2 and (Ir,Sn,Nb)O_2 thin film

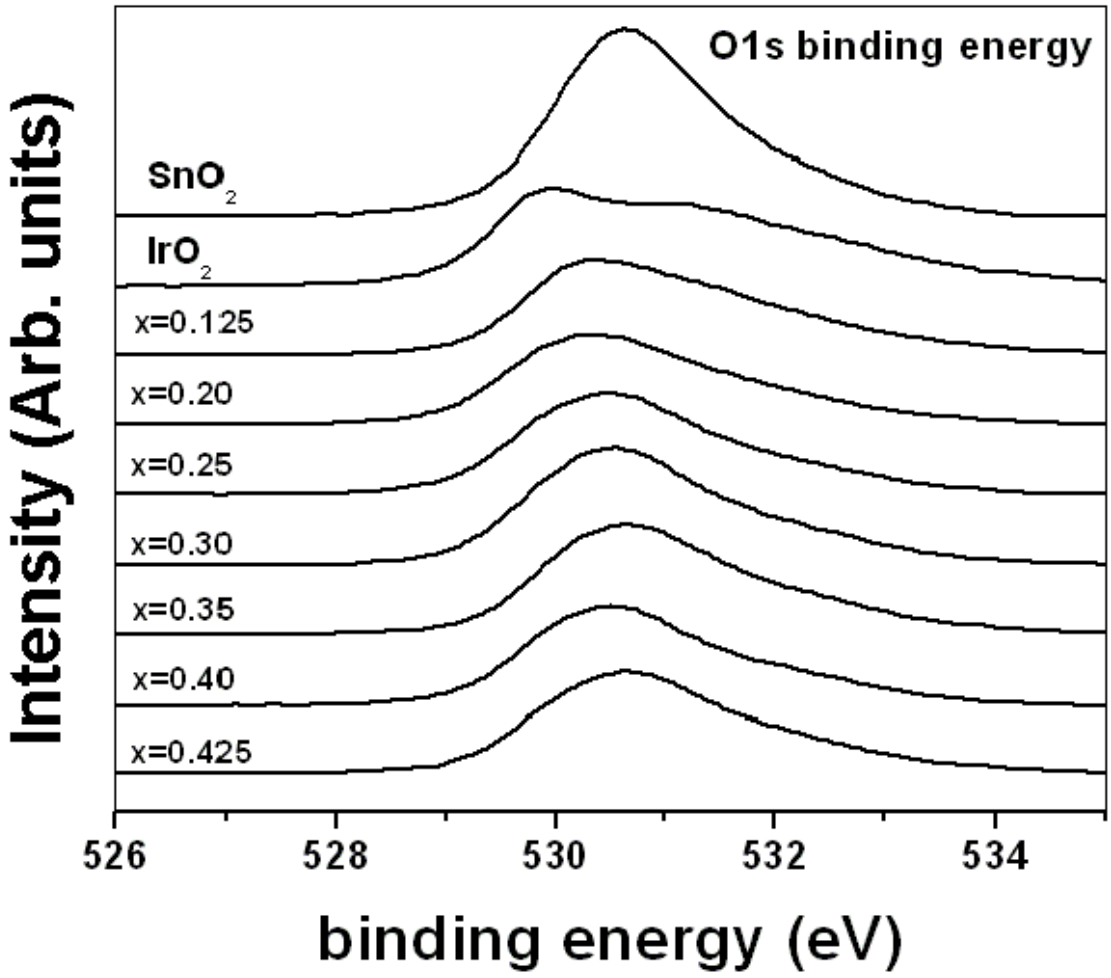

Figure 49. The XPS spectra of O1s of pure IrO_2, SnO_2 and (Ir,Sn,Nb)O_2 thin film

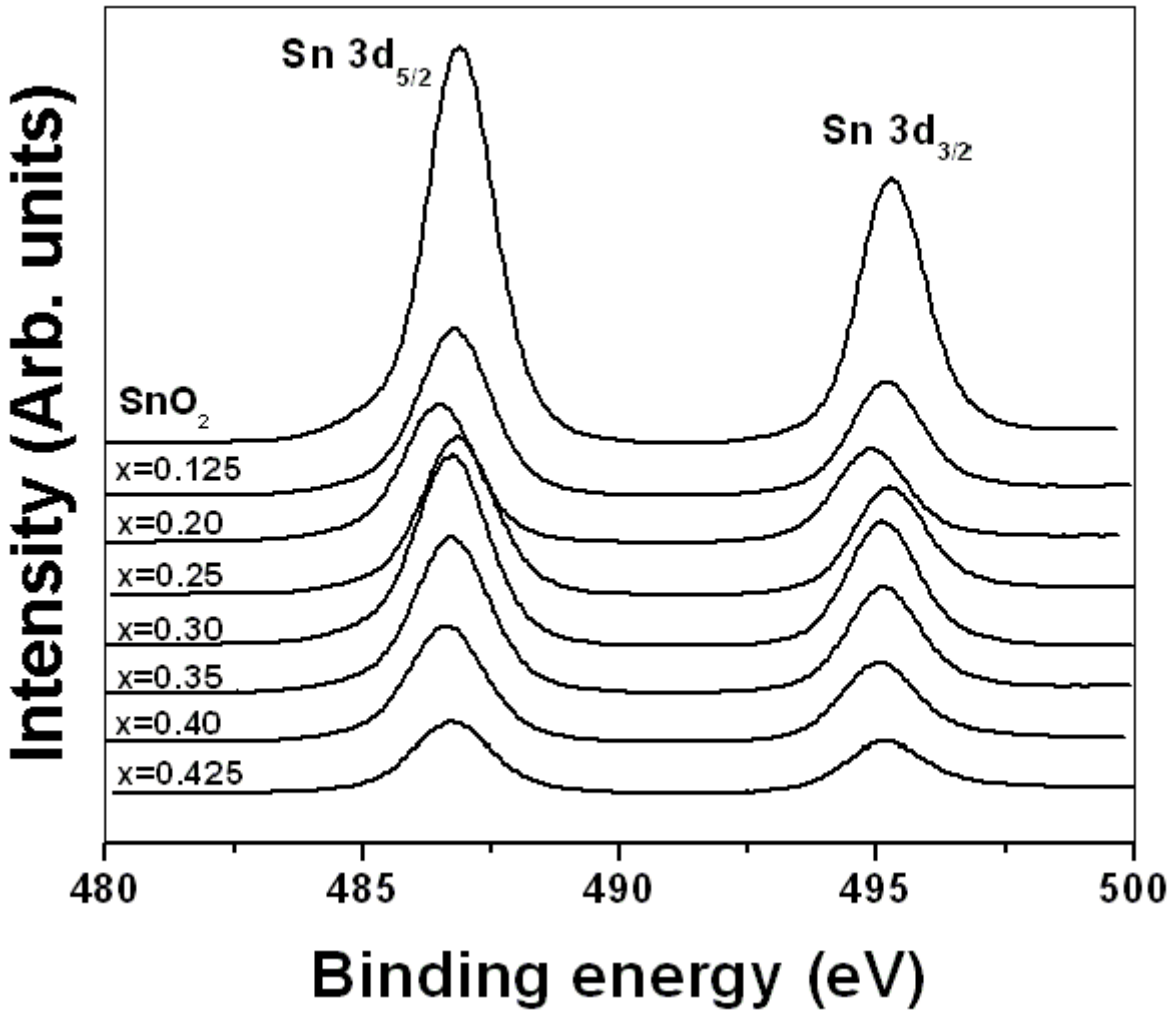

Figure 50. The XPS spectra of Sn $3d_{5/2}$ and Sn $3d_{3/2}$ doublet of pure SnO_2 and $(Ir,Sn,Nb)O_2$ thin film

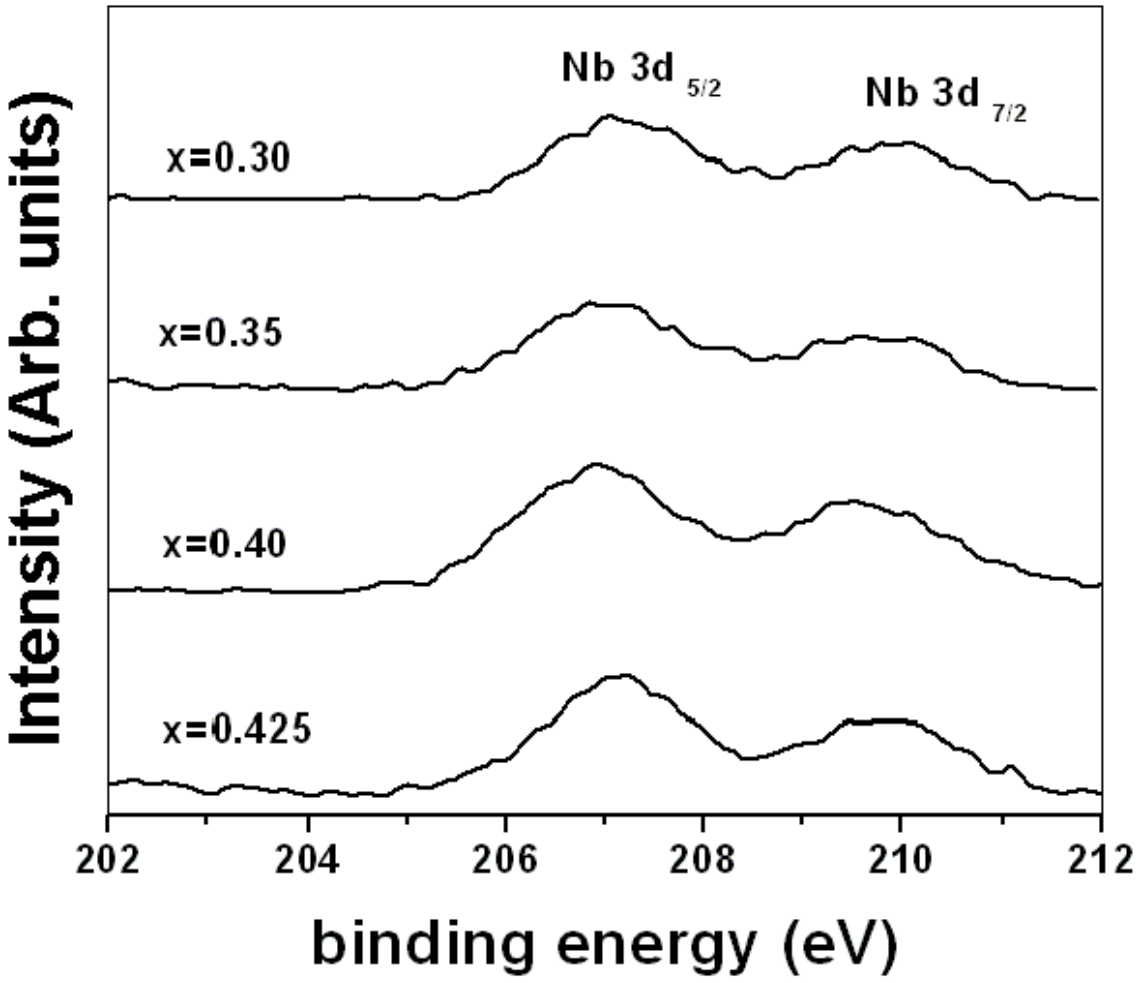

Figure 51. The XPS spectra of Nb $3d_{7/2}$ and Nb $3d_{5/2}$ doublet of (Ir,Sn,Nb)O_2 thin films

5.1.4.2 Electrochemical Testing

The electrochemical activity of thin film nanocrystalline IrO_2, (Sn,Nb)O_2 and (Ir,Sn,Nb)O_2 of different compositions has been studied as suitable oxygen reduction anode electro-catalyst for PEM based water electrolysis. The polarization curve of pure IrO_2 and $(Sn_{0.50}Nb_{0.50})O_2$ film, conducted in the presence of 1 N H_2SO_4 solution at 40°C with a scan rate of 1 mV/sec, is shown

in **Figure 52**. The polarization curve of IrO_2 clearly indicates that water splitting (oxygen evolution reaction) reaction occurring at a potential of ~ 1.43 V *vs.* NHE. The current density at ~ 1.65 V (*vs.* NHE), the typical voltage for determining the electrochemical activity is ~ 0.0094 A/cm^2 with a total loading ~ 0.3 mg/cm^2 of IrO_2. On the other hand, $(Sn,Nb)O_2$ shows no catalytic activity for water electrolysis as expected. In the present study, linear polarization curve and non-linear tafel plot are most often encountered due to large contribution of ohmic resistance (R_Ω) which mainly arises due to solution resistance of the electrolyte (solution resistance, R_s), oxide film electrode resistance (R_e) and accumulation of oxygen bubble covering the electrode surface during water electrolysis at higher current density (bubble resistance, R_{bub}) [51, 52]. **Figure 53** shows the polarization curve of selected $(Ir_{1-2x}Sn_xNb_x)O_2$ samples, before and after ohmic resistance correction ($iR_\Omega = iR_{sol} + iR_e$) without considering R_{bub}. It indicates that water splitting *i.e.* OER occurs at the potential of ~ 1.43 V (*vs.* NHE) irrespective of composition which is identical to that of pure IrO_2.

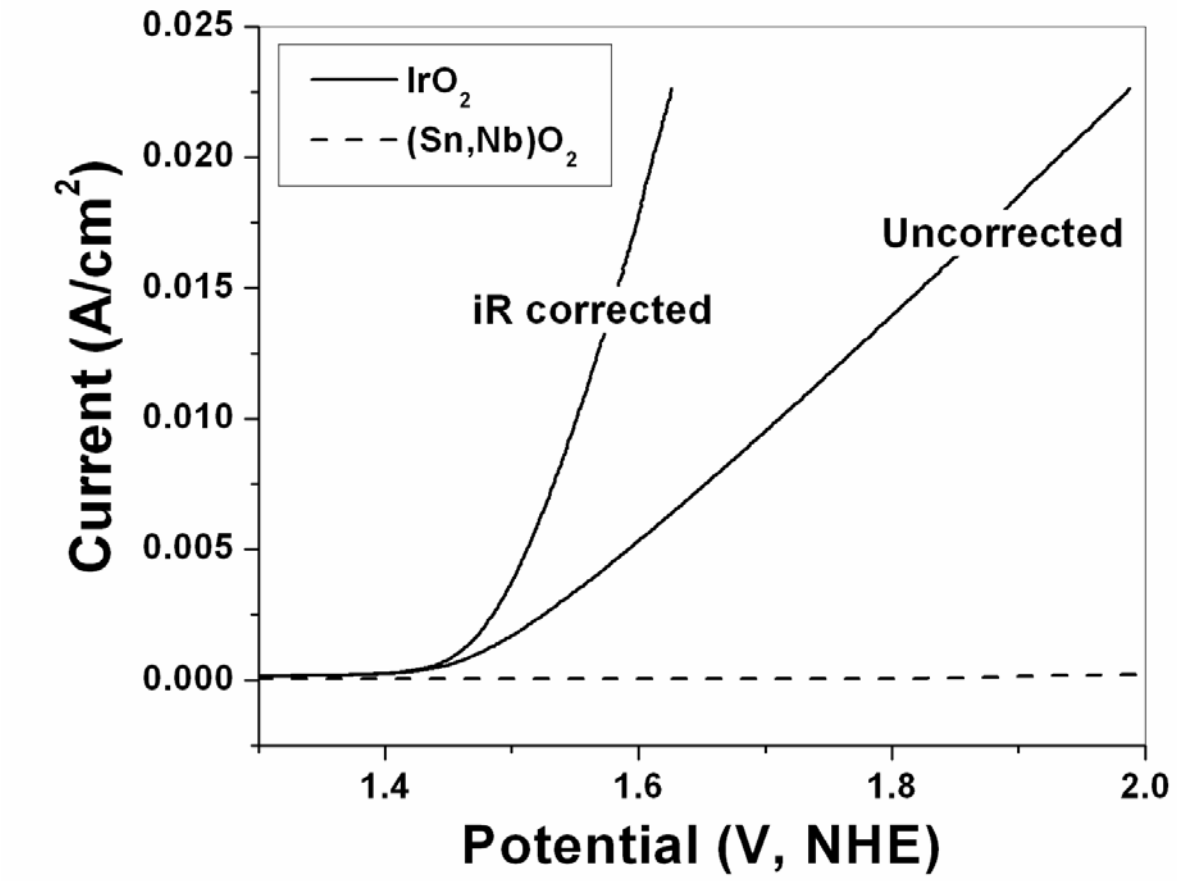

Figure 52. The polarization curve of pure IrO_2 and $(Sn_{0.50}Nb_{0.50})O_2$ film conducted in the presence of 1 N H_2SO_4 solution at 40°C

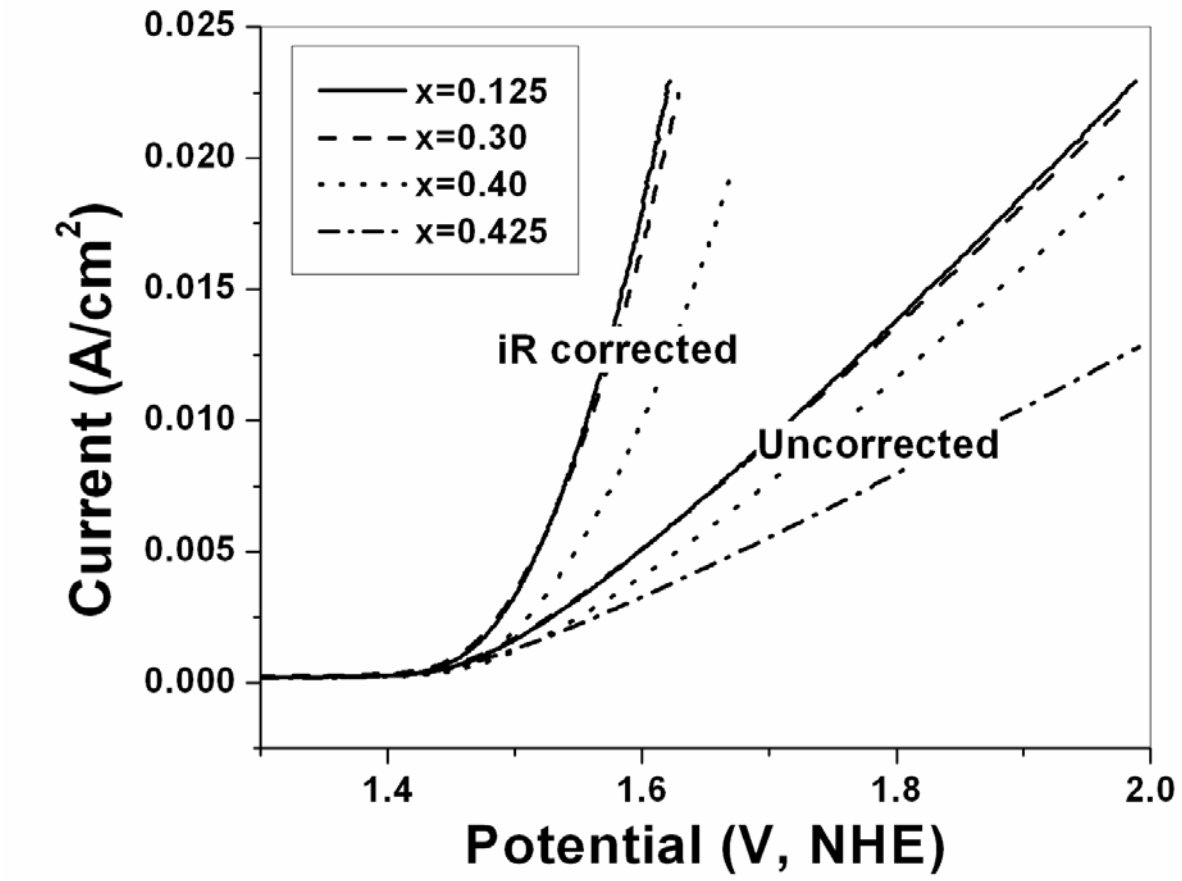

Figure 53. The polarization curve with iR correction of $(Ir_{1-2x}Sn_xNb_x)O_2$ films conducted in the presence of 1 N H_2SO_4 solution at 40°C

The current density at ~ 1.65V (*vs.* NHE) of $(Ir,Sn,Nb)O_2$ for the different compositions with a total loading ~ 0.3 mg/cm^2 is plotted in **Figure 54**. The current density of $(Ir_{1-2x}Sn_xNb_x)O_2$ up to x = 0.30 (*i.e.* 40 mol.% IrO_2) is ~ 0.0092 ± 0.0002 A/cm^2 which is similar to that of pure IrO_2. The above results clearly suggest that the capital cost *i.e.* the noble metal IrO_2 loading could be reduced by ~ 60 mol.% with the addition of $(Sn,Nb)O_2$ while still maintaining similar electrochemical activity as that of pure IrO_2. The electrochemical activity however decreases

with further reduction in IrO_2 below 40 mol.% (x = 0.3), which may be due to the lattice predominantly being $(Sn,Nb)O_2$ below 40 mol.% IrO_2; and as a result, the IrO_2 concentration at the surface is depleted with respect to $(Sn,Nb)O_2$. Nevertheless, it should be noted that the electrochemical activity of $(Ir_{0.20}Sn_{0.40}Nb_{0.40})O_2$ is only ~ 20 % lower than that of pure IrO_2 though the noble metal oxide loading is reduced by 80 mol.%.

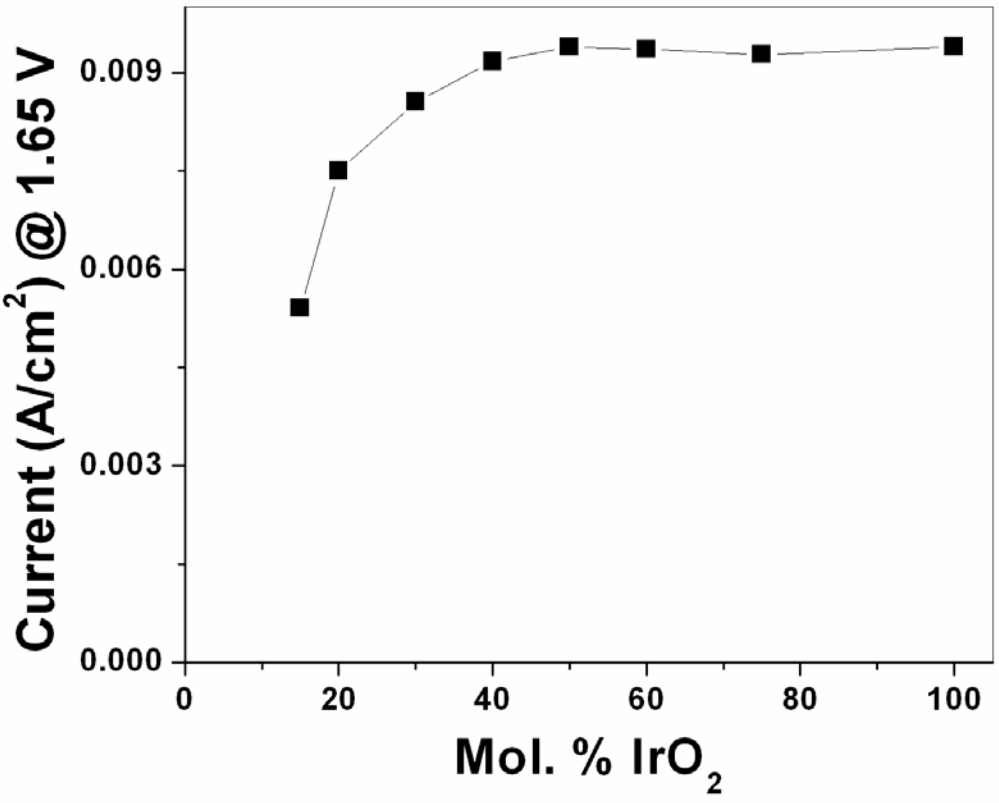

Figure 54. Variation of current density at ~ 1.65V (*vs.* NHE) for various compositions of $(Ir,Sn,Nb)O_2$ thin film electro-catalyst

In order to study the structural stability of anode electro-catalyst $(Ir,Sn,Nb)O_2$ in 1 N H_2SO_4, chronoamperometry (CA) is conducted for 48 hours at 40°C at a constant voltage of ~

1.65 V (*vs.* NHE) without iR correction for select samples. The CA curves, of (Ir,Sn,Nb)O_2 with a composition of ($Ir_{0.4}Sn_{0.3}Nb_{0.3}$)O_2 that displays similar electrochemical activity as pure IrO_2 is plotted along with pure IrO_2, in **Figure 55**. The CA curve shows a marked decay of current (~ 13 % of the initial value) for both electrodes in the initial period of 30 minutes during the oxygen evolution processes which may be due to significant dissolution of irregular coatings located at the edge of the mud cracks [30], or may be due to diffusion controlled reactions. A steady state of current ~ 0.006 A/cm^2 has been achieved after 1 hour of initial period for ($Ir_{0.4}Sn_{0.3}Nb_{0.3}$)O_2, whereas pure IrO_2 shows a continuous drop in current at a constant rate which may which may be due to the continuous loss of active IrO_2 catalyst from the surface.

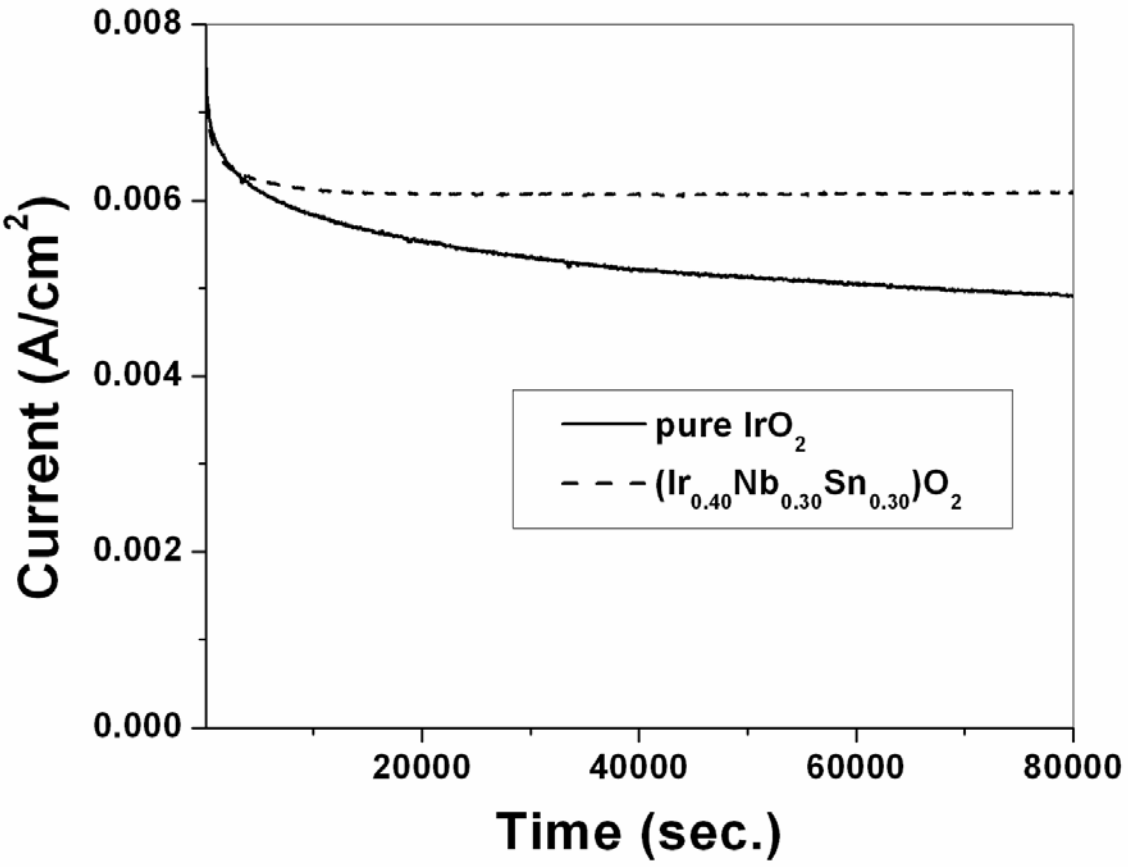

Figure 55. Variation of current *vs.* time in the accelerated life test of pure IrO_2 and $(Ir_{0.4}Sn_{0.3}Nb_{0.3})O_2$ performed in 1 N H_2SO_4 at 40°C at ~ 1.65 V

The ICP results, conducted in the H_2SO_4 electrolyte solution collected after CA measurement, show the presence of ~ 0.44 ppm of Sn, ~ 0.28 ppm of Nb and only ~ 0.14 ppm of Ir for $(Ir_{0.4}Sn_{0.3}Nb_{0.3})O_2$ whereas pure IrO_2 shows ~ 0.35 ppm of Ir which suggests that the incorporation of $(Sn,Nb)O_2$ improves the corrosion rate of IrO_2. The improved corrosion of $(Ir,Nb,Sn)O_2$ electrode compared to that of pure IrO_2 electrodes is primarily attributed to the formation of a solid solution of IrO_2-SnO_2-NbO_2. Since both SnO_2 and NbO_2 are chemically very

stable, the homogenous mixing of IrO_2 with SnO_2 and NbO_2 by forming a solid solution increases the overall chemical stability and decreases the rate of IrO_2 dissolution. This leads to a significant increase in the electrode service life under the operating conditions of PEM based water electrolysis.

After the conclusion of the CA test, the $(Ir_{0.4}Sn_{0.3}Nb_{0.3})O_2$ thin film electrode was subject to polarization testing as seen in **Figure 56** in order to determine the activity of the electrode after the long term structural stability test. The Tafel plot from these polarization curves after iR correction is shown in **Figure 57**. The Tafel slope after the CA test is ~ 84 mV/decade and is comparable to pure IrO_2 (~ 77 mV/decade) as seen in **Figure 23**. This test further demonstrates the robustness of the ternary electro-catalyst.

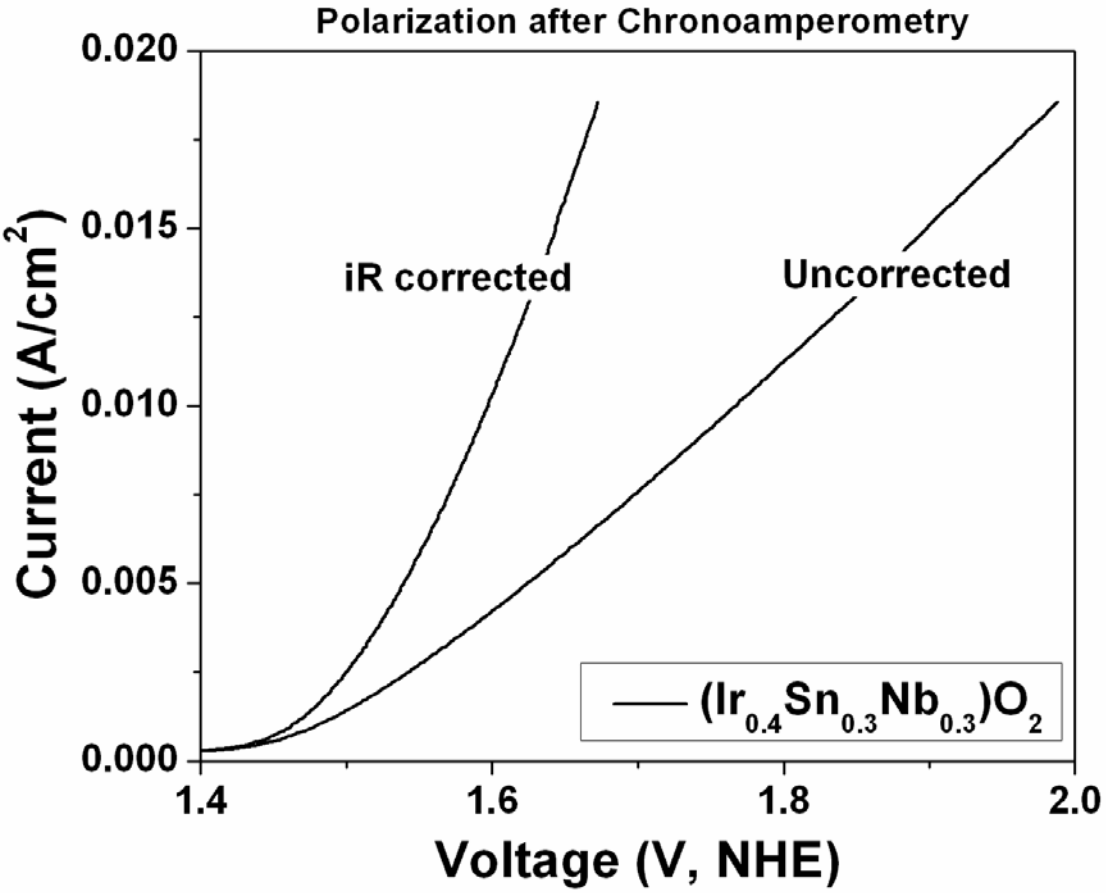

Figure 56. Polarization curve of (Ir,Sn,Nb)O_2 thin film after the CA test

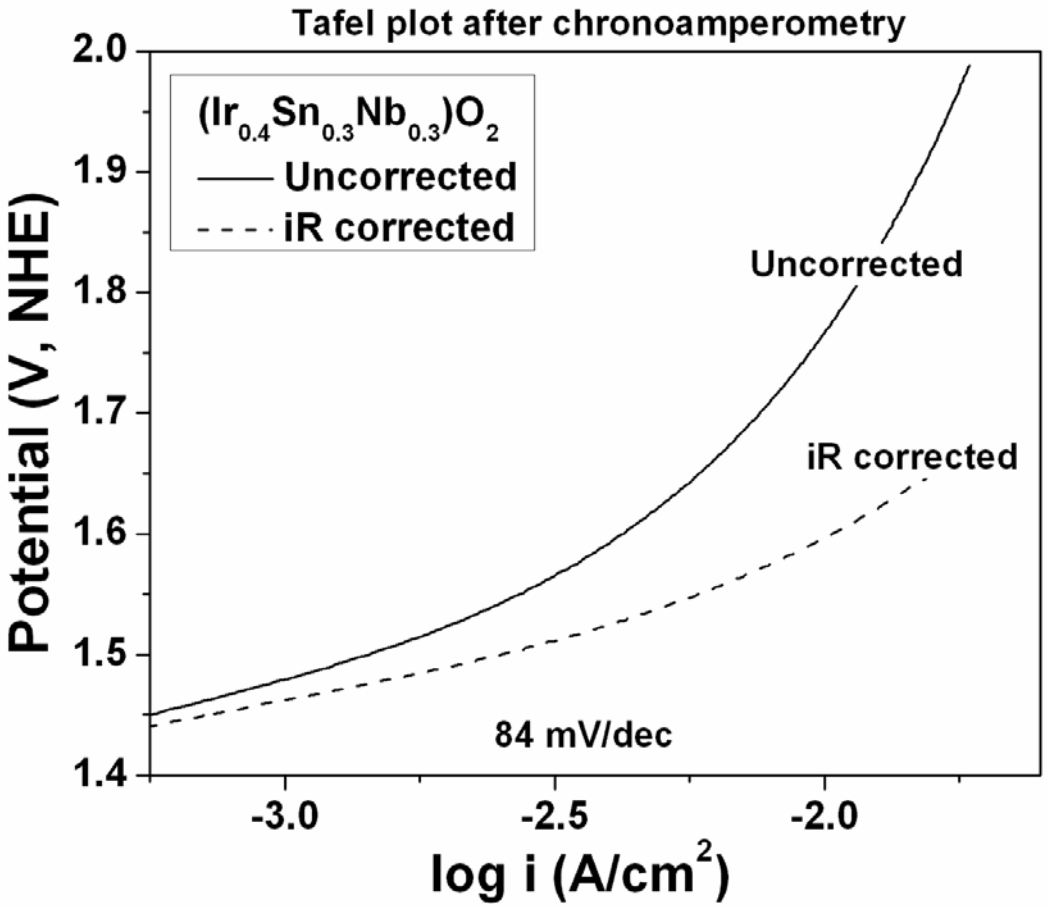

Figure 57. The Tafel plot of (Ir,Sn,Nb)O_2 thin film after the CA test

The present study therefore successfully identifies promising (Sn,Nb)O_2 supports or diluents for IrO_2 anode electro-catalyst with the ability to significantly reduce the noble metal oxide loading with enhanced durability / chemical stability, and without compromising the electro-catalytic performance. The (Ir,Sn,Nb)O_2 anode electro-catalysts are therefore expected to exhibit significant reduction in capital cost of PEM based water electrolyzers.

5.1.5 Ternary F doped $(Ir,Sn,Nb)O_2$

5.1.5.1 Structural Analysis

The x-ray diffraction (XRD) patterns of thin film $(Ir,Sn,Nb)O_2$:F synthesized by thermal decomposition of $IrCl_4$, $SnCl_2.2H_2O$, $NbCl_5$ and NH_4F solution coated on the Ti foil and heat treated at 400°C for 4 hours is shown in **Figure 58**. The XRD pattern of $(Ir,Sn,Nb)O_2$ exhibits a rutile type tetragonal structure similar to pure IrO_2 [24] suggesting the formation of complete solid solution between IrO_2, SnO_2 and NbO_2. No additional peaks are seen other than rutile IrO_2 which concludes there is no undesirable phase formation. Formation of solid solution of Nb_2O_5 with SnO_2, synthesized by the Pechni process, has also been reported [112]. The lattice parameter of $(Sn,Nb)O_2$ is comparable to pure SnO_2 since the ionic radius of Sn^{+4} (69 pm) is very close to that of Nb^{+4} (68 pm). Also, the molar volume of tin and niobium dioxides are ~ 21.65 and ~ 21.17 cm^3/mol respectively. In order to improve the electronic conductivity of $(Ir,Sn,Nb)O_2$, fluorine is incorporated in the structure to replace oxygen at nominal compositions of 5, 10, 15 and 20 wt.% F, as outlined in the **Section 4.1.5**. The XRD patterns showing the $(Ir,Sn,Nb)O_2$:F solid solution for up to 15 wt.% F compositions, confirms the retention of the tetragonal rutile structure similar to the parent $(Ir,Sn,Nb)O_2$ [24, 34, 57, 59]. The lattice parameter (a ~ 0.46 nm, c ~ 0.31 nm) and molar volume of $(Ir,Sn,Nb)O_2$:x wt.% F (~ 20 cm^3/mol), calculated using least square refinement technique, is similar to pure IrO_2 (~19.7 cm^3/mol). This clearly indicates no effect of F^- substitution for O^{2-} on the molar volume of $(Ir,Sn,Nb)O_2$:F. It should be noted that this might be due to the ionic radius of O^{2-} and F^- being similar (125 pm and 120 pm, respectively) [114]. The effective crystallite size of $(Ir,Sn,Nb)O_2$:F,

calculated using the Scherrer formula, is ~ 4 - 6 nm irrespective of the amount of fluorine doping. This elucidates the nanocrystallinity of all the synthesized electro-catalysts.

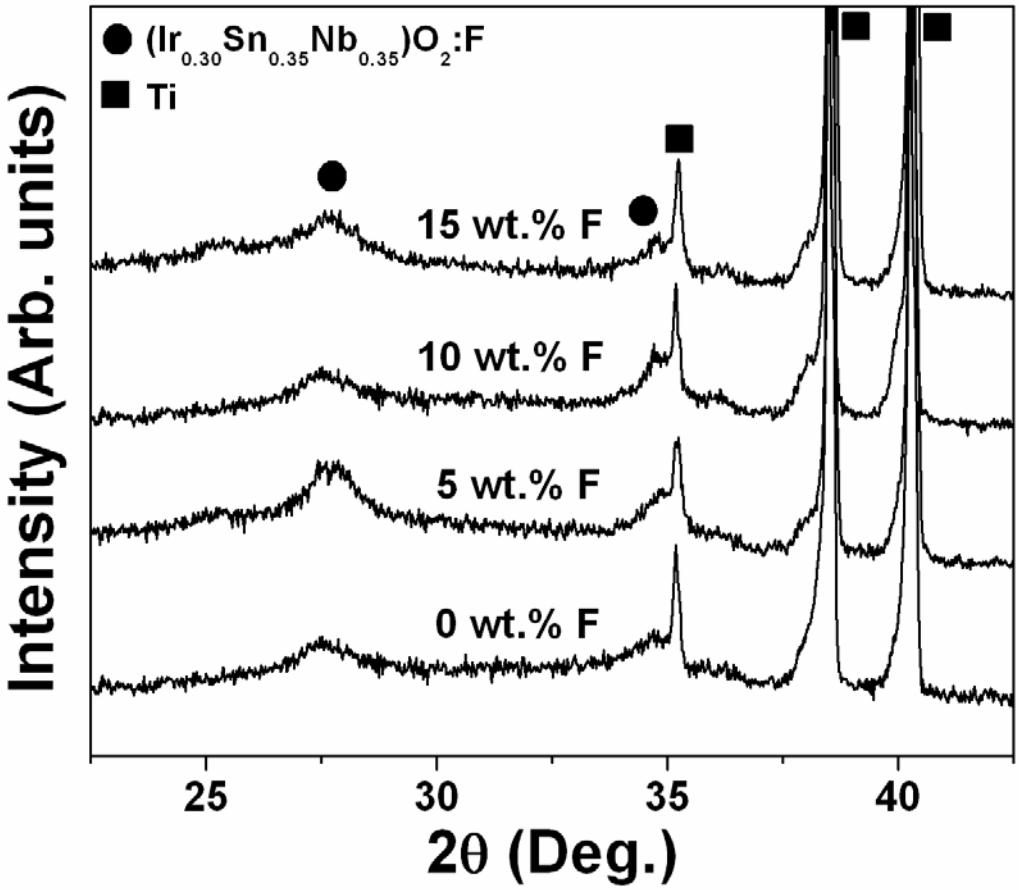

Figure 58. XRD patterns of thin film $(Ir_{0.30}Sn_{0.35}Nb_{0.35})O_2$:F of different compositions coated on Ti foil

Energy dispersive x-ray spectroscopy (EDX) confirms the presence of elemental Ir, Sn and Nb in the (Ir,Sn,Nb)O_2:x wt.% F thin film, where x ranges from 0 to 20. However, EDX

analysis could not detect the presence of F as expected (It has been outlined in **Section 5.1.1.1**). It should be noted that the final F content in the (Ir,Sn,Nb)O_2:F thin film might not be the same as the nominal composition we started with due to the expected loss of the highly volatile F species during heat treatment of the precursors in air at 400°C for 4 hours. The x-ray mapping and EDX of the representative ($Ir_{0.30}Sn_{0.35}Nb_{0.35}$)$O_2$:10 wt.% F film, is shown in **Figure 59** and **Figure 60**, respectively. **Figure 59** clearly indicates the presence of Ir, Sn, Nb and O, which are homogeneously distributed within the (Ir,Sn,Nb)O_2:F grains without being segregated on any specific site [59]. The SEM image shows a characteristic sintered “mud-crack” type morphology typically seen in chemically derived thin films. Quantitative composition analysis of the elements by EDX for all the (Ir,Sn,Nb)O_2:F films confirms that the final elemental composition is very similar to the starting / nominal composition of the films barring the presence of F. Although EDX could not categorically confirm the presence of F in this present study, the improved electrochemical performance serves as a testimony of the presence of fluorine in the lattice.

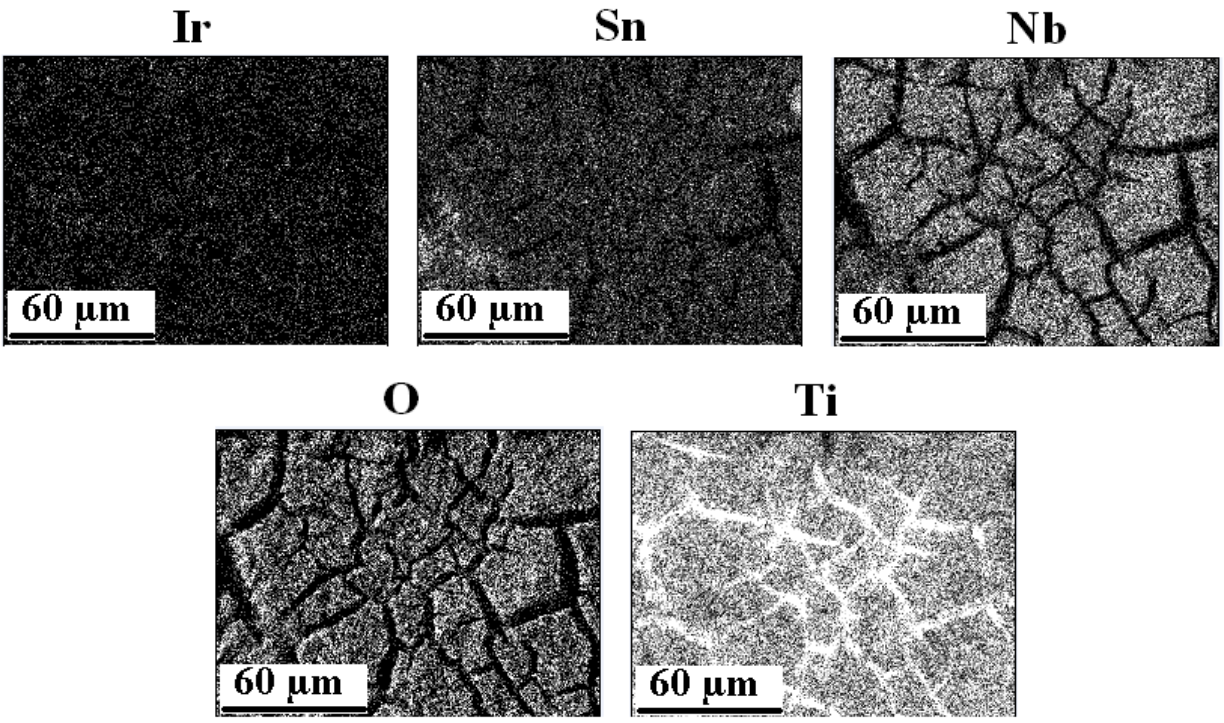

Figure 59. The x-ray mapping of Ir, Sn, Nb, O and Ti of the SEM micrograph of $(Ir_{0.30}Sn_{0.35}Nb_{0.35})O_2$:10 wt.% F film

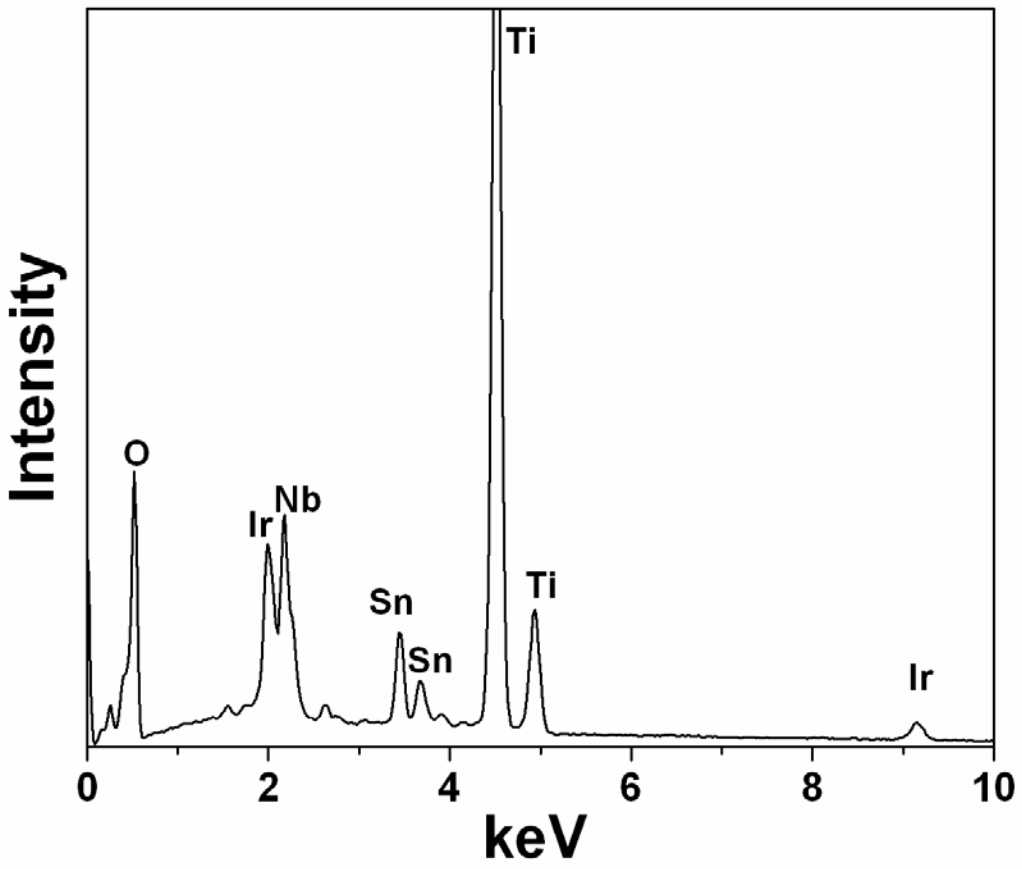

Figure 60. EDX of $(Ir_{0.30}Sn_{0.35}Nb_{0.35})O_2$:10 wt.% F coated on a Ti thin film

5.1.5.2 Electrochemical Testing

The electrochemical activity has been studied for the nanocrystalline thin film (Ir,Sn,Nb)O_2:F as a suitable anode electro-catalyst for the OER *via* PEM electrolysis. The linear polarization curve and non-linear Tafel plot are encountered due to ohmic resistance, which arises due to solution resistance (R_s) and electrode resistance (R_e) [51, 52]. The polarization curves of (Ir,Sn,Nb)O_2:F help us evaluate the electrode kinetics after we account for ohmic loss correction. Polarization

was done in presence of 1 N sulfuric acid at a scan rate of 1 mV/sec at 40°C. **Figure 61**, **Figure 62**, **Figure 63** and **Figure 64** shows the EIS plot of IrO_2, (Ir,Sn,Nb)O_2, (Ir,Sn,Nb)O_2:5 wt.% F, and (Ir,Sn,Nb)O_2:10 wt.% F, respectively obtained at open circuit potential (OCP), 1.5 V, 1.6 V and 1.8 V (*vs.* NHE) at 40°C in the frequency range of 100 mHz - 100 kHz. It is seen that R_s of IrO_2 and (Ir,Sn,Nb)O_2:F is unchanged at different voltages. From the EIS plot, the semicircle seen at low frequencies is due to OER which would be a measure of polarization resistance (R_{ct}). The R_{ct} values decrease with increase in F content, indicating increase in electrochemical activity of the electro-catalyst. **Table 5** shows R_s and R_{ct} at 1.6 V for different F doping along with the Tafel slope. These results suggest that the electrochemical activity of $(Ir_{0.30}Sn_{0.35}Nb_{0.35})O_2$:F increases with increase in F content up to 10 wt.% F.

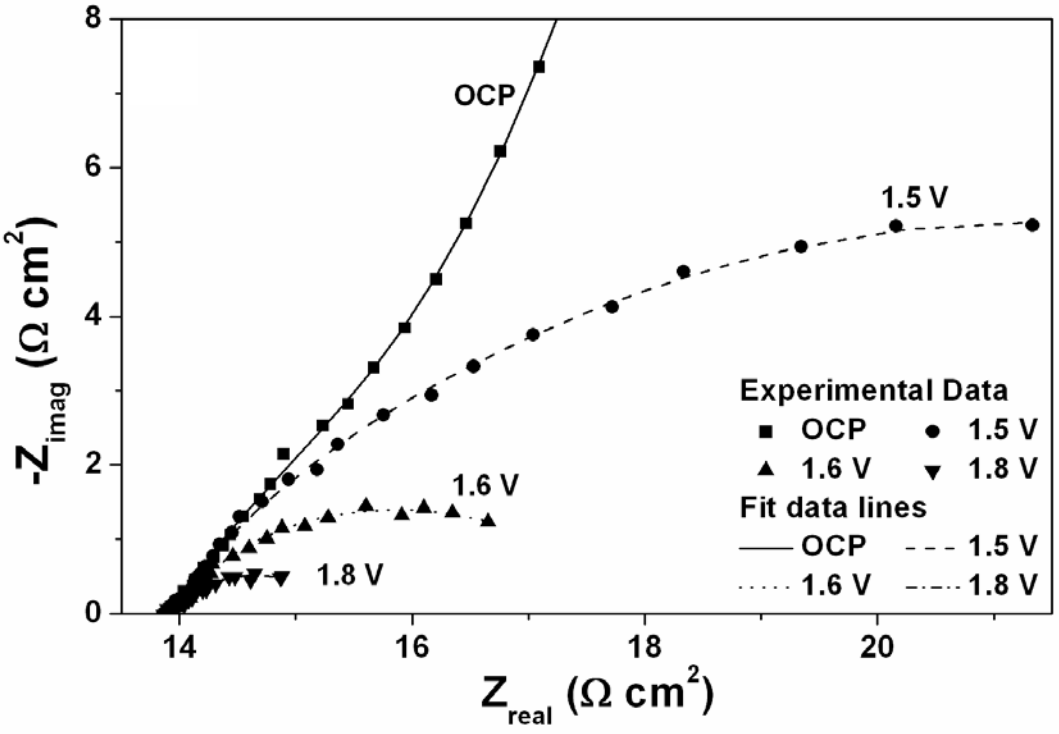

Figure 61. EIS spectra of pure IrO_2 obtained at OCP, 1.5 V, 1.6 V and 1.8 V in 1 N H_2SO_4

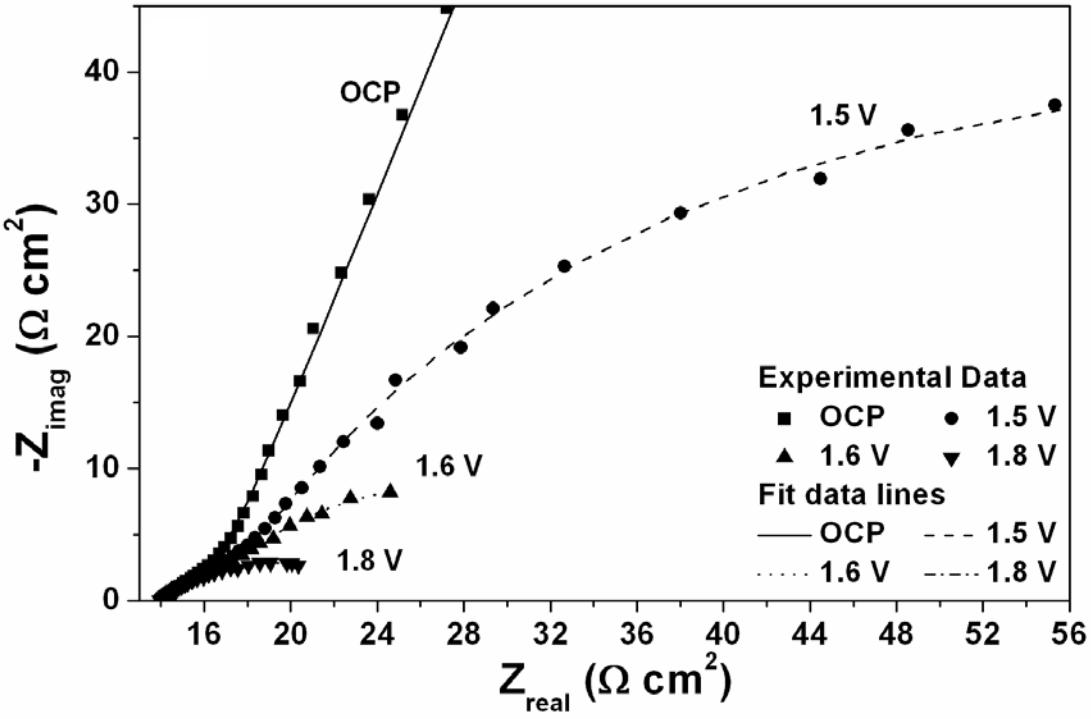

Figure 62. EIS spectra of (Ir,Sn,Nb)O_2 obtained at OCP, 1.5 V, 1.6 V and 1.8 V in 1 N H_2SO_4

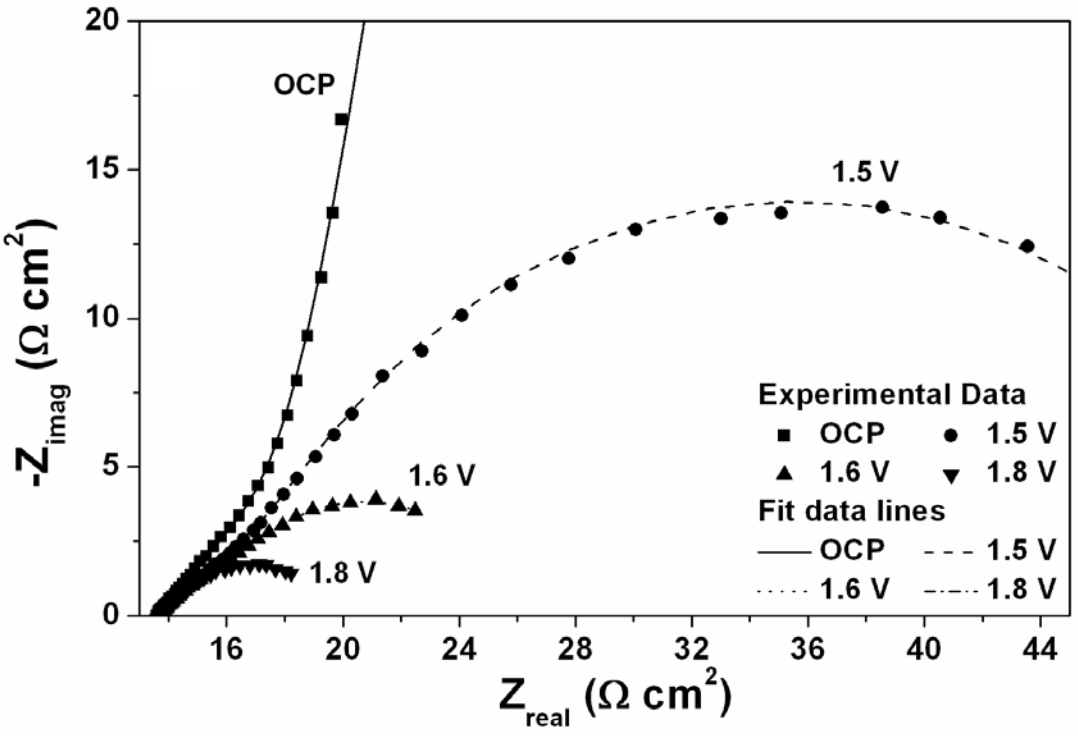

Figure 63. EIS spectra of (Ir,Sn,Nb)O_2:5 wt.% F obtained at OCP, 1.5 V, 1.6 V and 1.8 V in 1 N H_2SO_4

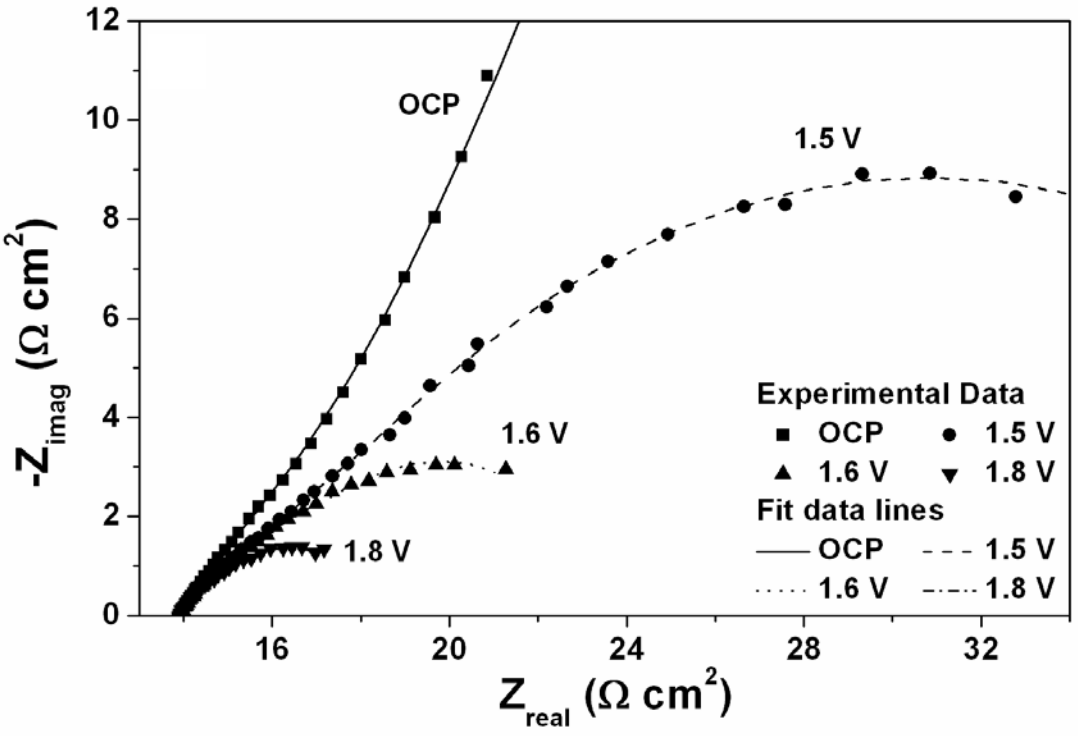

Figure 64. EIS spectra of (Ir,Sn,Nb)O_2:10 wt.% F obtained at OCP, 1.5 V, 1.6 V and 1.8 V in 1 N H_2SO_4

Table 5. Impedance parameters and Tafel slope of IrO_2 and $(Ir,Sn,Nb)O_2$:F thin film

Electro-catalyst composition	R_s (Ω cm^2)	R_{ct} (Ω cm^2)	Tafel slope (mV/dec)
IrO_2	13.84	6.48	71
$(Ir_{0.30}Sn_{0.35}Nb_{0.35})O_2$	14.02	23.75	98
$(Ir_{0.30}Sn_{0.35}Nb_{0.35})O_2$:5 wt.% F	13.69	11.99	85
$(Ir_{0.30}Sn_{0.35}Nb_{0.35})O_2$:10 wt.% F	13.87	9.98	77
$(Ir_{0.30}Sn_{0.35}Nb_{0.35})O_2$:15 wt.% F	13.48	15.18	102
$(Ir_{0.30}Sn_{0.35}Nb_{0.35})O_2$:20 wt.% F	13.55	16.73	106

Figure 65 shows the polarization curve of pure IrO_2 and $(Ir_{0.30}Sn_{0.35}Nb_{0.35})O_2$:F thin film with 0, 5 and 10 wt.% F, before and after ohmic resistance correction conducted at a scan rate of 1 mV/sec. Nanocrystalline pure IrO_2 clearly indicates that the onset of OER or water splitting occurs at a potential of ~ 1.43 V *vs.* NHE. The current density at ~ 1.55 V (*vs.* NHE), considered in the range of typically selected voltages for electrochemical activity for water electrolysis obtained from the iR corrected plot is ~ 0.012 A/cm^2 with a total loading ~ 0.3 mg/cm^2 of IrO_2. The Tafel slope of pure IrO_2, calculated from the iR corrected Tafel plot (over-potential η vs. log i) shown in **Figure 66**, is ~ 71 mV/decade, which corresponds to the well known two electron pathway reaction, assuming the transfer coefficient of ~ 0.5 [30, 48, 53, 101].

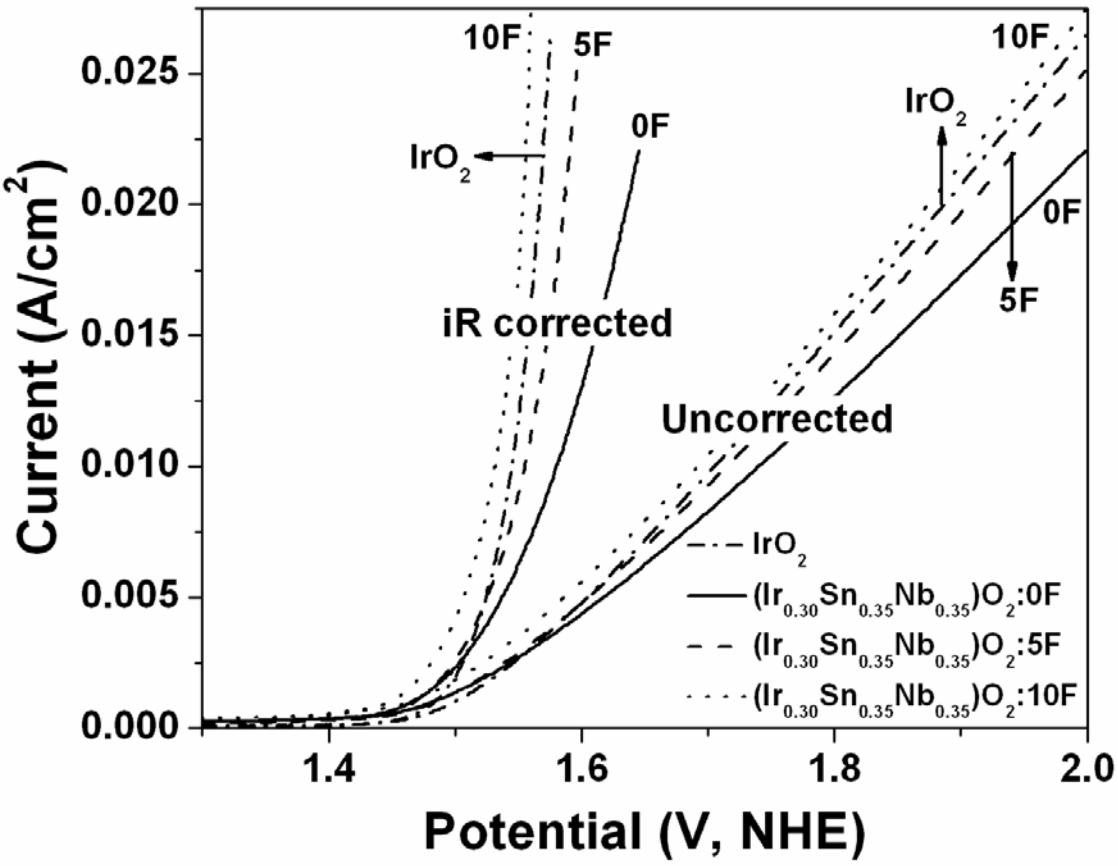

Figure 65. The polarization curve of pure IrO_2 and (Ir,Sn,Nb)O_2:F with 0, 5 and 10 wt.% F before and after iR correction conducted at a scan rate of 1 mV/sec

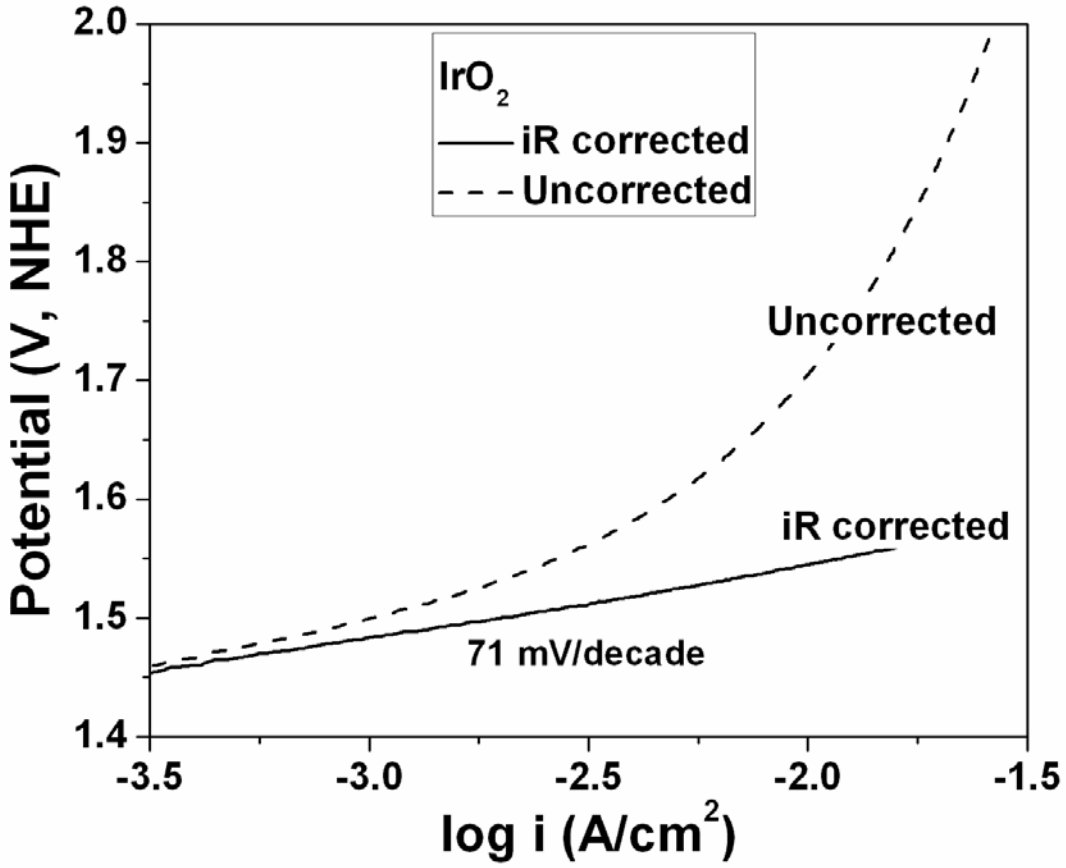

Figure 66. The Tafel plot of IrO_2 before and after iR correction

The polarization curve for the various (Ir,Sn,Nb)O_2:F films before and after iR correction corresponding to the different compositions of F, also shows OER occurring at a potential of ~ 1.43 V (*vs.* NHE) for all the compositions. Furthermore, the current density at ~ 1.55 V (*vs.* NHE) obtained from the iR corrected plot for undoped (Ir,Sn,Nb)O_2 solid solution (0 F) with an identical total loading of ~ 0.3 mg/cm^2 is ~ 0.0063 A/cm^2 which is almost half that of pure IrO_2 (**Figure 65**). Interestingly, the current density of (Ir,Sn,Nb)O_2:F increases with increasing F

content. In fact, (Ir,Sn,Nb)O_2:10 wt.% F shows a current density of ~ 0.016 A/cm^2 at ~ 1.55 V (*vs.* NHE) which is slightly more than that of pure IrO_2 for the same identical loading of ~ 0.3 mg/cm^2. But, we observe from **Figure 67** that the current density decreases with continued increase in F above 10 wt. % F. **Figure 68** shows the variation in current density of ($Ir_{0.30}Sn_{0.35}Nb_{0.35}$)$O_2$:F along with pure IrO_2 at ~ 1.75 V (*vs.* NHE) without iR correction. **Figure 69**, **Figure 70**, **Figure 71**, **Figure 72** and **Figure 73** shows the Tafel plots of (Ir,Sn,Nb)O_2, (Ir,Sn,Nb)O_2:5 wt.% F, (Ir,Sn,Nb)O_2:10 wt.% F, (Ir,Sn,Nb)O_2:15 wt.% F and (Ir,Sn,Nb)O_2:20 wt.% F respectively. The Tafel slope of (Ir,Sn,Nb)O_2:F with 0, 5, 10, 15 and 20 wt.% F, calculated from the corresponding iR corrected Tafel plots, are 98, 85, 77, 102 and 106 mV/decade. This clearly suggests that the electrochemical activity of (Ir,Sn,Nb)O_2:F increases with the corresponding decrease in the Tafel slope and increase in F content up to 10 wt.%. These results indicate that (Ir,Sn,Nb)O_2:10 wt.% F is the optimal composition exhibiting similar electrochemical activity as that of pure IrO_2.

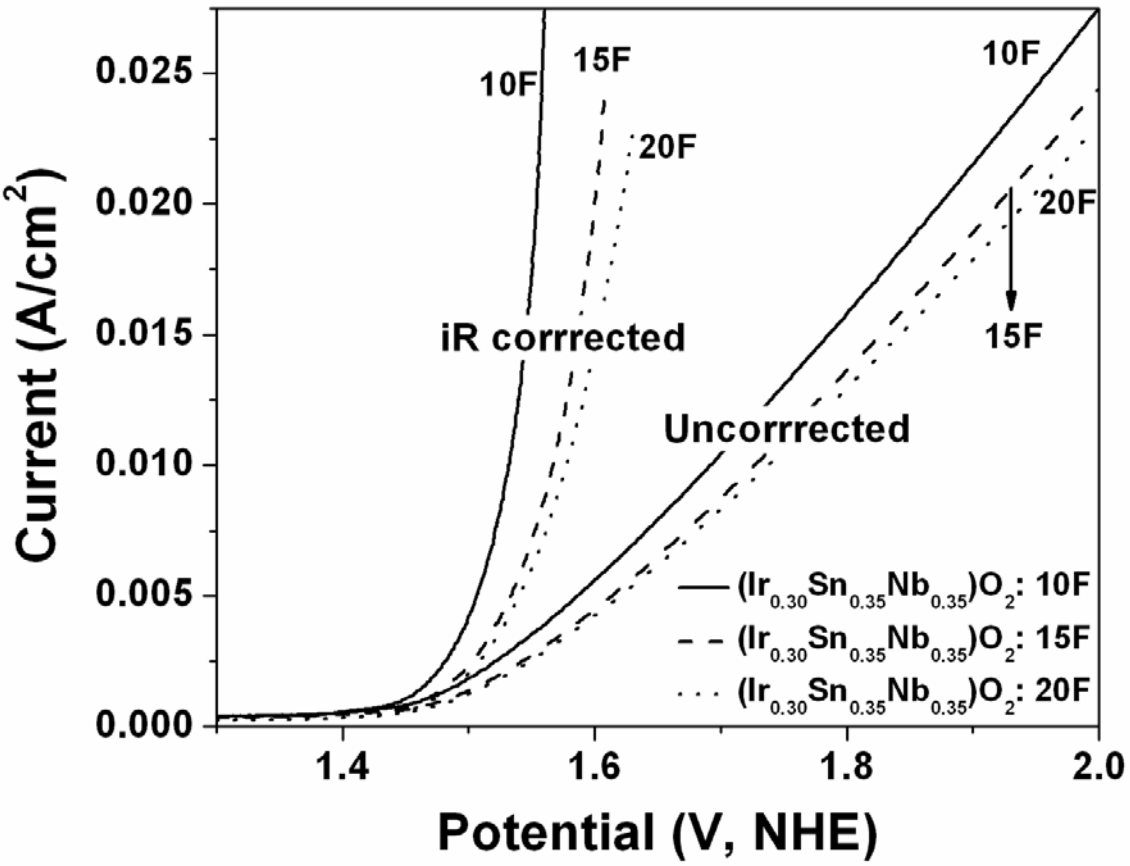

Figure 67. The polarization curve of (Ir,Sn,Nb)O_2:F with 10, 15 and 20 wt.% F before and after iR correction conducted at a scan rate of 1 mV/sec

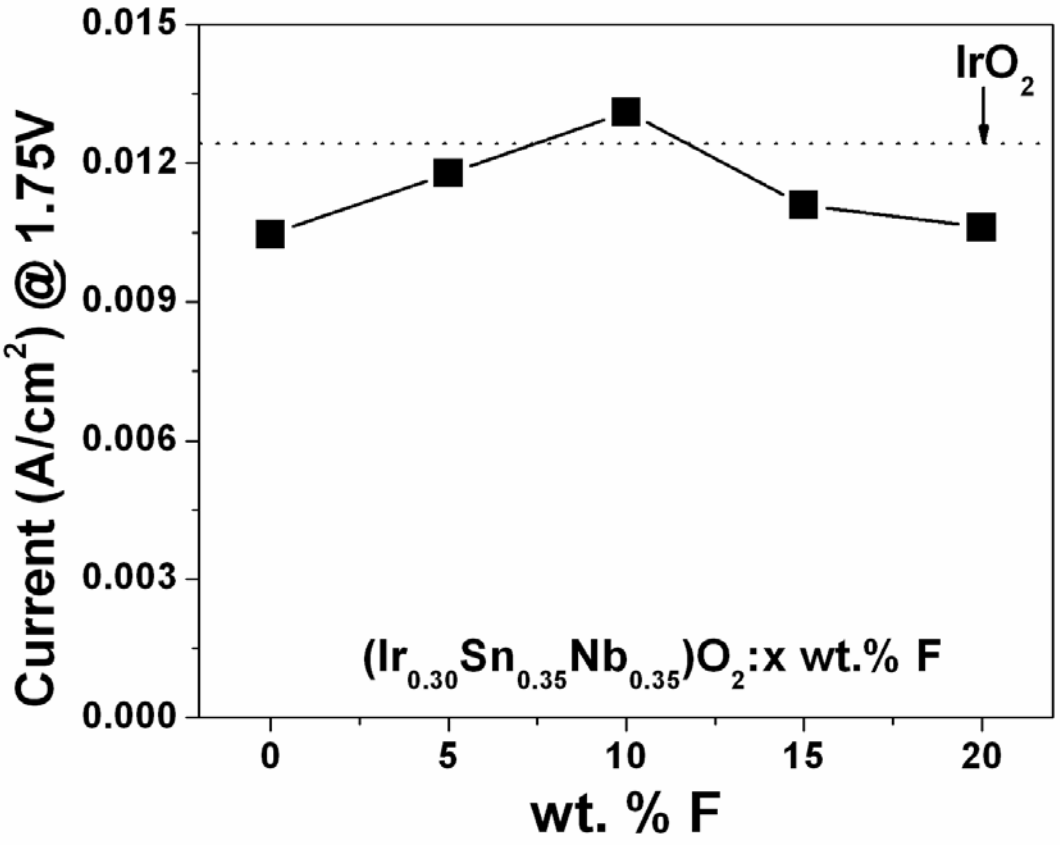

Figure 68. Variation of current density at ~ 1.75V (vs. NHE) for (Ir,Sn,Nb)O_2:F anode electro-catalyst

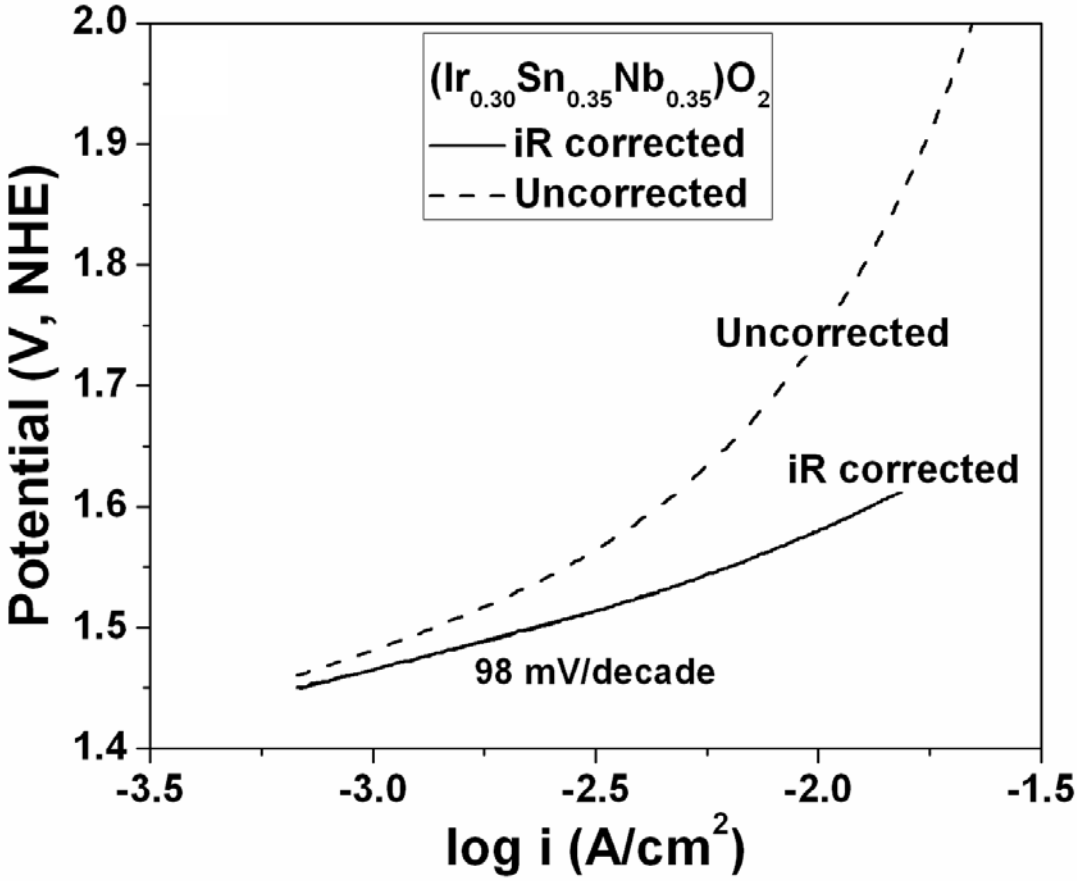

Figure 69. The Tafel plot of (Ir,Sn,Nb)O_2 before and after iR correction

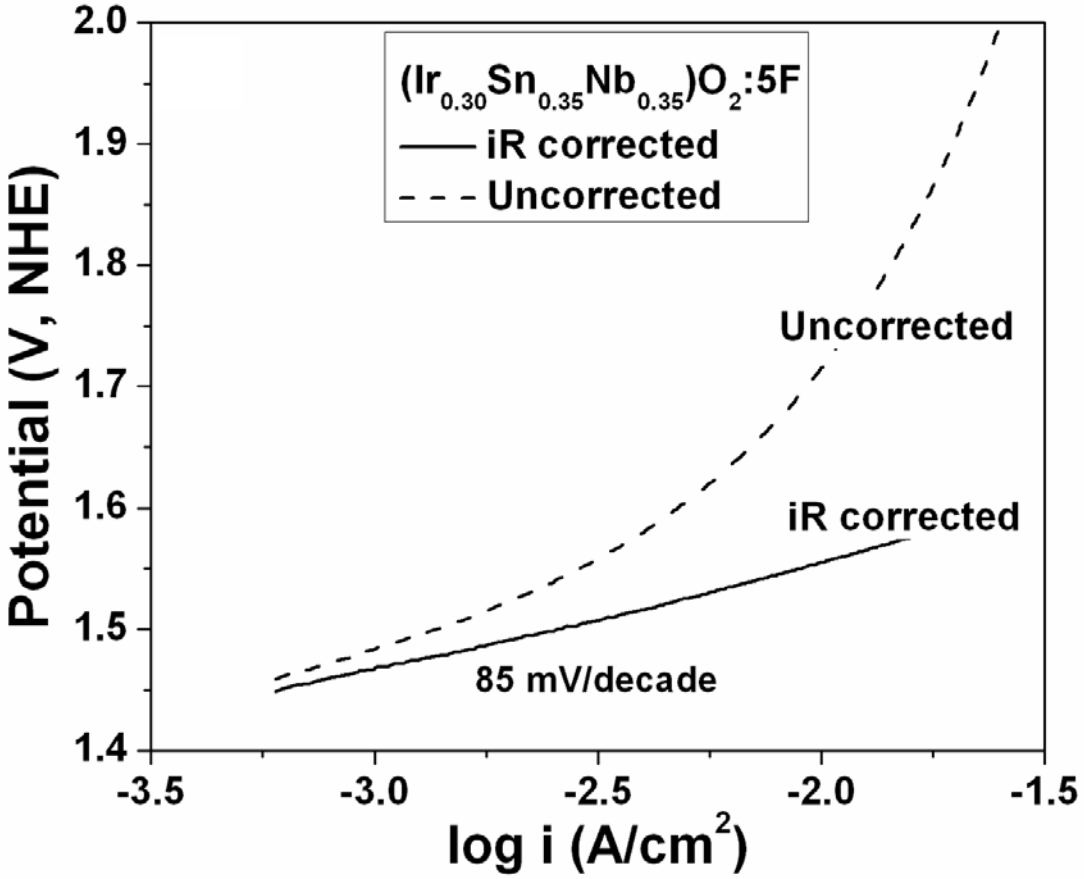

Figure 70. The Tafel plot of $(Ir,Sn,Nb)O_2$:5 wt.% F before and after iR correction

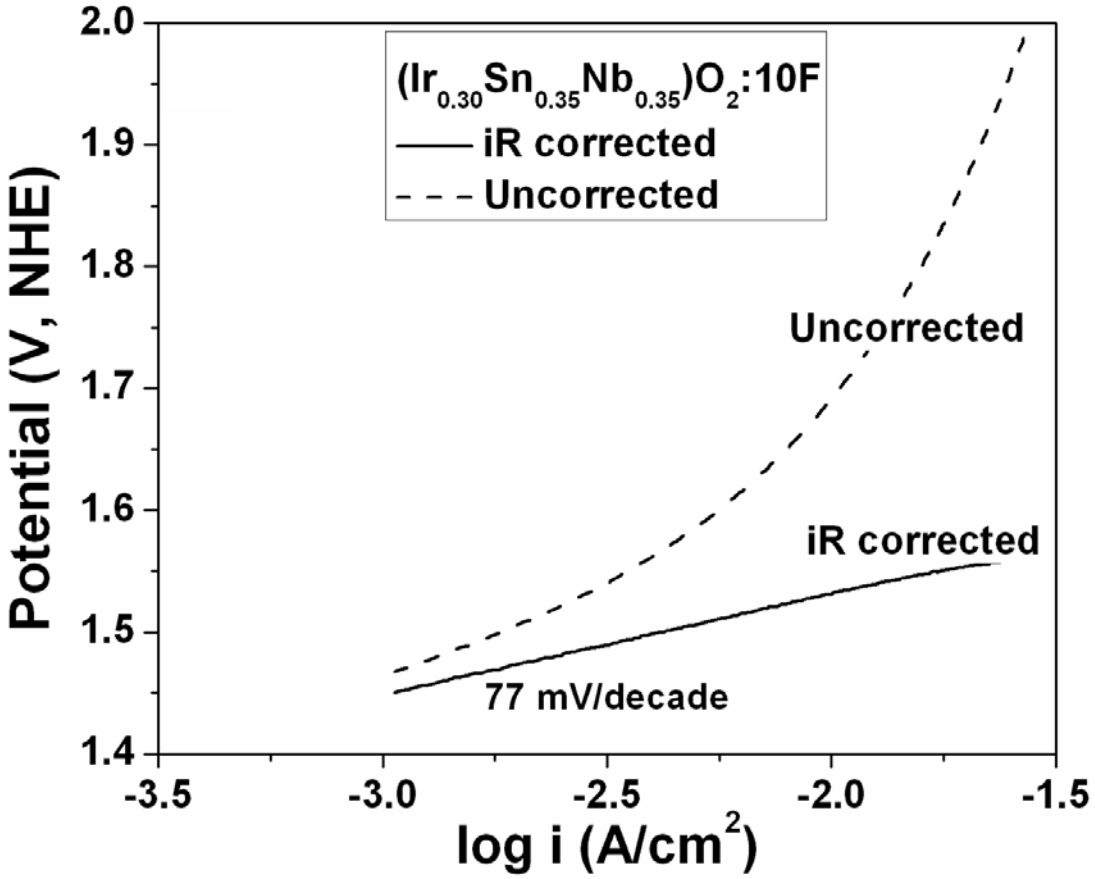

Figure 71. The Tafel plot of (Ir,Sn,Nb)O_2:10 wt.% F before and after iR correction

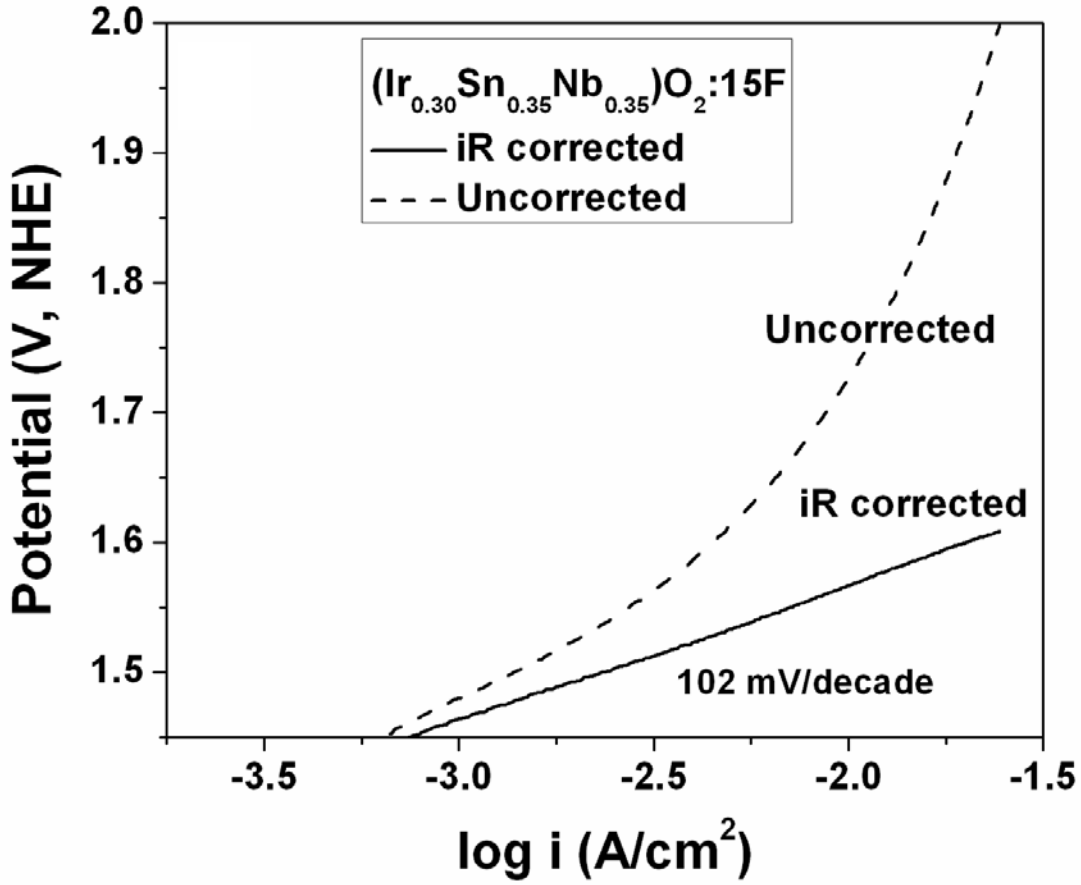

Figure 72. The Tafel plot of (Ir,Sn,Nb)O_2:15 wt.% F before and after iR correction

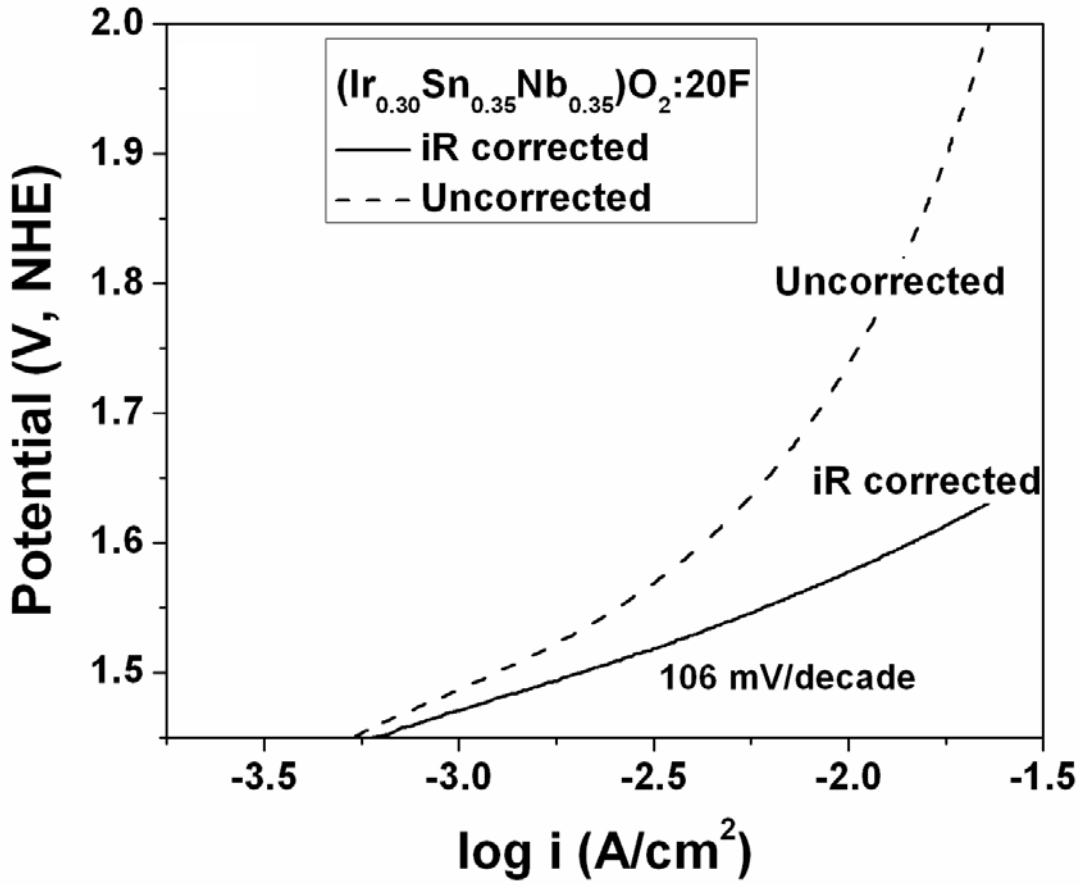

Figure 73. The Tafel plot of (Ir,Sn,Nb)O_2:20 wt.% F before and after iR correction

The durability of the anode electro-catalyst (Ir,Sn,Nb)O_2:F has been studied by choronoamperometry (CA) measurement *i.e.* current signal *vs.* time conducted at a constant potential for a duration of 24 hours. The CA curves of (Ir,Sn,Nb)O_2:F along with IrO_2, shown in **Figure 74**, are obtained at a constant voltage of ~ 1.65 V (*vs.* NHE without iR correction). The higher initial current for the (Ir,Sn,Nb)O_2:F electrodes is due to higher OER activity as demonstrated in **Figure 68**. There is a sharp drop in current for the initial small period of time (~

1 hour) for all the electrodes tested. This might be because of dissolution of the electro-catalyst material due to irregular coatings at the edge of the mud cracks [30]. A steady decay of current nevertheless, is seen after this initial period for (Ir,Sn,Nb)O_2:F up to 10 wt.% F which suggests that (Ir,Sn,Nb)O_2:F (up to 10 wt.% F) has similar long term durability as pure IrO_2. The steady decay of current for (Ir,Sn,Nb)O_2:F might be due to continuous exhaustion of fuel [34, 57]. As F content is increased over 10 wt. %, the stability seems to decrease compared to the undoped (Ir,Sn,Nb)O_2.

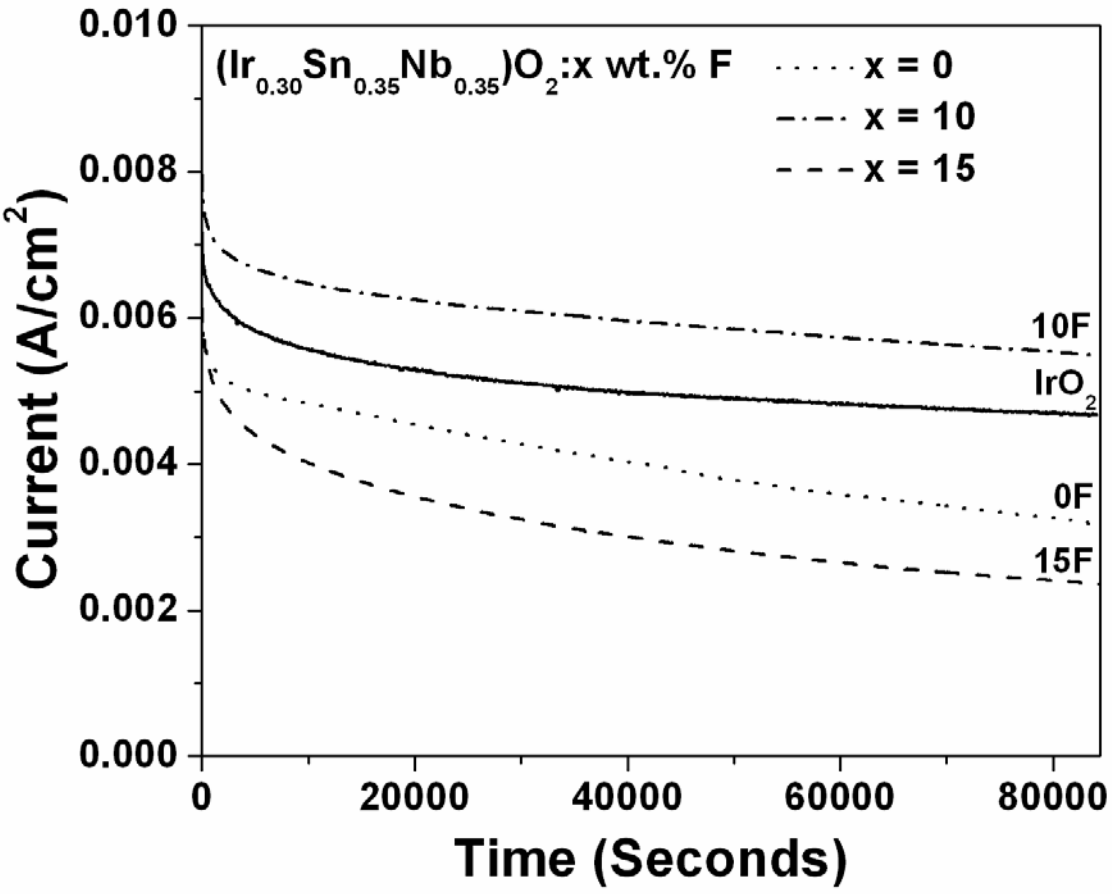

Figure 74. The variation of current *vs.* time measurement of pure IrO_2 and $(Ir_{0.30}Sn_{0.35}Nb_{0.35})O_2$:F performed in a 1 N H_2SO_4 solution under ~ 1.65 V at 40°C

ICP was conducted on the H_2SO_4 electrolyte solution collected after the CA curves have been recorded. Pure IrO_2 electro-catalyst also shows ~ 0.2 ppm Ir leached out into the solution and (Ir,Sn,Nb)O_2:10 wt.% F showed no Ir, ~ 0.15 ppm of Sn and ~ 0.15 ppm of Nb. However, the (Ir,Sn,Nb)O_2 electro-catalyst with 15 wt.% F dopant shows ~ 0.27 ppm of Ir, ~ 0.33 ppm of Sn and ~ 0.24 ppm of Nb in the solution after CA clearly reflecting a more unstable catalyst.

After the conclusion of the CA test, the (Ir,Sn,Nb)O_2:10 wt.% F thin film electrode was subject to polarization testing as seen in **Figure 75** in order to determine the activity of the electrodes after long term structural stability tests. The Tafel plot from the polarization curve (post CA measurement) after iR correction is shown in **Figure 76**. A Tafel slope of ~ 95 mV/decade is obtained for (Ir,Sn,Nb)O_2:10 wt.% F respectively. This is slightly higher but still close and comparable to the values obtained from the polarization test conducted before CA (**Figure 71**). This test further demonstrates the robustness of the electro-catalysts.

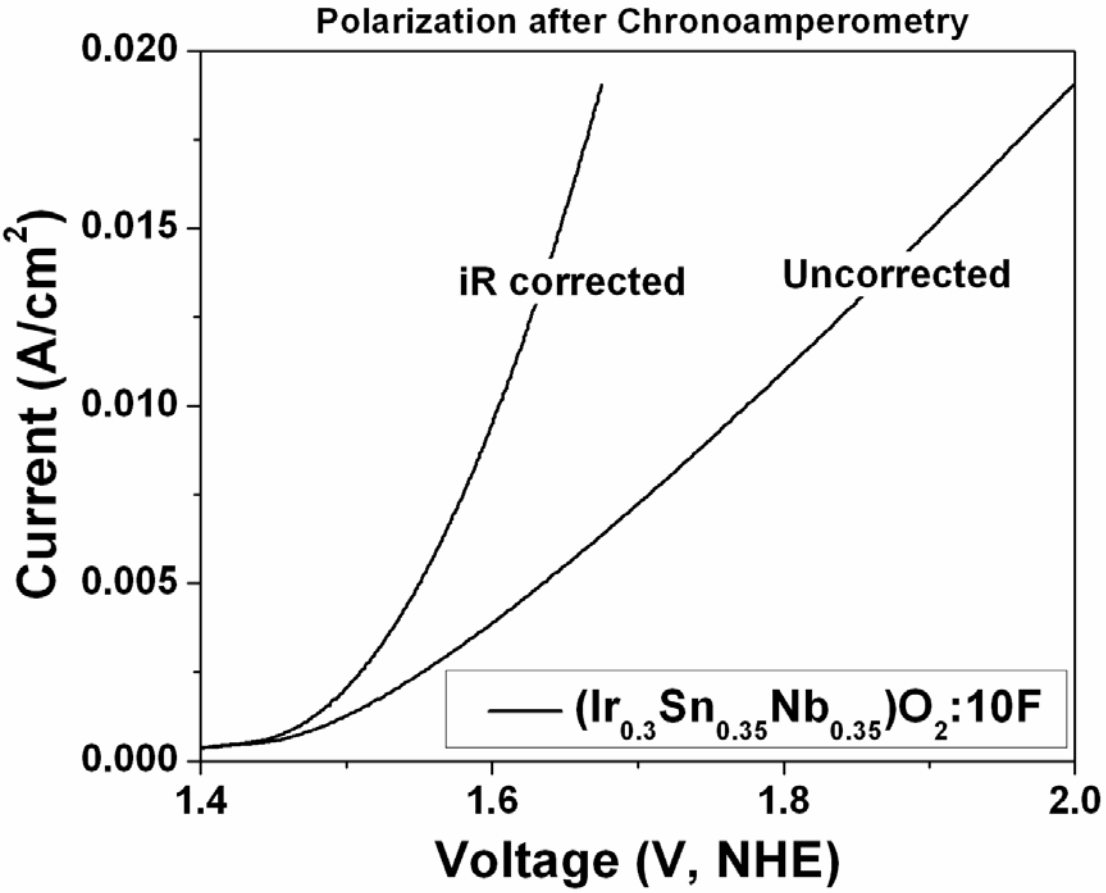

Figure 75. Polarization curve of (Ir,Sn,Nb)O_2:10 wt.% F thin film after the CA test

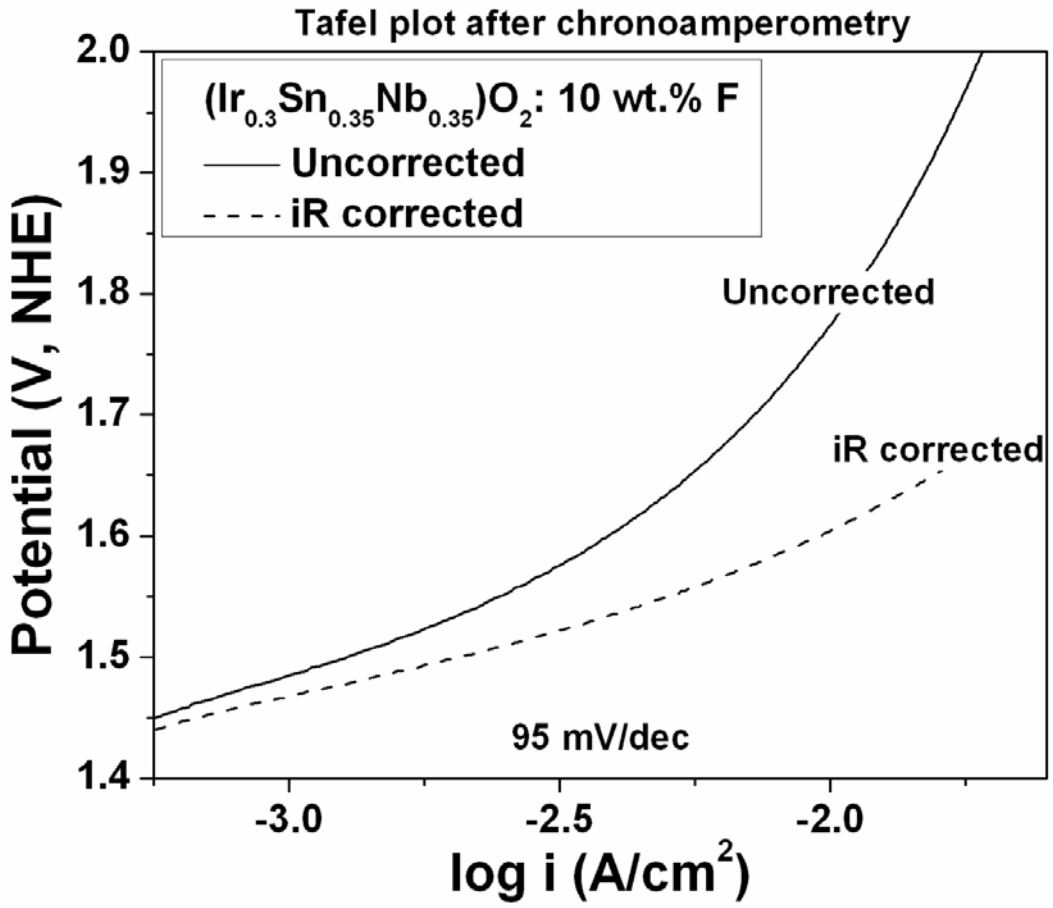

Figure 76. The Tafel plot of (Ir,Sn,Nb)O_2:10 wt.% F thin film after the CA test

The present study therefore successfully identifies ($Ir_{0.30}Sn_{0.35}Nb_{0.35}$)$O_2$:10 wt.% F as a promising anode electro-catalyst material that not only improves the catalytic activity but also the does not compromise the electrochemical stability. The excellent electrochemical activity and durability exhibited by ($Ir_{0.30}Sn_{0.35}Nb_{0.35}$)$O_2$:10 wt.% F renders it an excellent material for its use as an anode in PEM based electrolysis. We can thus expect the (Ir,Sn,Nb)O_2:F catalysts to exhibit significant reduction in the overall costs of PEM electrolyzers.

5.2 NANOSTRUCTURED POWDERS

5.2.1 F doped IrO_2

5.2.1.1 Structural Analysis

X-ray diffraction, specific surface area measurements and transmission electron microscopy characterization was done in order to study the structure of the electro-catalysts synthesized. The XRD patterns of the IrO_2:F powders after heat treatment to 500°C are shown in **Figure 77**. The XRD patterns show a rutile type tetragonal structure similar to pure IrO_2 for all the electro-catalysts. No additional peak (*E.g.* iridium fluoride) is observed which indicates formation of a complete solid solution between IrO_2 and F without any undesired phase separation as seen previously [34]. This might arise due to the fact that the ionic radius of O^{2-} (125 pm) is comparable to that of F^{1-} (120 pm) [114]. The relative broad peaks seen in the XRD patterns are due to the nanocrystalline nature of the synthesized catalysts. The effective crystallite size of IrO_2:F, calculated using the Scherrer formula from the integral breadth of the Lorentzian contribution determined from peak profile analysis using single line approximation method after eliminating the instrumental broadening and lattice strain contribution [88] is ~ 3 - 4 nm for different F compositions which is similar to that of pure undoped IrO_2 (~ 4 nm).

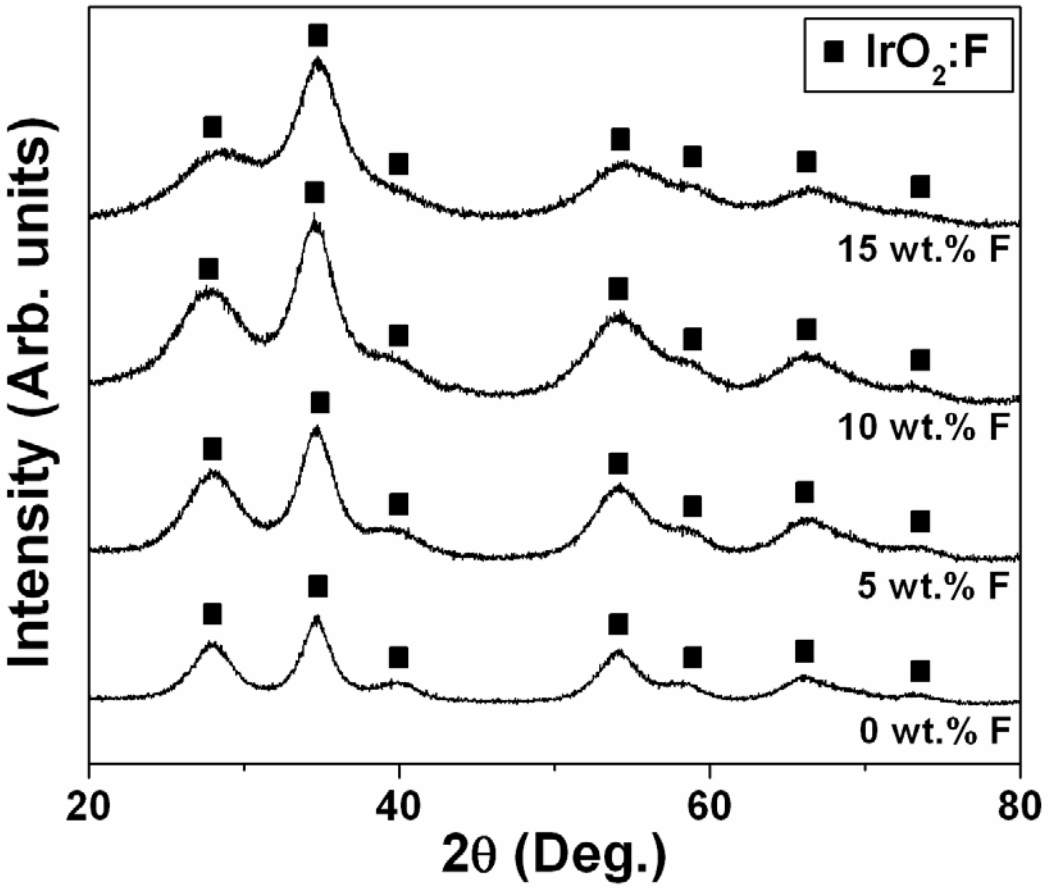

Figure 77. The XRD pattern of the nanostructured IrO_2:F of different compositions

The specific surface area (SSA) of IrO_2:F measured by the BET technique ranged from 100 - 200 m^2/g for varying F compositions. Pure IrO_2 had a SSA of ~ 191 m^2/g and IrO_2:x wt.% F had a SSA of ~ 184 m^2/g, 157 m^2/g, 129 m^2/g and 100 m^2/g for x = 5, 10, 15 and 20 respectively. These SSA values are much higher than that of commercial IrO_2 (~ 20 m^2/g). The decrease in the SSA of IrO_2:F with increasing F doping might be because of heat released due to the exothermic phenomenon of NH_4F burning, occurring during the synthesis of the catalyst

powders. This heat released might lead to agglomeration of IrO_2:F nanoparticles causing a decrease in the SSA [115]. A decrease in the specific surface area with incorporation of F for other materials and catalyst systems has been reported by other researchers too [115-118]. The bright field TEM image shown in **Figure 78**, of a representative electro-catalyst composition of IrO_2:10 wt.% F confirms the nanometer scale (~5 - 10 nm) of the particles. The HRTEM image, shown in **Figure 79**, confirms the nanostructured nature of the electro-catalysts, with the d spacing being ~0.312 nm ± 0.005 nm, that matches well with the d_{110} spacing of pure IrO_2 which is 0.318 nm [119].

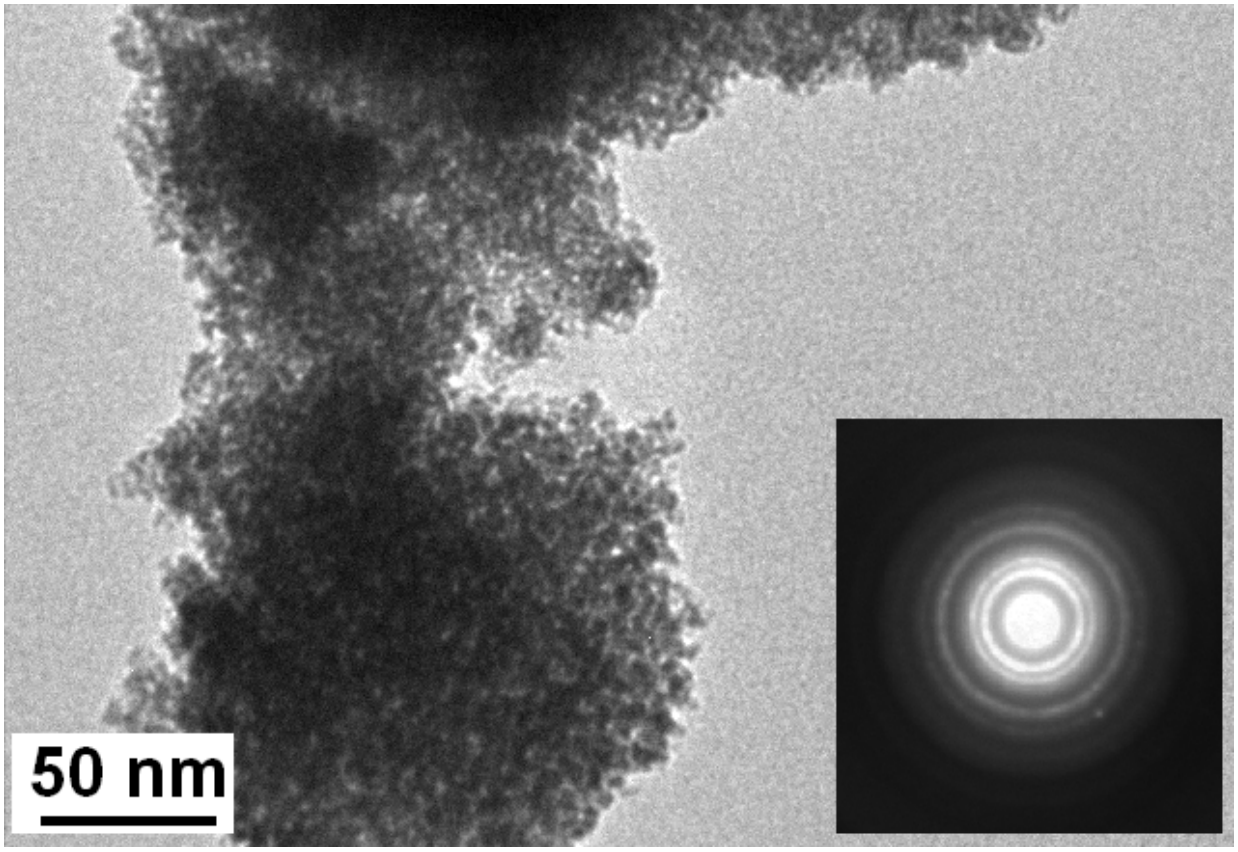

Figure 78. The bright field TEM image of nanostructured IrO_2:10 wt.% F electro-catalyst

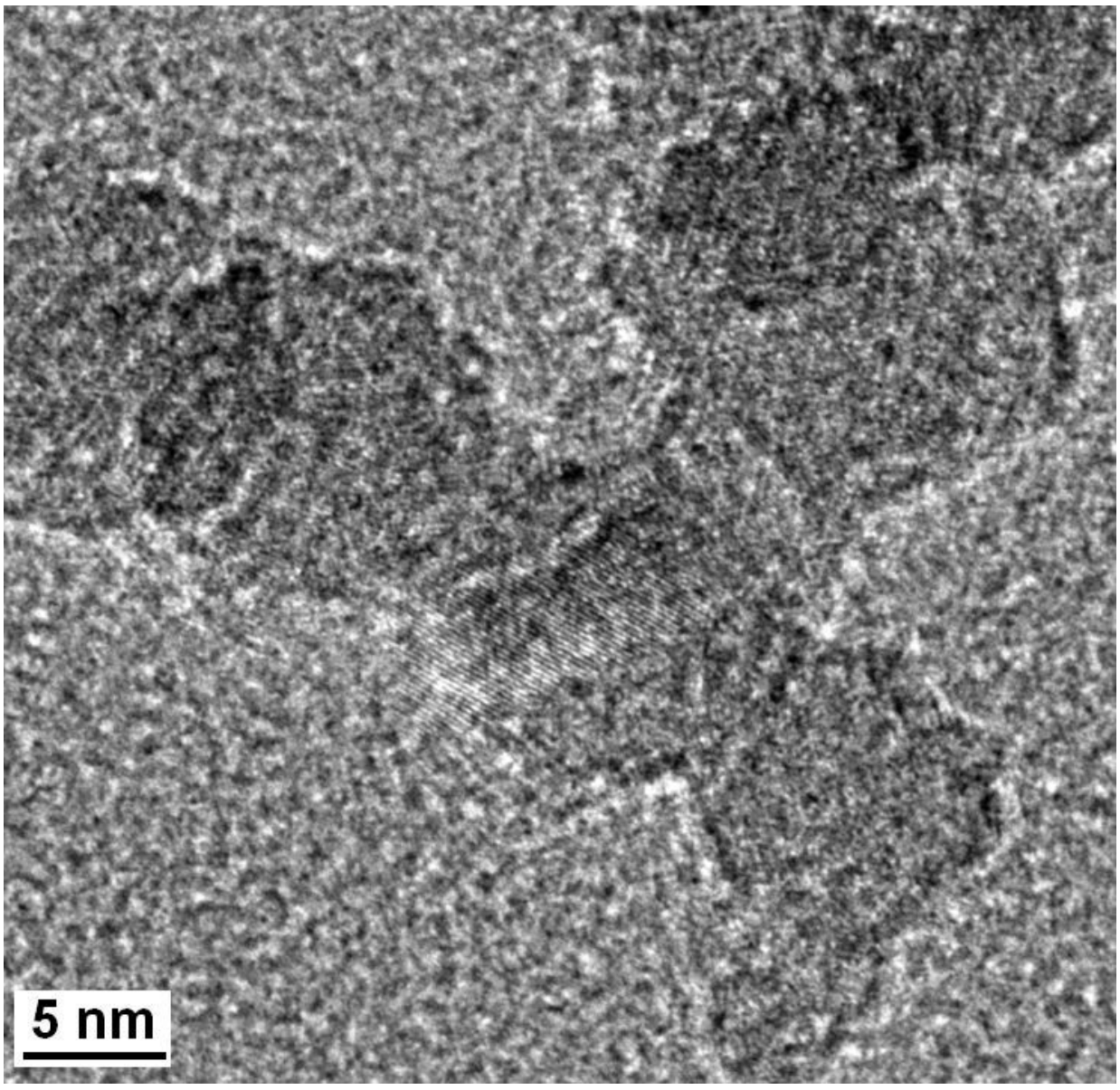

Figure 79. The HRTEM image of IrO_2:10 wt.% F confirming the nanoparticulate nature of the electro-catalyst

5.2.1.2 Electrochemical Testing

The electrochemical activity of nanostructured IrO_2:F with F doping ranging from 0 to 20 wt.% has been studied as an OER catalyst for use as an anode in PEM based water electrolysis. Polarization was conducted at a scan rate of 1 mV/sec in 1 N H_2SO_4 at 40°C. The uncorrected polarization curve and the non-linear Tafel plot encounters a large amount of ohmic/solution resistance (R_s) which is determined from the electrochemical impedance spectroscopy (EIS) plot at high frequencies [51, 52]. This helps us in preparing the linear Tafel plots and the iR corrected polarization curves. The plots after correcting for the ohmic loss help us in evaluating the inherent electro-catalytic property of the electrodes. **Figure 80** and **Figure 81** shows the EIS plots of undoped IrO_2 and IrO_2:5 wt.% F, respectively at open circuit potential (OCP), 1.5 V, 1.6 V and 1.7 V (*vs.* NHE). The EIS curves of IrO_2:10 wt.% F, IrO_2:15 wt.% F, and IrO_2:20 wt.% F are plotted in **Figure 82**, **Figure 83** and **Figure 84**, respectively at OCP, 1.5 V, 1.6 V and 1.7 V (*vs.* NHE). It is observed that the R_s values obtained at high frequencies for all IrO_2:F electrodes at various potentials is very similar (~ 16.1 ± 0.4 Ωcm^2). The EIS plots show a well formed semi-circular arc at low frequencies and its diameter gives the polarization resistance (R_{ct}). **Table 6** enlists the impedance parameters *i.e.* R_s and R_{ct} for all the synthesized electro-catalysts (IrO_2:F) at different potentials. It is observed that the R_{ct} value at all potentials decreases when F doping is increased from 0 to 10 wt.% F. R_{ct} is the resistance due to electron transfer at the electrochemical interface. A lower value of R_{ct} indicates there will be less resistance faced by the electrode during the OER and would result in enhanced catalytic performance and activity. It is also seen that the R_{ct} increases when F doping is raised to 15 and 20 wt.% F. As the R_{ct} increases, a decrease in the electrochemical activity is expected.

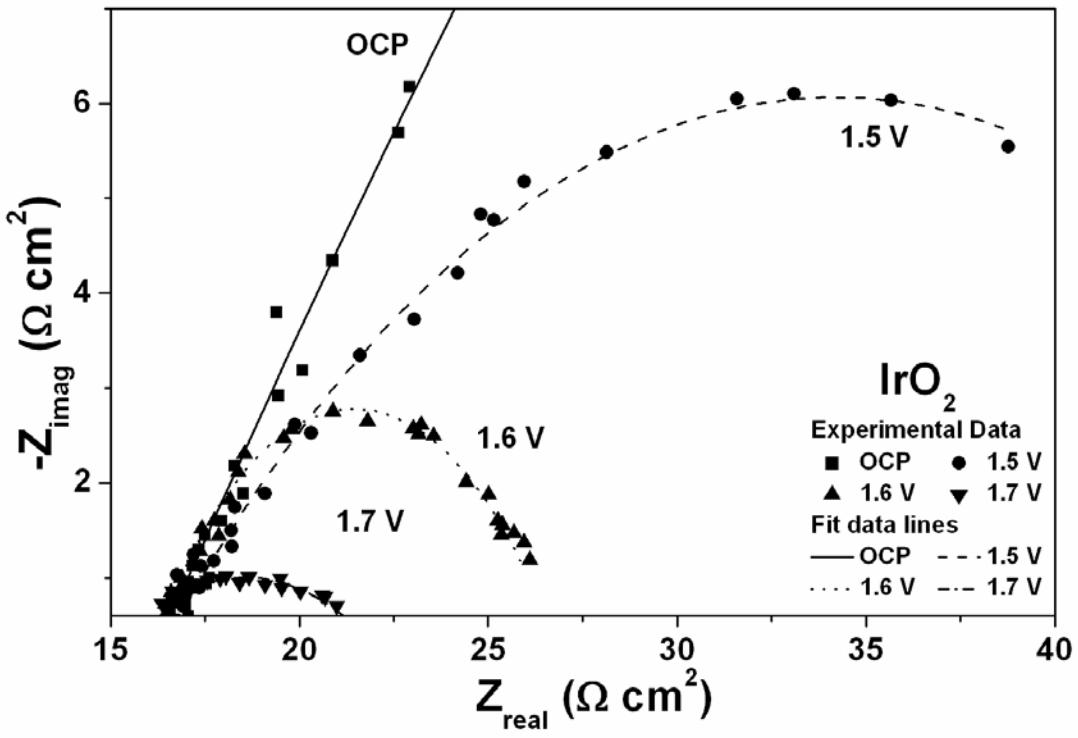

Figure 80. EIS spectra of undoped IrO_2 in a solution of 1 N H_2SO_4 at 40°C

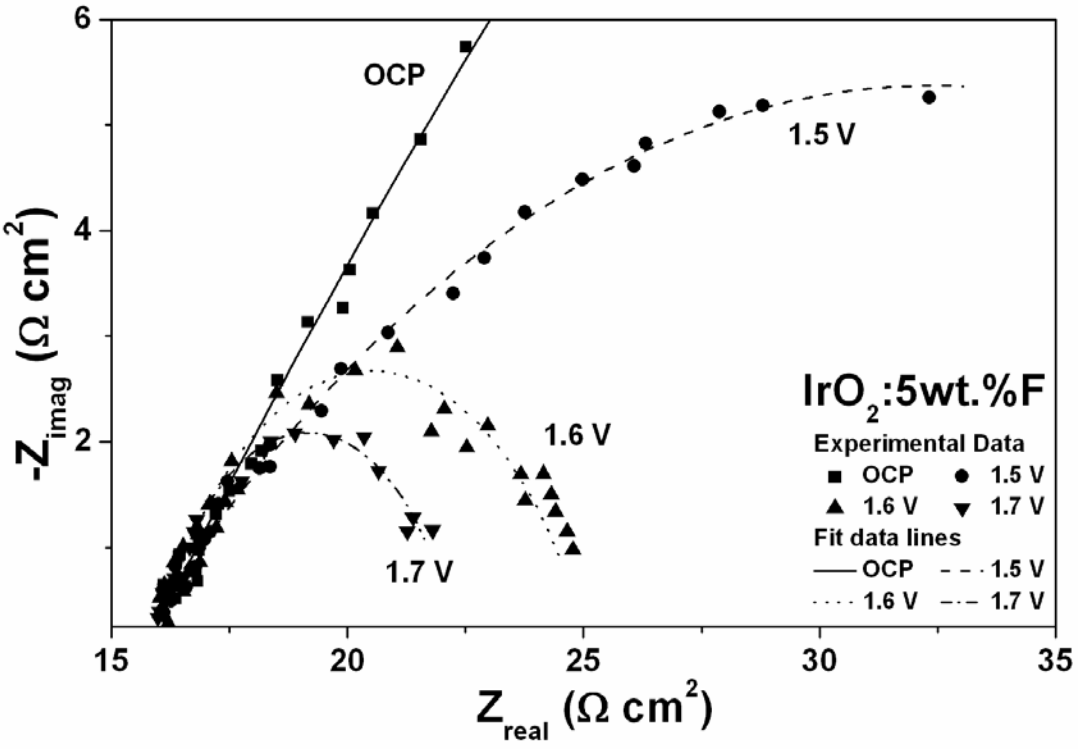

Figure 81. EIS spectra of IrO_2:5 wt.% F in a solution of 1 N H_2SO_4 at 40°C

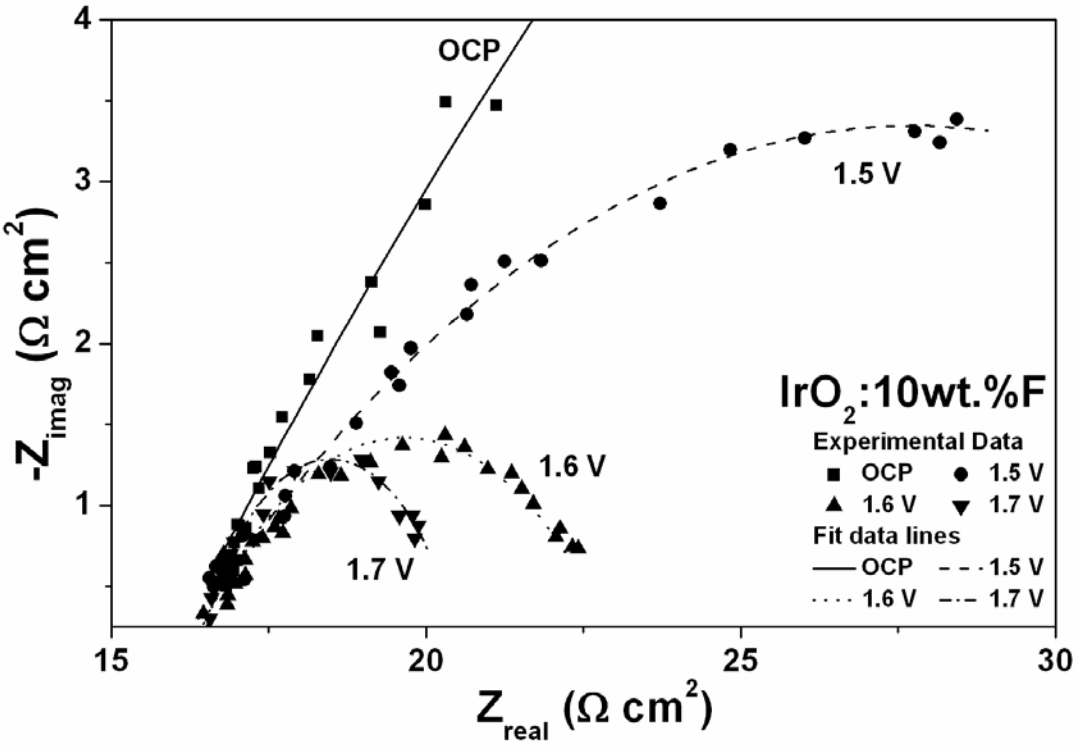

Figure 82. EIS spectra of IrO_2:10 wt.% F in a solution of 1 N H_2SO_4 at 40°C

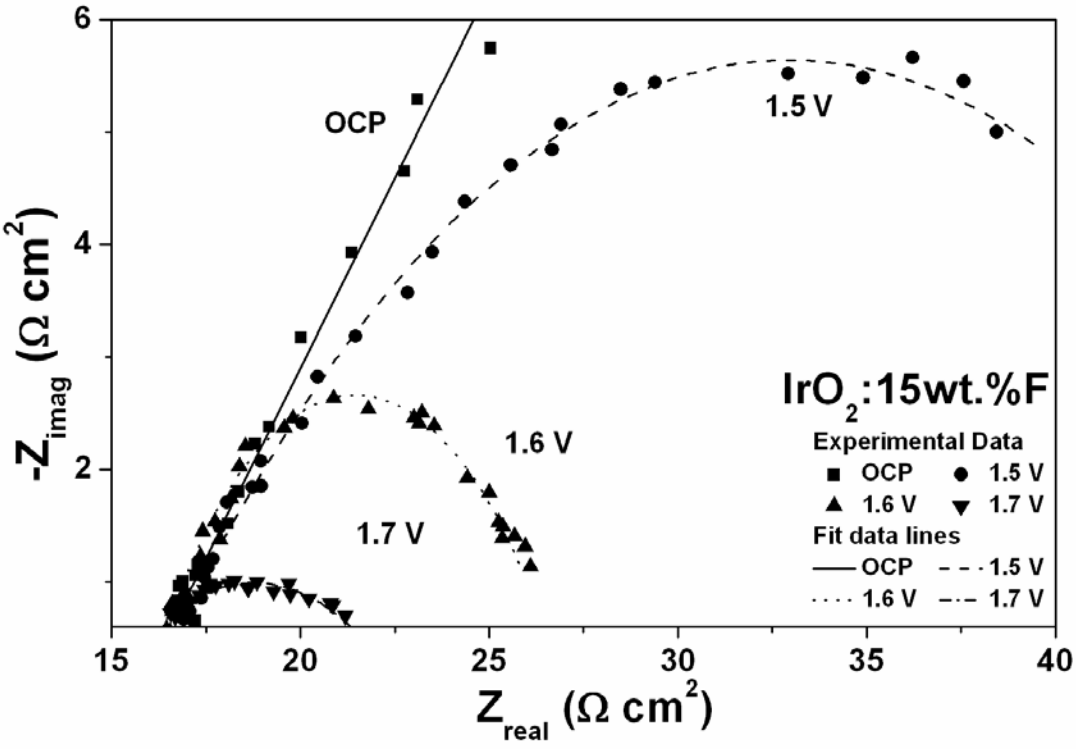

Figure 83. EIS spectra of IrO_2:15 wt.% F in a solution of 1 N H_2SO_4 at 40°C

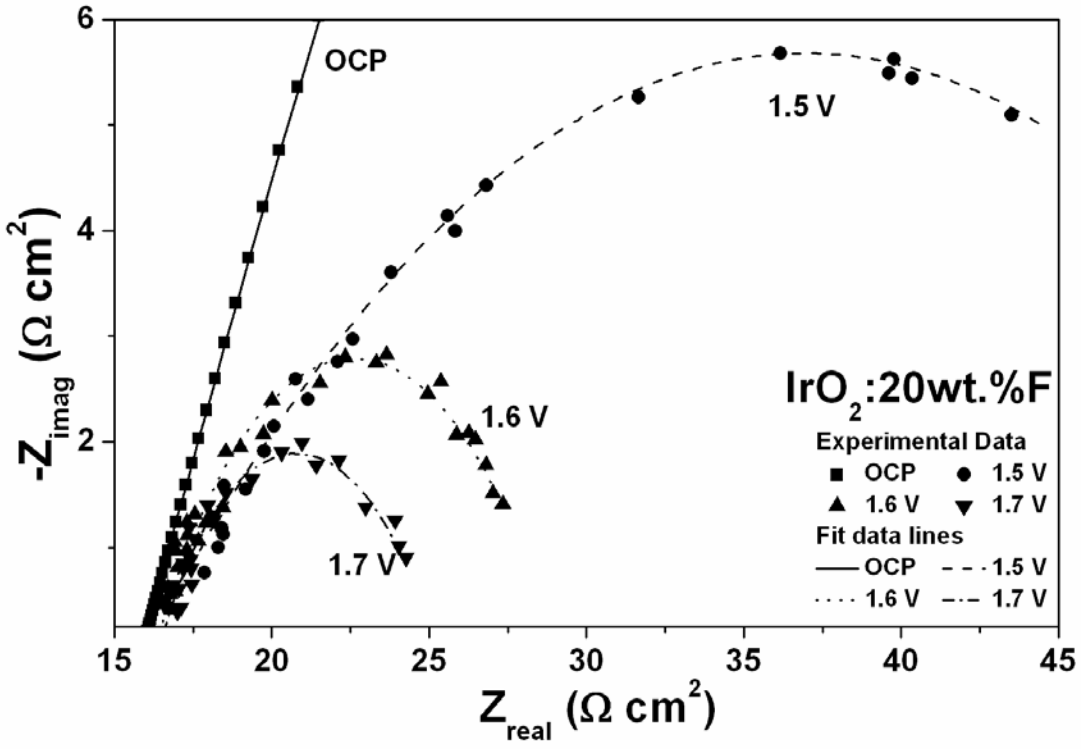

Figure 84. EIS spectra of IrO_2:20 wt.% F in a solution of 1 N H_2SO_4 at 40°C

Table 6. Impedance parameters of IrO_2:F powder catalyst

	F doping (wt.%)	OCP	1.5 V	1.6 V	1.7 V
R_s (Ω cm^2)	0	15.96	15.99	16.04	16.30
	5	16.08	15.95	15.87	16.01
	10	16.07	15.87	16.17	16.39
	15	15.71	15.96	15.94	16.46
	20	15.84	15.95	16.24	16.40
R_{ct} (Ω cm^2)	0	203.4	36.42	11.53	8.13
	5	154.2	32.39	9.29	5.65
	10	126.4	23.69	6.96	3.76
	15	175.5	33.99	11.03	8.04
	20	200.8	42.00	12.75	6.98

Figure 85 shows the polarization tests on nanocrystalline IrO_2, IrO_2:5 wt.% F and IrO_2:10 wt.% F. It is clearly seen that the onset of electrolysis or the OER starts at ~ 1.43 V (*vs.* NHE). The current density at ~ 1.48 V after iR correction (*vs.* NHE), which is in the standard range of accepted voltages for determining electro-catalytic activity in PEM electrolysis conditions, is ~ 0.0088 ± 0.0002 A/cm^2 for undoped IrO_2 with a total loading of ~ 0.3 mg/cm^2.

At the same voltage of ~ 1.48 V and a total loading of ~ 0.3 mg/cm^2; IrO_2:5 wt% F and IrO_2:10 wt.% F have a current density of ~ 0.0133 ± 0.0002 A/cm^2 and 0.030 ± 0.0002 A/cm^2, respectively. Fluorine doping of 10 wt.% thus shows an appreciable increase in the current density with respect to pure IrO_2 (*ca.* 3.3 times) implying a great increase in the electrochemical activity of the catalyst. As F doping is increased to 15 and 20 wt.%, it is observed *via* **Figure 86** that the onset of the OER remains similar and is ~ 1.43 V (*vs.* NHE) for the catalysts. But, the current obtained decreases for the same loading of ~ 0.3 mg/cm^2. The current density at ~ 1.48 V (*vs.* NHE) for 15 wt.% F and 20 wt.% F doped IrO_2 is ~ 0.0112 ± 0.0002 A/cm^2 and 0.010 ± 0.0002 A/cm^2, respectively. These results also agree very well with the EIS plots as an increase in R_{ct} is seen after increasing F doping above 10 wt.% (**Table 6**). This suggests that IrO_2:10 wt.% F is the most optimized electro-catalyst yielding very high electro-catalytic activity than pure IrO_2.

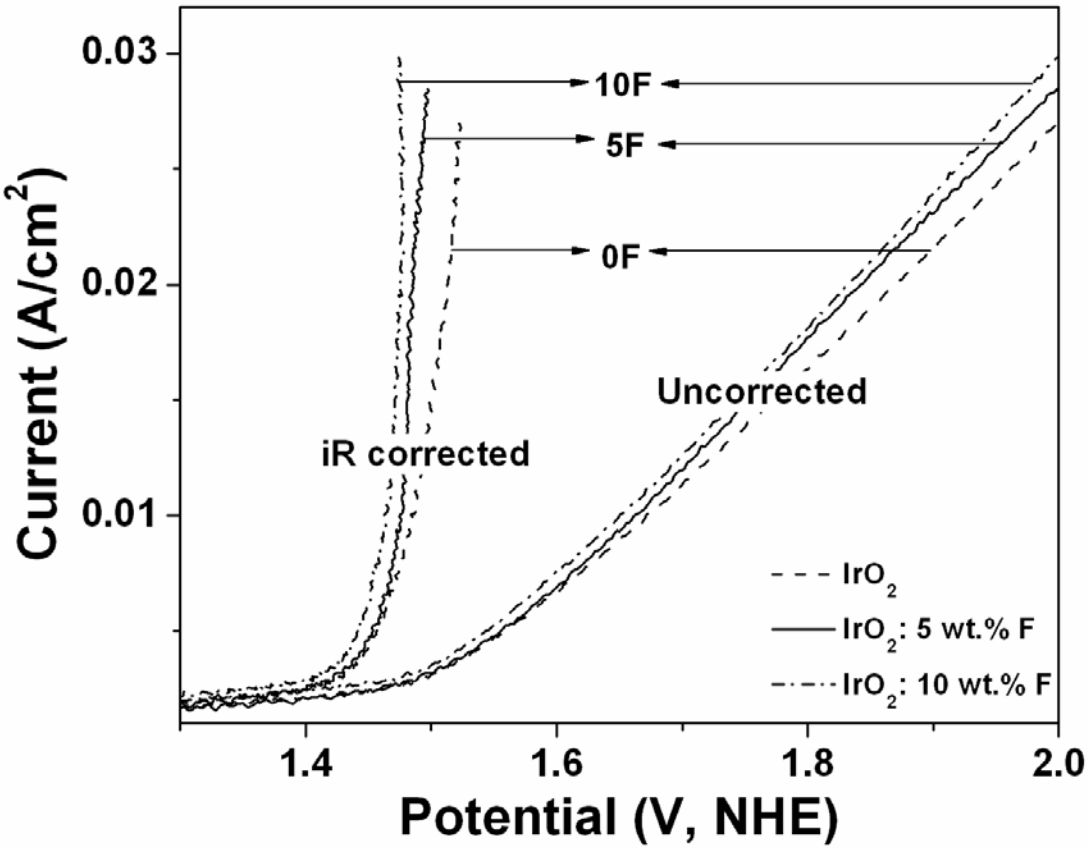

Figure 85. Polarization testing of undoped IrO_2, IrO_2:5 wt.% F and IrO_2:10 wt.% F conducted at a scan rate of 1 mV/sec in 1 N H_2SO_4 at 40°C

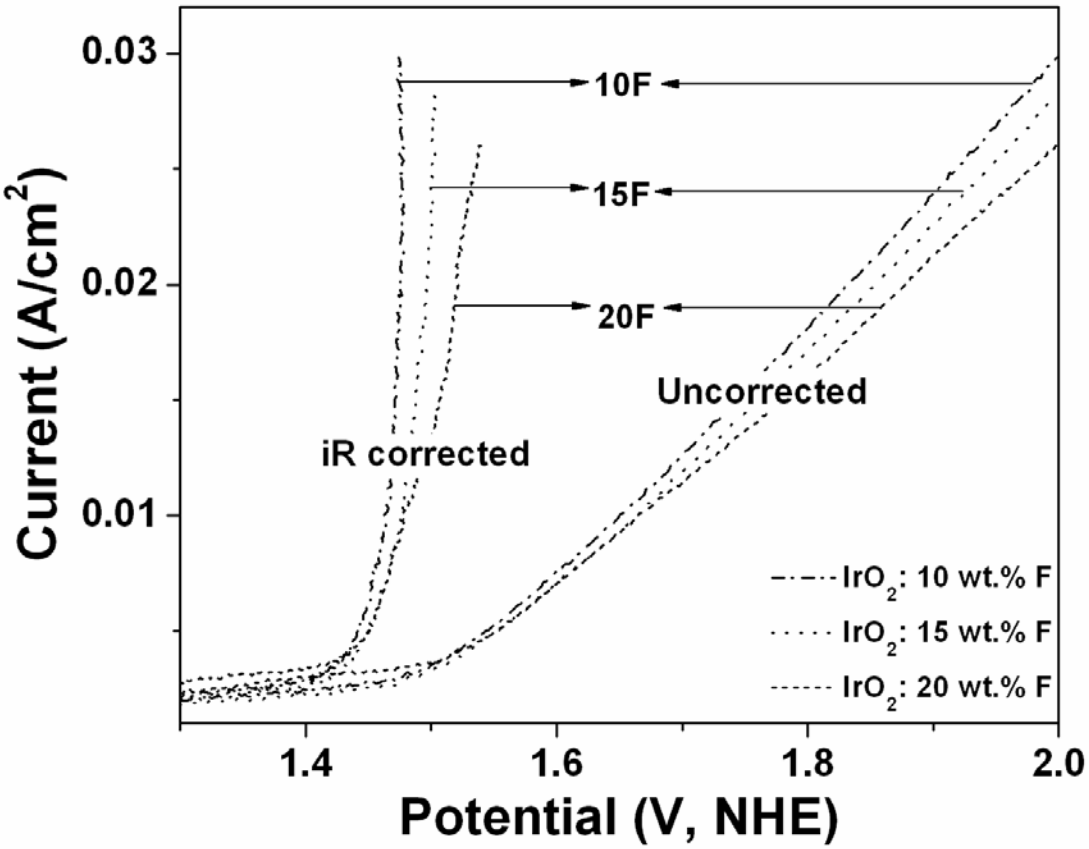

Figure 86. Polarization testing of IrO_2:10 wt.% F, IrO_2:15 wt.% F and IrO_2:20 wt.% F conducted at a scan rate of 1 mV/sec in 1 N H_2SO_4 at 40°C

Figure 87, **Figure 88**, **Figure 89**, **Figure 90** and **Figure 91** show the uncorrected and iR corrected Tafel plots for IrO_2:F with 0, 5, 10, 15 and 20 wt.% F, respectively and the Tafel slopes are calculated from these iR corrected Tafel plots. An ideal Tafel slope of ~ 62 mV/dec would correspond to the well known two electron pathway mechanism, assuming a transfer coefficient of 0.5 [30, 48, 53]. It is observed that undoped pure IrO_2 has a Tafel slope of ~ 93 mV/dec. It has been determined that with 5, 10, 15 and 20 wt.% F doping of IrO_2, the Tafel slope is ~ 77

mV/dec, 64 mV/dec, 85 mV/dec and 116 mV/dec, respectively. The Tafel slopes along with other RDE parameters have been reported in **Table 7**. This explains the increase in electrochemical activity or current density, which is favored by a decrease in the Tafel slope and corresponding increase in F content up to 10 wt.% as demonstrated in the polarization curves (**Figure 85** and **Figure 86**). These results further confirm that 10wt.% F doped IrO_2 is the most optimized composition resulting in enhanced catalytic activity with the least Tafel slope.

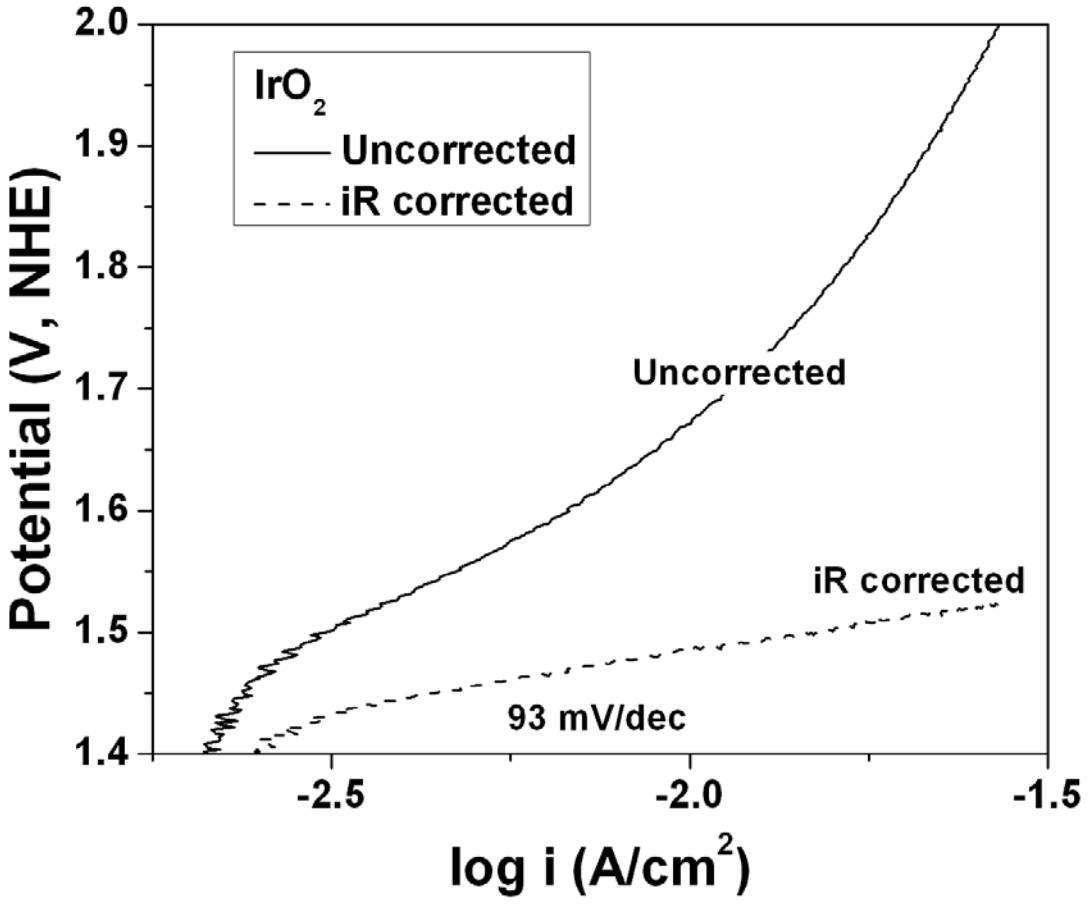

Figure 87. The Tafel plot of undoped IrO_2 before and after iR correction

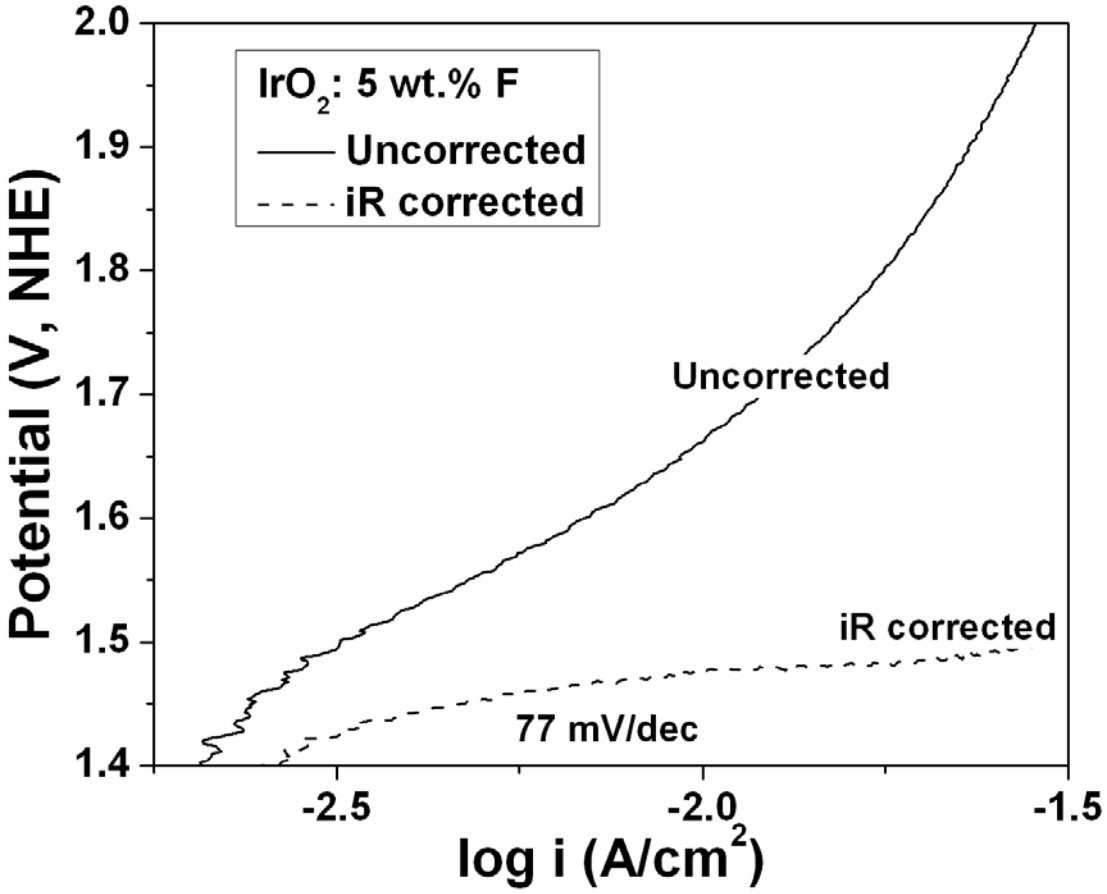

Figure 88. The Tafel plot of IrO_2:5 wt.% F before and after iR correction

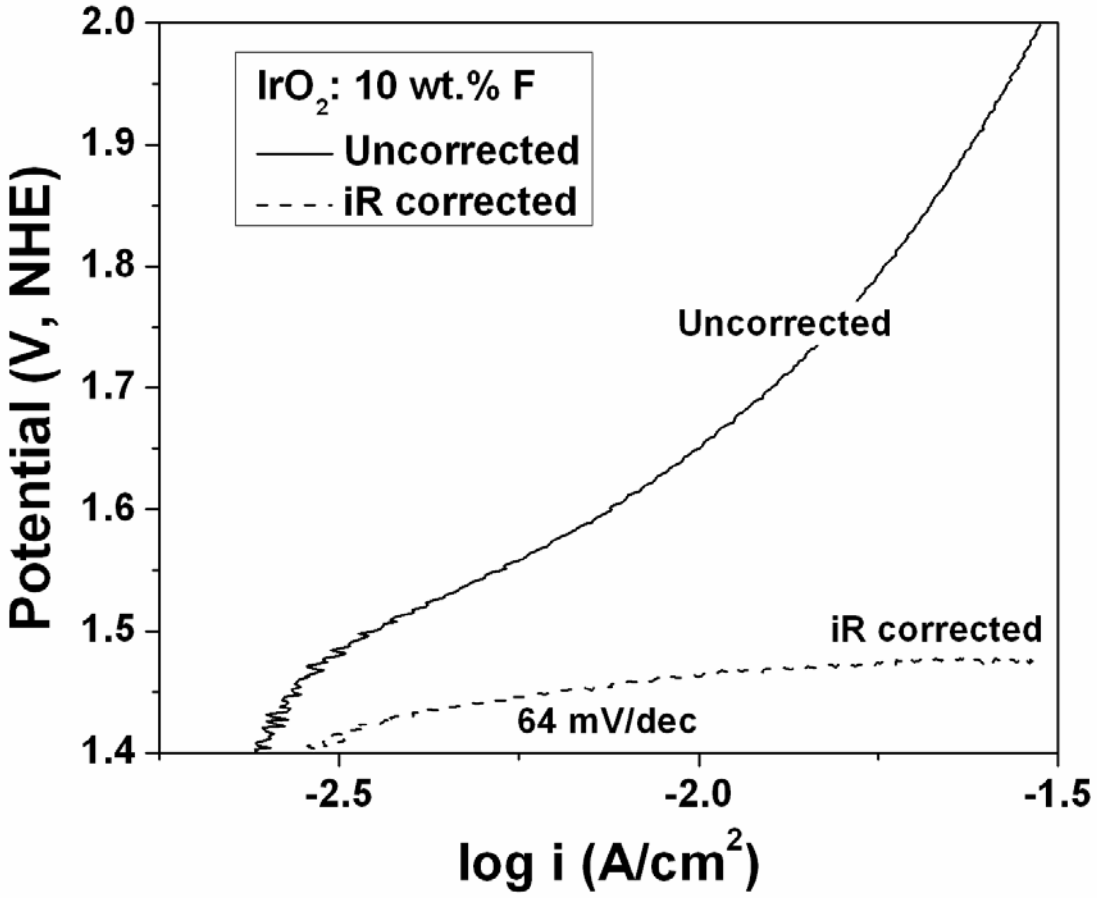

Figure 89. The Tafel plot of IrO_2:10 wt.% F before and after iR correction

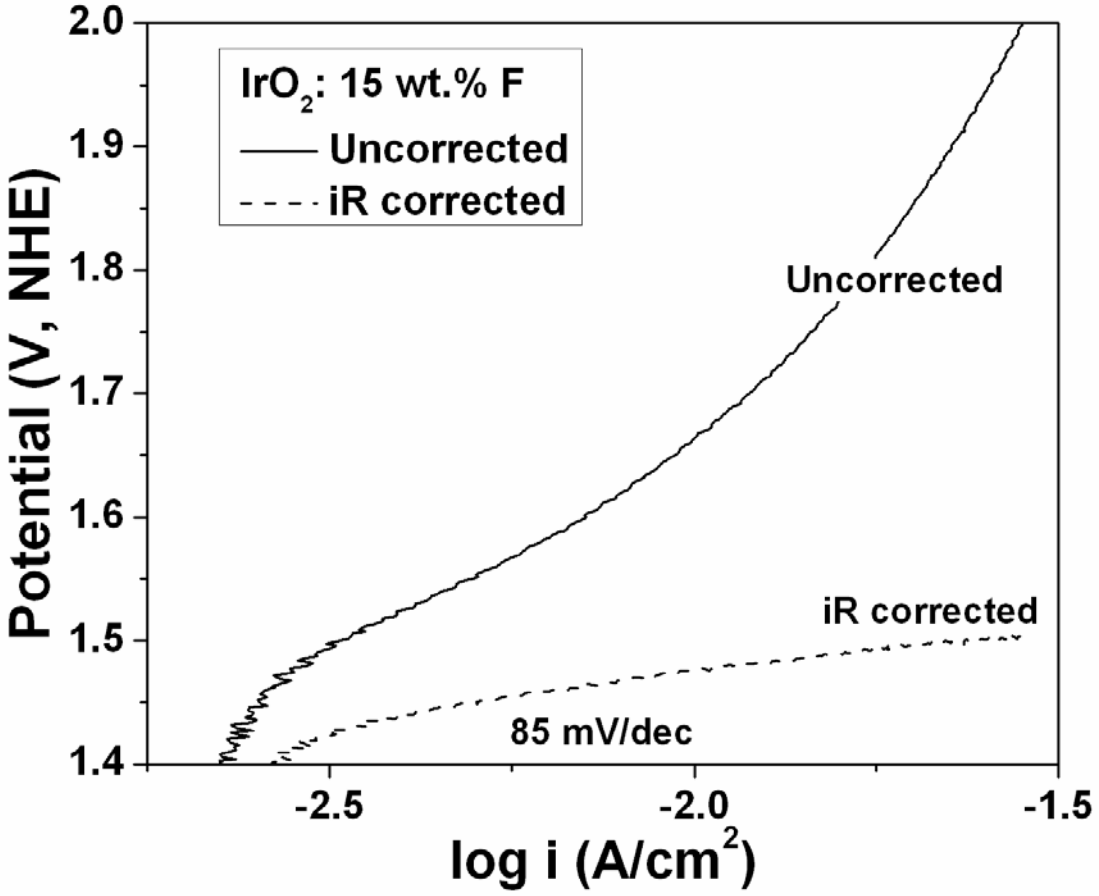

Figure 90. The Tafel plot of IrO_2:15 wt.% F before and after iR correction

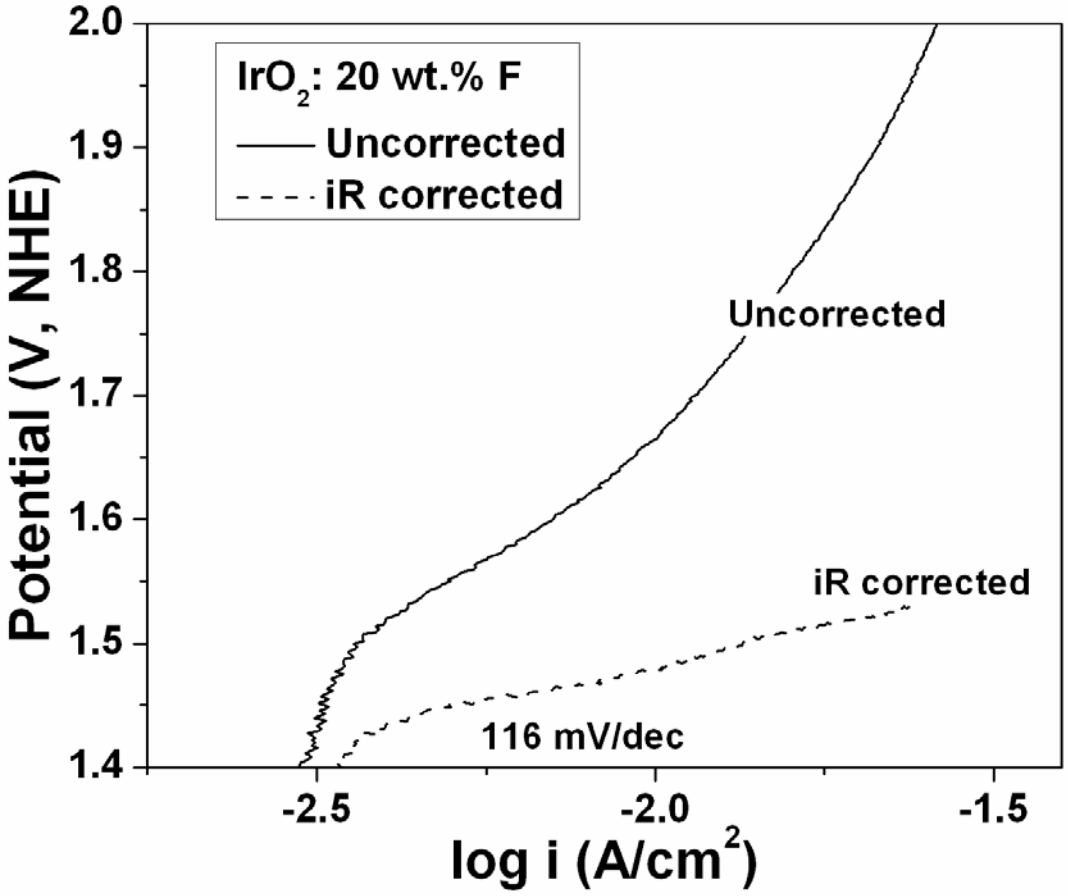

Figure 91. The Tafel plot of IrO_2:20 wt.% F before and after iR correction

Table 7. The Tafel slope, number of electrons transferred in the OER and the kinetic rate constant from the Koutecky - Levich plots for IrO_2:F

F doping (wt. %)	Tafel slope (mV/dec)	n	k (cm/s)		
			1.55 V	1.65 V	1.75 V
0	93	1.78	0.0618	0.0708	0.0826
5	77	1.86	0.0660	0.0763	0.0853
10	64	1.92	0.0656	0.0717	0.0823
15	85	1.82	0.0652	0.0743	0.0874
20	116	1.61	0.0679	0.0810	0.1010

Multiple small potential step voltammetry was performed for the rotating disk electrode studies in order to study the fundamental kinetics and calculate the apparent activation energy of the OER. The catalyst ink coated Ti disk insert was rotated at speeds varying from 500 rpm to 2000 rpm. **Figure 92** and **Figure 93** shows the Koutecky - Levich plot *i.e.* i^{-1} *vs.* $\omega^{-1/2}$ for undoped IrO_2 and IrO_2:5 wt.% F, respectively. **Figure 94**, **Figure 95** and **Figure 96** shows the Koutecky - Levich plot for IrO_2:10 wt.% F, IrO_2:15 wt.% F and IrO_2:20 wt.% F, respectively. The current values at different rotation speeds have been plotted at three potentials of 1.55 V, 1.65 V and 1.75 V (*vs.* NHE) without iR correction. The potentials are not iR corrected since the tests have been conducted in-situ (*via* multiple small potential step voltammetry) from which the RDE results are reported directly. This dynamic testing process does not allow accounting for the

iR drop from the solution resistance. These RDE plots at different potentials give parallel straight lines of similar nature; and the current increases with increase in voltage as expected, causing a decrease in the value of i^{-1}. At any given potential and rotation speed, it is observed that the current density increases categorically when the F doping is increased up to 10 wt.% and then decreases with 15 and 20 wt.% F doping. This trend is thus consistent with the results obtained from the polarization curves (**Figure 85** and **Figure 86**). From the slope of the graphs, the number of electrons transferred (n) is determined as explained in **Section 4.4.4**. The average value of 'n' determined at the three voltages for all IrO_2:F electro-catalysts along with the Tafel slope and kinetic rate constant (k) has been tabulated in **Table 7**. The kinetic rate constant of an electrochemical reaction not only varies with the applied potential, but is also dependent on many other factors *viz.*, temperature, electrode surface structure, composition of the catalyst, surface adsorption and reaction intermediates [95, 96, 102, 103]. The RDE tests and the Koutecky - Levich plot confirm the two electron pathway mechanism for the OER in PEM electrolysis for all our explored catalyst compositions. The 'n' value is closest to 2 for IrO_2:10 wt.% F doped electro-catalyst (**Figure 94**) corroborating the fact that it is the best composition amongst all the other F doped and undoped IrO_2 electro-catalyst. Increased F doping (above 10 wt.% F) leads to slight decrease in the 'n' value which is the number of electrons transferred during the OER. This is because the polarization resistance increases as observed in the impedance plots and reported in **Table 6**, impeding the electron transfer process in the electrochemical interface. This in turn also gives us lesser values of current density for the catalysts with higher F doping amounts as seen in the polarization curves (**Figure 86**). This further elucidates the high electrochemical activity and the close to ideal Tafel slope of the 10

wt.% F doped IrO_2, portending it to be a preferred OER electro-catalyst composition for PEM electrolyzer cells.

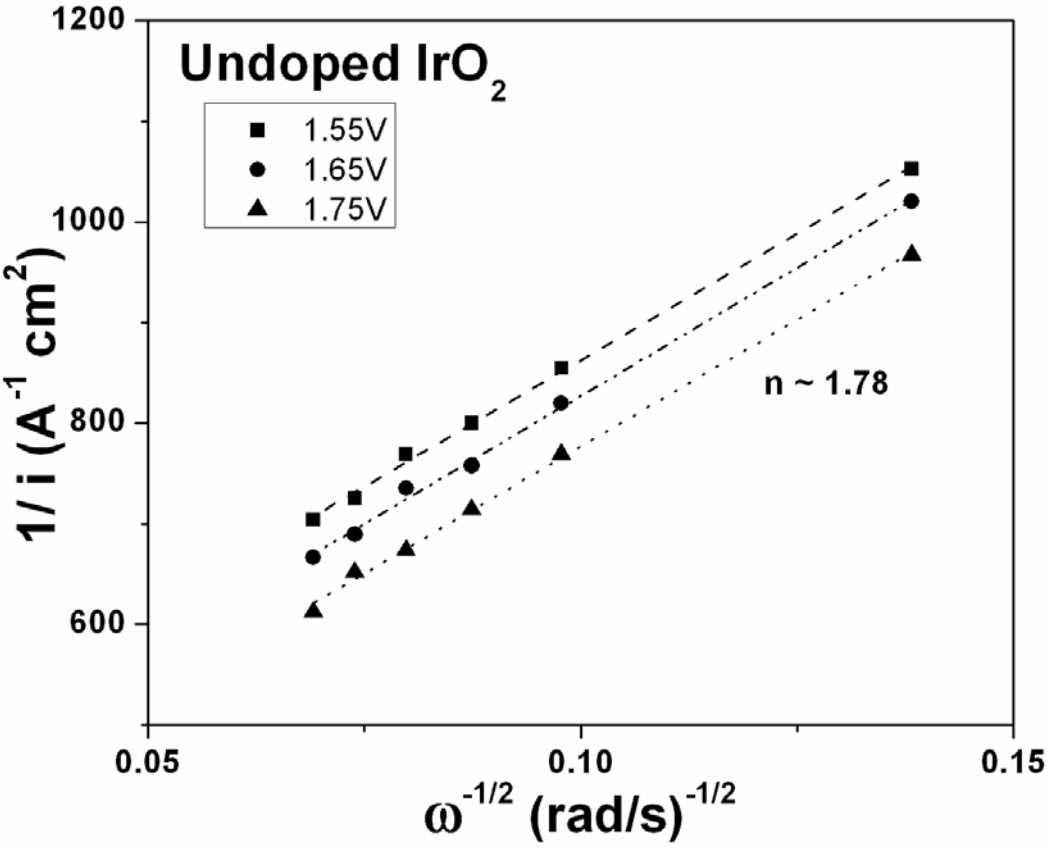

Figure 92. Koutecky - Levich plots in PEM based water electrolysis at 1.55 V, 1.65 V and 1.75 V (*vs.* NHE) in 1 N H_2SO_4 at 25°C for undoped IrO_2

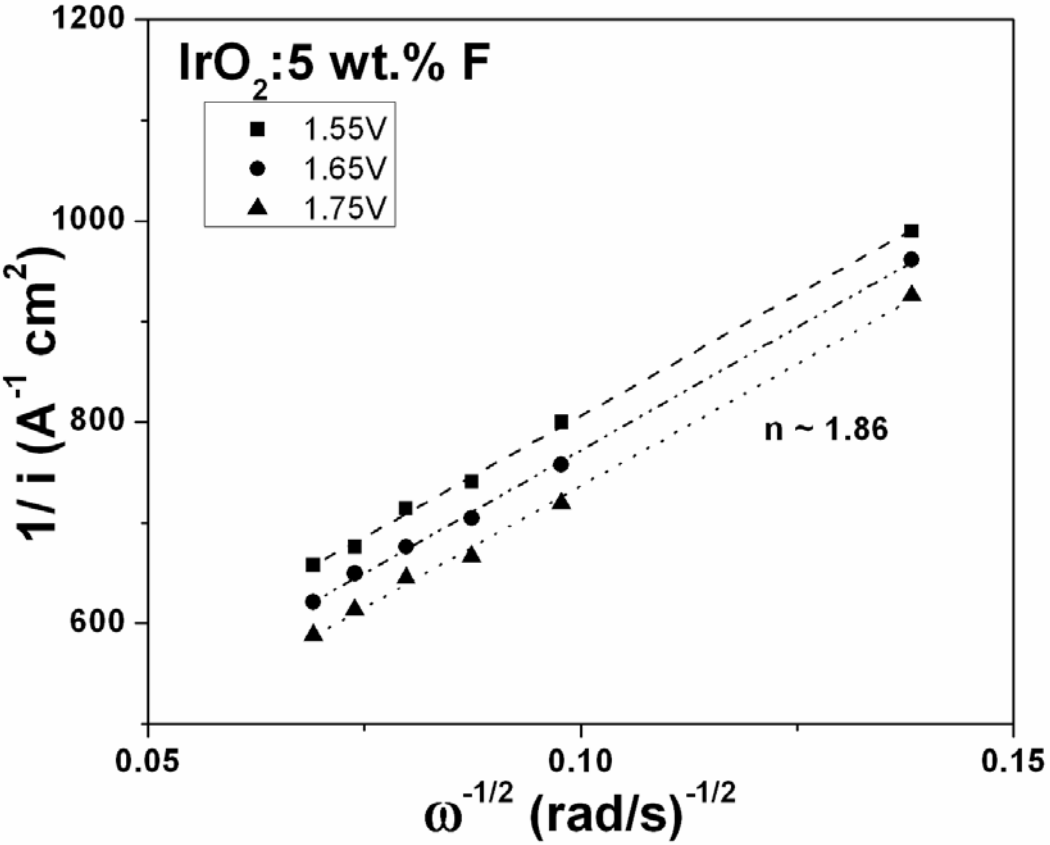

Figure 93. Koutecky - Levich plots in PEM based water electrolysis at 1.55 V, 1.65 V and 1.75 V (*vs.* NHE) in 1 N H_2SO_4 at 25°C for IrO_2:5 wt.% F

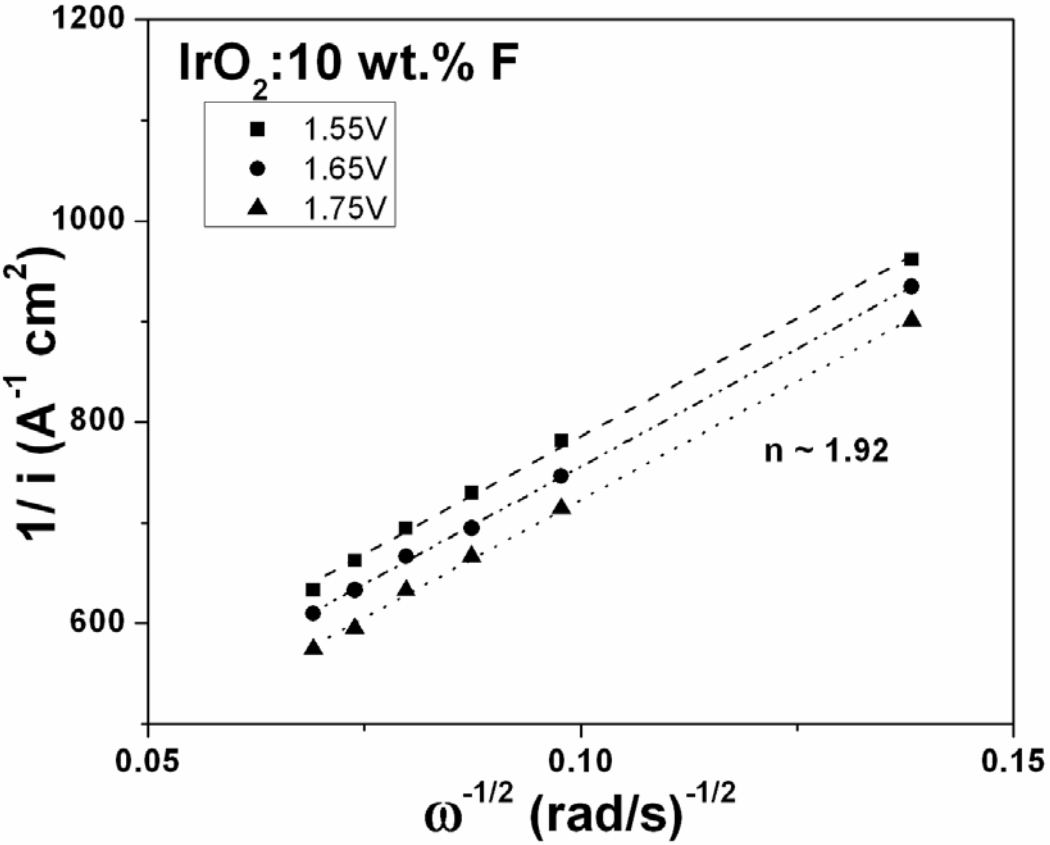

Figure 94. Koutecky - Levich plots in PEM based water electrolysis at 1.55 V, 1.65 V and 1.75 V (*vs.* NHE) in 1 N H_2SO_4 at 25°C for IrO_2:10 wt.% F

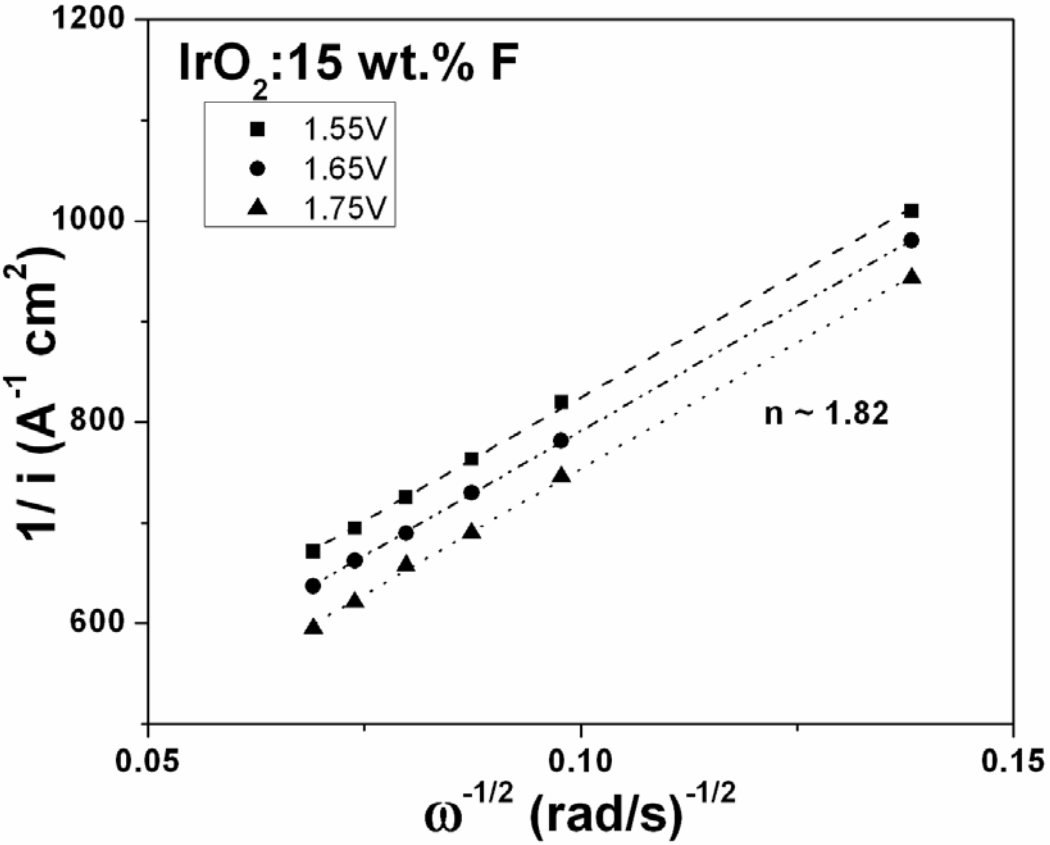

Figure 95. Koutecky - Levich plots in PEM based water electrolysis at 1.55 V, 1.65 V and 1.75 V (*vs.* NHE) in 1 N H_2SO_4 at 25°C for IrO_2:15 wt.% F

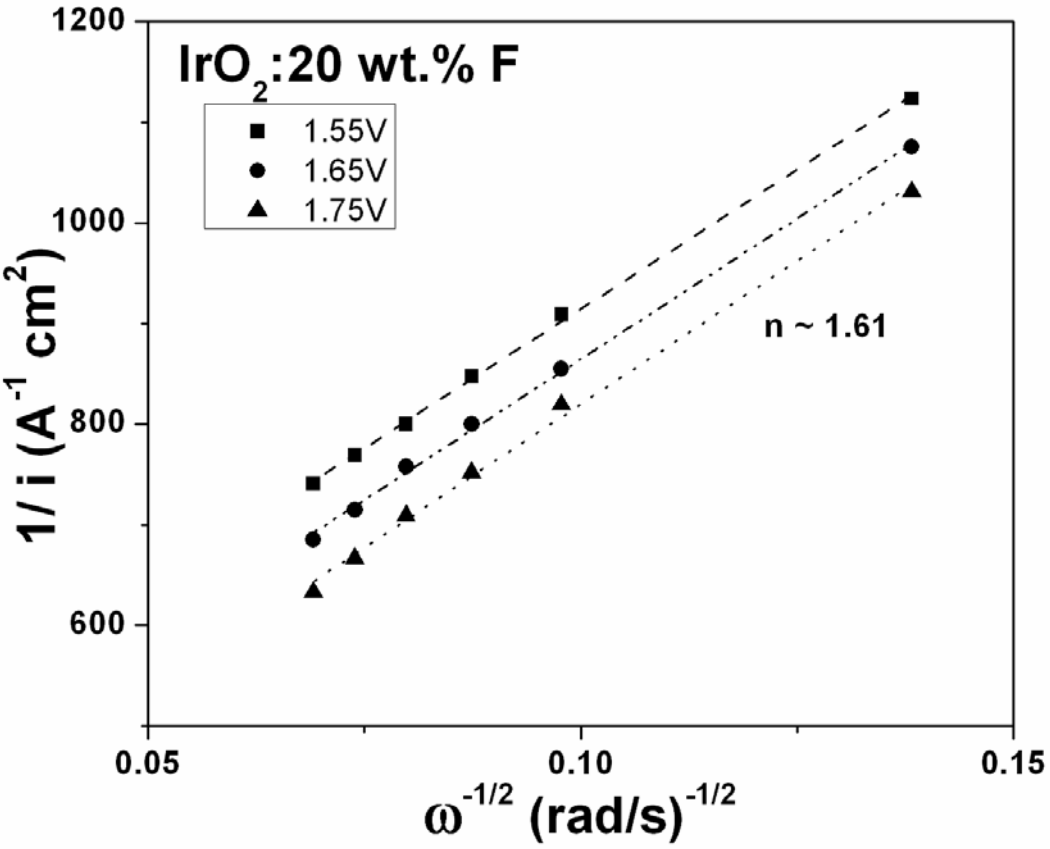

Figure 96. Koutecky - Levich plots in PEM based water electrolysis at 1.55 V, 1.65 V and 1.75 V (*vs.* NHE) in 1 N H_2SO_4 at 25°C for IrO_2:20 wt.% F

The influence of temperature on the OER was studied in order to calculate apparent activation energy from the Arrhenius relationship as explained previously in **Section 4.4.4**. The Arrhenius plots *i.e.* ln i *vs.* T^{-1} for IrO_2, IrO_2:5 wt.% F, IrO_2:10 wt.% F, IrO_2:15 wt.% F and IrO_2:20 wt.% F, are shown in **Figure 97**, **Figure 98**, **Figure 99**, **Figure 100**, and **Figure 101** respectively. The temperature was varied between 25 - 70°C and data points in these graphs have been plotted at three different potentials of 1.55 V, 1.65 V and 1.75 V (*vs.* NHE) as used before.

The slopes of these lines was averaged in order to calculate the E_a which is ~ 25.2 ± 1.5 kJ/mol for the IrO_2:F electro-catalysts. This E_a value is lesser and in the range and order of values reported for the OER by other researchers [97, 98, 104-107]. The E_a value for all the electrodes being similar suggests that the OER on all electrodes proceeds *via* the same reaction mechanism [97, 108]. The reaction mechanism has been previously reported by Nørskov *et al.* and in our earlier publication [53-55]. This four step reaction mechanism occurring during PEM based water electrolysis has been reported in **Section 2.2.2**.

Although there is no difference in the activation barrier owing to similar E_a values for all the synthesized powder catalysts, the inherent kinetics are most optimal for the IrO_2:10 wt.% F electro-catalyst possibly due to difference in the activity and number of catalytically active sites [108]. This has not only been confirmed from the polarization curves (**Figure 85** and **Figure 86**), but is also evident from the different 'n' values obtained from the Koutecky - Levich plots (**Table 7**). This is because of the difference in the anodic polarization and charge transfer properties as observed in the impedance and Tafel plots.

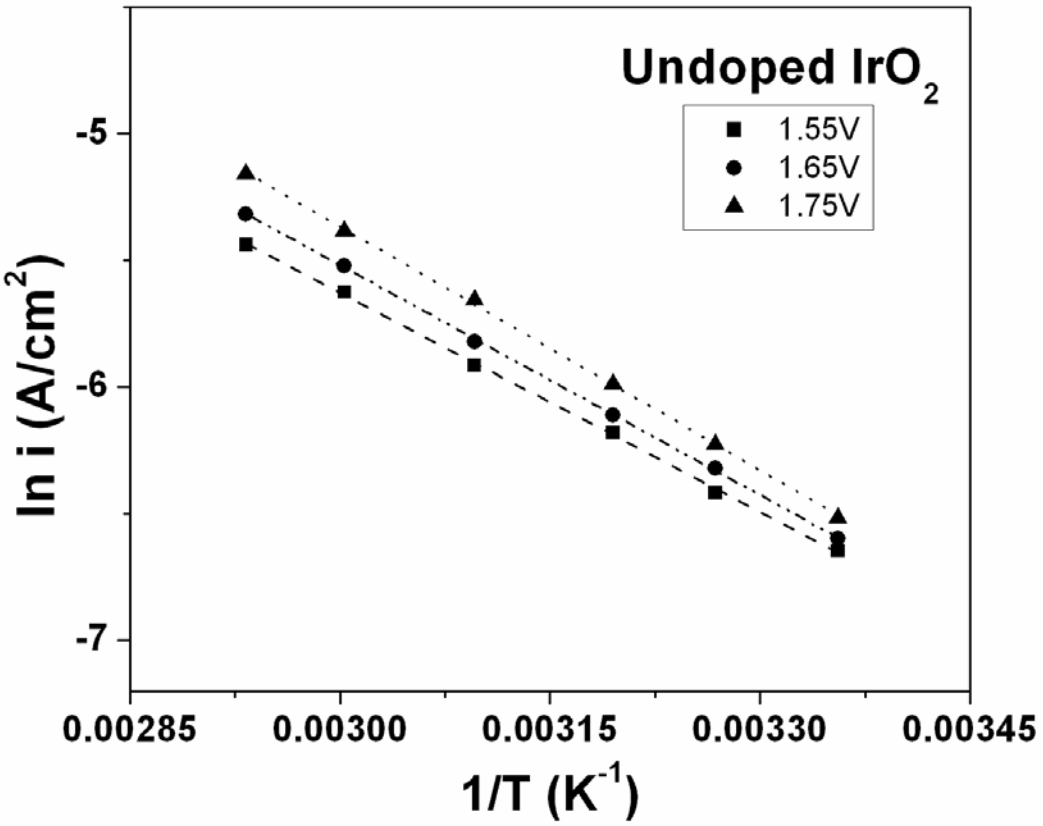

Figure 97. Arrhenius plots for undoped IrO_2 over a temperature range of 25°C to 70°C in 1 N H_2SO_4

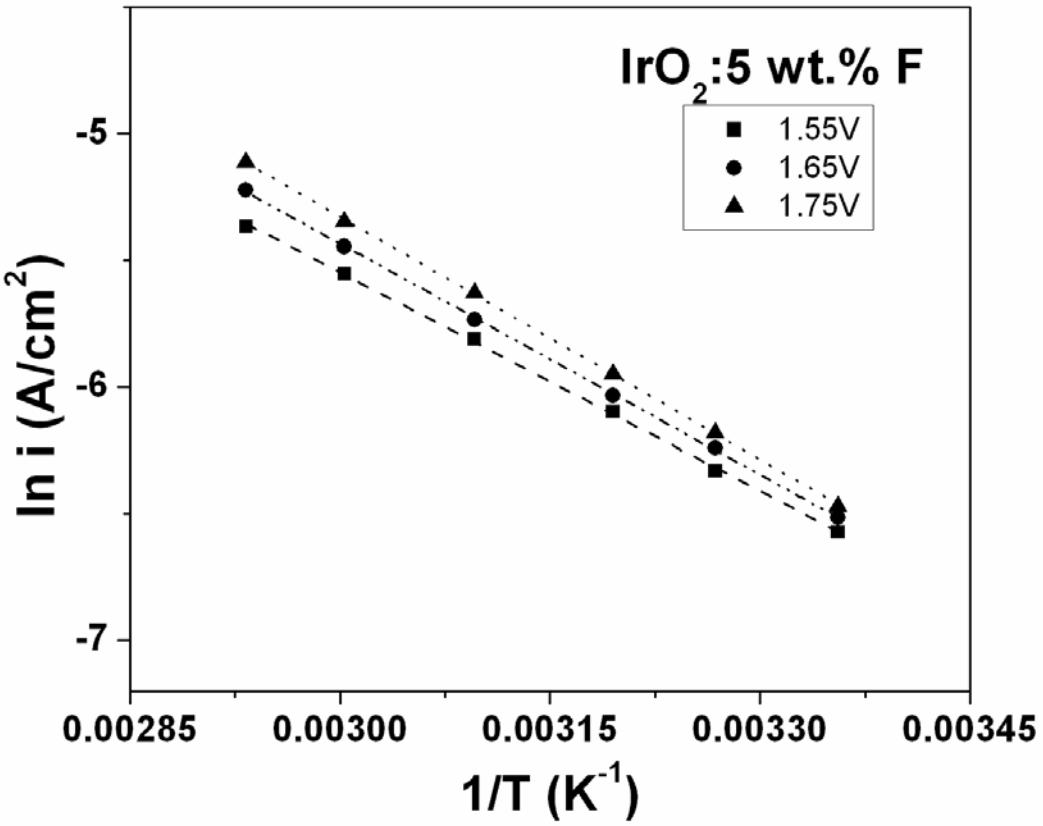

Figure 98. Arrhenius plots for IrO_2:5 wt.% F over a temperature range of 25°C to 70°C in 1 N H_2SO_4

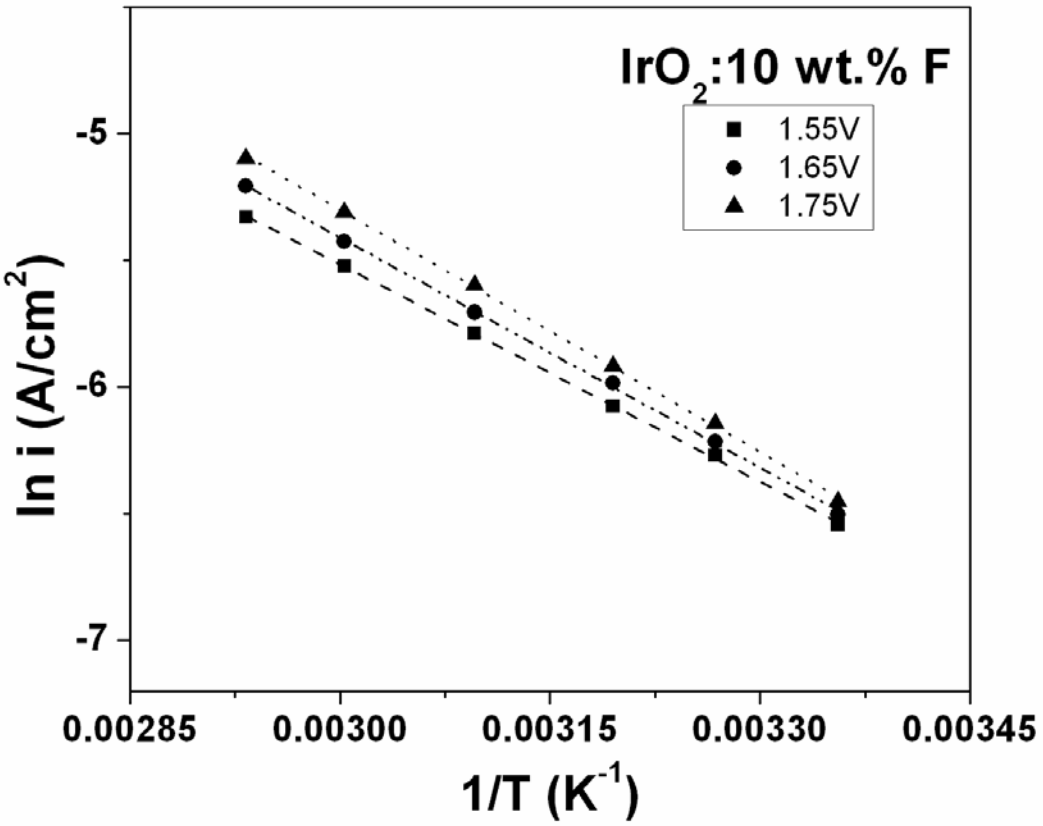

Figure 99. Arrhenius plots for IrO_2:10 wt.% F over a temperature range of 25°C to 70°C in 1 N H_2SO_4

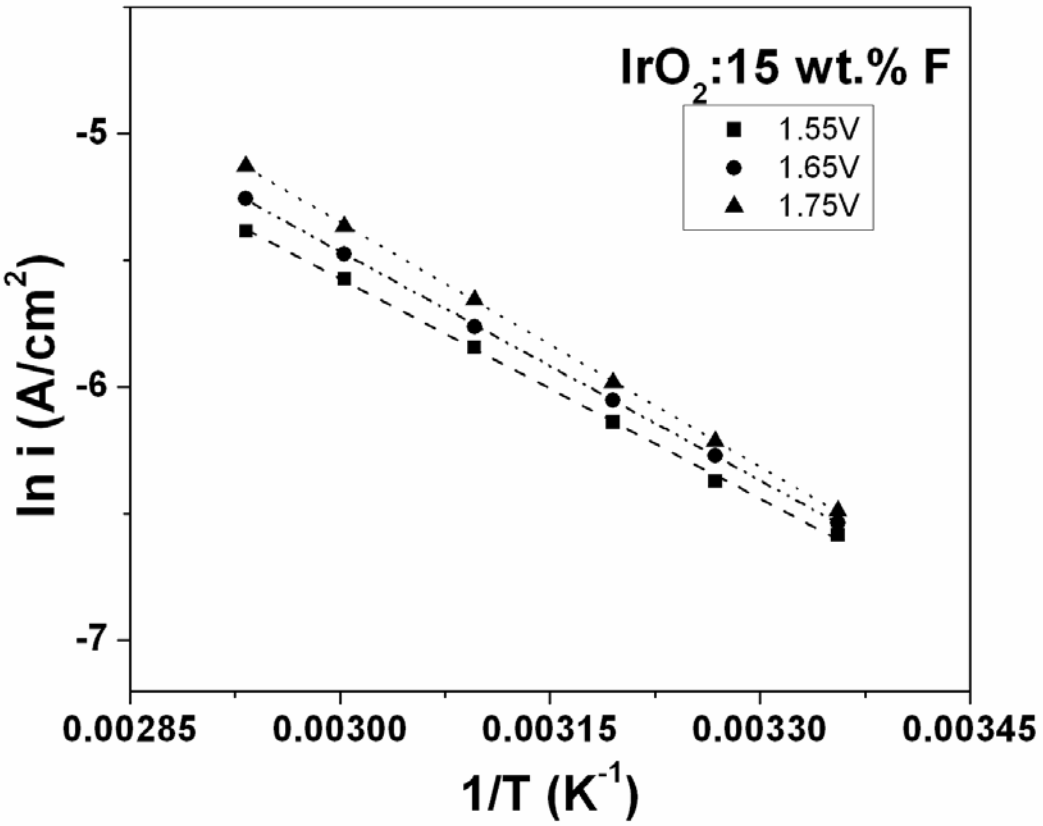

Figure 100. Arrhenius plots for IrO_2:15 wt.% F over a temperature range of 25°C to 70°C in 1 N H_2SO_4

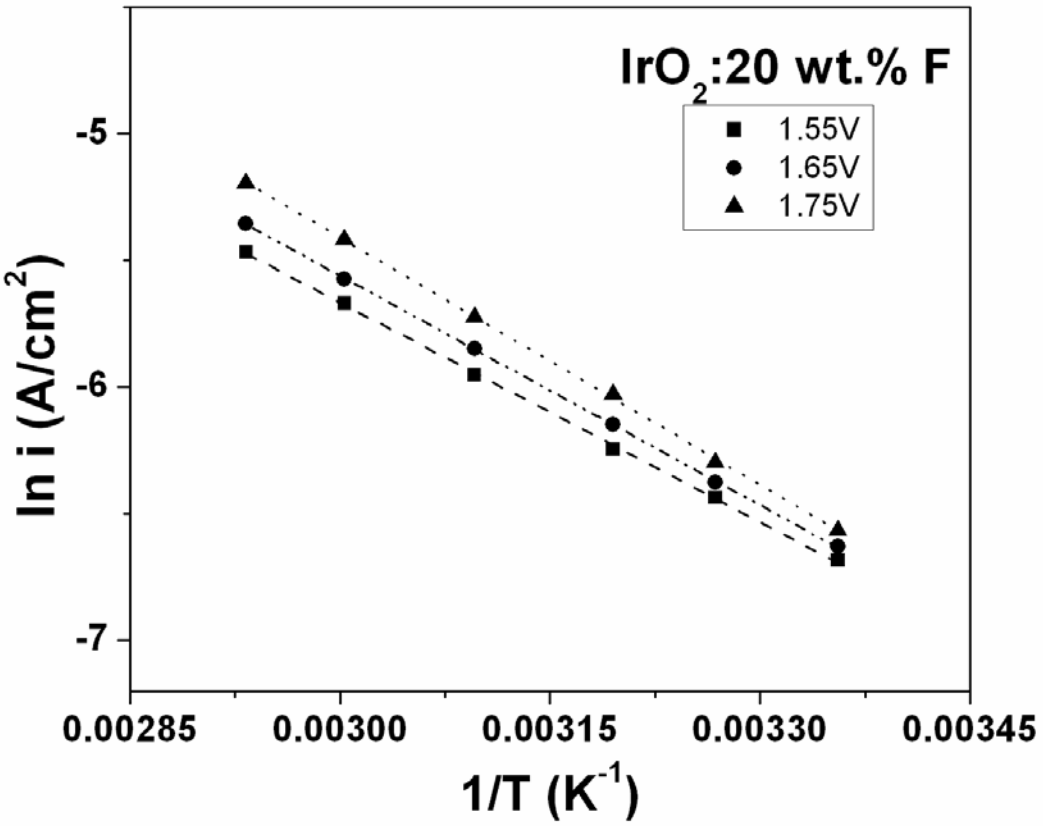

Figure 101. Arrhenius plots for IrO_2:20 wt.% F over a temperature range of 25°C to 70°C in 1 N H_2SO_4

The robustness and chemical stability of the synthesized electro-catalysts have been studied by chronoamperometry (CA) testing. **Figure 102** shows the CA curves for the IrO_2:F catalysts conducted at a constant voltage of ~ 1.65 V (*vs.* NHE) without iR correction for 12 hours. The IrO_2:10 wt.% F electrode shows higher current than the other electrodes since it inherently has higher catalytic activity. A steady decay of current may arise due to the dissolution of the catalyst material along the edges of the support [24, 30, 58], or due to

continuous exhaustion of the electrolyte/fuel (H_2SO_4) owing to the high electrochemical activity of the electro-catalysts [34, 59, 120]. It is evident in **Figure 102** by the slope of the different curves that the higher fluorine doped catalysts *i.e.* IrO_2 doped with 15 and 20 wt.% F degrade slightly faster than the undoped, 5 and 10 wt.% F doped IrO_2. The best powder electro-catalyst material reported herein (IrO_2:10 wt.% F), shows excellent durability and current retention, albeit exhibiting very high electrochemical activity. On an overall basis, the CA response shows an acceptable stability with respect to the drop in current observed and reported widely by researchers in other publications [57, 120, 121]. Inductively coupled plasma optical emission spectroscopy (ICP-OES) studies were conducted on the electrolyte media after the conclusion of the CA test (*i.e.* after 12 hours). No Ir was found to have leached out from any of the F doped or undoped IrO_2 catalysts, confirming that the drop in current is mainly because of the exhaustion of the fuel due to the high catalytic activity of the nanostructured powder electro-catalysts. The stability results complement and strengthen our earlier claims and findings; suggesting that IrO_2:10 wt.% F electro-catalyst is an optimized composition for use as an OER anode catalyst in PEM based water electrolysis.

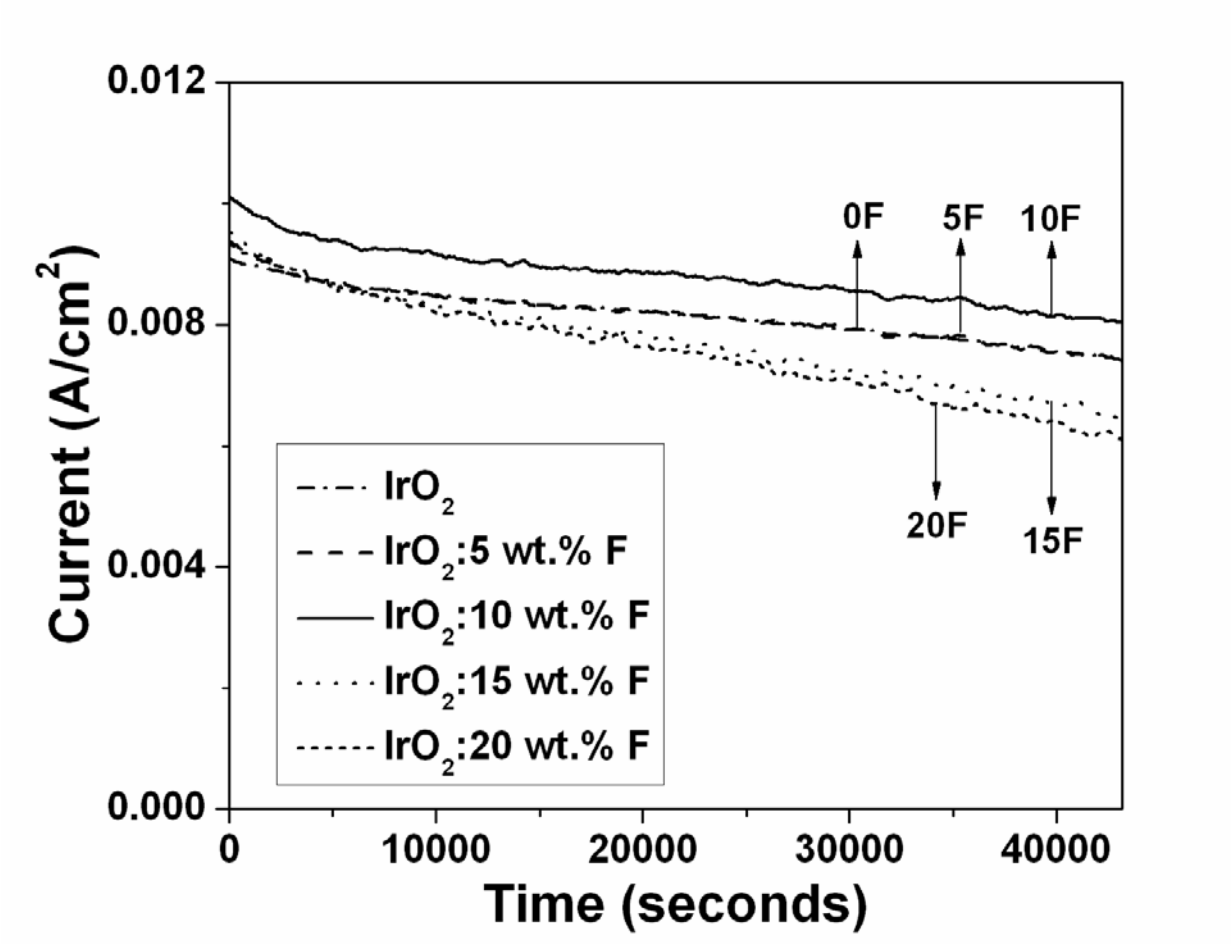

Figure 102. The variation of current *vs.* time for the IrO_2:F electrodes in 1 N H_2SO_4 under a constant potential of ~ 1.65 V at 40°C

After the conclusion of the CA test, the undoped and 10 wt.% F doped IrO_2 electrodes were subject to polarization testing as seen in **Figure 103** in order to determine the activity of the electrodes after long term structural stability tests. The Tafel plots from these polarization curves (post CA measurement) after iR correction are shown in **Figure 104** and **Figure 105**. A Tafel slope of ~ 112 mV/decade and ~ 90 mV/decade was obtained for undoped IrO_2 and IrO_2:10 wt.% F, respectively. This is slightly higher (~ 93 mV/decade for IrO_2 and ~ 64 mV/decade for IrO_2:10

wt.% F) but still close and comparable to the values obtained from the polarization tests conducted before CA (**Figure 87** and **Figure 89**). This test further demonstrates the robustness of the electro-catalysts.

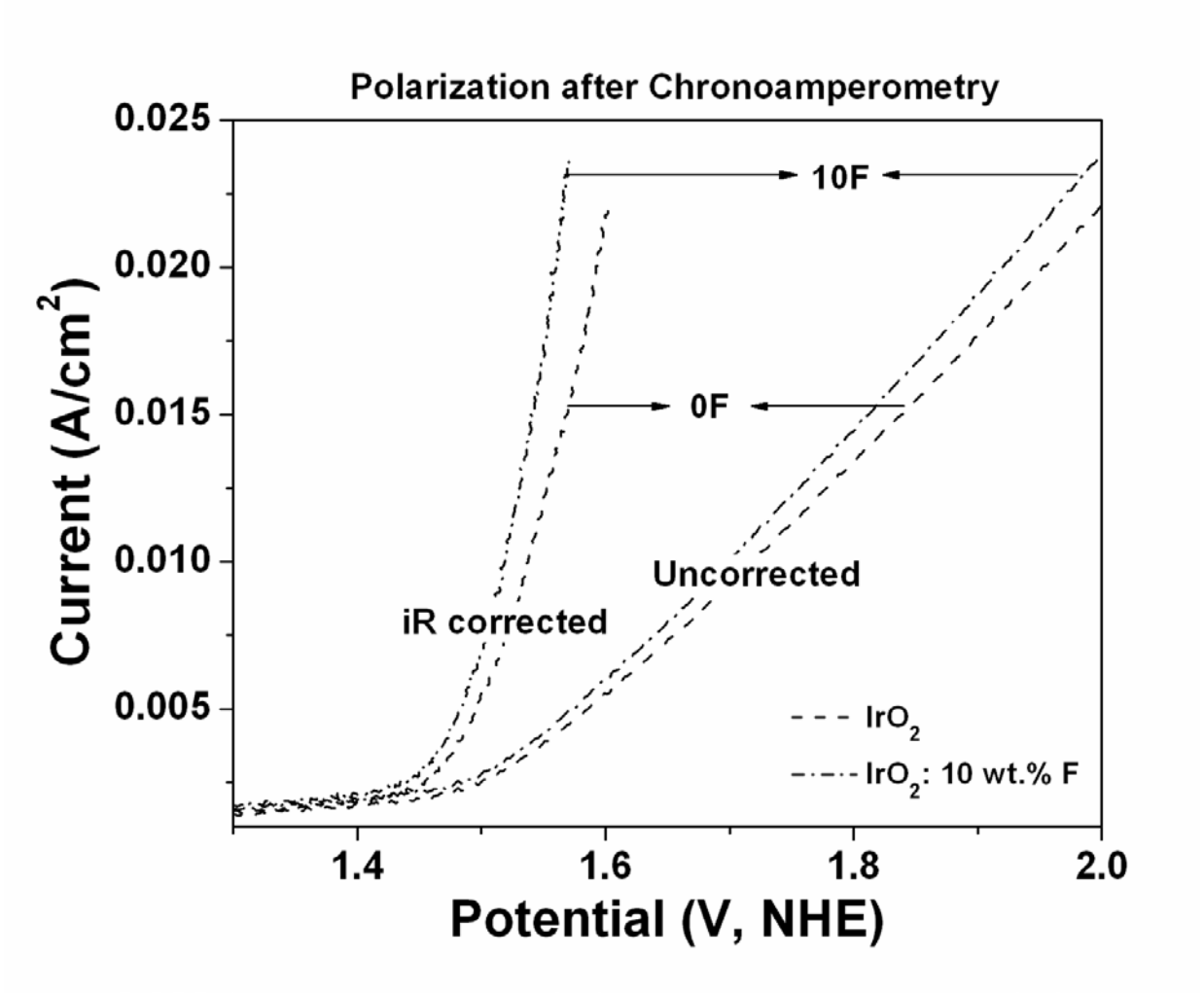

Figure 103. Polarization curve of undoped and 10 wt.% F doped IrO_2 after the CA test

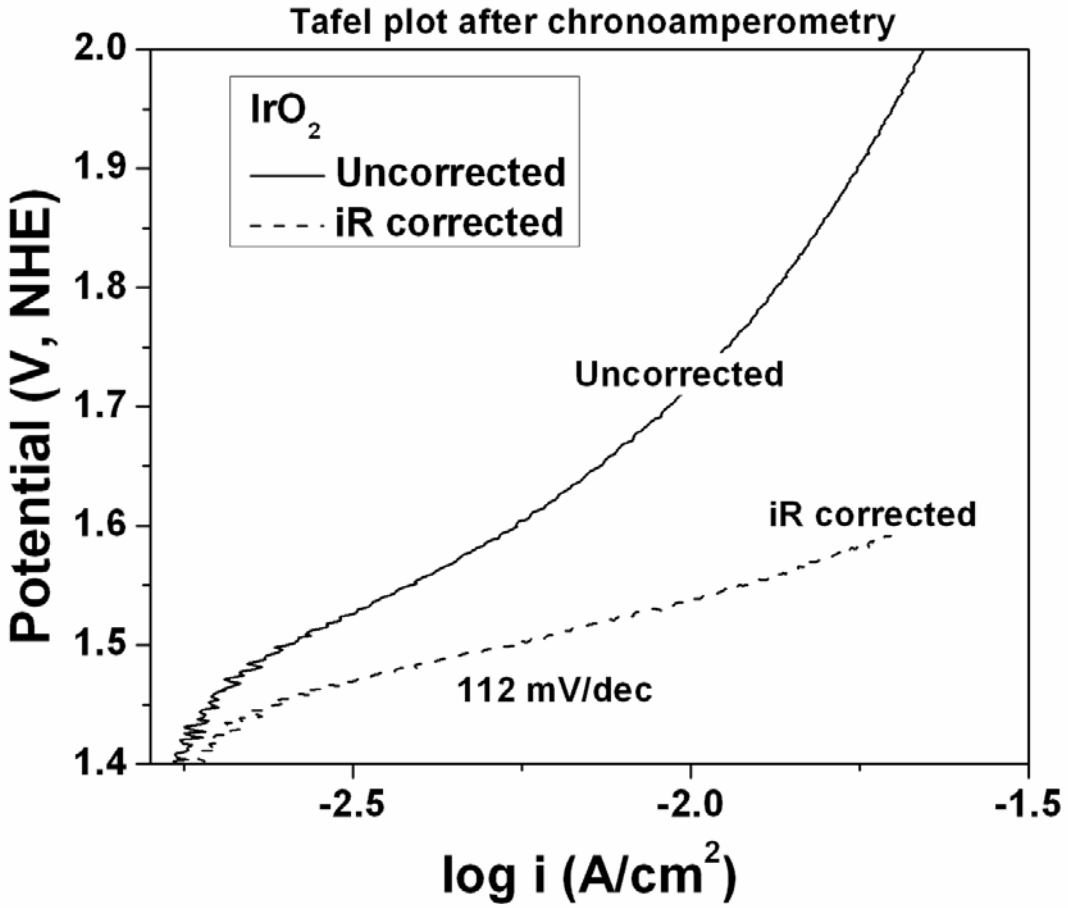

Figure 104. The Tafel plot of undoped IrO_2 powder after the CA test

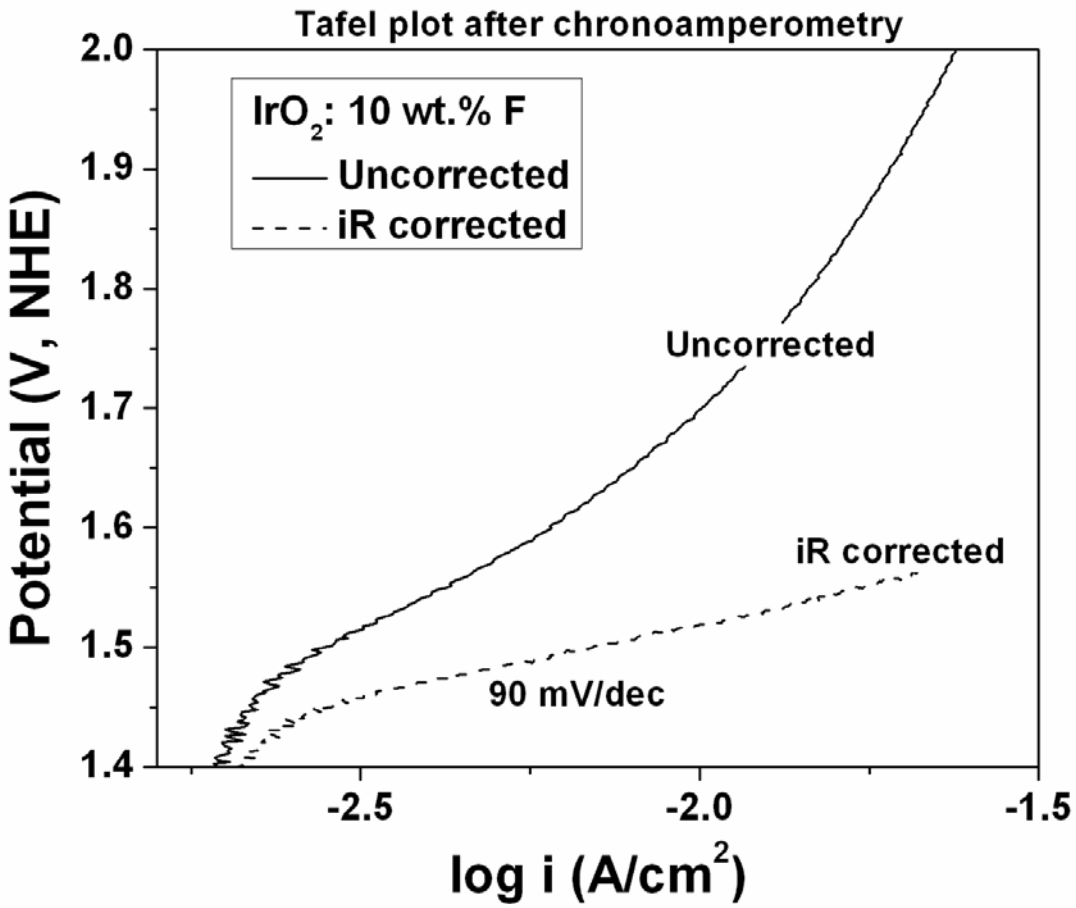

Figure 105. The Tafel plot of IrO_2:10 wt.% F powder after the CA test

Finally, the best electro-catalyst composition of IrO_2:10 wt.% F was tested at Proton OnSite in a single full cell set-up for PEM based water electrolysis. These results were compared with undoped pure IrO_2 which was also tested in the same conditions. The polarization curve, shown in **Figure 106**, was obtained by ramping up and down the current at 1 minute intervals until the forward and reverse scans overlaid each other. It is seen that the 10 wt.% F doped IrO_2 electro-catalyst exhibits much superior electro-catalytic activity than its undoped counterpart. The current density at ~ 2 V, a standard assessment voltage for single full PEM electrolyzer tests,

is ~ 1.1 A/cm^2 and ~ 0.5A/cm^2 for IrO_2:10 wt.% F and IrO_2, respectively. This implies an approximately 2.2 times rise in the current for the F doped electro-catalyst with respect to pure IrO_2. This is in good agreement with the polarization curves (**Figure 85**) and the increase in current observed. The polarization curves in the half cell and full cell set-up, along with the electrochemical impedance spectra, Tafel plots and the RDE graphs confirm that 10 wt.% F doping enhances the electrochemical activity of IrO_2 to a very great extent. A higher loading of pure IrO_2 (~ 3.4 mg) was done for the full cell PEM electrolyzer test at at 50°C and 80°C, and the results have been shown in **Figure 107**. The polarization curves show much more electrochemical activity as expected. The current density at ~ 2 V is ~ 0.8 A/cm^2 and ~ 1.75 A/cm^2, for the tests at 50°C and 80°C, respectively.

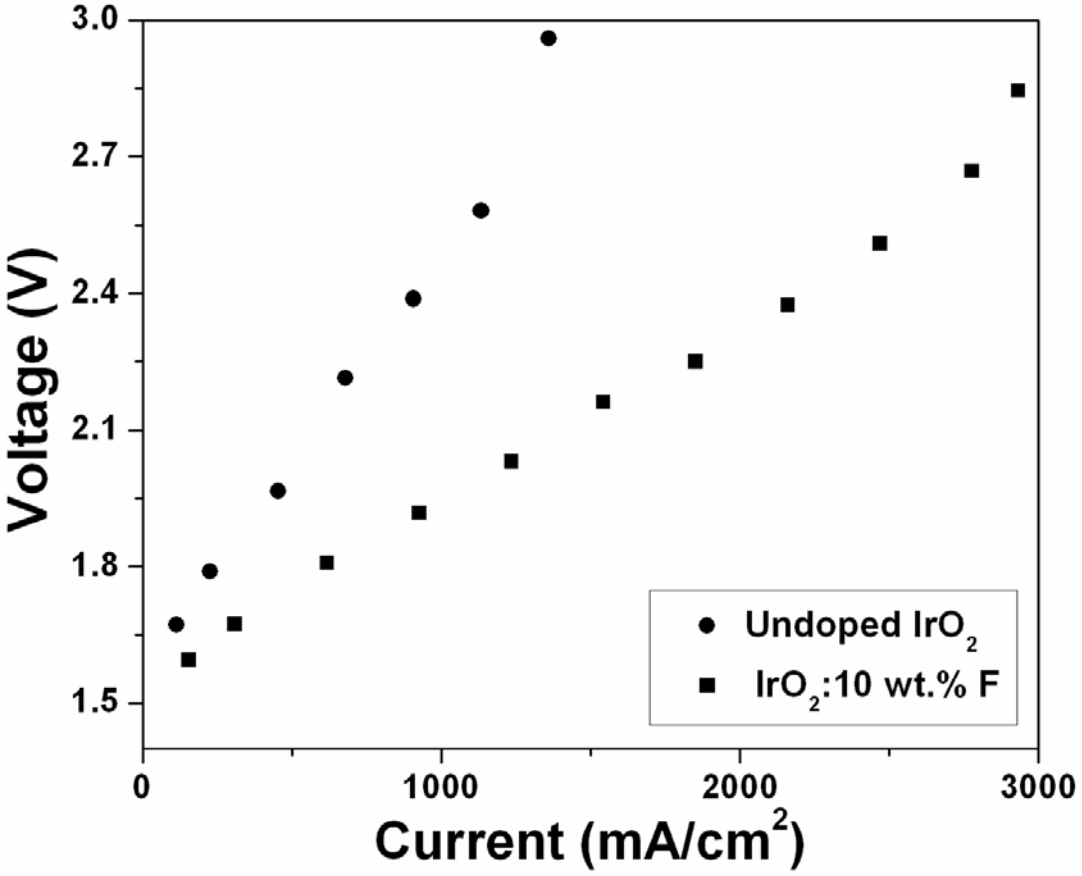

Figure 106. Polarization curve obtained in a single full cell PEM electrolyzer test for undoped IrO_2 and IrO_2:10 wt.% F powders at 50°C

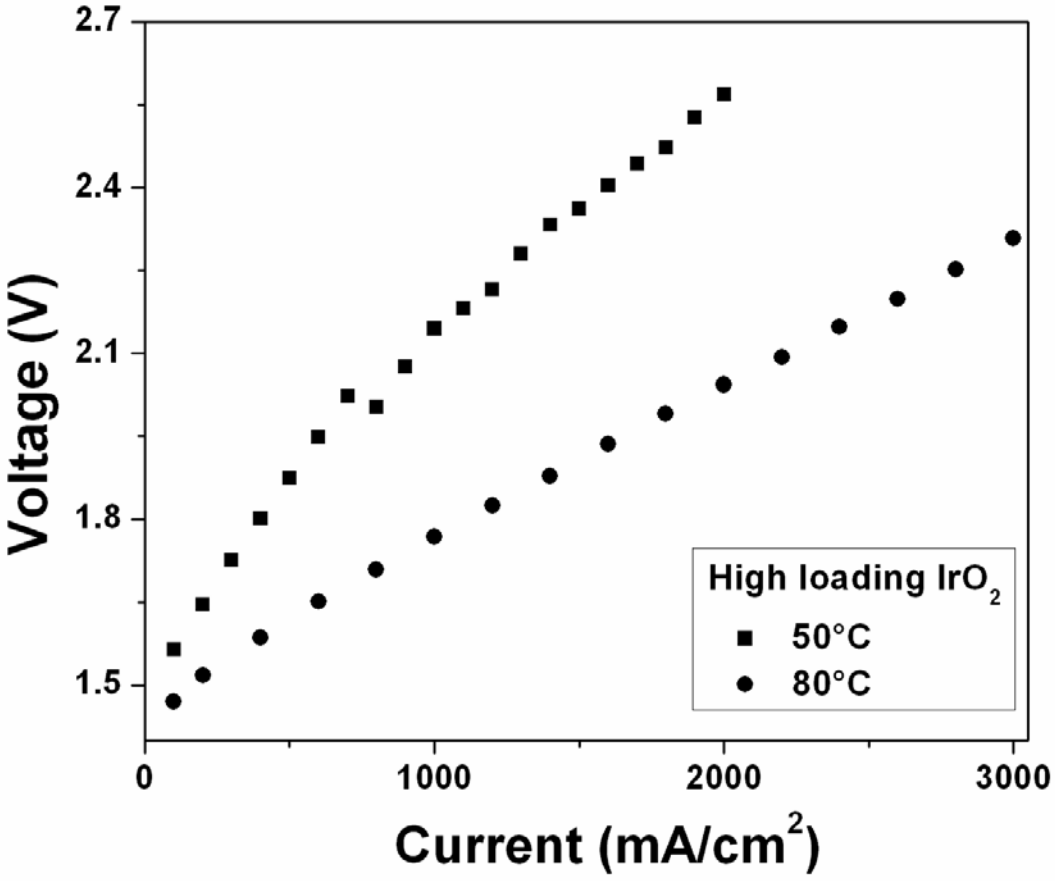

Figure 107. Polarization curve obtained in a single full cell PEM electrolyzer test for undoped IrO_2 at 50°C and 80°C

5.2.2 Binary F doped (Ir,Sn)O_2

5.2.2.1 Structural Analysis

Figure 108 shows the XRD pattern of the as-prepared SnO_2:F powder after oven drying at 50°C. The XRD pattern showed broad peaks corresponding to tin oxide which represents the

amorphous nature of the powder. We observe all crystalline phases of SnO_2 with possibly nanocrystalline peaks only after the powder is heat treated to 300°C. The specific surface area (SSA), measured by the BET technique, of 10 wt.% F doped SnO_2 powder is ~ 240 m^2/g while undoped SnO_2 has a SSA of ~ 160 m^2/g. **Figure 109** shows the XRD pattern of the electro-catalysts developed from mixed SnO_2:F and $IrCl_4$ solutions and heat treated to 400°C in air. They exhibit nanocrystalline peaks associated with single phase rutile type tetragonal IrO_2. The XRD pattern confirms the formation of a single phase homogeneous IrO_2 and SnO_2:F solid solution [$(Ir,Sn)O_2$:F], with no undesirable phase separation and/or mixed phase formation which is critical for better catalytic activity. The effective crystallite size of $(Ir,Sn)O_2$ and $(Ir,Sn)O_2$:F, calculated using the Scherrer formula from the integral breadth of the Lorentzian contribution determined from peak profile analysis using single line approximation method after eliminating the instrumental broadening and lattice strain contribution [88], is ~ 6.1 nm and ~ 5.5 nm respectively. $(Ir_{0.3}Sn_{0.7})O_2$ and $(Ir_{0.3}Sn_{0.7})O_2$:10wt.% F showed a SSA of ~ 47 m^2/g and ~ 56 m^2/g respectively as measured by the BET technique. The increase in surface area for the $(Ir,Sn)O_2$:F might be due to decrease in crystallite size. The TGA-DTA analysis of $(Ir_{0.3}Sn_{0.7})O_2$:10F and $(Ir_{0.3}Sn_{0.7})O_2$ carried out in air up to 700°C is shown in **Figure 110**. The undoped $(Ir,Sn)O_2$ shows no weight loss whereas its doped counterpart shows ~ 7 % weight loss. The weight loss thus would nearly correspond to the final amount of F (which is the volatile species) present in the $(Ir_{0.3}Sn_{0.7})O_2$:10 wt.% F electro-catalyst.

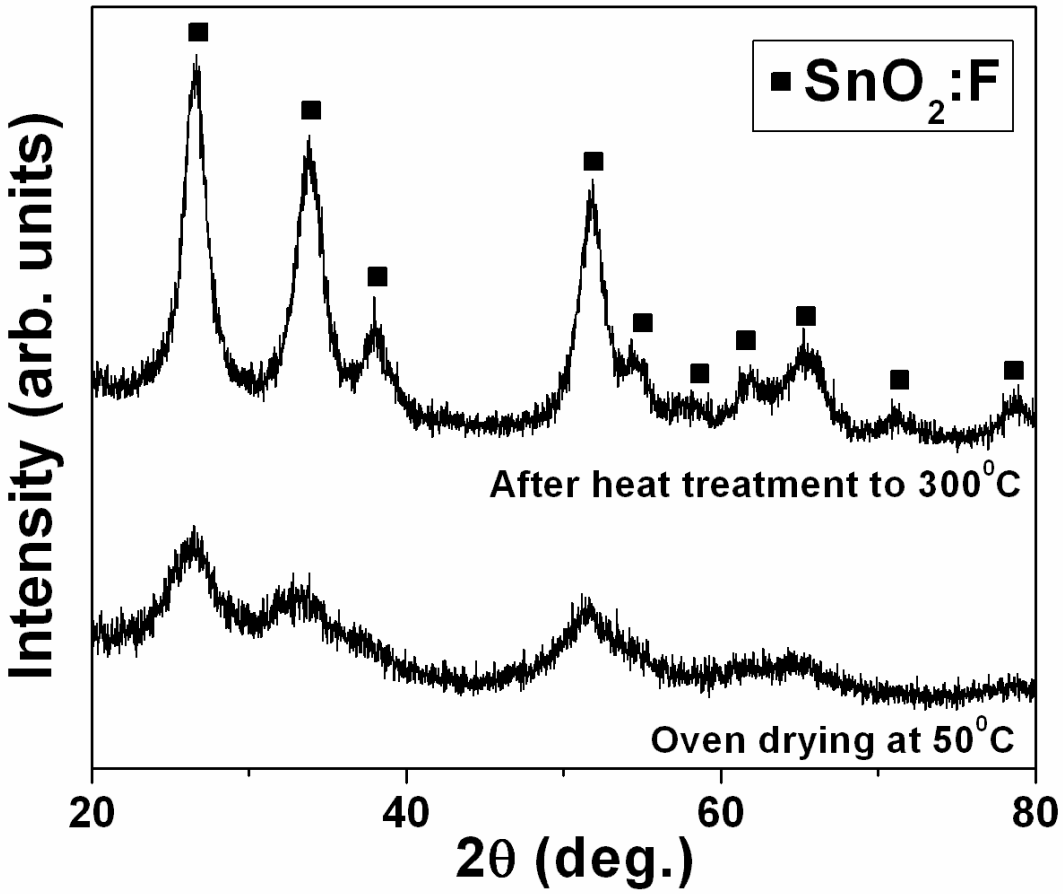

Figure 108. XRD pattern of as prepared SnO_2:F after drying in the oven at 50°C and subsequent heat treatment at 300°C

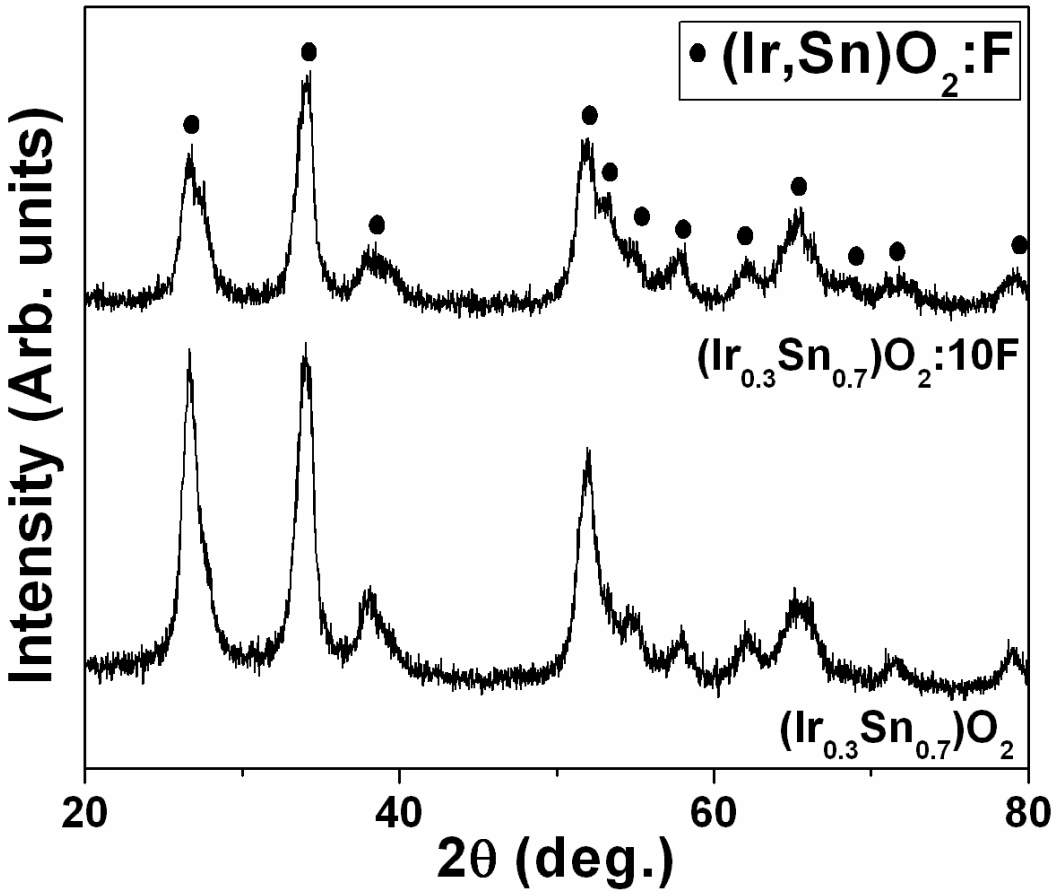

Figure 109. XRD pattern of undoped and F doped $(Ir,Sn)O_2$ after heat treatment to 400°C

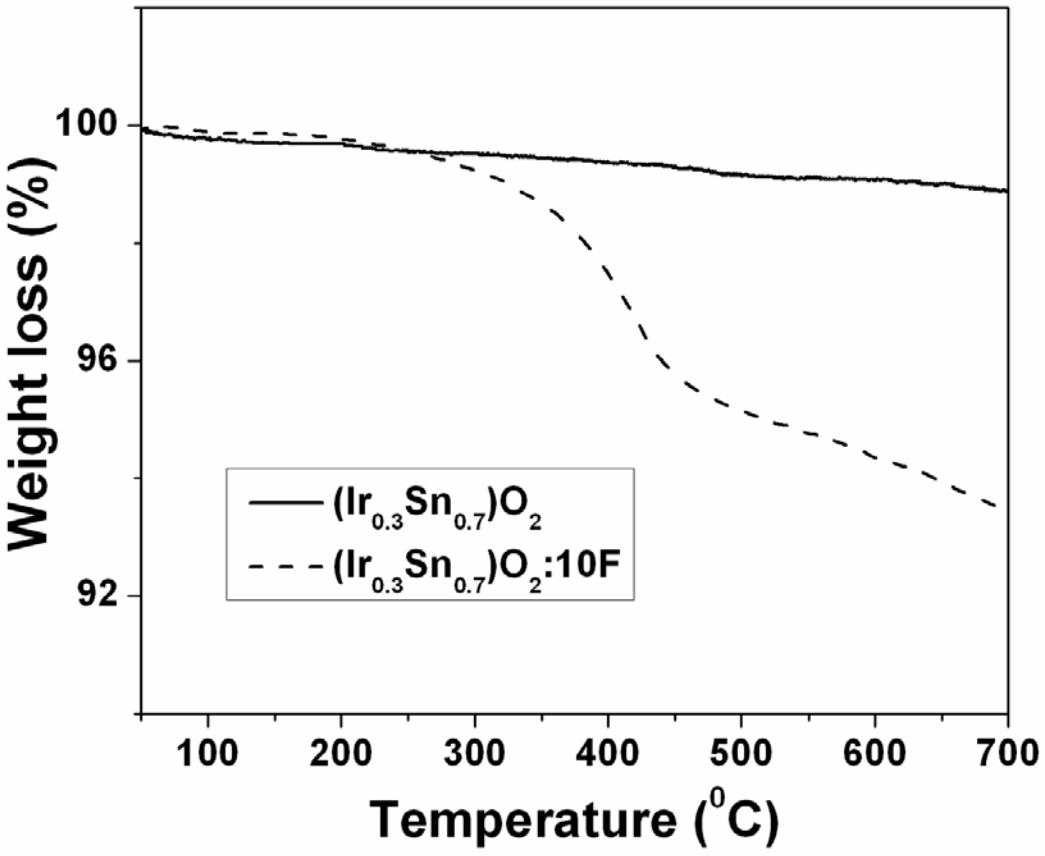

Figure 110. The TGA-DTA traces in air of $(Ir_{0.3}Sn_{0.7})O_2$ and $(Ir_{0.3}Sn_{0.7})O_2$:10 wt.% F showing weight loss with respect to temperature

The presence of elemental Ir and Sn in the (Ir,Sn)O_2:F powder has been confirmed using EDX attached to the SEM. **Figure 111** shows the elemental x-ray mapping *i.e.* the distribution of Ir, Sn, O and F in the powder. Elemental x-ray maps confirm that all the elements *viz.* Ir, Sn, O and F are homogeneously distributed within the (Ir,Sn)O_2:F particles without segregation on any specific site. Quantitative elemental composition analysis of the powders obtained by EDX further shows that the measured elemental compositions of Ir and Sn are close to the nominal

composition. The bright field TEM image of the $(Ir_{0.3}Sn_{0.7})O_2$:10 wt.% F powder shown in **Figure 112** reveals that the electro-catalyst size is in the range of ~ 5 – 10 nm nanometer.

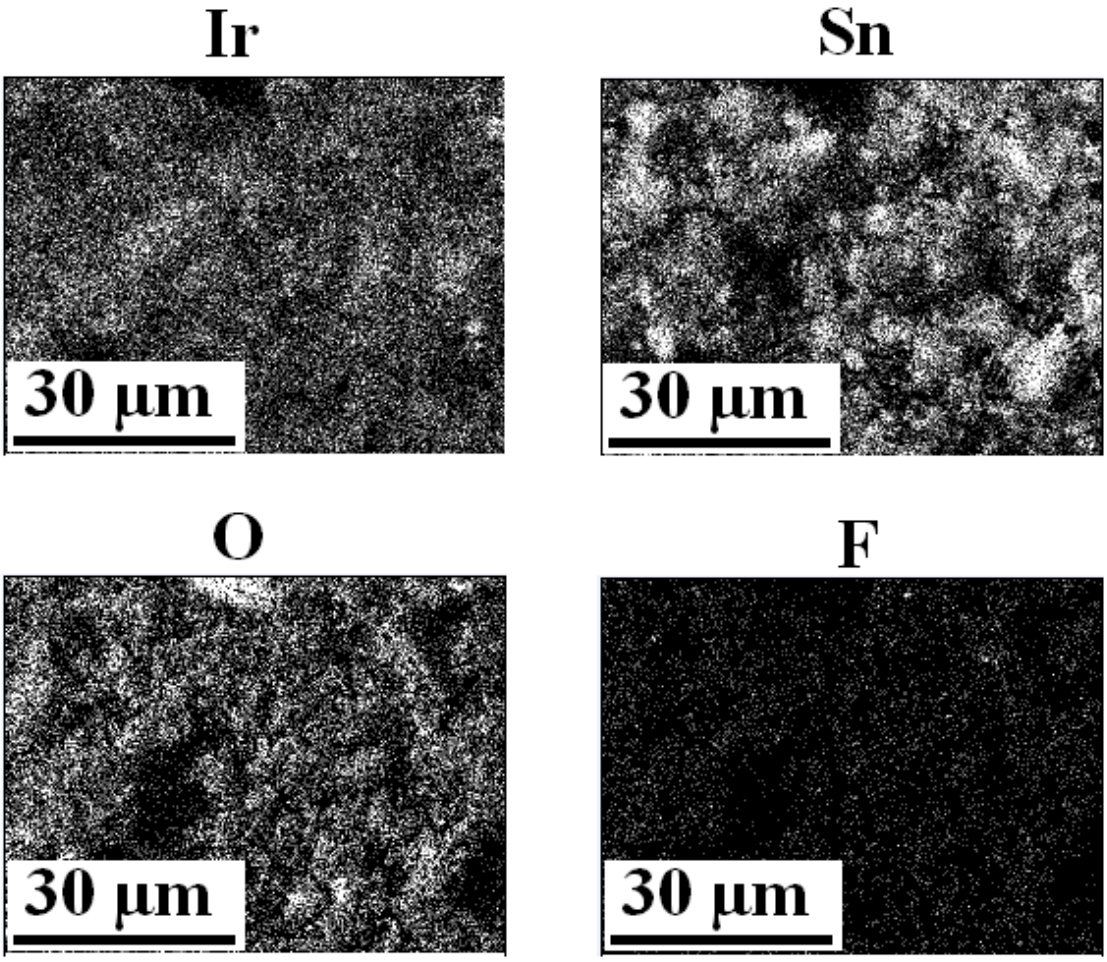

Figure 111. The elemental x-ray mapping of Ir, Sn, O and F in $(Ir_{0.3}Sn_{0.7})O_2$:10 wt.% F

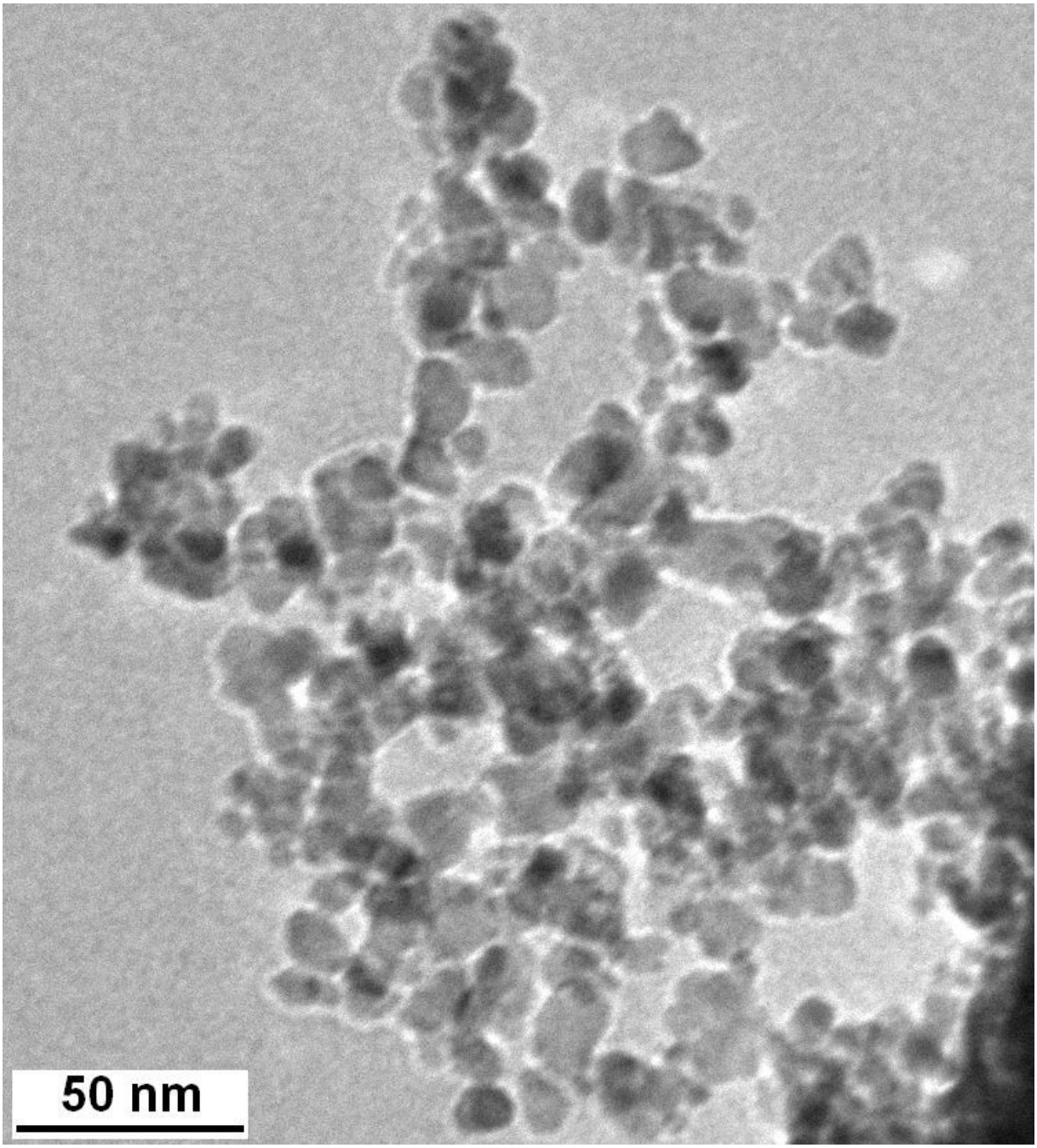

Figure 112. The bright field TEM image $(Ir_{0.3}Sn_{0.7})O_2$:10 wt.% F showing fine particles in the nanometer range

XPS has been carried out for $(Ir_{0.3}Sn_{0.7})O_2$ and $(Ir_{0.3}Sn_{0.7})O_2$:10F in order to determine the valence state of the elements. The XPS spectra of Ir, Sn and O1s are shown in **Figure 113**, **Figure 114** and **Figure 115**, respectively. The XPS spectra of Ir in $(Ir,Sn)O_2$ shows the presence of Ir $4f_{5/2}$ and Ir $4f_{7/2}$ doublet of binding energy ~ 61.6 eV and ~ 64.5 eV respectively, with the O1s peak being centered at ~ 530.7 eV. These values are associated with that of bulk IrO_2. The XPS spectra of Sn in $(Ir_{0.3}Sn_{0.7})O_2$ shows the Sn $3d_{5/2}$ and Sn $3d_{3/2}$ doublet with a binding energy of ~ 486.9 eV and ~ 495.3 eV respectively, which is consistent with the SnO_2. It is known that XPS is not adequate in determining the F content in F doped SnO_2. However, the binding energy of Ir 4f, Sn 3d and O1s core level increases by ~ 0.4 - 0.6 eV for $(Ir,Sn)O_2$:10F. This clearly indicates that there is stronger binding due to the higher electronegative F present in the lattice. Although the exact amount of fluorine could not be ascertained by XPS [57, 122], a weight loss of ~ 7 wt.% as seen in the TGA-DTA (**Figure 110**) confirms the presence of F in the electro-catalyst. The incorporation of F has a positive impact on the electrochemical activity of $(Ir,Sn)O_2$:F which is described later.

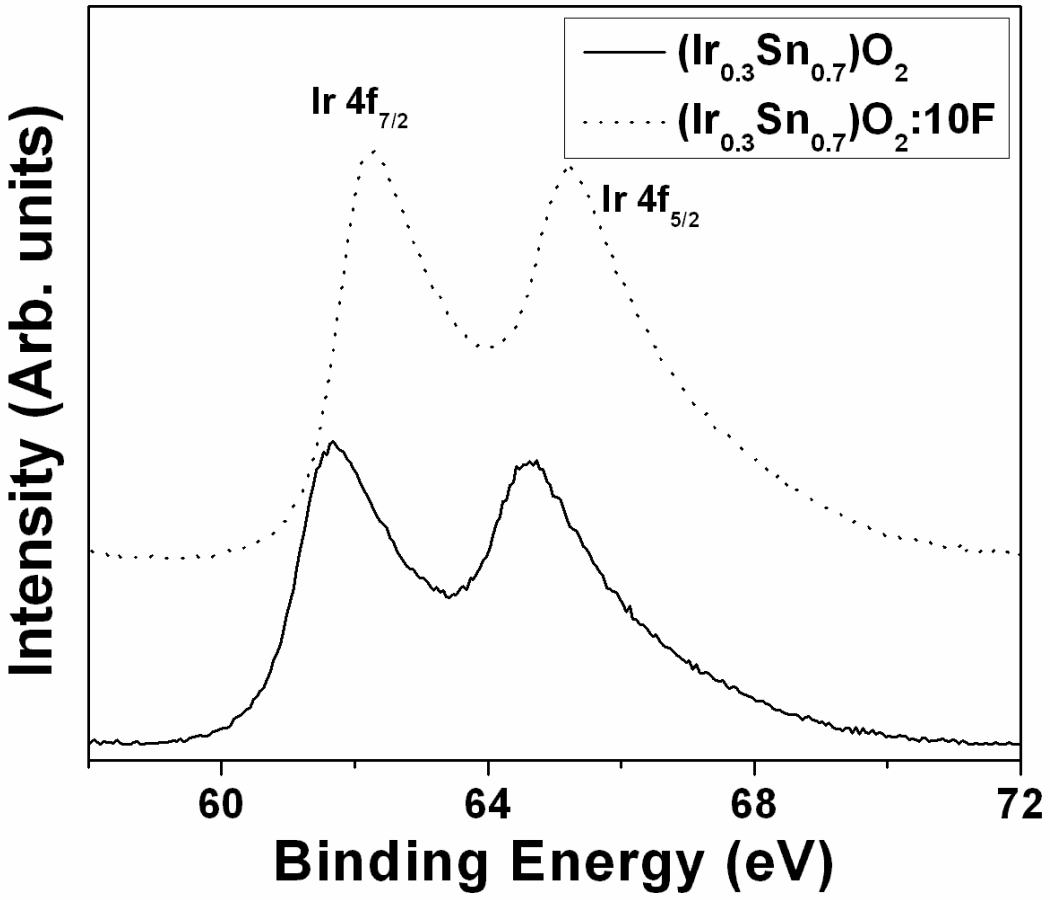

Figure 113. The XPS spectra of Ir $4f_{7/2}$ and $4f_{5/2}$ doublet of $(Ir,Sn)O_2$ and $(Ir,Sn)O_2$:F

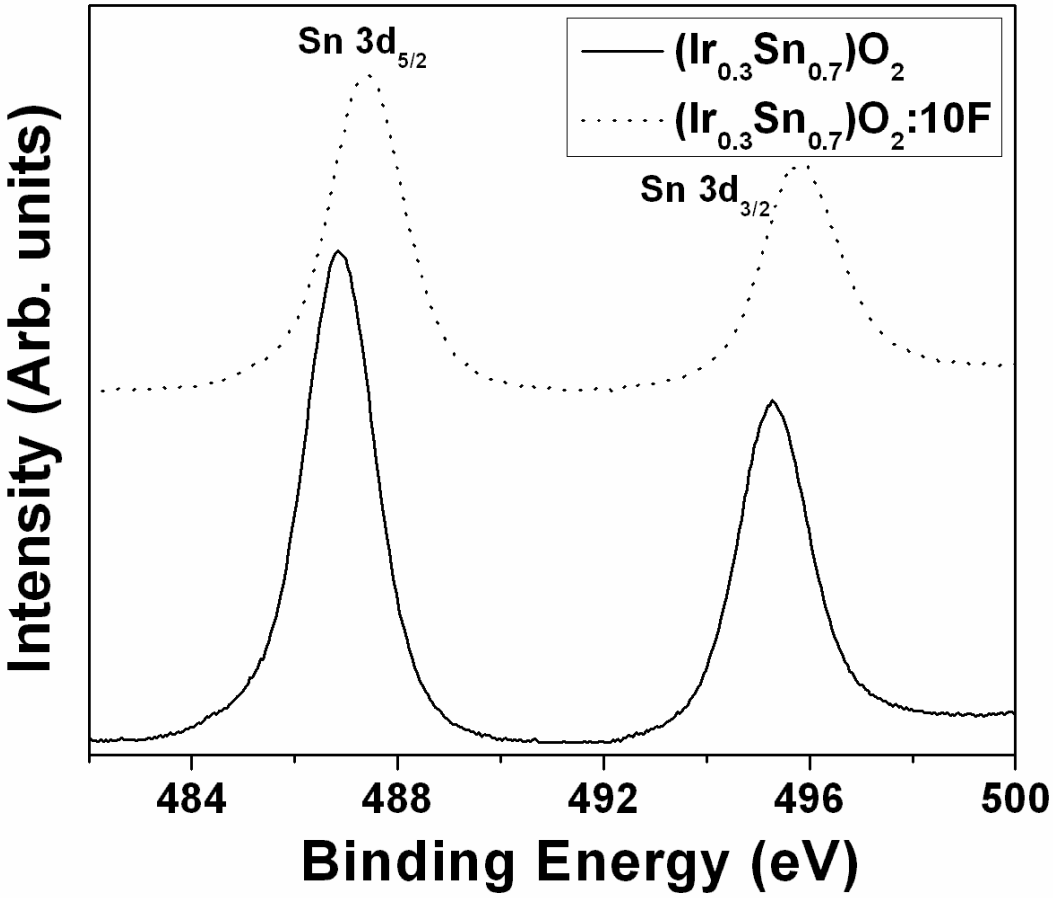

Figure 114. The XPS spectra of Sn $3d_{5/2}$ and Sn $3d_{3/2}$ doublet of (Ir,Sn)O_2 and (Ir,Sn)O_2:F

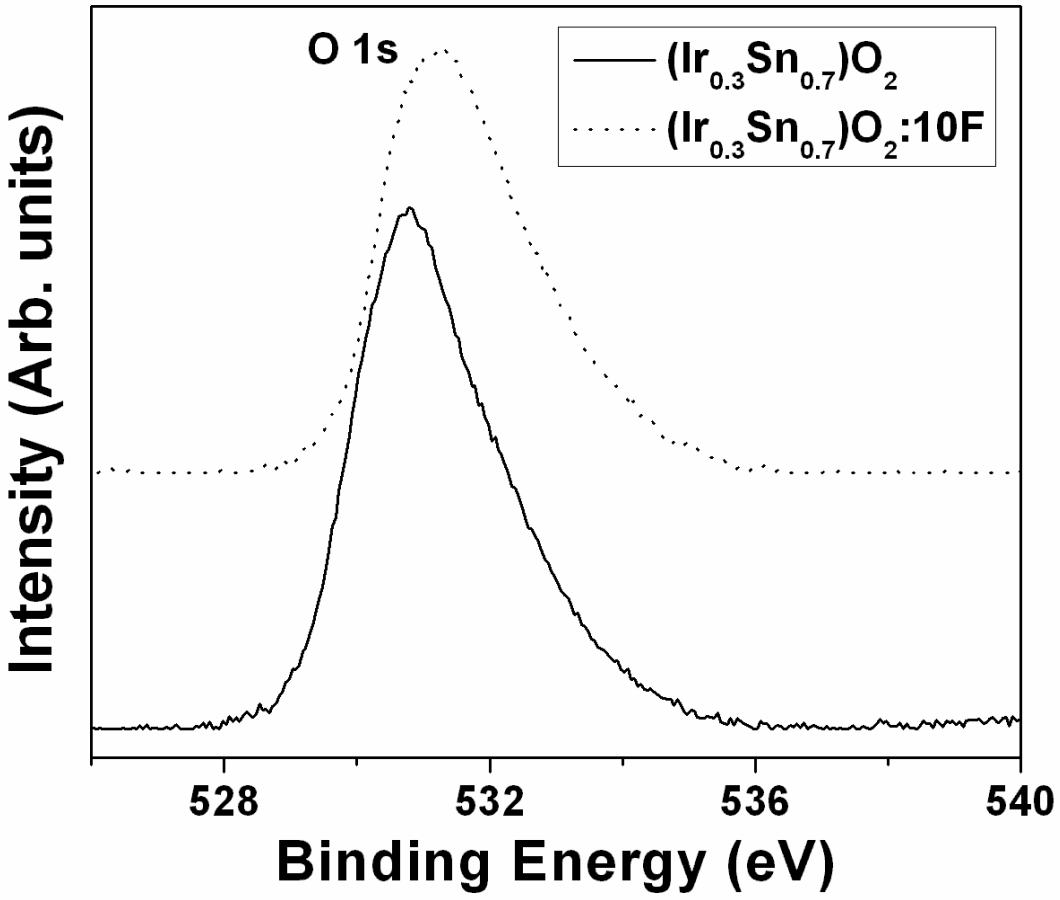

Figure 115. The XPS spectra of O 1s of (Ir,Sn)O_2 and (Ir,Sn)O_2:F

5.2.2.2 Electrochemical Testing

The electrochemical activity of commercial IrO_2 (Alfa Aesar), (Ir,Sn)O_2 and (Ir,Sn)O_2:F has been studied as an OER anode electro-catalyst for PEM electrolysis. The linear polarization curve and non-linear Tafel plot are encountered due to large contribution of R_Ω which mainly arises due to the R_s and R_e [51, 52]. In order to accurately know the electrode kinetics of the

electro-catalyst, the polarization curve, is plotted after appropriately correcting for the total ohmic loss (iR_Ω). The value of R_s, R_e, and R_{ct} for the catalysts, tabulated in **Table 8**, is obtained from EIS measurements conducted at different potentials (*vs*. NHE) in 1 N H_2SO_4 at 40^oC. **Figure 116, Figure 117** and **Figure 118** shows the EIS of $(Ir,Sn)O_2$, $(Ir,Sn)O_2$:10F and commercial IrO_2 obtained at open circuit potential (OCP), 1.5 V, 1.6 V and 1.8 V (*vs*. NHE) in the frequency range of 100 mHz - 100 kHz. It is seen that R_s for the electro-catalysts is similar and in the range of ~ 16 - 17 Ωcm^2 at various potentials. As seen in **Table 8**, R_e for $(Ir,Sn)O_2$:F is less compared to undoped $(Ir,Sn)O_2$ which may arise due to the improved electronic conductivity of $(Ir,Sn)O_2$:F. The low frequency EIS plot shows a semicircular arc related to OER whose diameter gives the polarization resistance (R_{ct}). F doped $(Ir,Sn)O_2$ has similar or even lesser R_{ct} values than commercial IrO_2 and undoped $(Ir,Sn)O_2$, which explains the increase in catalytic activity of the electrode with incorporation of F.

Table 8. Impedance parameters of nanoparticulate $(Ir,Sn)O_2$:F and commercial IrO_2

Voltage	Electro-catalyst	R_s (Ωcm^2)	R_e (Ωcm^2)	R_{ct} (Ωcm^2)
Open Circuit	$(Ir,Sn)O_2$:0F	16.96	7.69	2639
	$(Ir,Sn)O_2$:10F	16.38	3.42	1327
	IrO_2 (Alfa)	16.42	4.03	3577
1.5V	$(Ir,Sn)O_2$:0F	16.89	4.73	251.0
	$(Ir,Sn)O_2$:10F	17.16	3.87	198.8
	IrO_2 (Alfa)	16.31	2.57	44.89
1.6V	$(Ir,Sn)O_2$:0F	16.08	5.12	86.09
	$(Ir,Sn)O_2$:10F	16.81	2.16	29.2
	IrO_2 (Alfa)	16.38	3.36	14.76
1.8V	$(Ir,Sn)O_2$:0F	16.32	1.91	43.23
	$(Ir,Sn)O_2$:10F	16.67	1.23	13.82

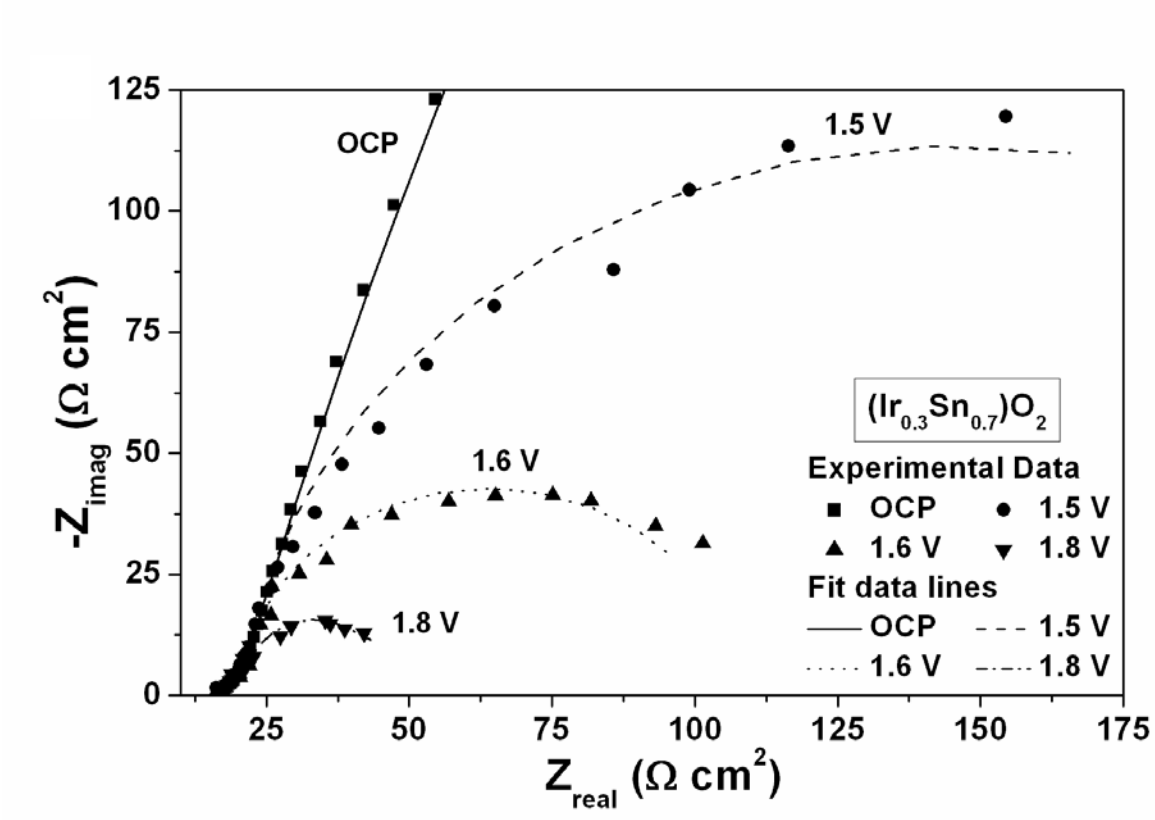

Figure 116. EIS spectra of $(Ir,Sn)O_2$ obtained at OCP, 1.5 V, 1.6 V and 1.8 V in 1 N H_2SO_4

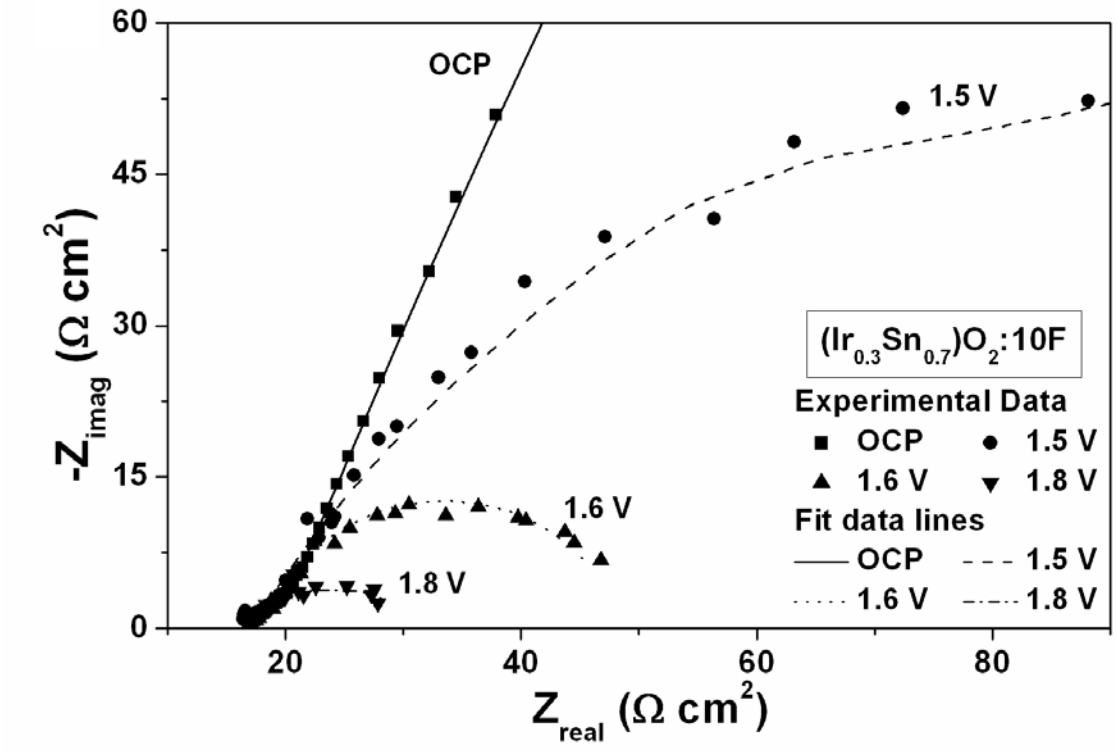

Figure 117. EIS spectra of (Ir,Sn)O_2:10 wt.% F obtained at OCP, 1.5 V, 1.6 V and 1.8 V in 1 N H_2SO_4

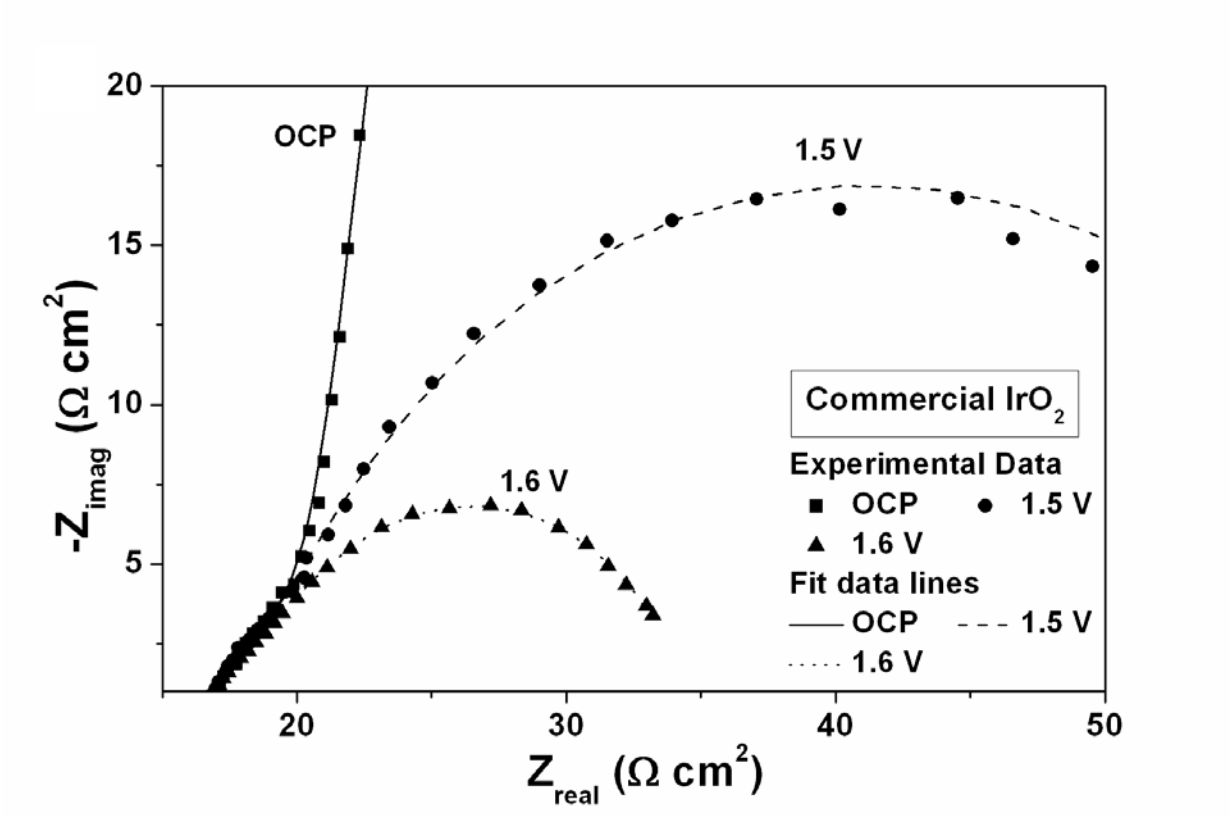

Figure 118. EIS spectra of commercial IrO_2 obtained at OCP, 1.5 V and 1.6 V in 1 N H_2SO_4

The polarization curve of commercial IrO_2 (Alfa Aesar), $(Ir,Sn)O_2$ and $(Ir,Sn)O_2$:F, before and after ohmic resistance correction ($iR_\Omega = iR_s + iR_e$) has been performed in 1 N H_2SO_4 solution at 40^oC with a scan rate of 1 mV/sec as shown in **Figure 119**. The water splitting reaction (OER) occurs at a potential of ~ 1.43 V *vs*. NHE. The current density of IrO_2 at ~ 1.5 V (*vs*. NHE) after iR_Ω correction, a typical voltage selected to check for electrochemical activity for water electrolysis, is ~ 0.0125 ± 0.0002 A/cm^2 for a total loading ~ 0.3 mg/cm^2 of IrO_2. The current density at ~ 1.5 V (*vs*. NHE) obtained from the iR_Ω corrected curve for undoped $(Ir_{0.3}Sn_{0.7})O_2$ with the same IrO_2 loading (~ 0.3 mg/cm^2) is ~ 0.0032 ± 0.0002 A/cm^2 which is *ca.* 74% lower than commercial IrO_2. However, there is an increase in current density for

$(Ir_{0.3}Sn_{0.7})O_2$:10 wt.% F. The F doped electro-catalyst shows a current density of ~ 0.013 ± 0.0002 A/cm^2 at ~ 1.5 V (*vs.* NHE) which is slightly better than commercial IrO_2.

The Tafel slope of commercial pure IrO_2 is ~ 83 mV/decade and is calculated from the Tafel plot as shown in **Figure 120**. It is slightly higher than a two electron pathway reaction (Tafel slope ~ 62 mV/dec) assuming a transfer coefficient of ~ 0.5 [48, 53, 101]. The Tafel slope of $(Ir,Sn)O_2$ and $(Ir,Sn)O_2$:10F, calculated from their corresponding Tafel plots as shown in **Figure 121** and **Figure 122**, are ~ 108 mV/decade and ~ 70 mV/decade, respectively. This observation clearly suggests that the catalytic or electrochemical activity of $(Ir,Sn)O_2$:F increases with increase in F content with a decrease in the Tafel slope. An optimal value for $(Ir_{0.3}Sn_{0.7})O_2$:10 wt.% F is reached that exhibits comparable electrochemical activity as commercial IrO_2. These results indicate that $(Ir_{0.3}Sn_{0.7})O_2$:10 wt.% F is a promising candidate as an OER anode electro-catalyst especially with reduced noble metal content for PEM based water electrolysis.

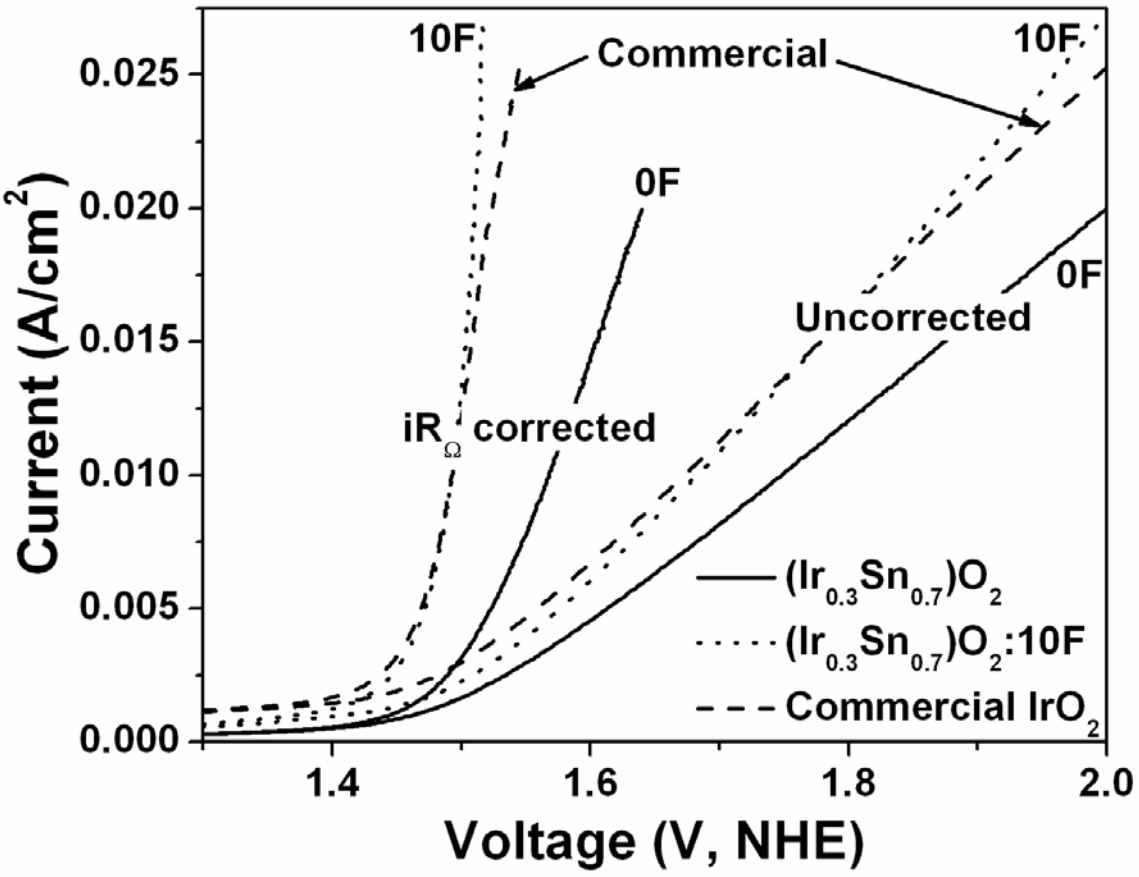

Figure 119. The polarization curve of undoped and F doped (Ir,Sn)O_2 along with commercial IrO_2 in the presence of 1 N H_2SO_4 solution at 40°C with a scan rate of 1 mV/sec before and after iR correction

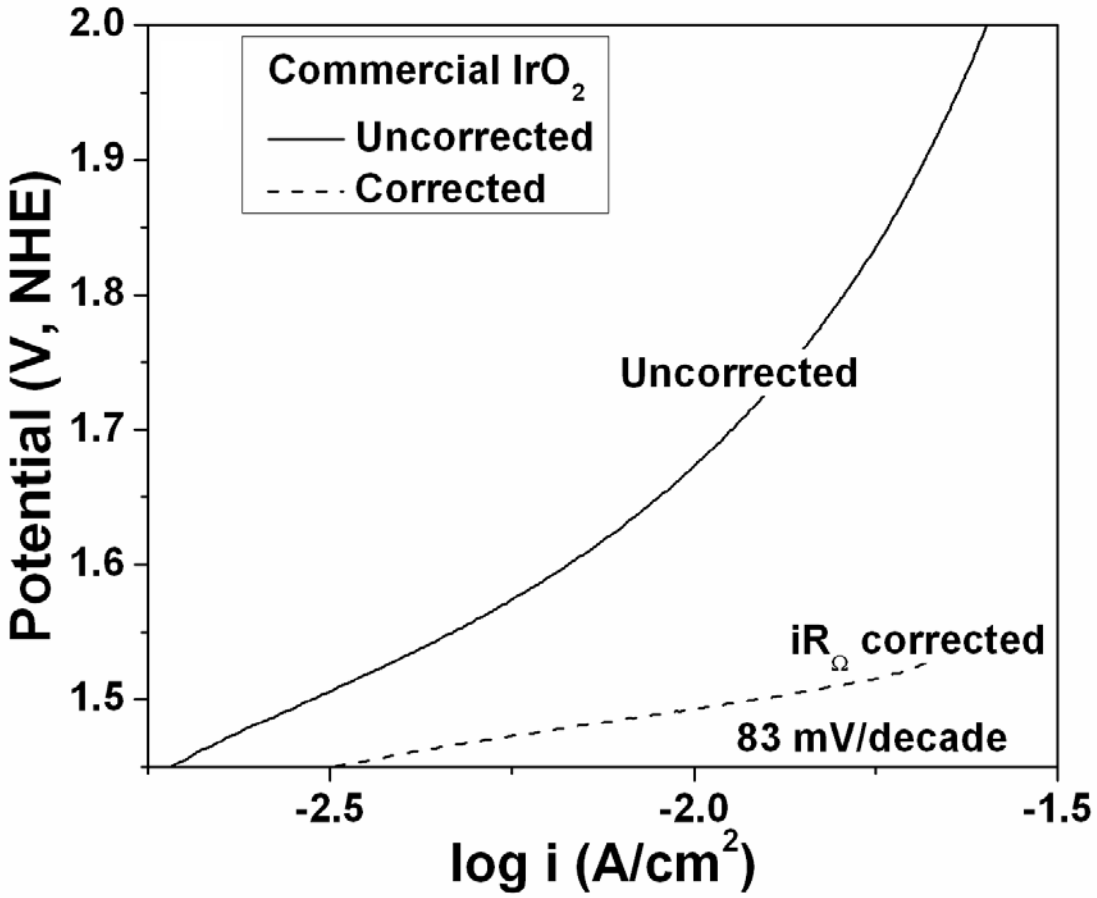

Figure 120. The Tafel plot of commercial IrO_2 before and after iR correction

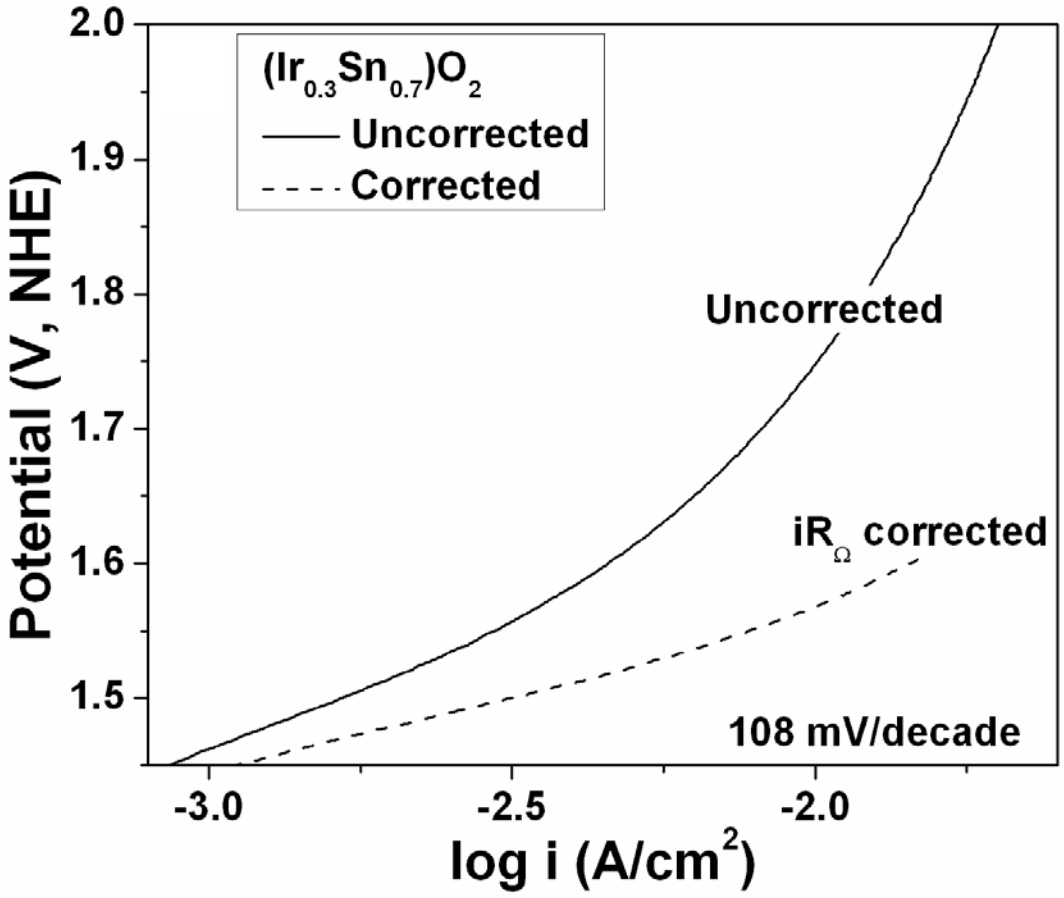

Figure 121. The Tafel plot of $(Ir,Sn)O_2$ before and after iR correction

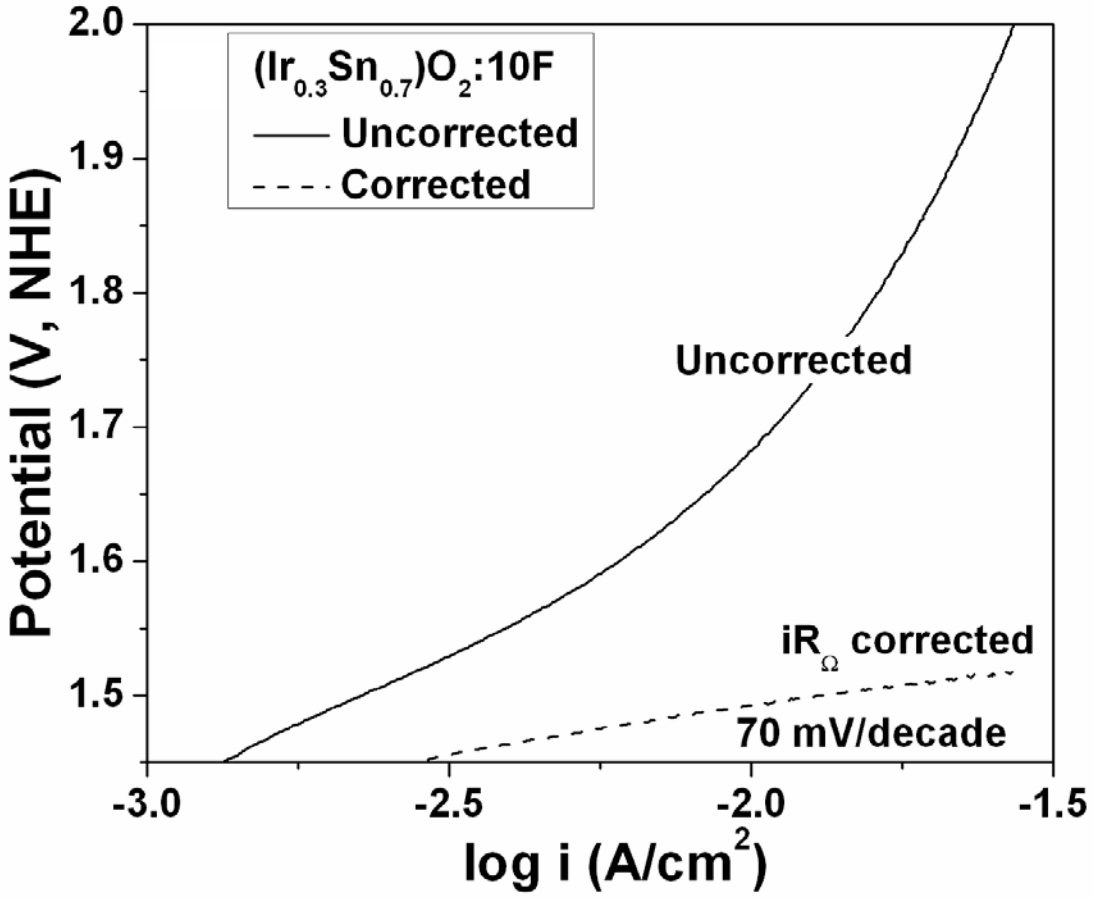

Figure 122. The Tafel plot of (Ir,Sn)O_2:10 wt.% F before and after iR correction

In order to study the stability of these anode electro-catalysts, chronoamperometry (CA) is conducted for 12 hours at a constant voltage of ~1.65 V (*vs.* NHE), for assessing the loss in the electrochemical activity of the catalyst. The CA curves for ($Ir_{0.3}Sn_{0.7}$)O_2, ($Ir_{0.3}Sn_{0.7}$)O_2:10wt.% F and commercial IrO_2 are compared in **Figure 123**. The undoped (Ir,Sn)O_2 has less initial current than the (Ir,Sn)O_2:10F and commercial IrO_2 because it inherently gives less current at a particular voltage (**Figure 119**). The decay of current for the catalysts can be attributed to

dissolution of electro-catalyst coating at the edge of the porous titanium support [30] and due to diffusion controlled reactions or by induced loss of electrolyte due to constant exhaustion of fuel [34, 57]. Commercial IrO_2 undergoes a lot of degradation and exhibits a steep decrease in current over time showing its instability whereas a steady decay of current is observed for the $(Ir,Sn)O_2$:F catalysts. This suggests that the chemical stability / durability of the reduced noble metal oxide catalysts is enhanced due to SnO_2 and F doped SnO_2 support, thus making them more robust than commercially pure IrO_2 which is regarded as a gold standard OER electro-catalyst for PEM electrolyzers.

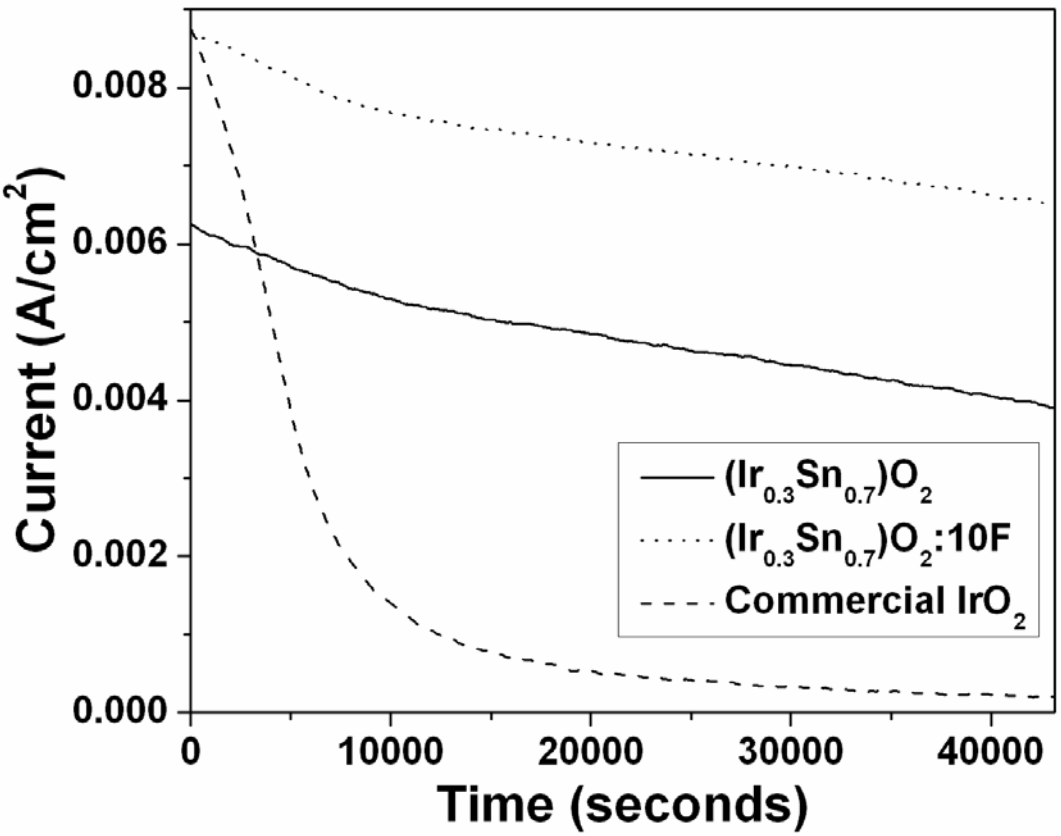

Figure 123. The variation of current *vs.* time for (Ir,Sn)O_2:F powders and commercial IrO_2 in the CA test performed in a 1 N H_2SO_4 solution at a constant potential of ~ 1.65 V

The ICP results conducted on the 1 N H_2SO_4 electrolyte solution after the CA measurement *i.e.* 12 hours shows the absence of Ir for the (Ir,Sn)O_2:F electro-catalysts whereas, commercial IrO_2 shows ~ 0.35 ppm of Ir leached out in the solution. $(Ir_{0.3}Sn_{0.7})O_2$ has ~ 0.16 ppm of Sn and $(Ir_{0.3}Sn_{0.7})O_2$:10 wt.% F has ~ 0.12 ppm of Sn present in the electrolyte solution after CA. This suggests that the steady decrease in current for the electro-catalysts may arise due to slight dissolution of the electro-catalyst from the surface.

After the conclusion of the CA test, the $(Ir_{0.3}Sn_{0.7})O_2$:10 wt.% F electrode was subject to polarization testing as seen in **Figure 124** in order to determine the activity of the electrodes after long term structural stability tests. The Tafel plot from the polarization curve (post CA measurement) after iR correction is shown in **Figure 125**. A Tafel slope of ~ 121 mV/decade was obtained for $(Ir,Sn)O_2$:10 wt.% F which is comparable to that of undoped IrO_2 after CA (~ 112 mV/decade) as seen in **Figure 104**. The present study therefore identifies $(Ir,Sn)O_2$:F as a promising anode electro-catalyst with the ability to significantly reduce the noble metal oxide loading with increased electro-catalytic performance as well as chemical and structural stability.

A single full cell test was done at Proton OnSite for the $(Ir_{0.3}Sn_{0.7})O_2$:10 wt.% F catalyst which has been shown and compared in **Section 5.2.3.2** along with the reduced noble metal $(Ir,Nb)O_2$:F catalyst powder.

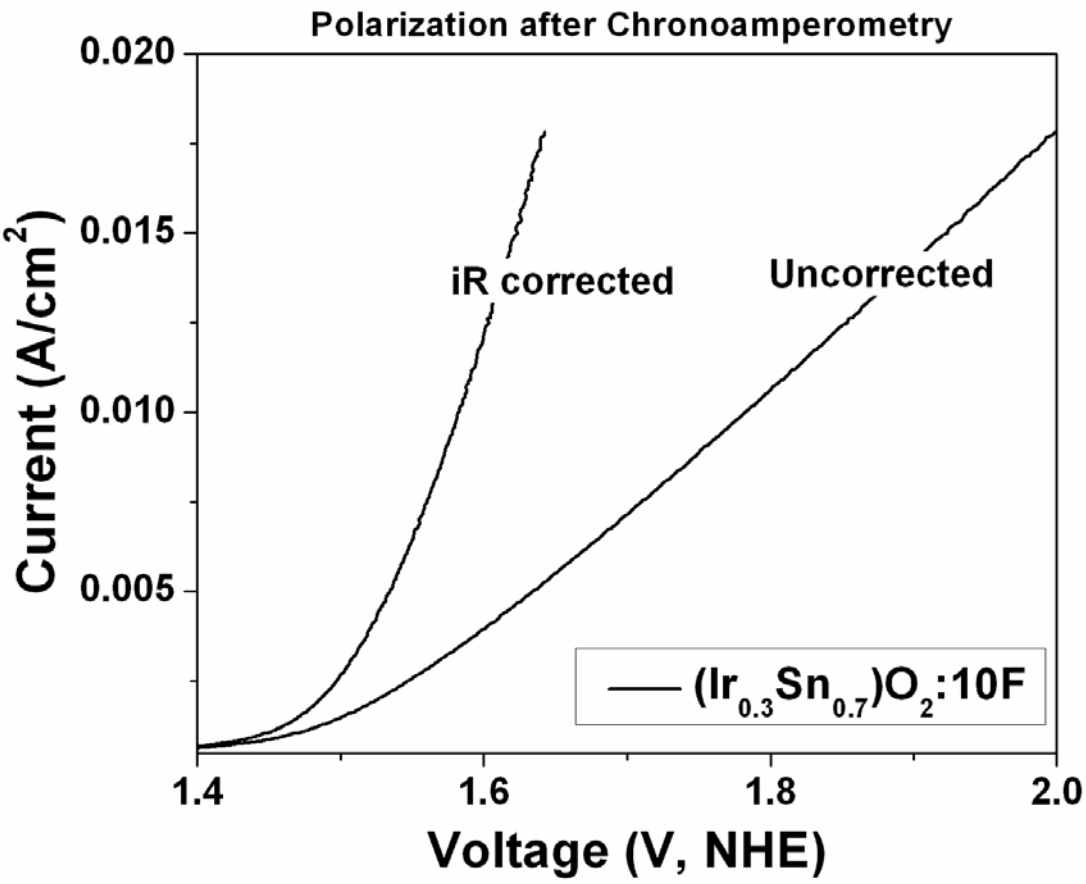

Figure 124. Polarization curve of (Ir,Sn)O_2:10 wt.% F powder after the CA test

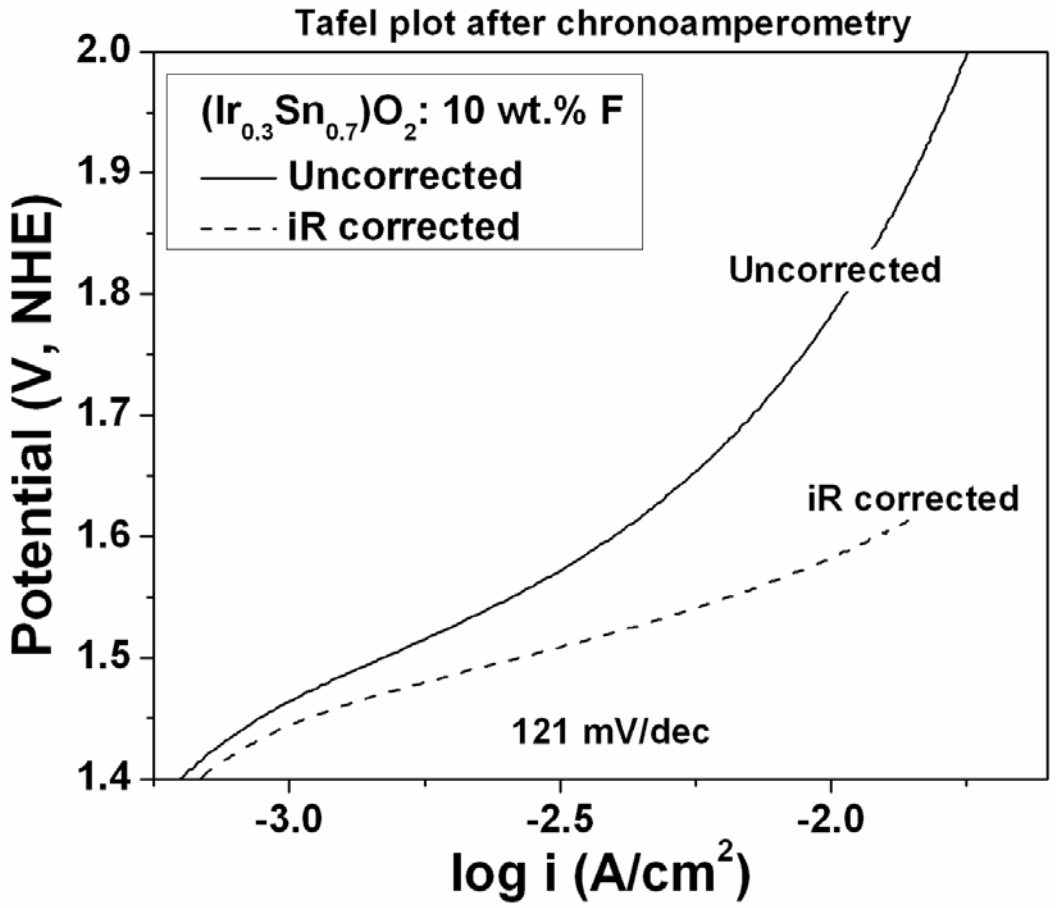

Figure 125. The Tafel plot of (Ir,Sn)O_2:10 wt.% F powder after the CA test

5.2.3 Binary F doped (Ir,Nb)O_2

5.2.3.1 Structural Analysis

The XRD pattern of the as-prepared Nb_2O_5: 10 wt.% F powder after drying in air at 75°C shown in **Figure 126** exhibits peaks corresponding to niobium oxide. The relatively broad nature of the peaks indicates the amorphous nature of the powder. According to the BET analysis, the

specific surface area of 10 wt.% F doped Nb_2O_5 powder is ~ 389 m^2/g while the specific surface area of undoped Nb_2O_5 is ~ 257 m^2/g. The solutions of Nb_2O_5:F and $IrCl_4$ were mixed and heat treated to 400°C in air. **Figure 127** reveals the XRD pattern of the electro-catalysts are nanocrystalline and contain crystalline phases mainly associated with tetragonal IrO_2. It is clear that all the peaks correspond to single phase rutile type tetragonal IrO_2 structure suggesting the formation of a homogeneous IrO_2 and Nb_2O_5:F solid solution, [(Ir,Nb)O_2:F] with no undesirable phase separation (*E.g.* IrO_2 + Nb_2O_5) and / or mixed phase formation which is critical for achieving the high catalytic activity. The effective crystallite size of (Ir,Nb)O_2 and (Ir,Nb)O_2:F, calculated using the Scherrer formula from the integral breadth of the Lorentzian contribution determined from peak profile analysis using single line approximation method after eliminating the instrumental broadening and lattice strain contribution [123], is ~ 5.4 nm and ~ 4.9 nm respectively. The TGA-DTA traces of undoped and 10 wt.% F doped (Ir,Nb)O_2 is shown in **Figure 128**. A weight loss of ~ 4 - 5 % is observed for the F doped electro-catalyst and confirms the removal of the volatile species *i.e.* fluorine from the catalyst. The TGA-DTA of undoped (Ir,Nb)O_2 shows almost no weight loss when subject to thermogravimetric analysis in air. The weight loss thus would nearly correspond to the final amount of F present in the ($Ir_{0.25}Nb_{0.75}$)O_2 :10 wt.% F electro-catalyst. ($Ir_{0.25}Nb_{0.75}$)O_2 and ($Ir_{0.25}Nb_{0.75}$)O_2:10 wt.% F have a specific surface area, measured by the BET technique, of ~ 77 m^2/g and ~ 99 m^2/g respectively. The increase in surface area for the (Ir,Nb)O_2:F is attributed to decrease in crystallite size.

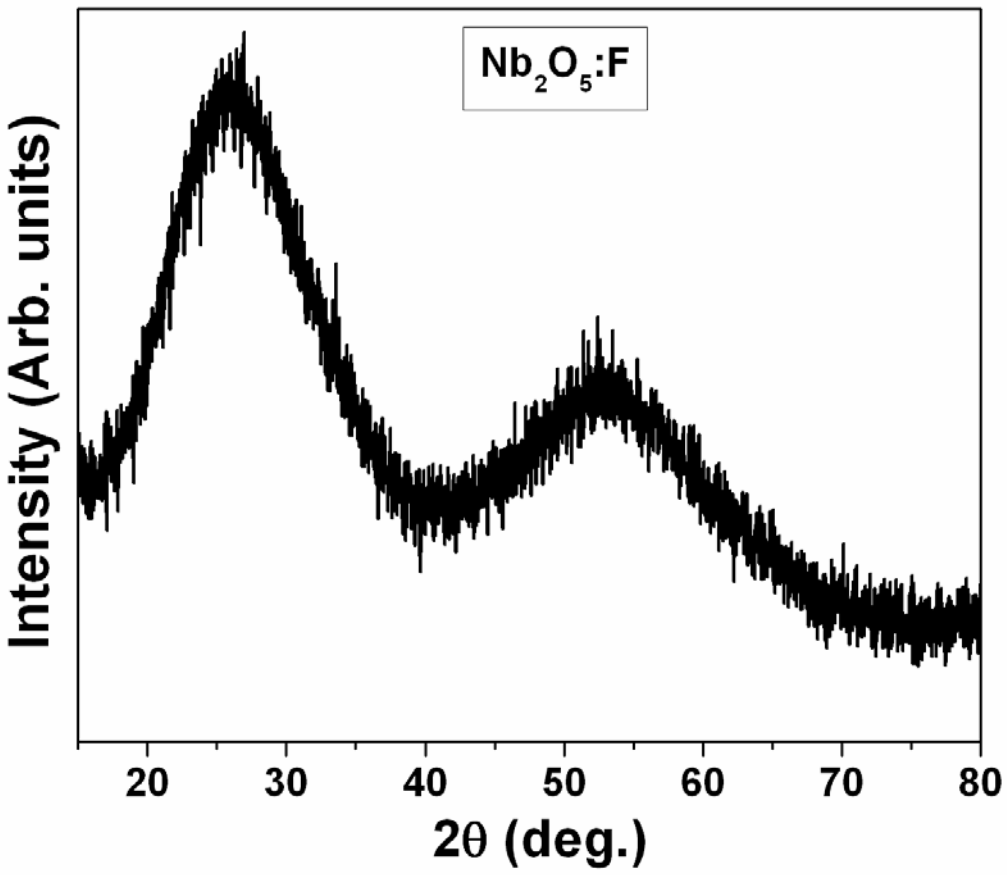

Figure 126. XRD pattern of the as prepared Nb_2O_5:F

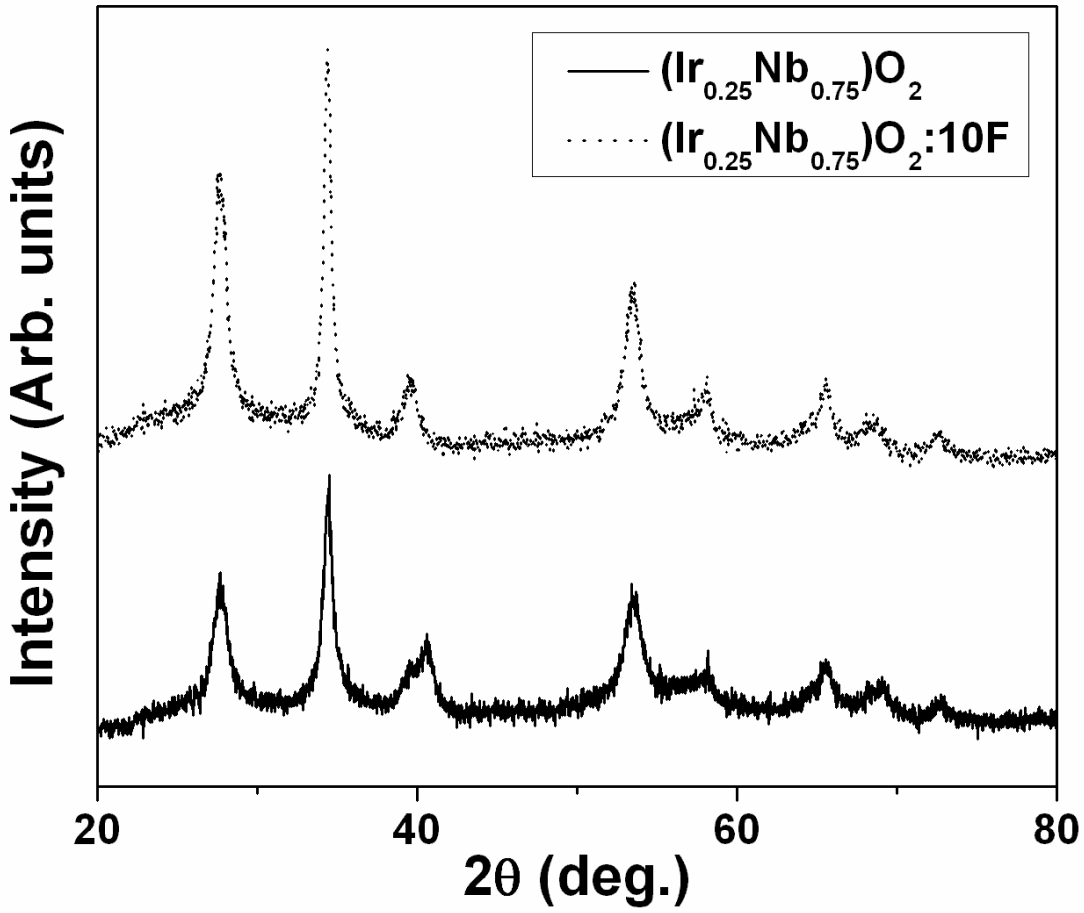

Figure 127. XRD pattern of undoped and F doped (Ir,Nb)O_2

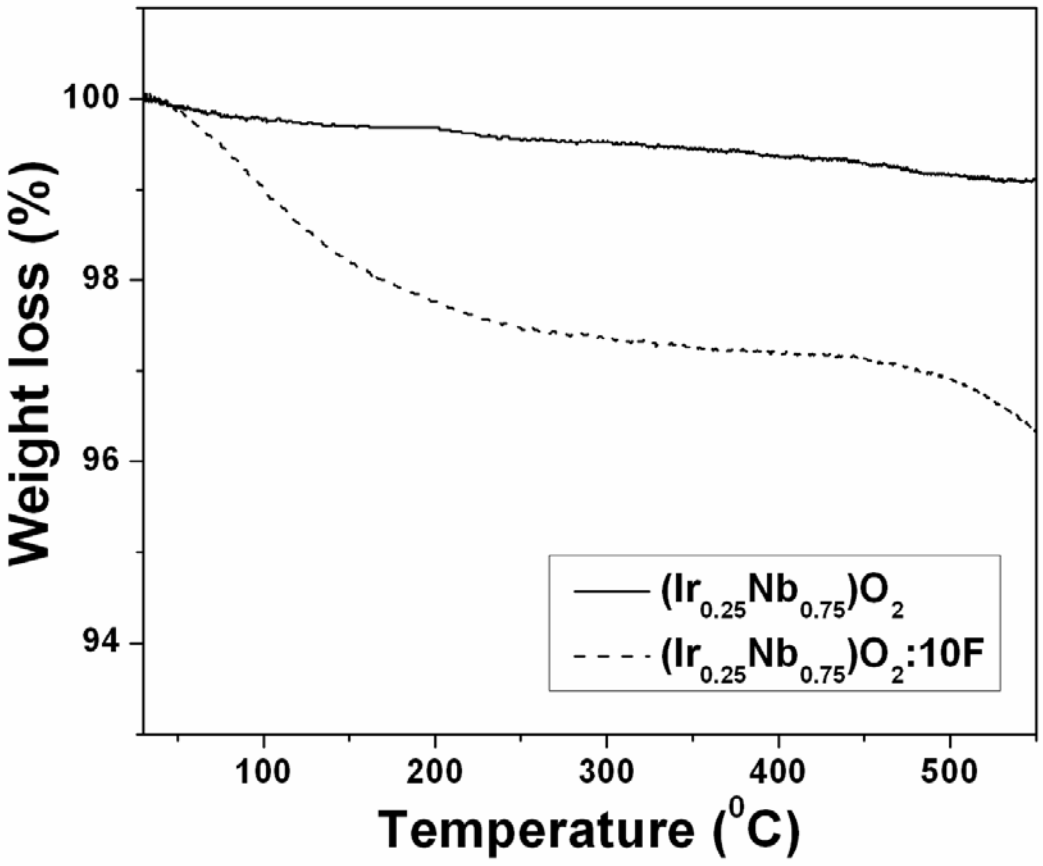

Figure 128. The TGA-DTA traces in air of $(Ir_{0.25}Nb_{0.75})O_2$:F showing weight loss corresponding to fluorine in the electro-catalyst

The presence of elemental Ir, Nb and O in (Ir,Nb)O_2:F representative sample has been confirmed using energy dispersive X-ray spectroscopy (EDX) attached to the SEM. The elemental x-ray mapping in **Figure 129** shows the distribution of Ir, Nb, O and F in (Ir,Nb)O_2:F. It confirms that all the elements *viz.* Ir, Nb, O and F are homogeneously distributed within the (Ir,Nb)O_2:F particles without segregation or separation at any specific site. Quantitative elemental composition analysis of the powders obtained by EDX further confirmed that the

measured elemental compositions of Ir and Nb are close to the nominal composition. The bright field TEM image of $(Ir_{0.25}Nb_{0.75})O_2$:10 wt.% F shown in **Figure 130** corroborates the nanometer sized fine particles in the range of ~ 4 - 8 nm. This corroborates well with the crystallite size calculated using the Scherrer formula from the x-ray diffraction patterns.

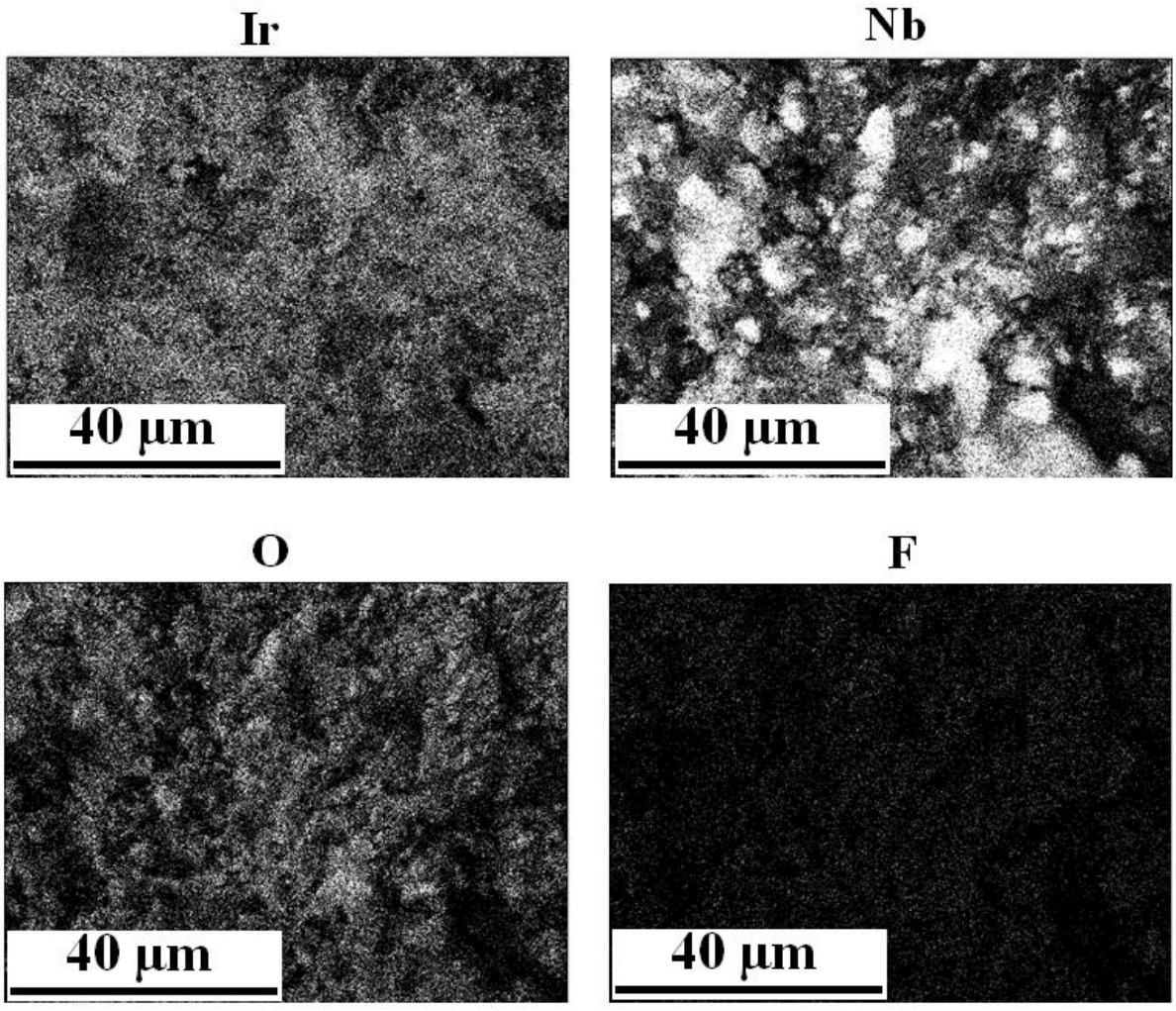

Figure 129. The elemental x-ray mapping of Ir, Nb, O and F in $(Ir_{0.25}Nb_{0.75})O_2$:10 wt.% F

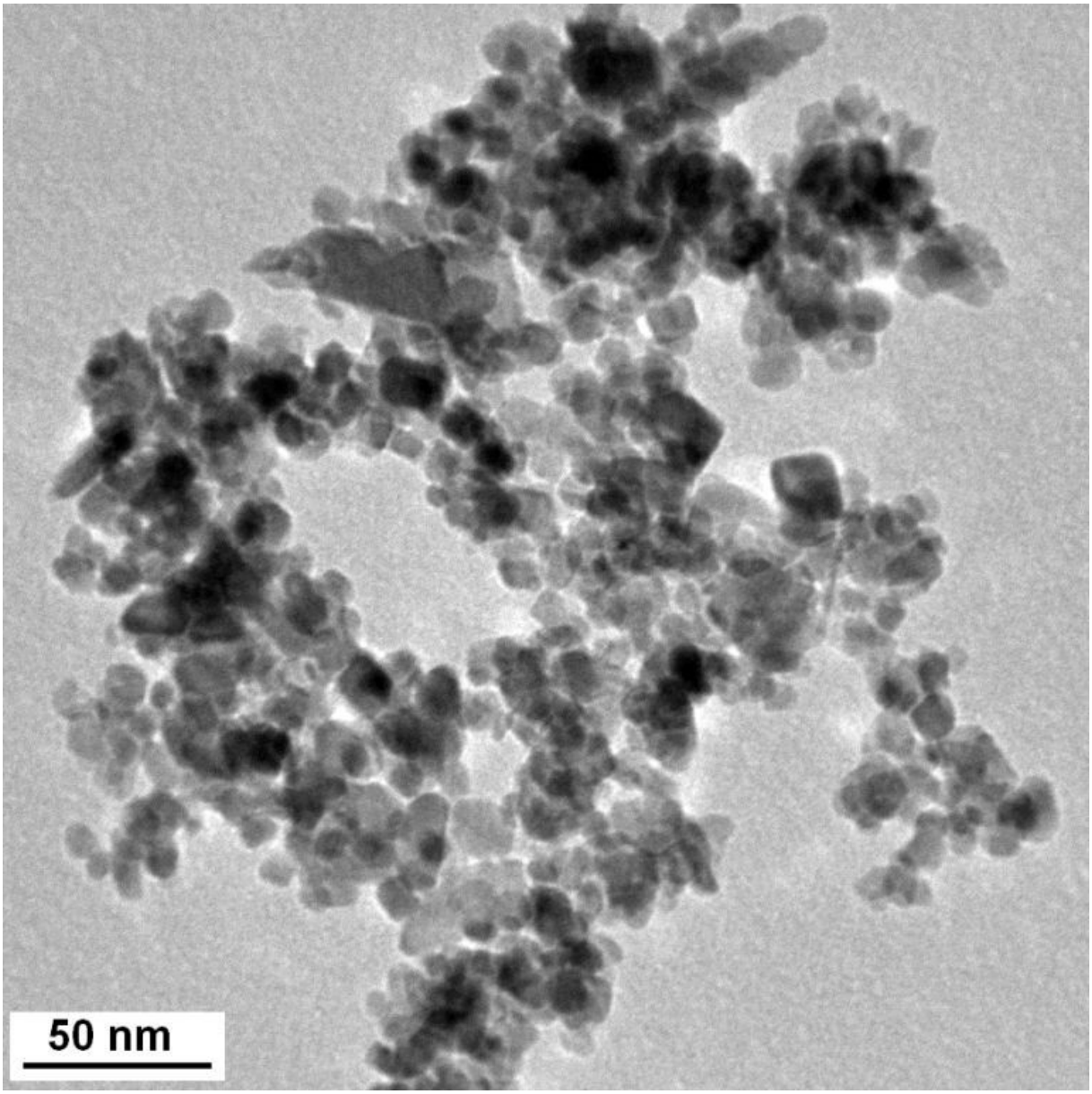

Figure 130. The bright field TEM image $(Ir_{0.25}Nb_{0.75})O_2$:10 wt.% F shows the presence of fine nanoparticles

In order to determine the surface composition and chemical oxidation states, x-ray photoelectron spectroscopy (XPS) was carried out on the catalysts. The XPS spectra of Ir 4f, Nb 3d and O 1s of $(Ir,Nb)O_2$ and $(Ir,Nb)O_2$:F are shown in **Figure 131**, **Figure 132** and **Figure 133**,

respectively. The XPS spectra of Ir of $(Ir_{0.25}Nb_{0.75})O_2$ shows the presence of Ir $4f_{7/2}$ and Ir $4f_{5/2}$ doublet with binding energy ~ 61.6 eV and ~ 64.5 eV respectively, and the O 1s peak is centered at ~ 530.5 eV which is consistent with the values of bulk IrO_2. Also, the XPS spectra of Nb shows peak separation of Nb $3d_{5/2}$ and Nb $3d_{3/2}$ with a binding energy of ~ 207.5 eV and ~ 210.3 eV respectively (with the O1s line centered at ~530.5 eV), which is consistent with the values of stoichiometric NbO_x. But, XPS did not show any specific peak for fluorine. As reported previously, unequivocal confirmation of F could not be made by XRD and XPS measurements [57, 100, 124]. But, it is observed that the binding energy of Ir 4f, Nb 3d and O1s core level increases by ~ 0.4 - 0.6 eV for $(Ir_{0.25}Nb_{0.75})O_2$:10 wt.% F. This is an indirect indication of the stronger binding due to higher electro-negativity of F, suggesting its incorporation in the lattice. Although the exact amount and the nominal composition could not be conclusively stated [122], a weight loss of ~ 5 wt.% observed in the TGA-DTA (**Figure 128**) is caused due to F since the undoped electro-catalyst shows no weight loss in the TGA-DTA. Nevertheless, F incorporation clearly has a great impact on the electrochemical activity of $(Ir,Nb)O_2$:F solid solution as seen in the electrochemical results which is most likely attributed to the improved electronic conductivity and durability.

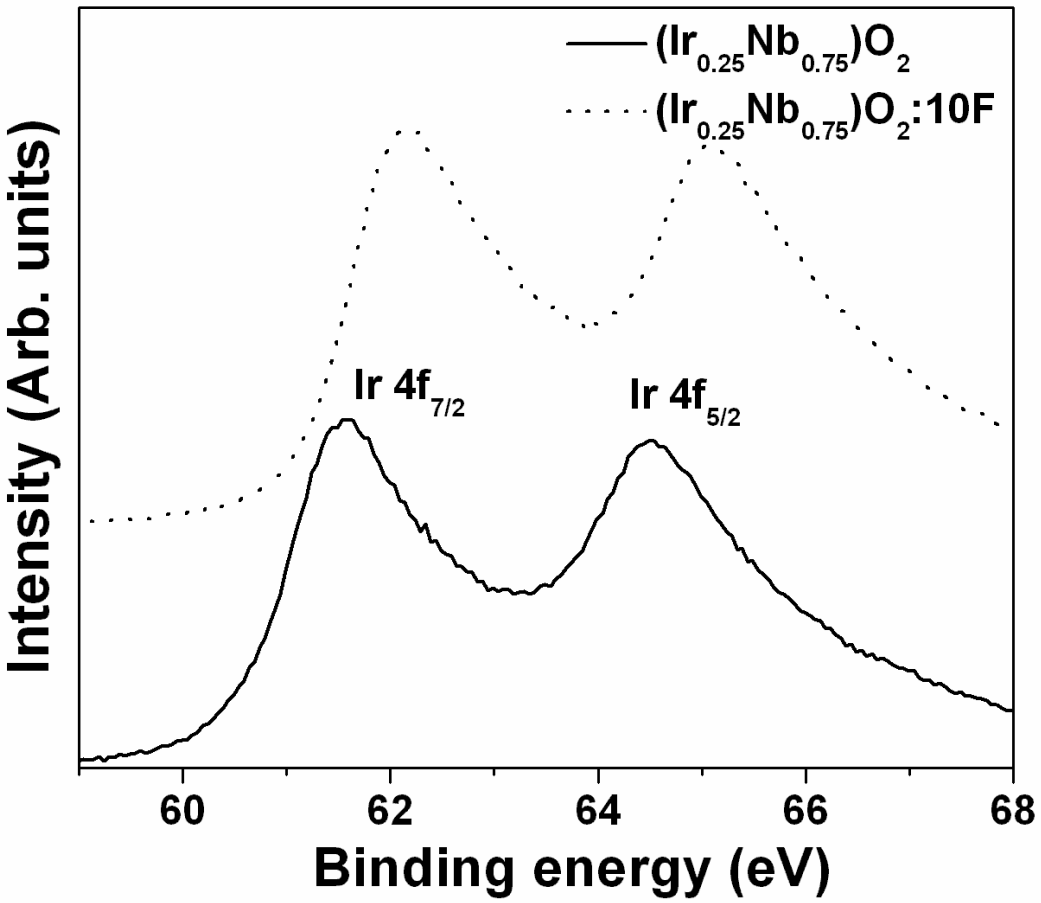

Figure 131. The XPS spectra of Ir $4f_{7/2}$ and Ir $4f_{5/2}$ doublet of (Ir,Nb)O_2 and (Ir,Nb)O_2:F

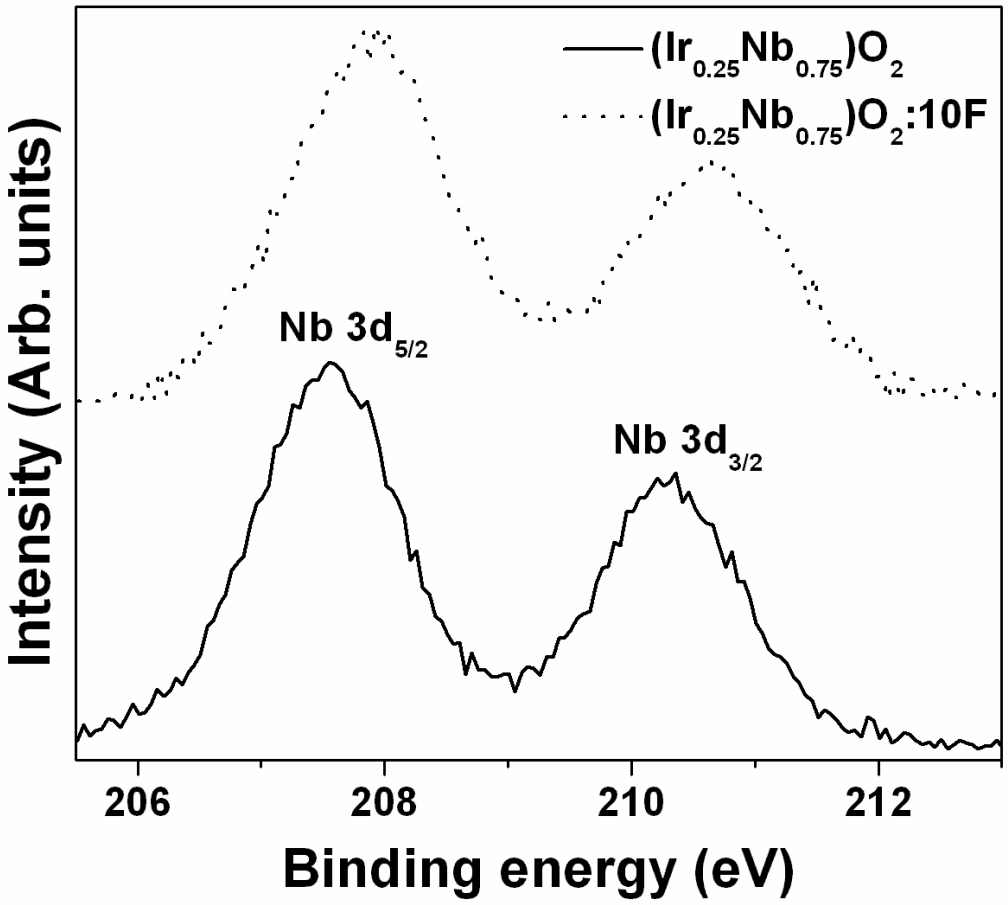

Figure 132. The XPS spectra of Nb $3d_{5/2}$ and Nb $3d_{3/2}$ doublet of (Ir,Nb)O_2 and (Ir,Nb)O_2:F

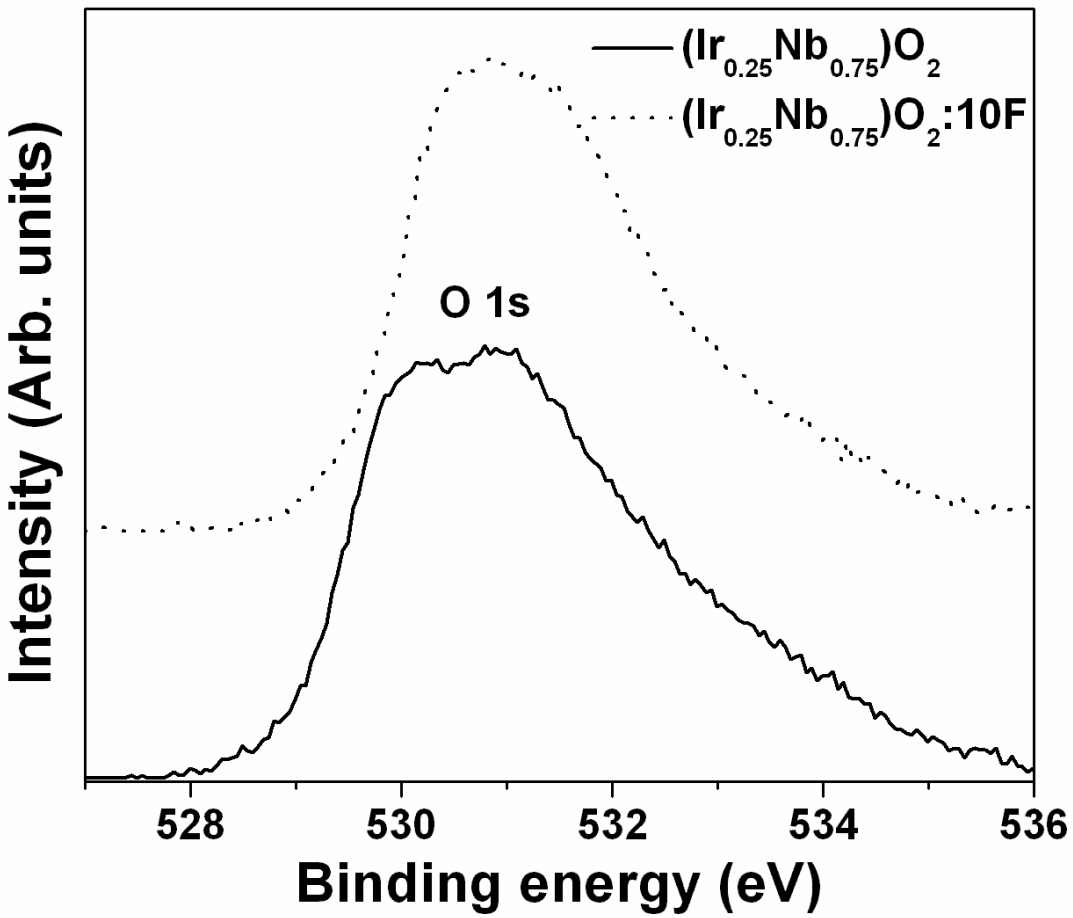

Figure 133. The XPS spectra of O 1s of (Ir,Nb)O_2 and (Ir,Nb)O_2:F

5.2.3.2 Electrochemical Testing

The electrochemical activity of commercially available IrO_2 (Alfa Aesar), (Ir,Nb)O_2 and (Ir,Nb)O_2:F has been examined as an OER anode electro-catalyst for PEM based water electrolysis. The linear polarization curve and non-linear Tafel plot are most often encountered due to large contribution of ohmic resistance (R_Ω) which is mainly due to R_s, R_e and bubble

resistance (R_{bub}) [51, 52]. The polarization curve of the electro-catalysts, is conducted in the presence of 1 N H_2SO_4 solution at 40^oC with a scan rate of 1 mV/sec in order to evaluate the inherent electrochemical property and electrode kinetics of the electro-catalyst studied herein. The value of R_s, R_e and R_{ct} is obtained from EIS measurements conducted at different potentials and are presented in **Table 9**.

Figure 134 and **Figure 135** show the electrochemical impedance spectroscopy (EIS) plot of (Ir,Nb)O_2 and (Ir,Nb)O_2:10F respectively, measured at open circuit potential (OCP), 1.5 V, 1.6 V and 1.8 V in the frequency range of 100 mHz - 100 kHz. The EIS polt for commercial IrO_2 has been plotted and shown in **Figure 118** (**Section 5.2.2.2**). The impedance parameters (**Table 9**) are calculated by fitting the experimental data using the ZView software from Scribner Associates with a circuit model $R_s(R_eQ_1)(R_{ct}Q_{dl})$. It should be noted that R_s for the undoped and doped electro-catalysts is unchanged with change in potential (~ 16.8 Ωcm^2). R_e is due to the resistance encountered due to electron transfer from the electrode to the current collector. The value of R_e for (Ir,Nb)O_2:F is less than the undoped (Ir,Nb)O_2 and is comparable to commercial IrO_2 which may arise due to the improved electronic conductivity of (Ir,Nb)O_2:F. A well formed semicircular arc is observed at low frequencies in the EIS plots. The diameter of this arc is typically a measure of the polarization / charge transfer resistance (R_{ct}). (Ir,Nb)O_2:F has similar or even lower R_{ct} values compared to commercial IrO_2 and (Ir,Nb)O_2, which explains the increase in catalytic activity of the electrode with incorporation of F.

Table 9. Impedance parameters of nanoparticulate $(Ir,Nb)O_2$:F and commercial IrO_2

Voltage	Electro-catalyst	R_s (Ωcm^2)	R_e (Ωcm^2)	R_{ct} (Ωcm^2)
Open Circuit	$(Ir,Nb)O_2$:0F	16.90	3.12	2958
	$(Ir,Nb)O_2$:10F	16.85	2.67	2445
	IrO_2 (Alfa)	16.42	4.03	3577
1.5V	$(Ir,Nb)O_2$:0F	16.69	6.11	77.56
	$(Ir,Nb)O_2$:10F	16.70	5.00	47.20
	IrO_2 (Alfa)	16.31	2.57	44.89
1.6V	$(Ir,Nb)O_2$:0F	16.71	4.71	17.90
	$(Ir,Nb)O_2$:10F	16.79	4.00	10.39
	IrO_2 (Alfa)	16.38	3.36	14.76
1.8V	$(Ir,Nb)O_2$:0F	16.78	2.75	6.81
	$(Ir,Nb)O_2$:10F	16.88	1.23	5.91

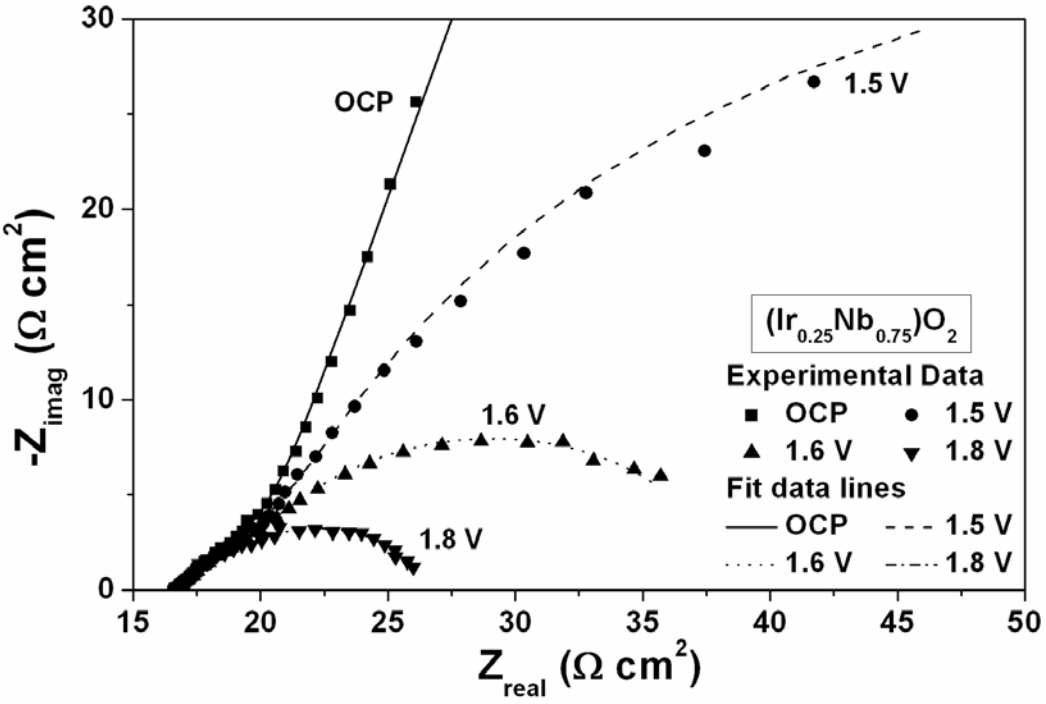

Figure 134. EIS spectra of (Ir,Nb)O_2 obtained at OCP, 1.5 V, 1.6 V and 1.8 V in 1 N H_2SO_4

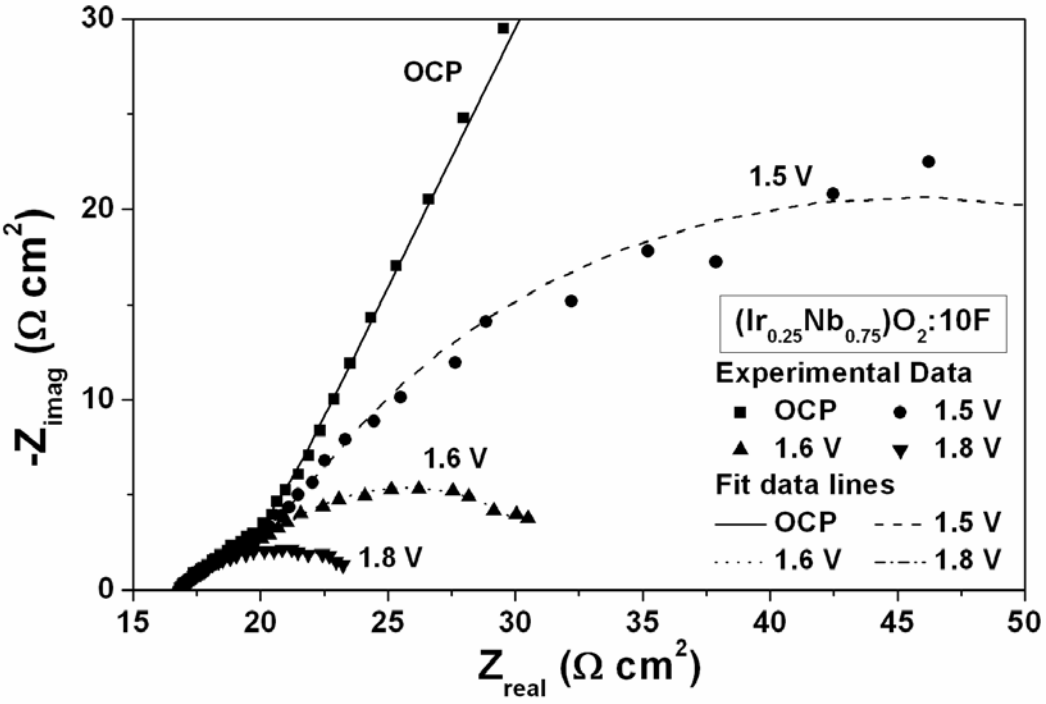

Figure 135. EIS spectra of (Ir,Nb)O_2:10 wt.% F obtained at OCP, 1.5 V, 1.6 V and 1.8 V in 1 N H_2SO_4

The polarization curve of commercial IrO_2 (Alfa Aesar), (Ir,Nb)O_2 and (Ir,Nb)O_2:F, before and after ohmic resistance correction ($iR_\Omega = iR_s + iR_e$) without considering R_{bub}, is shown in **Figure 136**. The water splitting reaction (OER) for commercial IrO_2 occurs at a potential of ~ 1.43V *vs.* NHE. The current density of IrO_2 at ~ 1.5V (*vs.* NHE), which is in the typical range of voltages selected to verify the electrochemical activity for water electrolysis, obtained from the iR_Ω corrected plot is ~ 0.0125 ± 0.0002 A/cm^2 for ~ 0.3 mg/cm^2 loading of IrO_2. The Tafel plot of commercial IrO_2 has been shown earlier in **Figure 120** (**Section 5.2.2.2**), which has a Tafel slope of ~ 83 mV/decade, which is slightly higher than what corresponds to a two electron

pathway reaction (Tafel slope ~ 62 mV/dec) assuming the transfer coefficient to be ~ 0.5 [48, 53, 57, 58]. The polarization curve for the (Ir,Nb)O_2 and (Ir,Nb)O_2:F before and after iR_Ω correction also shows OER occurring at a potential of ~ 1.43 V (*vs.* NHE) which is identical to that of pure IrO_2. But, the current density at ~ 1.5 V (*vs.* NHE) for undoped $(Ir_{0.25}Nb_{0.75})O_2$ with an identical IrO_2 loading of ~ 0.3 mg/cm^2 is ~ 0.008 ± 0.0002 A/cm^2 at 40^{o}C which is ~ 36 % lower than commercial IrO_2. However, the current density of $(Ir_{0.25}Nb_{0.75})O_2$:10 wt.% F increases. In fact, (Ir,Nb)O_2:F shows a current density of ~ 0.0133 ± 0.0002 A/cm^2 at ~ 1.5 V (*vs.* NHE) after iR_Ω correction which is slightly better than commercial IrO_2. The Tafel slope of (Ir,Nb)O_2 and (Ir,Nb)O_2:10F, calculated from the corresponding iR_Ω corrected Tafel plots, shown in **Figure 137** and **Figure 138**, is ~132 and ~78 mV/decade, respectively. This suggests that the electrochemical activity of (Ir,Nb)O_2:F increases with increase in F and corresponding decrease in the Tafel slope. It reaches an optimal value for (Ir,Nb)O_2:10 wt.% F exhibiting very similar electro-catalytic activity to that of commercial IrO_2 (~ 83 mV/decade). These results clearly suggest that $(Ir_{0.25}Nb_{0.75})O_2$:10 wt.% F is a promising candidate as an OER anode electro-catalyst for PEM based water electrolysis.

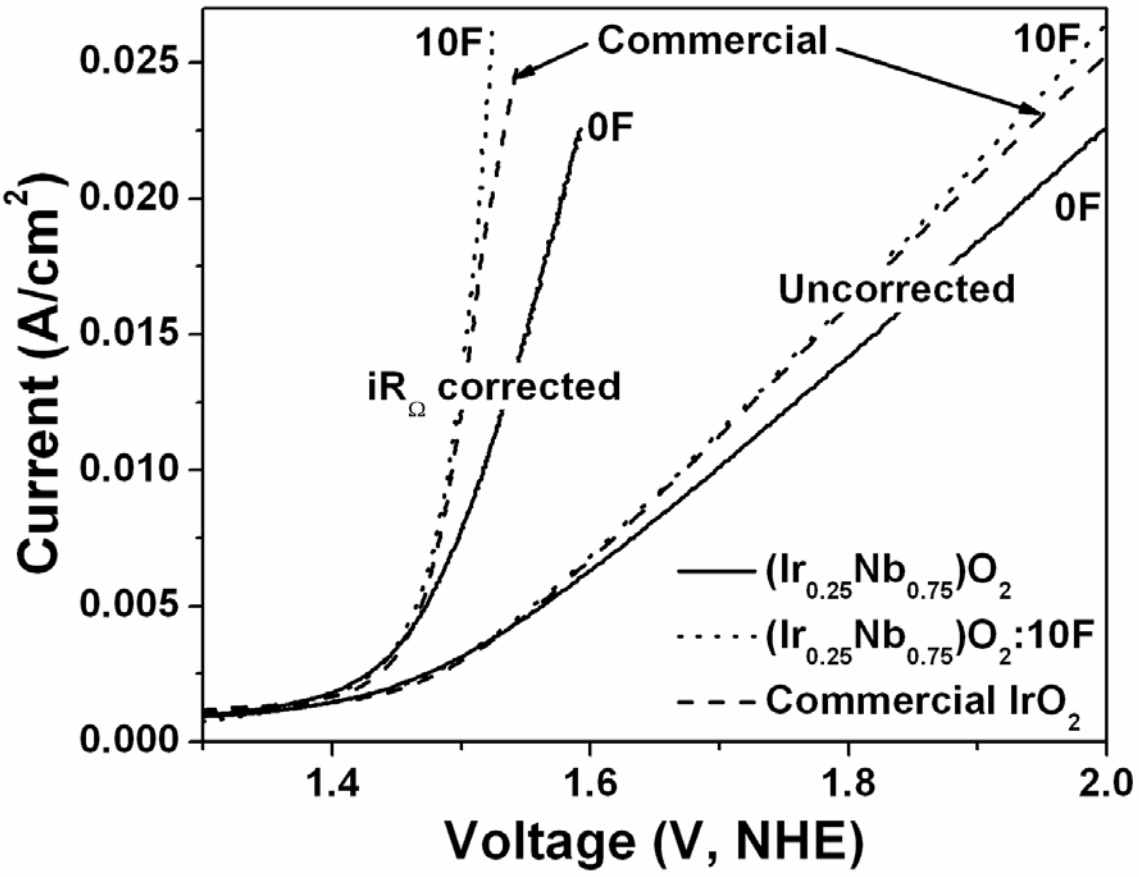

Figure 136. The polarization curve of undoped and F doped (Ir,Nb)O_2 along with commercial IrO_2 in the presence of 1 N H_2SO_4 solution at 40°C with a scan rate of 1 mV/sec before and after iR correction

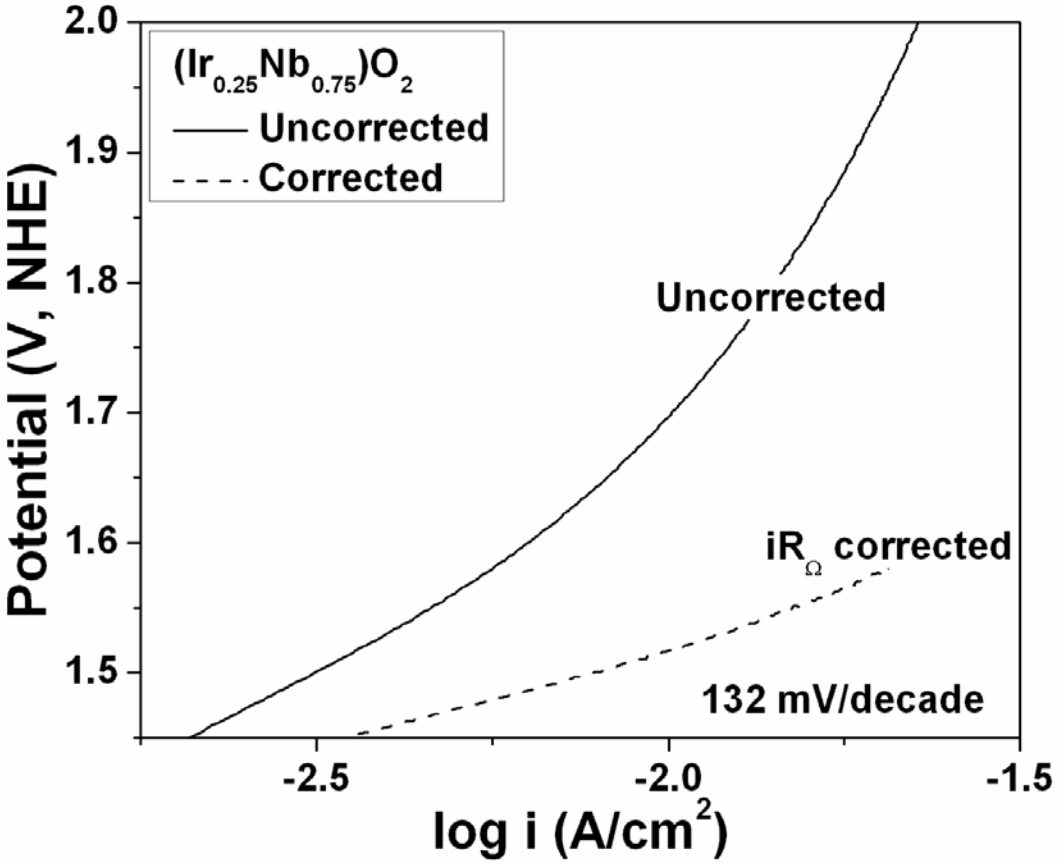

Figure 137. The Tafel plot of $(Ir,Nb)O_2$ before and after iR correction

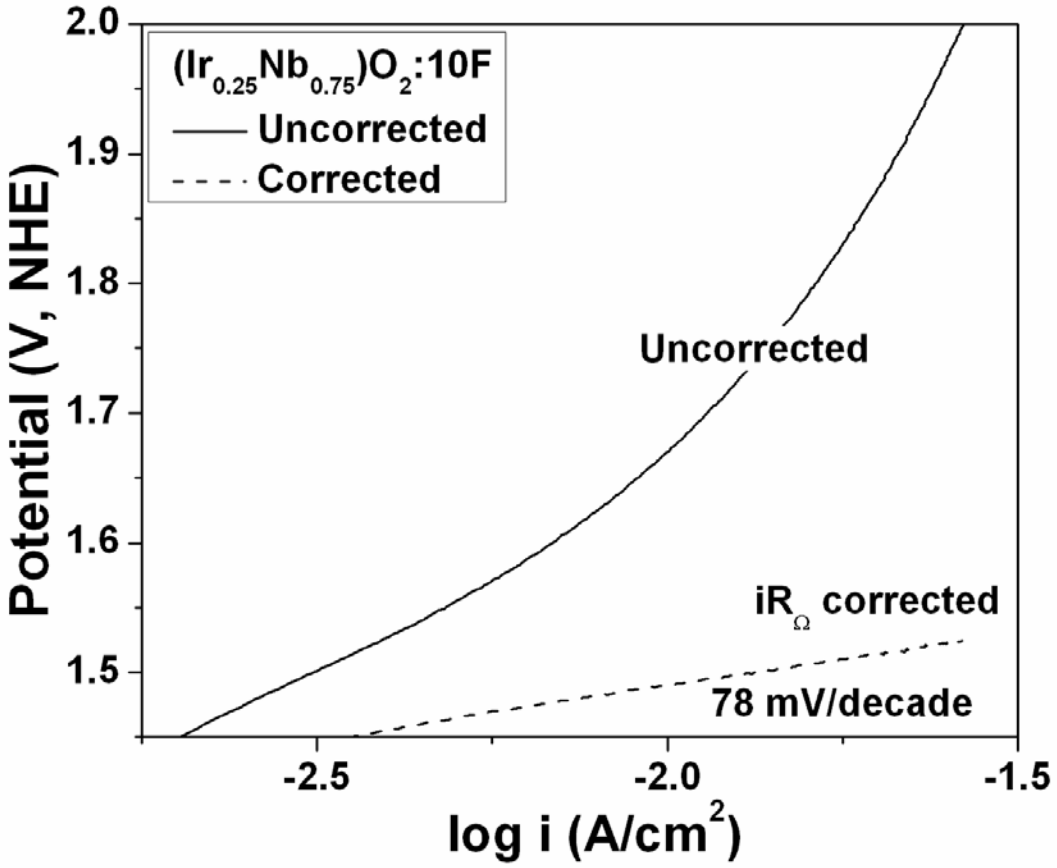

Figure 138. The Tafel plot of (Ir,Nb)O_2:10 wt.% F before and after iR correction

In order to examine the stability, chronoamperometry (CA) *i.e.* current measurement *vs.* time is conducted for 12 hours at a constant voltage of ~ 1.65 V (*vs.* NHE, without iR_Ω correction), to determine the degradation or loss of activity in CA studies. The CA curves of $(Ir_{0.25}Nb_{0.75})O_2$, $(Ir_{0.25}Nb_{0.75})O_2$:10 wt.% F and commercial IrO_2 are shown in **Figure 139**. The undoped $(Ir_{0.25}Nb_{0.75})O_2$ shows lesser initial current density because it inherently gives lesser catalytic activity than the doped catalyst and commercial IrO_2 (**Figure 136**). The decay of

current for the catalysts can be attributed to dissolution of coating at the edge of the porous titanium support [30], and by the induced loss of electrolyte [34, 57]. But, commercial IrO_2 undergoes a lot of degradation and gives a steep decrease in current over time showing its instability whereas a steady decay of current is observed for the $(Ir,Nb)O_2$:F electro-catalysts. This clearly suggests that Nb_2O_5:F support enhances the stability of IrO_2 to a very great extent.

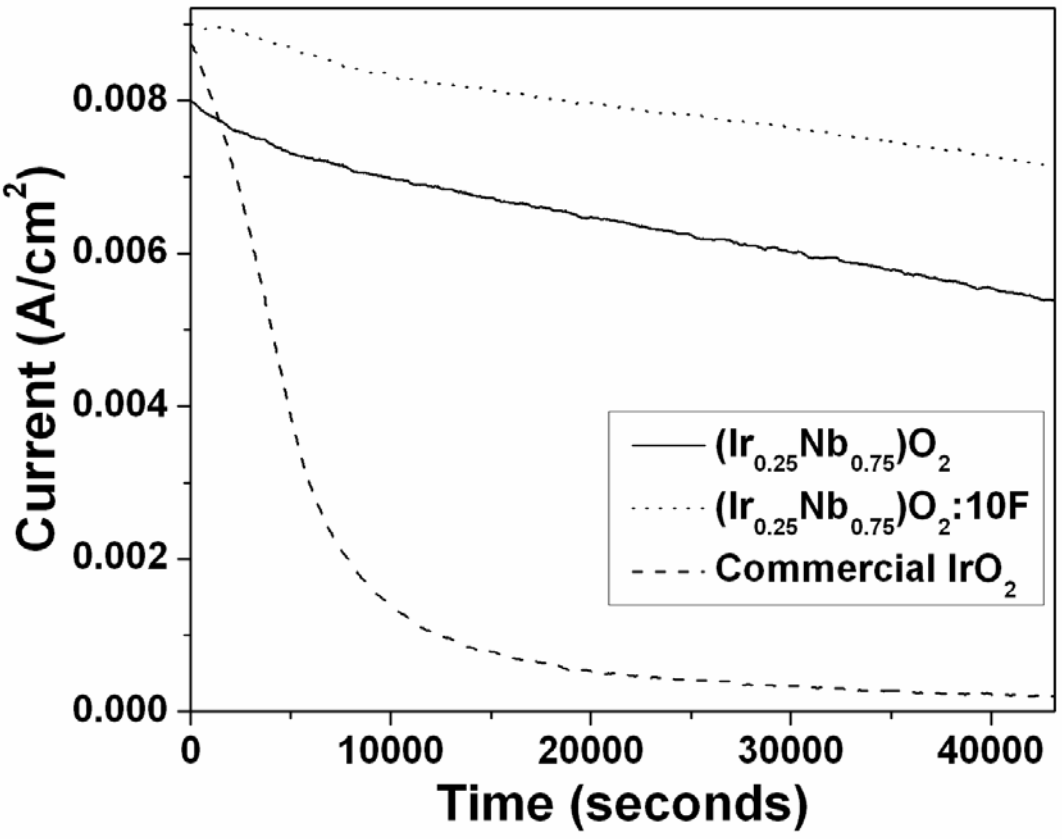

Figure 139. The variation of current *vs.* time for $(Ir,Nb)O_2$:F powders and commercial IrO_2 in the CA test performed in a 1 N H_2SO_4 solution at a constant potential of ~ 1.65 V

The ICP results conducted on the 1 N H_2SO_4 electrolyte solution after the CA measurement shows no presence of Ir and Nb for undoped and doped (Ir,Nb)O_2. However, commercial IrO_2 shows ~ 0.35 ppm of Ir leached out in the solution. This indicates that the decrease in current for the electro-catalysts may arise due to dissolution of the electro-catalyst from the surface.

After the conclusion of the CA test, the $(Ir_{0.25}Nb_{0.75})O_2$:10 wt.% F electrode was subject to polarization testing as seen in **Figure 140** in order to determine the activity of the electrodes after long term structural stability tests. The Tafel plot from the polarization curve (post CA measurement) after iR correction is shown in **Figure 141**. A Tafel slope of ~ 117 mV/decade was obtained for (Ir,Nb)O_2:10 wt.% F which is comparable to that of undoped IrO_2 after CA (~ 112 mV/decade) as seen in **Figure 104**. This test further demonstrates the robustness of the (Ir,Nb)O_2:F electro-catalyst.

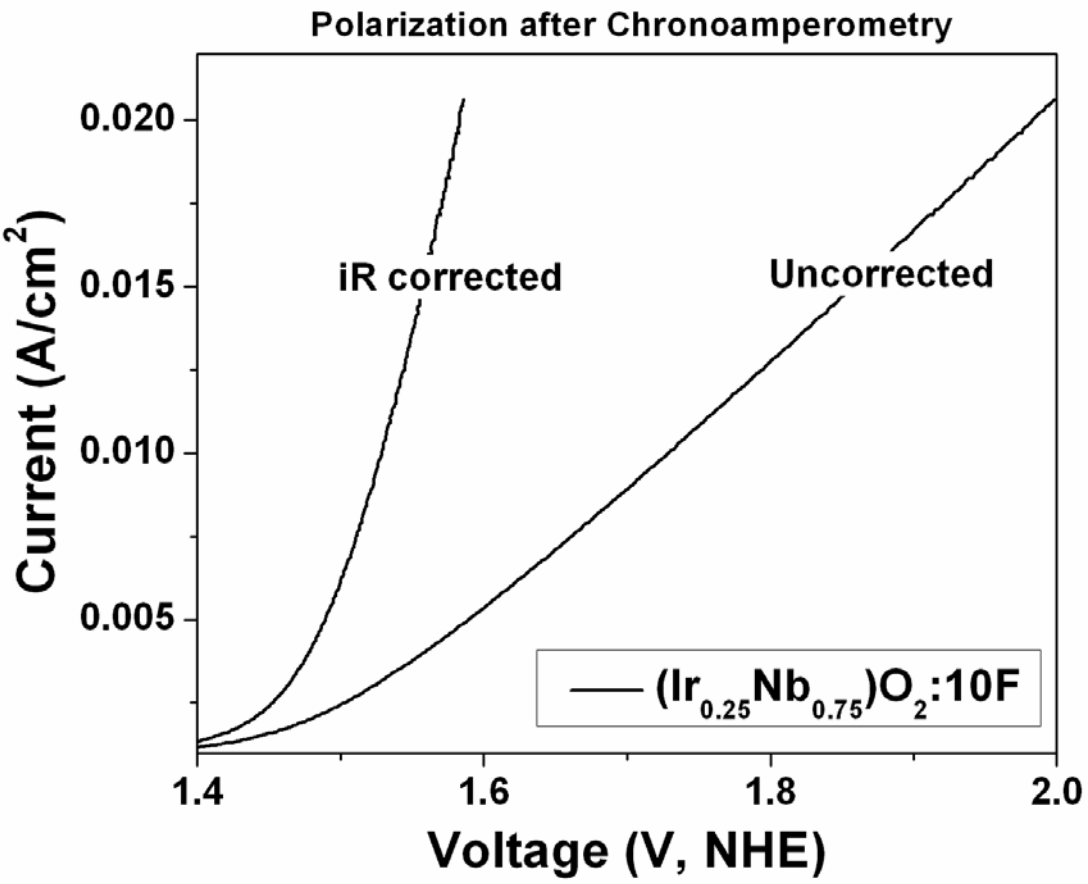

Figure 140. Polarization curve of (Ir,Nb)O_2:10 wt.% F powder after the CA test

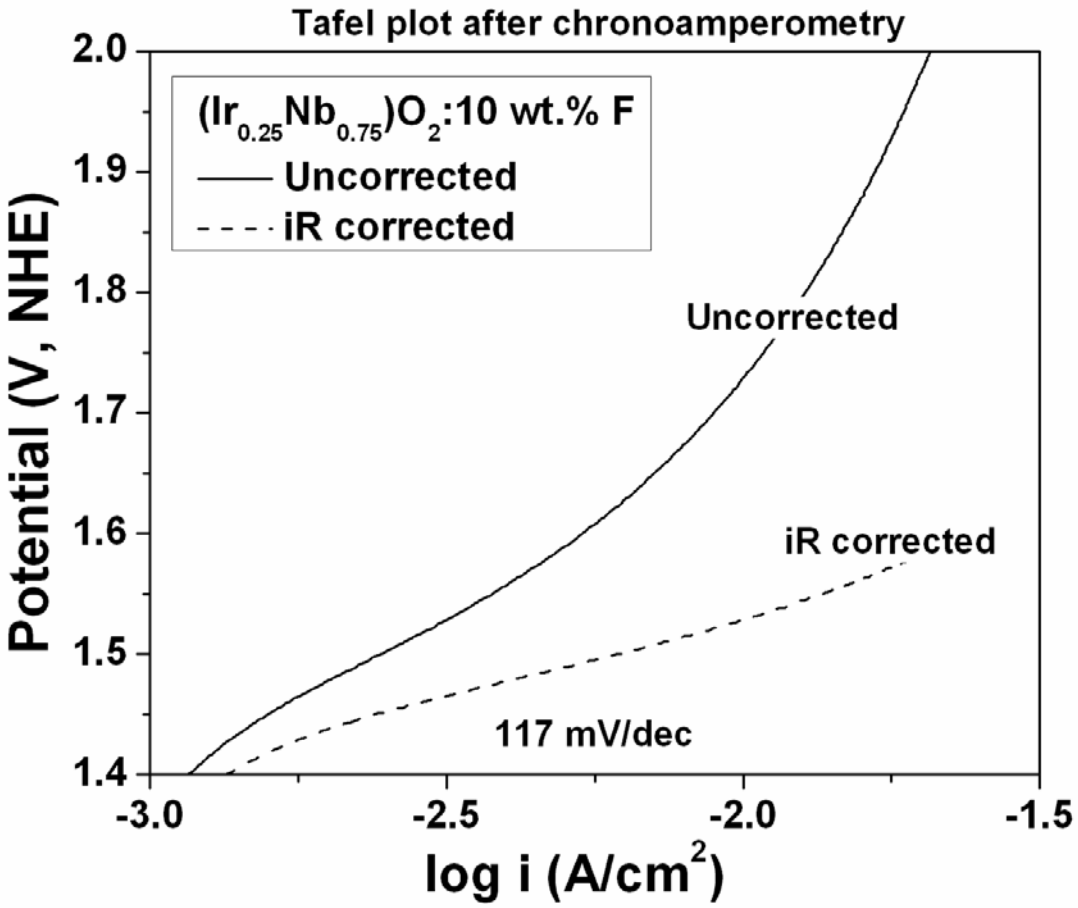

Figure 141. The Tafel plot of (Ir,Nb)O_2:10 wt.% F powder after the CA test

The best and optimized binary electro-catalyst compositions of ($Ir_{0.25}Nb_{0.75}$)O_2:10 wt.% F were studied and tested along with ($Ir_{0.3}Sn_{0.7}$)O_2:10 wt.% F at Proton OnSite in a single full cell set-up for PEM based water electrolysis. The polarization curve, shown in **Figure 142**, was obtained by ramping up and down the current at 1 minute intervals until the forward and reverse scans overlaid each other. It is seen that the (Ir,Nb)O_2:F exhibits much superior electro-catalytic activity than (Ir,Sn)O_2:F. The current density at ~ 2 V, a standard assessment voltage for single full PEM electrolyzer tests, is ~ 0.6 A/cm^2 and ~ 0.25A/cm^2 for ($Ir_{0.25}Nb_{0.75}$)O_2:10 wt.% F and

$(Ir_{0.3}Sn_{0.7})O_2$:10 wt.% F, respectively. Pure (undoped) IrO_2 shows a current of ~ 0.5 A/cm^2 at ~ 2 V as shown in **Section 5.2.1.2**. This implies that the reduced noble metal $(Ir,Nb)O_2$ catalyst is similar and comparable to pure IrO_2 and much better than $(Ir,Sn)O_2$:F. This might be due to the fact that no metal ions leach out in the stability test (chronoamperometry) for the binary $(Ir,Nb)O_2$:F catalyst as opposed to $(Ir,Sn)O_2$:F, where Sn leaches out to some extent (~ 0.12 ppm).

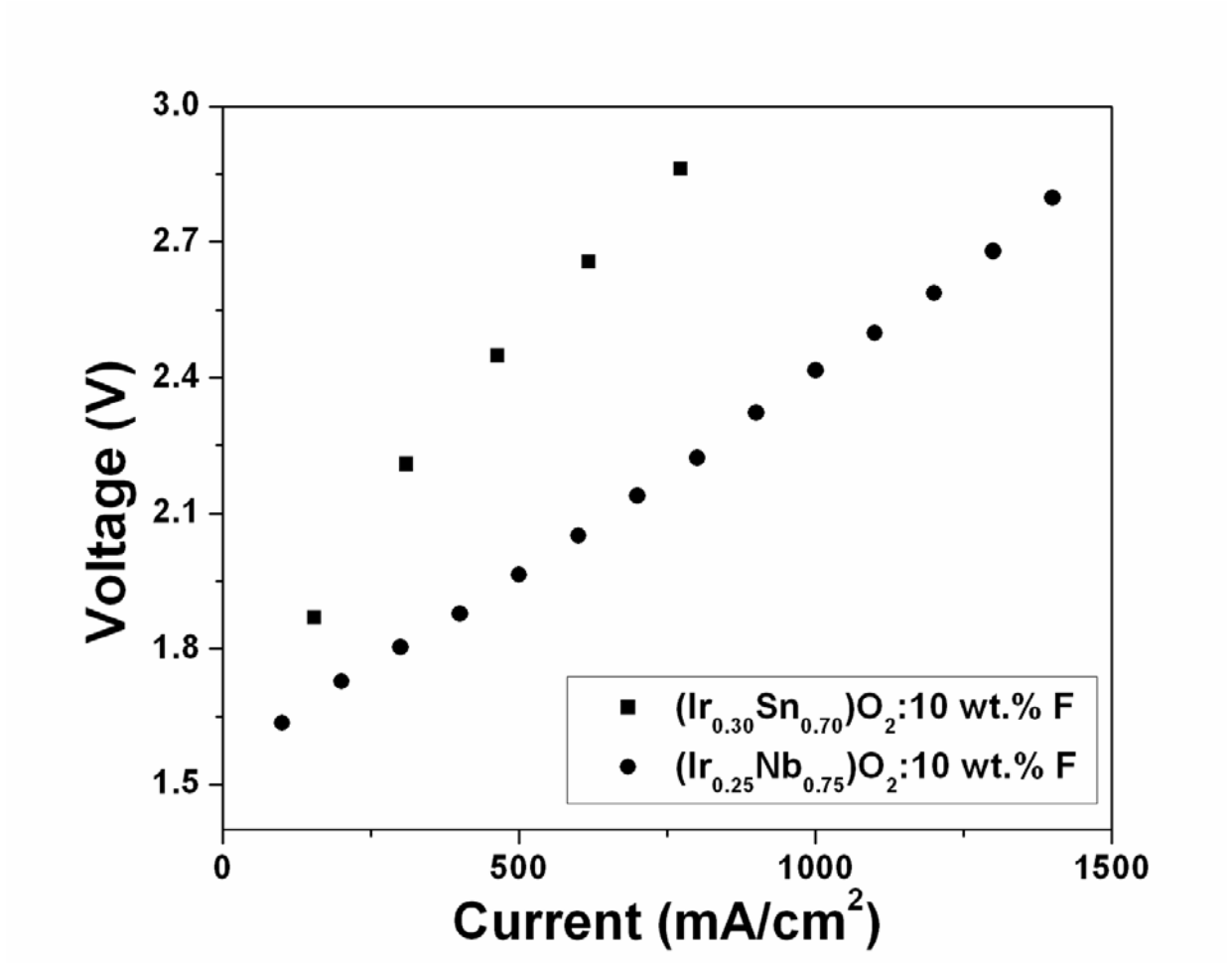

Figure 142. Polarization curve obtained in a single full cell PEM electrolyzer test for $(Ir,Nb)O_2$:F and $(Ir,Sn)O_2$:F powders at 50°C

In the present work, it is evident that the overall performance of $(Ir_{0.25}Nb_{0.75})O_2$:10 wt.% F catalyst is better than $(Ir_{0.3}Sn_{0.7})O_2$:F, and much superior to the commercially used pure IrO_2. This present study thus helps identify (Ir,Nb)O_2:F as a promising OER electro-catalyst with reduced noble metal oxide loading and increased catalytic performance, and chemical and structural stability.

6.0 FIRST PRINCIPLES CALCULATIONS

The Proton Exchange Membrane (PEM) water electrolysis cell consists primarily of a proton exchange membrane on which the anode and cathode are bonded. In a typical system, noble metal (*E.g.* Pt) or noble metal oxides (*E.g.* IrO_2) are utilized as catalysts for the anode with Pt being the catalyst for the cathode, respectively. Hydrogen is produced by supplying water to the anode decomposing into oxygen, protons, and electrons. At the cathode the electrons and protons re-combine to yield hydrogen gas. This is represented by the following equations:

Anode (oxidation): $2\ H_2O_{\ (l)} \rightarrow O_{2\ (g)} + 4\ H^+ + 4\ e^-$

Cathode (reduction): $4\ H^+ + 4\ e^- \rightarrow 2H_{2\ (g)}$

Overall Reaction: $2H_2O_{\ (l)} \rightarrow 2\ H_{2\ (g)} + O_{2\ (g)}$

The above reactions are primarily catalytically driven requiring the use of electro-catalysts as mentioned and discussed below. In order to develop electro-catalysts with high electrochemical activities, selectivity and stability, the fundamental dynamics of all the elementary processes occurring at the catalytically active sites must be understood. Modifications in the electronic structure of the system may strongly affect the thermodynamically stable intermediate states of the electrolytic process and hence, drastically change the overall catalytic activity of the material itself.

In the present day, using modern theoretical approaches *viz.*, Density Functional Theory (DFT), tremendous progress has been achieved in fundamental understanding of water splitting mechanisms in general and anodic oxygen evolution reactions in particular. Substantial effort in search of a single universal parameter describing catalytic activity of the given material has been made by Nørskov *et al.* [53, 54, 125, 126]. One of a very popular concept suggested by them was a position of the noble metal electronic d-band center serving as a simple descriptor for determining the catalytic activity of the surface. This descriptor has been defined as a gravity center of the d-band center of the noble metal ε_d usually located in the vicinity of the Fermi level. An optimal position of the d-band center thus provides an optimal interaction between the catalytic surface and the various species participating in the catalytic reactions predominantly occurring at the surface thus leading to an expected optimal catalytic activity [125, 126]. Later, they showed that transition metal as well as rutile oxide surfaces obey linear relations between O^* binding energy and the binding energy of other species relevant to the oxidation of water (OH^* and HOO^*) [53, 54]. Based in such relations they proposed a more reliable descriptor of the catalytic activity – the binding energy of O to the surface (ΔE_O). A volcano plot reflecting a dependence of the catalytic activity *vs.* ΔE_O demonstrated possible room for improving the electro-catalyst. Modifying electronic structure of the catalytic surface in such a way that binding energies of the intermediate species become more optimal in term of a position on the volcano plot may improve the catalytic activity to some extent.

All the first principle calculations reported herein have been done by *Dr. Oleg I. Velikokhatnyi*, a research faculty at University of Pittsburgh (*Dr. Kumta's Lab*). The theoretical studies complement the experimental results and help in the fundamental understanding of the catalytic activity and durability of the catalysts.

6.1 F DOPED IRIDIUM OXIDE

The present study is an attempt to reveal and analyze the reasons underlying the high electro-catalytic activity of fluorine doped IrO_2 synthesized by us [34]. Such a phenomenon needs to be analyzed and understood however; since this knowledge may prove to be vital in the design and development of novel electro-catalysts with excellent catalytic performance for PEM based electrolyzers.

It has been observed (**Figure 7**, **Figure 85** and **Figure 86**) that the onset potential is the same for all compositions of the IrO_2:F. The difference is in the slopes of the lines which points to the fact that the kinetics of the OER rather than thermodynamics is dependent on the F content. However, as a first approximation for determining just qualitative trend but not the precise value of the catalytic activity as a function of the F concentration, only the thermodynamic aspects of the problem have been considered. Various kinetic barriers such as effects of the electric field and surface charges as well as proton transfer barriers although quite important, would not probably significantly change the qualitative trends derived from the pure thermodynamic considerations. Only experimental in situ spectroscopy of surface intermediates combined with atomic-level analysis and a reliable theoretical computational framework will ultimately be able to resolve kinetic activation barriers, elementary steps, and nature of the active site of the OER on metal oxide surfaces [127].

6.1.1 Computational Methodology

In PEM based water electrolysis, the water splitting process in an acidic media where the corresponding anodic reaction mechanism similar to [53] could be sequentially written as follows:

$$2H_2O \rightarrow HO^* + H_2O + H^+ + e^-$$

$$\rightarrow O^* + H_2O + 2H^+ + 2e^-$$

$$\rightarrow HOO^* + 3H^+ + 3e^-$$

$$\rightarrow O_2 + 4H^+ + 4e^-$$

The * represents an active site on the metal oxide surface. Under acidic conditions due to the weak interactions between hydrogen and the metal cathode, hydrogen evolution is much faster on the cathode rather than oxygen evolution on the anode and hence cannot be considered to be the primary rate determining step of the overall catalytic activity [54].

Free energies ΔG of all the four anodic intermediate reactions described above determine electric potentials at which a certain specific reactions would occur. Thus a systematic analysis of all calculated free energies may elucidate the rate determining / limiting step of the electrolysis reaction which can serve as a measure of the electro-catalytic activity of the specific material that is under investigation. In order to obtain the free energies of all the intermediate reactions we will use an approach suggested and described in detail by Rossmeisl *et al.* [53, 54] and successfully applied for calculation of the catalytic activities of metals and metal oxides for water splitting. The general trend for the calculated over-potentials, such as $TiO_2 > IrO_2 > RuO_2$ appeared to be consistent with experimental observations although the absolute values are

slightly overestimated. Detailed analysis of the results may help understand role of fluorine in contributing to the improvement of the observed catalytic activity of IrO_2.

For the calculations, the reference potential was set to be that of the standard hydrogen electrode, in order to relate the chemical potential (the free energy per H) for ($H^+ + e^-$) to that of ½ H_2 in the gas phase. At pH 0 in the electrolyte and 1 bar of H_2 in the gas phase at 25°C, the reaction free energy of ½ $H_2 \rightarrow H^+ + e^-$ is zero at zero electrode potential. At standard conditions, the free energy ΔG_0 of the reaction $^*AH \rightarrow A + H^+ + e^-$, can be calculated as the free energy of the reaction $^*AH \rightarrow A + ½ H_2$.

ΔG_0 is represented as the following: $\Delta G_0 = \Delta E + \Delta ZPE - T\Delta S$. The reaction energy ΔE is calculated using density functional theory (DFT). The zero point energy correction (ΔZPE), and change in entropy (ΔS) is calculated using DFT calculations of the vibrational frequencies taken from Kandoi *et al.* [128] and from the standard tables for gas phase molecules [129]. For the adsorbed O, OH and OOH species, the corrections are 0.05 eV, 0.35 eV and 0.4 eV, respectively. H_2O and H_2 in the gas phase are used as references states. Also, the entropy for gas phase water is calculated at 0.035 bars since this is the equilibrium pressure in contact with liquid water at 298 K. The free energy of gas phase water at these conditions is equal to the free energy of liquid water. ΔG_0 of the total reaction is fixed at the experimental value of 2.46 eV to avoid the calculation of the O_2 bond energy which is difficult to calculate accurately with DFT.

All the DFT calculations have been conducted using the generalized gradient approximation (GGA) for the exchange-correlation energy functional in a form suggested by Perdew and Wang [130]. The projector augmented wave (PAW) method and a plane wave basis set, as implemented in the Vienna Ab initio Simulation Package (VASP) has been used [131-133]. The atomic positions and the cell parameters, including the cell volume, are optimized by

minimizing the forces and stresses *via* the Hellmann - Feynman theorem. Standard PAW potentials were employed for the elemental constituents of all pure and doped compounds. For all the materials considered the plane wave cutoff energy of 520 eV has been chosen to maintain a high accuracy of the total energy calculations. The lattice parameters and internal positions of atoms were fully optimized during the double relaxation procedure employed, and consequently, the minima of the total energies with respect to the lattice parameters and internal ionic positions have been correspondingly determined. This geometry optimization was obtained by minimizing the Hellman - Feynman forces *via* a conjugate gradient method, so that the net forces applied on every ion in the lattice is maintained close to zero. The total electronic energies were converged within 10^{-5} eV/unit cell resulting in the residual force components on each atom to be lower than 0.01 eV/Å/atom, thus allowing for the accurate determination of the internal structural parameters. Bader charges were calculated by integrating electron densities within zero flux surfaces around nuclei and are converged to within 0.1 e compared to a grid 1.5 times denser along each lattice vector [134].

A surface covered with oxygen is chosen in contrast to the OH^* covered surface, since such a surface is less active and less stable than the O^* covered surface [53]. Thus, the rutile type (110) preferred surface covered with oxygen has been chosen for calculation of the free energies for undoped IrO_2 and with fluorine atoms located at the surface. The 2 x 2 surface unit cell for a symmetric 7 layer slab ~ 10.3 Å thick separated between its images perpendicular to the surface direction by vacuum space of ~ 20 Å, to prevent interaction between the slab and its adjacent images. All intermediate species such as O^*, OH^*, and OOH^* have been attached to the coordinated unsaturated sites on both sides of the slab. Three middle layers were fixed with the lattice parameter corresponding to the bulk IrO_2, while all other layers of the slab together with

the intermediate species were fully relaxed. Hence, all the numerical data obtained from such a model should be divided by two. **Figure 143** shows a unit cell chosen for the calculations in the present study. Three different atomic distributions of F as a replacement of oxygen in the unit cell have been considered to analyze the difference between the electronic structures of pure and doped IrO_2 compounds as well as to assess the role and contribution of F on the catalytic activity. The first F atomic distribution consists of only one F atom located in place of oxygen and denoted with a number 1 in **Figure 143**. The second distribution is characterized by the introduction of an additional F atom marked with the number 2. And finally, the third arrangement of the F atoms in the unit cell consists of three F atoms positioned at all three places marked with the numbers 1, 2, and 3. Furthermore, in the text we will refer to these three F-configurations as F1, F2, and F3, respectively. Such unit cells covered by adsorbed oxygen monolayer together with intermediate species at the surface were used for calculations of the free energies of all the four elementary reactions.

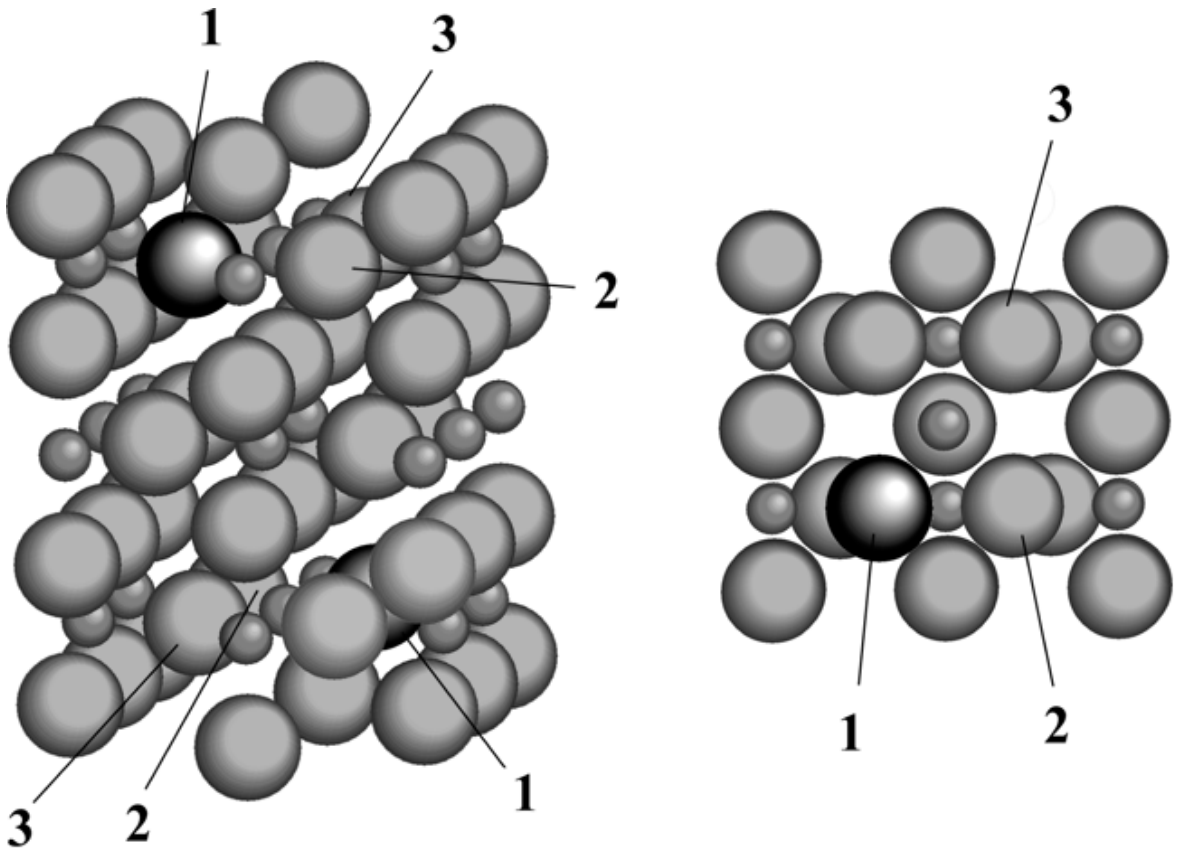

Figure 143. Angle and top view of the elementary unit cell of the (110) rutile surface slab used: small - Ir, big - O, dark: F (for F1 configuration). Atoms denoted as 2 and 3 correspond to F2 and F3 configurations of fluorine distributions

6.1.2 Theoretical Discussion

The resulting free energies for all the four intermediate reaction steps for pure IrO_2 are presented in **Figure 144**. One can see that the third step of the stairs for undoped IrO_2 has a largest value of 1.51 eV and corresponds to the formation of HOO^* at the surface. This step can be considered as truly rate limiting because an applied potential not less than 1.51 V is required to render all the

four reactions to be exothermic and to force the overall water-splitting process to proceed on the surface. These results agree quite well with the literature [53] wherein the authors also confirmed the third step as rate limiting, although with higher overpotential (~ 0.56 V). The overpotential obtained in the present study is lower (~ 0.28 V) and is more close to the experimentally obtained value (~ 1.43 V). The seemingly large difference between the experimentally observed and calculated results can be attributed to a difference between the models of the surface slabs used in these two studies.

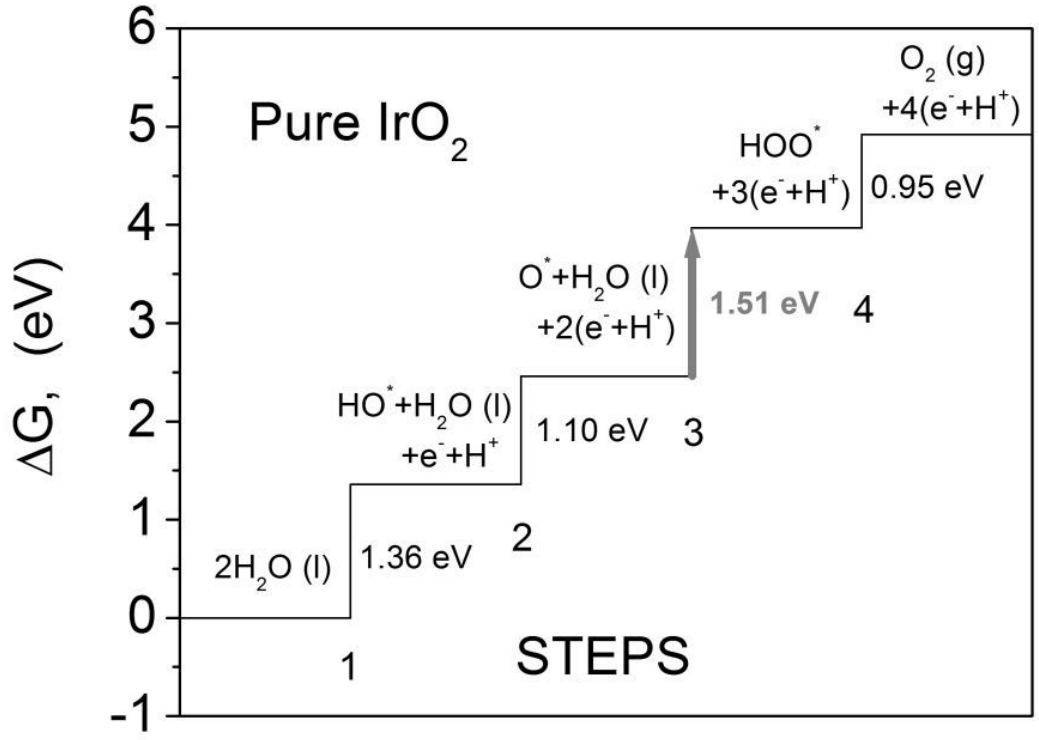

Figure 144. Free energies of the intermediate reactions for pure IrO_2

Quite similar energetics to pure IrO_2 are observed for F doped IrO_2 with different F distributions shown in **Figure 145**. For all the three cases again the formation of HOO^* is the largest step as that calculated for pure IrO_2 although with lower values than that calculated for the undoped oxide. One can see that the corresponding values of the HOO^* formation for all F configurations are less than that of pure IrO_2 and decrease with gradual F content increments in the material. Corresponding overpotentials for F1, F2, and F3 configurations are 0.21, 0.15, and 0.11 V, respectively. This rather noticeable decrease in the overpotential for F doped IrO_2 in comparison with pure IrO_2 (~ 0.28 V) indicates an increase in the catalytic activity in the presence of fluorine in the oxide matrix, which correlates well with the experimental data.

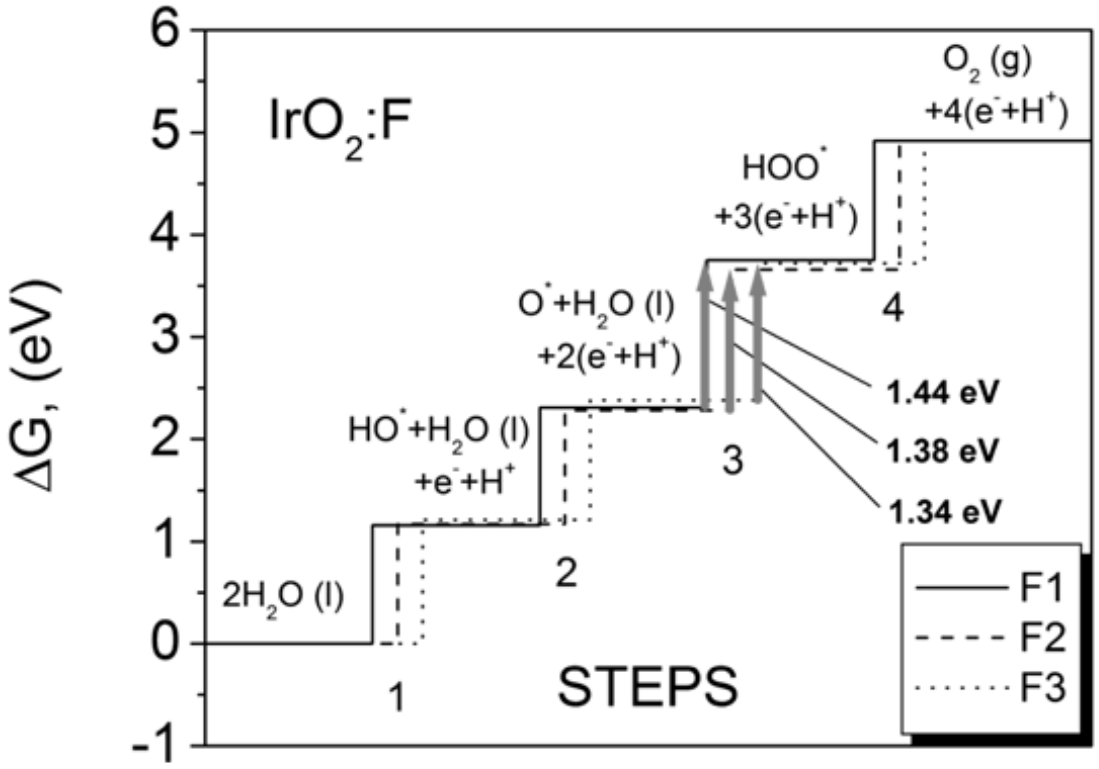

Figure 145. Free energies of the intermediate reactions for F doped IrO_2

Such a decrease in the energy difference for the third elementary step in the case of F doped IrO_2 is due to a stronger interaction between the adsorbed oxygen O^* and the surface. As a result, there is a decrease in the total energy of the system in comparison with undoped IrO_2, making it more feasible for the species to adsorb at the surface, consequently rendering the system more electrochemically active. Such an enhancement in adsorption could be understood from consideration of the effective ionic charges by means of the Bader charge analysis conducted in the present study. Using this technique [134], the total electronic charges of the constituent ions of the intermediates and adjacent ions on the pure and F doped IrO_2 surfaces are calculated. **Table 10** summarizes the effective electronic charges for the terminating oxygen atoms $^*O$ in all intermediates as well as for F ion adjacent to these $^*O$ atoms in case of F1 doped surface and charges for O ions located at the same site as F but in the pure IrO_2. One can see that F charges are systematically smaller than those of substituted oxygen ones. This charge reduction leads to decrease of the partial electrostatic repulsion between F doped surface and the intermediates. The electrostatic energy is directly proportional to the product of the charges, so that we can roughly estimate contribution of such repulsion to the total energy of the system. The next line in **Table 10**, q($^*O$)q(O)/q($^*O$)q(F), contains products of the corresponding charges for pure and doped surfaces. One can see that in case of F doping such products are lower than that for pure IrO_2 due to a smaller effective F ion charge. Since the electrostatic repulsion generally contributes towards destabilization of the interatomic interactions, one can conclude that F doping decreases the repulsive component of the total energy making the system more stable with stronger binding between F doped surface and all intermediate species.

Table 10. Bader charges of the terminated oxygen ions $^{*}O$ adsorbed to the pure and F doped surfaces for $^{*}OH$, $^{*}O$ and $^{*}OOH$

	$^{*}OH$		$^{*}O$		$^{*}OOH$	
	IrO_2	**F1**	**IrO_2**	**F1**	**IrO_2**	**F1**
$^{*}O$--	-1.35	-1.36	-0.62	-0.64	-0.42	-0.39
O / F	-0.76	-0.60	-0.75	-0.61	-0.79	-0.59
q(*O)q(O) / q(*O)q(F)	1.03	0.82	0.465	0.39	0.33	0.23
Δ	-0.21		-0.075		-0.10	

But, making the binding stronger does not necessarily lead to lowering the rate limiting step or ΔG. The relative difference between ΔG_{OOH} and ΔG_O for F doped surface must be lower than that for undoped material. In **Table 10**, the last line contains differences between corresponding charge products for F doped and pure surfaces. Such a difference could be considered as a qualitative measure of change in the electrostatic repulsive contribution into the free energy ΔG of the system in each intermediate step. The change of the charge product for $^{*}O$ contributing to lowering ΔG_O is smaller than the same quantity contributing to ΔG_{OOH} (- 0.075 *vs.* - 0.10) resulting in the overall decrease of the relative difference ΔG_{OOH} - ΔG_O. Thus, decreasing the free energy for splitting of the second water molecule with the formation of the HOO^{*} intermediate on the surface lowers the energy for the rate limiting step and correspondingly enhances the overall catalytic activity of the material.

For qualitative estimation of the structural and electrochemical stability of the F-doped IrO_2, the binding energy of F^* atom at the surface layer as well as the cohesive energy E_{coh} of the material has been calculated. Since the reaction $F_{2\,(g)} + 2\,H^+ + 2\,e^- \rightarrow 2\,HF_{(aq)}$ occurs at 3.05 V [135], considering $F_{2\,(g)}$ and $H_{2\,(g)}$ as reference states it seems plausible to determine whether F would be more stable on the surface or in the acidic form by means of comparison of the binding energy of F^* at the mentioned standard potential (3.05 V). In other words, if the binding energy of F^* is greater than - 3.05 eV, it would mean that F remains on the surface and does not dissolve into the acidic solution. The following relation for F^* binding energy has been used:

$$E_{bind}(F^*) = E(F^*) - [\,E(^*) + \tfrac{1}{2}\,E(F_2)\,]$$

Here, $E(F^*)$ and $E(^*)$ are the corresponding total energies of the slabs with fluorine atom and without it. $E(F_2)$ is the calculated energy for the isolated F_2 molecule. The corresponding calculation of E_{bind} (F^*) gives the value of - 3.96 eV, which is noticeable larger than the surface stability limit of - 3.05 eV. This result is confirmed by the chronoamperometry experiments conducted for a series of IrO_2:F with different F content in 1 N H_2SO_4 as shown in **Figure 9** and **Figure 102**. The calculations of the cohesive energies of the bulk materials with different F concentrations demonstrated slight decrease of E_{coh} with increase in the F content. It originates from lower Ir - F bond energies than Ir - O due to the reduced charge of F ions (bond lengths for Ir - O and Ir - F are 2.12 Å and 2.37 Å, respectively).

6.2 F DOPED IRIDIUM - TIN OXIDE

6.2.1 Computational Methodology

In this study, the thin film of $(Ir,Sn)O_2$ doped with F has been considered to exhibit the rutile structure with a tetragonal unit cell and space group P42/mnm following experimental validation. The rutile structure of $(Ir,Sn)O_2$:F thin film electrode has been confirmed experimentally from XRD analysis (**Figure 10** and **Figure 109**). This unit cell has been chosen as the basis for construction of the different super cells corresponding to the specific Ir, Sn and F concentrations of the oxide solid solution. To facilitate convenient calculations, the basic composition has been chosen as 25 at.% IrO_2 - 75 at. %SnO_2 . Such 25/75 composition although slightly different from the experimental ratio allows selection of smaller representative super-cells for all the calculation of bulk and surface electronic structures employed in the present study. Thus, $(Ir_{0.25}Sn_{0.75})O_2$ compound doped with different amounts of F has been considered for theoretical evaluation of the electronic conductivity, structural and electrochemical stability and catalytic activity.

For bulk calculations, the super cell has been chosen as the double rutile unit cell with four metals and eight oxygen atoms in the unit cell. Fluorine doping was simulated by replacing corresponding number of oxygen atoms with F according to the general formula unit as $(Ir_{0.25}Sn_{0.75})O_{2-x}F_x$, where x = 0, 0.5, 1.0, 1.5 corresponding to 0, 5.6, 11.0, and 16.4 wt.% F, respectively. For calculation of the (1 1 0) surface electronic properties of the materials, a two - dimensional slab repeated in (1 -1 0) direction with 36 atom unit cell and a vacuum distance ~ 12 Å between adjacent images of the slab was selected.

For calculating the total energies, electronic structure and density of electronic states the Vienna Ab-initio Simulation Package (VASP) was used within the projector-augmented wave (PAW) method [131-133] and the generalized gradient approximation (GGA) for the exchange-correlation energy functional in a form suggested by Perdew and Wang [130]. This program calculates the electronic structure and *via* the Hellmann - Feynman theorem, the inter-atomic forces are determined from first-principles. Standard PAW potentials were employed for the elemental constituents and the Ir, Sn, O and F potentials thus contained nine, four, six and seven valence electrons, respectively.

For all the materials considered, the plane wave cutoff energy of 520 eV has been chosen to maintain a high accuracy of the total energy calculations. The lattice parameters and internal positions of atoms were fully optimized employing the double relaxation procedure, and consequently, the minima of the total energies with respect to the lattice parameters and internal ionic positions have been determined. This geometry optimization was obtained by minimizing the Hellman - Feynman forces *via* a conjugate gradient method, so that the net forces applied on every ion in the lattice are close to zero. The total electronic energies were converged within 10 - 5 eV/un.cell resulting in the residual force components on each atom to be lower than 0.01 eV/Å/atom, thus allowing for an accurate determination of the internal structural parameters for the oxide. The Monkhorst - Pack scheme was used to sample the Brillouin Zone (BZ) and generate the ***k*** point grid for the solids and the different isolated atoms used in the present study. A choice of the appropriate number of ***k*** points in the irreducible part of the BZ was based on convergence of the total energy to 0.1 meV/atom.

It should also be noted that for Ir-Sn-O-F compositions, the corresponding atomic distributions are ambiguous and can be represented by different spatial configurations. To

eliminate this uncertainty several atomic configurations for each given composition have been constructed and only those configurations corresponding to minimal total energies have been selected for further numerical investigations of these specific compositions of the binary oxides. The elementary unit cells for bulk and surface calculations for $Ir_{0.25}Sn_{0.75}O_{1.5}F_{0.5}$ is presented in **Figure 146**.

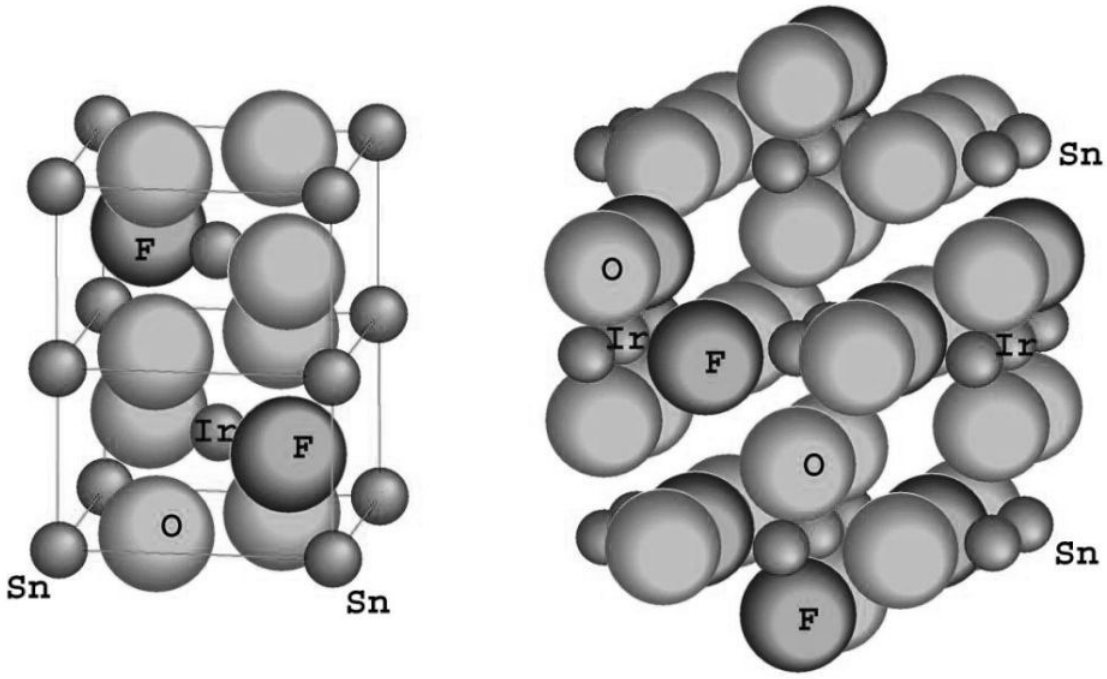

Figure 146. The unit cells for bulk (left) and (110) surface (right) calculations used for the atomic configuration of $Ir_{0.25}Sn_{0.75}O_{1.5}F_{0.5}$

6.2.2 Theoretical Discussion

The experimental results indicate that formation of single phase rutile type solid solution of F doped $(Sn_{0.80}Ir_{0.20})O_2$ with reduced Ir content and incorporation of F has a tremendous impact on the electrochemical activity (**Figure 16** and **Figure 119**) as well as the stability (**Figure 21** and **Figure 123**). The remarkable electrochemical activity of $(Ir,Sn)O_2$:F with 10 wt.% F is expected to depend on the electronic structure as well as electronic conductivity of the electrode since no significant change in structural parameters of molar volume and crystallite size with addition of different amount of F is observed. Improvement in electronic conductivity of F doped SnO_2 is well known and it has also been reported that 10 wt.% F exhibits the lowest resistivity [76, 77]. From a theoretical perspective, the effect of composition on the electronic structure in general, and the electronic conductivity with increase in F concentration in the oxide can thus be considered as one of the factors contributing to the improved electrochemical performance.

There are various published theoretical studies on pure IrO_2 and the electronic structure of the oxide is widely presented in the literature [78, 79, 136]. Furthermore, considering that IrO_2 is the gold standard for OER catalysts, a comparison of the IrO_2 electronic structure with that of $(Ir,Sn)O_2$:F oxides would certainly help provide insight into the role of fluorine in the context of the improved electrochemical performance observed. A systematic computational study was conducted to investigate the electronic properties of the solid solution of $(Ir_{0.25}Sn_{0.75})O_2$ doped with different F amounts. The total energy, electronic and optimized crystal structures, together with the total and projected densities of electronic states has been calculated using the first principles approach within the density functional theory. An effect of the introduction of F into

$(Ir,Sn)O_2$ on the electronic conductivity and the structural stability as well as the Ir d-band center position with increase in F concentration in the oxide is also discussed.

The total and projected densities of electronic states calculated for pure IrO_2 are shown in **Figure 147**. The main energy band structure of IrO_2 consists of two bands. The low energy band between - 19.2 eV and - 17.5 eV is composed of the 2s states of oxygen and the wide valence band around Fermi level consists of hybridized O 2p - Ir 5d states with two prominent peaks; correspond to the O 2p and Ir 5d states, thus contributing to the well known metallic conductivity of IrO_2. Incorporation of Sn into the IrO_2 matrix is however likely to augment the electronic properties of the compound and hence, the electronic structure of the bulk as well as the electronic structure of the most stable (1 1 0) surface have been calculated for $(Ir_{0.25}Sn_{0.75})O_{2-x}F_x$ with x = 0, 0.5, 1, and 1.5. The total electronic densities of states for all these compositions are correspondingly shown in **Figure 148**. It is seen that all of the compounds demonstrate metallic behavior although to different extents. Since in general, metallic conductivity is proportional to the density of states at Fermi level $n(E_F)$, it provides an opportunity to qualitatively evaluate the correlation between F concentration and the electronic conductivity of the oxide. **Figure 149** depicts the dependence of $n(E_F)$ *vs.* composition for $(Ir,Sn)O_2$:F. For comparison, the value of $n(E_F)$ are normalized to electrons per one $(Ir,Sn)O_2$:F formula unit. The graph clearly shows the reduction in conductivity of pure IrO_2 to $(Ir_{0.25}Sn_{0.75})O_2$ with IrO_2 introduction into the SnO_2 lattice representing a decrease in Ir-content of 0.25 atoms per formula unit. However, the incorporation of fluorine improves the conductivity drastically to an optimal value almost matching that of pure IrO_2 rendered at a F content of ~ 10 - 11 wt.% in the oxide.

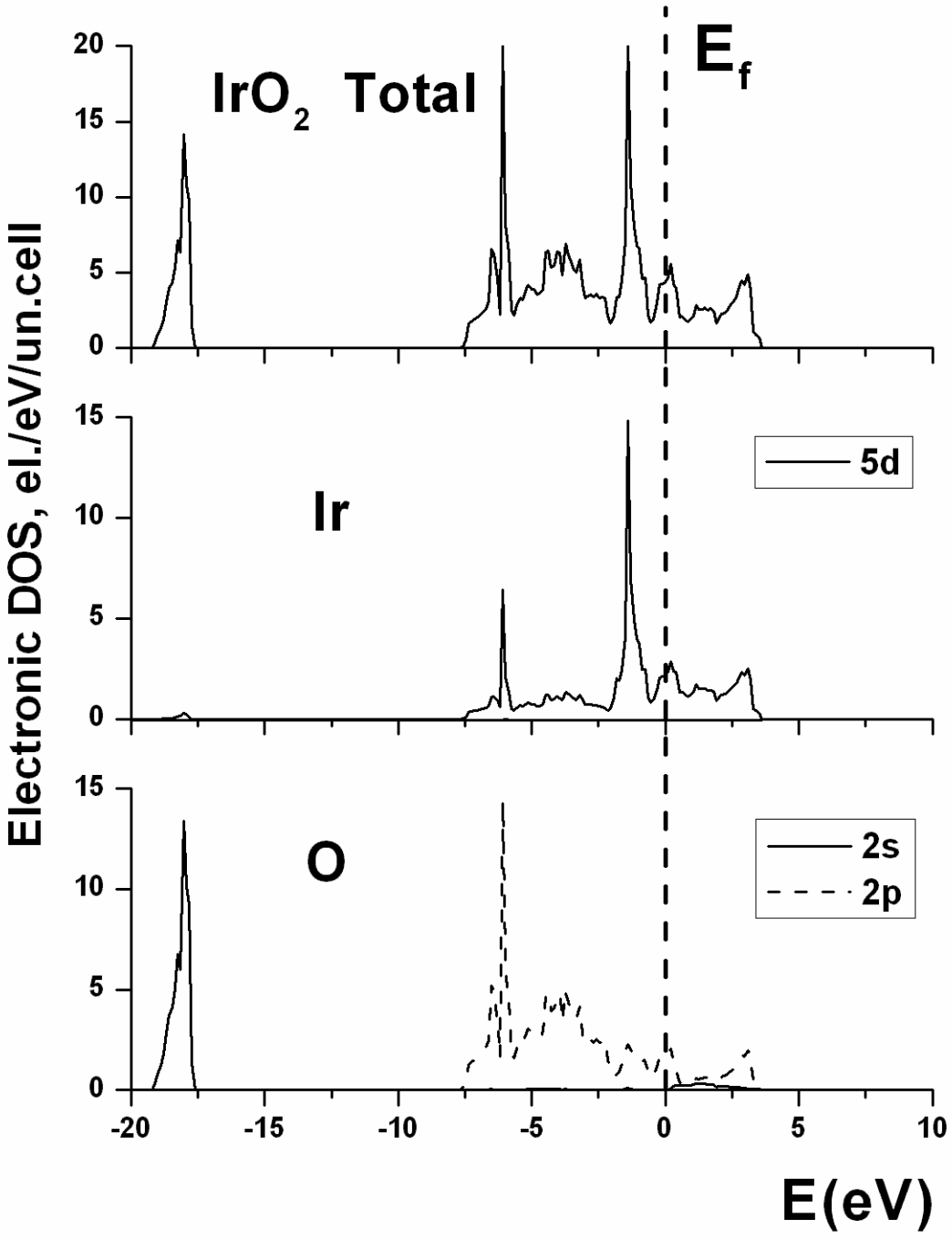

Figure 147. Total and partial density of states for IrO_2

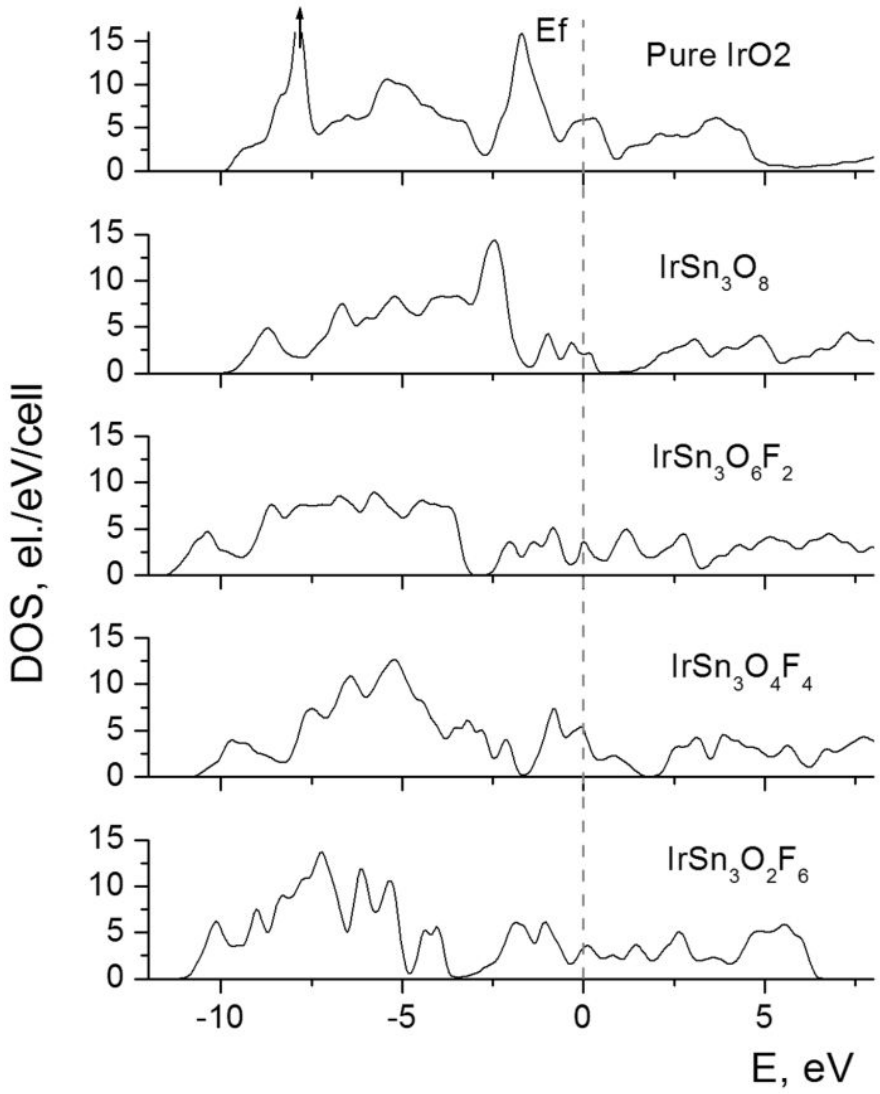

Figure 148. Total density of states for IrO_2 and $(Ir,Sn)O_2$:F

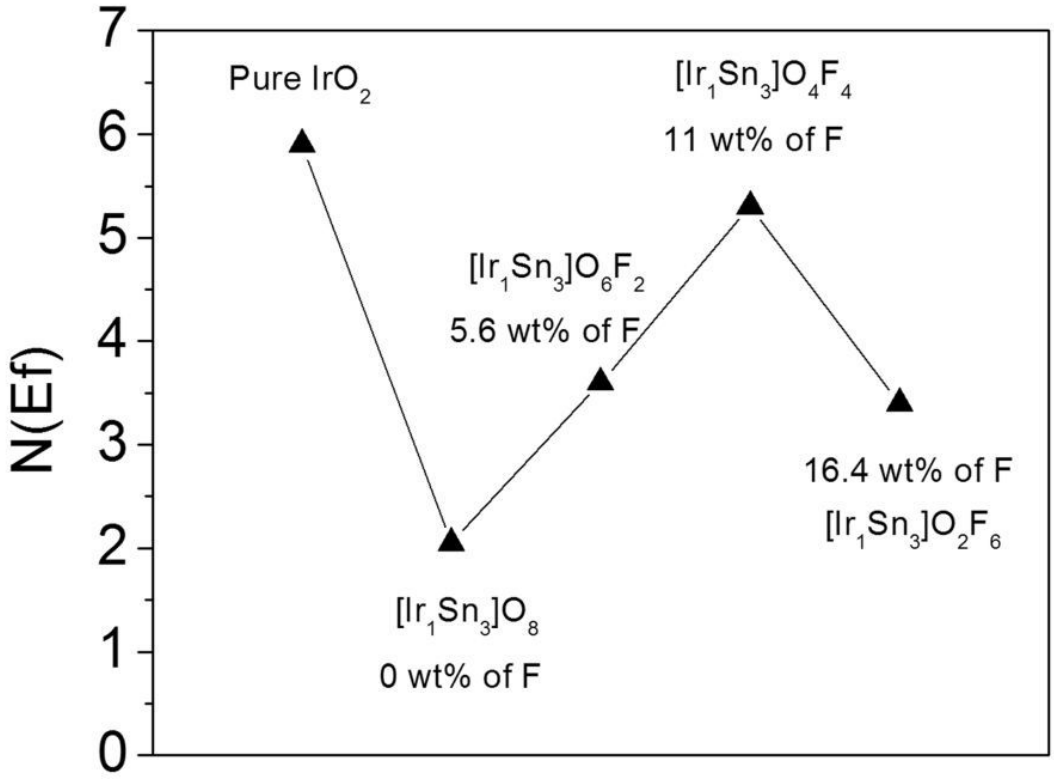

Figure 149. Density of states at Fermi level for $(Ir,Sn)O_2$:F

In recent years, a wide spread concept has been proposed by Nørskov *et al.* [125, 126] has been used effectively to define the catalytic activity of the surface. This descriptor has been defined as a gravity center of the d-band center of the noble metal ε_d usually located in the vicinity of the Fermi level. An optimal position of the d-band center thus provides an optimum highly favorable interaction between the catalytic surface and the various species participating in the catalytic reactions predominantly occurring on the surface leading to an expected maximum catalytic activity. Thus, such an interaction should be considered "just appropriate" implying leading to a moderate effect allowing the reagents and products to both adsorb at the surface and

also desorb most efficiently. Hence, an adjustment of the d-band center position with respect to the Fermi level may likely play a critical role contributing to the design of novel highly active and electrochemically stable electro-catalysts discussed herein.

In the present study the electronic structure of the stable (1 1 0) surfaces for all the $(Ir,Sn)O_2$ has been calculated and the positions of the corresponding Ir d-band centers have been obtained as a first moment of $n_d(E)$: $\varepsilon_d = \int n_d(E)E\mathrm{d}E \,/\, \int n_d(E)\mathrm{d}E$. **Figure 150** shows the partial Ir d-band densities of states together with the corresponding centers of these zones marked with vertical arrows on the graphs. One can see that the d-center for pure IrO_2 is located at ~ 1.33 eV below the Fermi level. This position was considered as a reference point for comparison of the catalytic activities of the other oxides considered in this study. Introduction of substantial amount of Sn (namely, 75 at %) to the oxide results in hybridization between Sn 5s, 5p and Ir 5d states leading to a shift of the Ir d-band center up to the position at - 0.75 eV below the Fermi level indicating that in general, an overall chemisorption reaction of the different species reacting at the surface is noticeably stronger for this composition rather than for pure IrO_2.

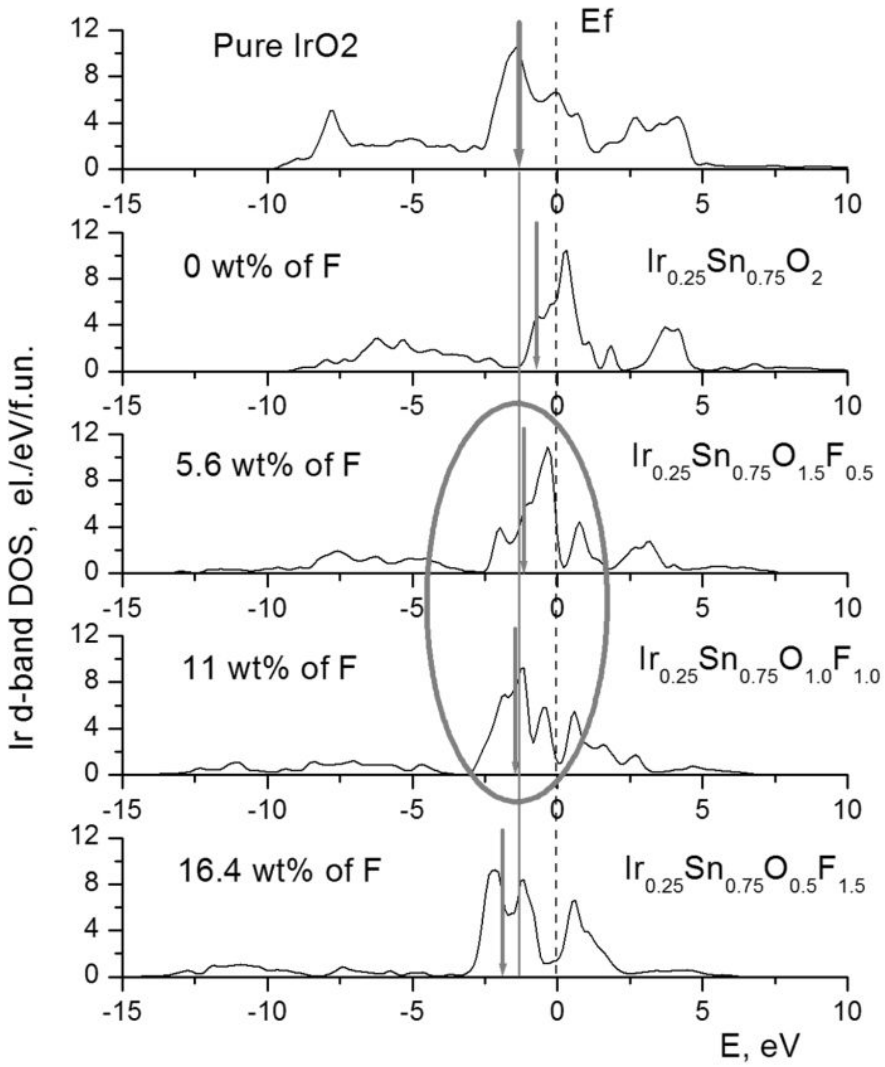

Figure 150. Ir d-band partial density of states for IrO_2 and $(Ir,Sn)O_2$:F. The arrows denote positions of the d-band centers (ε_d)

Assuming pure IrO_2 the gold standard OER catalyst demonstrates optimal catalytic activity corresponding to ε_d = - 1.33 eV one can therefore suggest that a significant drop in the activity observed experimentally for the undoped $(Ir,Sn)O_2$ (**Figure 16** and **Figure 119**) could be

most likely explained by the positive shift of the Ir d-band center deviating the catalytic activity from its optimal value. Such a behavior of the d-band center could be attributed to the complex hybridization of the electronic Ir d states and corresponding s and p states of Sn and O during the solid solution formation of the two binary oxides. Further consideration of the effects of fluorine doping in the formation of the electronic structure in general, can be explained in terms of this shift of the d-band center.

Figure 151 shows the total and partial density of states for $(Ir_{0.25}Sn_{0.75})O_{1.0}F_{1.0}$. Introduction of fluorine manifests in an appearance of the F 2p band mostly below - 5 eV with negligible amount of other states in the entire energy domain. Increase in F content results in more pronounced 2p states leading to a stronger hybridization effect between F 2p and Ir 5d states. As a result, the Ir d-band center location moves from - 0.75 eV for the non-fluorine composition downward towards the position corresponding to pure IrO_2 (- 1.33 eV) with increase in the F content. Thus, it is observed from **Figure 150** that at 5.6, 11 and 16.4 wt% of F, the d-band center passes accordingly through - 1.23 eV, - 1.41 eV and - 1.87 eV positions, respectively; indicating significant improvement in the overall catalytic activity with increase in the F concentration. The optimal F concentration at which the d-center of $(Ir,Sn)O_2$:F returns back to the position corresponding to pure IrO_2 can therefore be expected to be around 9 - 10 wt.% F which is in excellent agreement with our experimental results.

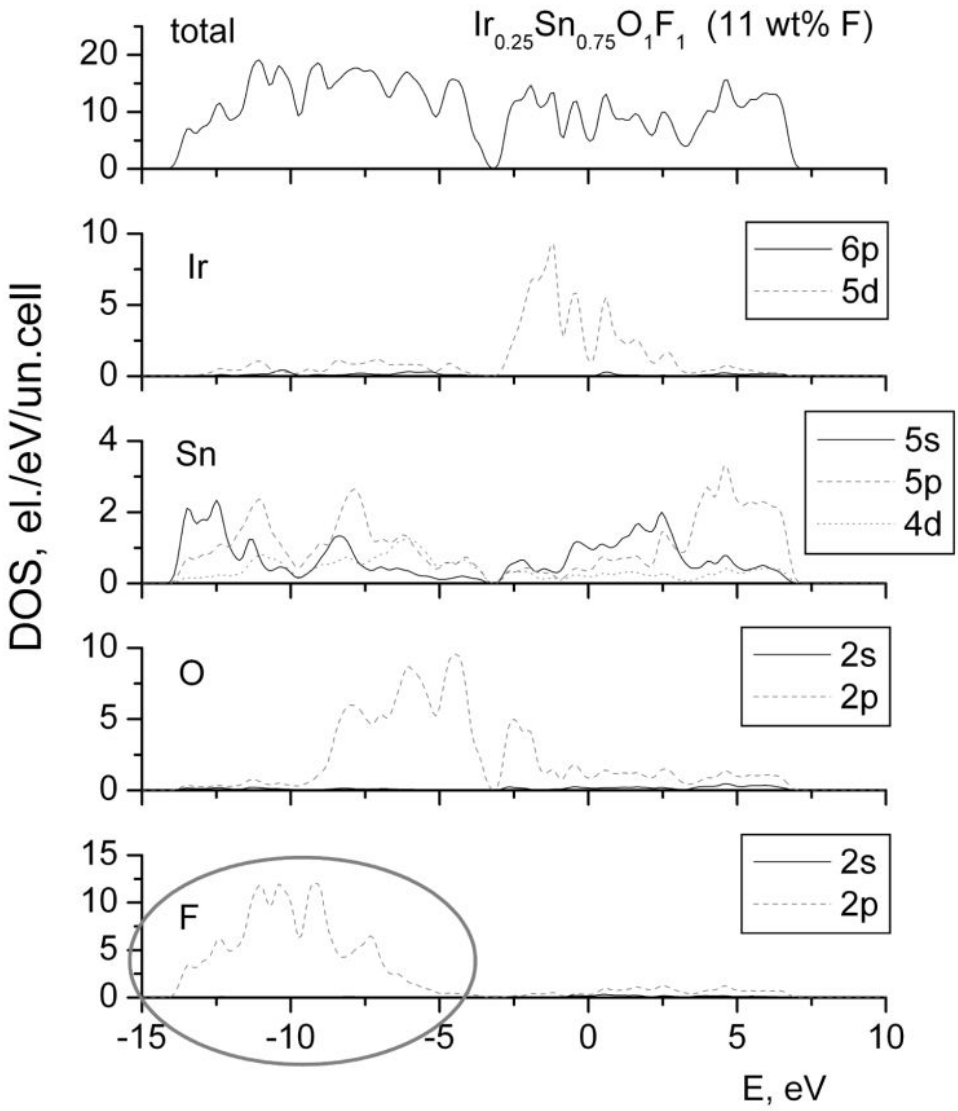

Figure 151. Total and partial density of states for $(Ir_{0.25}Sn_{0.75})O_1F_1$

Thus, with incorporation of F it can be seen that with the increase in F content, the d-band center shifts downward on the energy scale returning back to the position corresponding to pure IrO_2 at ~ 10 wt.% F rendering the system essentially mimicking the electronic and electro-catalytic properties of pure IrO_2. A combination of the improved metallic electronic conductivity

and the d-band center position being optimal conceivably renders this oxide demonstrating high catalytic activity experimentally observed comparable to pure IrO_2. The addition of a relatively small amount of Ir into the SnO_2 matrix thus drastically modifies the overall electronic structure of the resulting oxide introducing highly prominent 5d band of Ir modified by the 2p band of F.

6.3 F DOPED RUTHENIUM - TIN OXIDE

6.3.1 Computational Methodology

In order to obtain deeper insight into the intrinsic properties of the undoped $(Ru,Sn)O_2$ and F doped solid solutions, a continuous string of first principles studies have been conducted using Density Functional Theory methodology implemented in the Vienna Ab-initio Simulation Package (VASP) [131-133]. The projector augmented wave (PAW) method with the generalized gradient approximation (GGA) [130] for conducting the exchange - correlation corrections has been used for calculation of the total energies, electronic structures and optimized lattice parameters of the different model materials with chemical compositions similar to those compounds studied experimentally and described above in the present work. All the atoms were allowed to relax with the residual force components on each atom to be lower than ~ 0.01 eV/Å/atom, thus resulting in the accurate determination of the atomic positions; and total energy of the whole system. The Monkhorst - Pack scheme was used to sample the Brillouin Zone (BZ) and generate the ***k*** point grid for the solids and the different isolated atoms used in the present

study. A choice of the appropriate number of ***k*** points in the irreducible part of the BZ was based on convergence of the total energy to be 0.1 meV/atom. Standard PAW potentials were employed for the elemental constituents of all pure and doped compounds in the study.

As a model system, a 12 atom supercell containing two rutile type unit cells has been constructed to represent the following compositions of the materials considered: RuO_2, $(Sn_{0.25}Ru_{0.75})O_2$, $(Sn_{0.5}Ru_{0.5})O_2$, $(Sn_{0.75}\ Ru_{0.25})O_2$, $(Sn_{0.75}\ Ru_{0.25})O_{1.5}F_{0.5}$ and $(Sn_{0.75}\ Ru_{0.25})O_{1.0}F_{1.0}$. The last two compositions correspond to 6.4 and 12.7 wt.% F respectively. It should also be noted that for the Ru-Sn-O-F compositions, the corresponding atomic distributions are ambiguous and can be represented by different spatial configurations. To eliminate this uncertainty several atomic configurations for each given composition has been constructed and only those configurations corresponding to minimal total energies has been selected for further electronic structure analysis of these specific compositions of the binary oxides.

6.3.2 Theoretical Discussion

Theoretical studies help provide a fundamental understanding of the excellent electrochemical activity demonstrated by the $(Ru,Sn)O_2$:F electro-catalyts (**Figure 31** and **Figure 32**). A well known concept proposed by Nørskov *et al.* [125, 126] that a gravity center of the d-band of the noble metal ε_d may serve as a simple descriptor for determining the catalytic activity of the surface. Such a d-band center is usually located in the vicinity of the Fermi level and an optimal position of the d-band center would provide an optimal interaction between the catalytic surface and the various species participating in the catalytic reactions predominantly occurring on the surface. Thus, an adjustment of the d-band center position with respect to the Fermi level may

likely play a critical role in contributing to the design of novel highly active and electrochemically stable (Ru,Sn)O_2:F electro-catalysts.

For these purposes, the electronic structures of all the Ru based oxides has been calculated and the positions of the corresponding Ru d-band centers have been obtained as a first moment of $nd(E)$: $\varepsilon d = \int nd(E)E\mathrm{d}E / \int nd(E)\mathrm{d}E$. **Figure 152** shows the partial Ru d-band densities of states together with the corresponding centers of these zones marked with vertical arrows on the graphs. One can see that the d-band center for pure RuO_2 is located at ~ - 0.39 eV below the Fermi level. This position will be considered as a reference point for comparison of the catalytic activities of the other compounds; and correspondingly simulated in this theoretical study. Gradual introduction of increased amount of Sn (up to 75 at.%) to the oxide results in hybridization between the Sn 5s, 5p and Ru 4d-states leading to a shift of the Ru d-band center up to the position at - 0.22 eV below the Fermi level. This indicates an overall chemisorption reaction of different species reacting at the surface becoming noticeably stronger with increase of Sn concentration rather than for pure RuO_2.

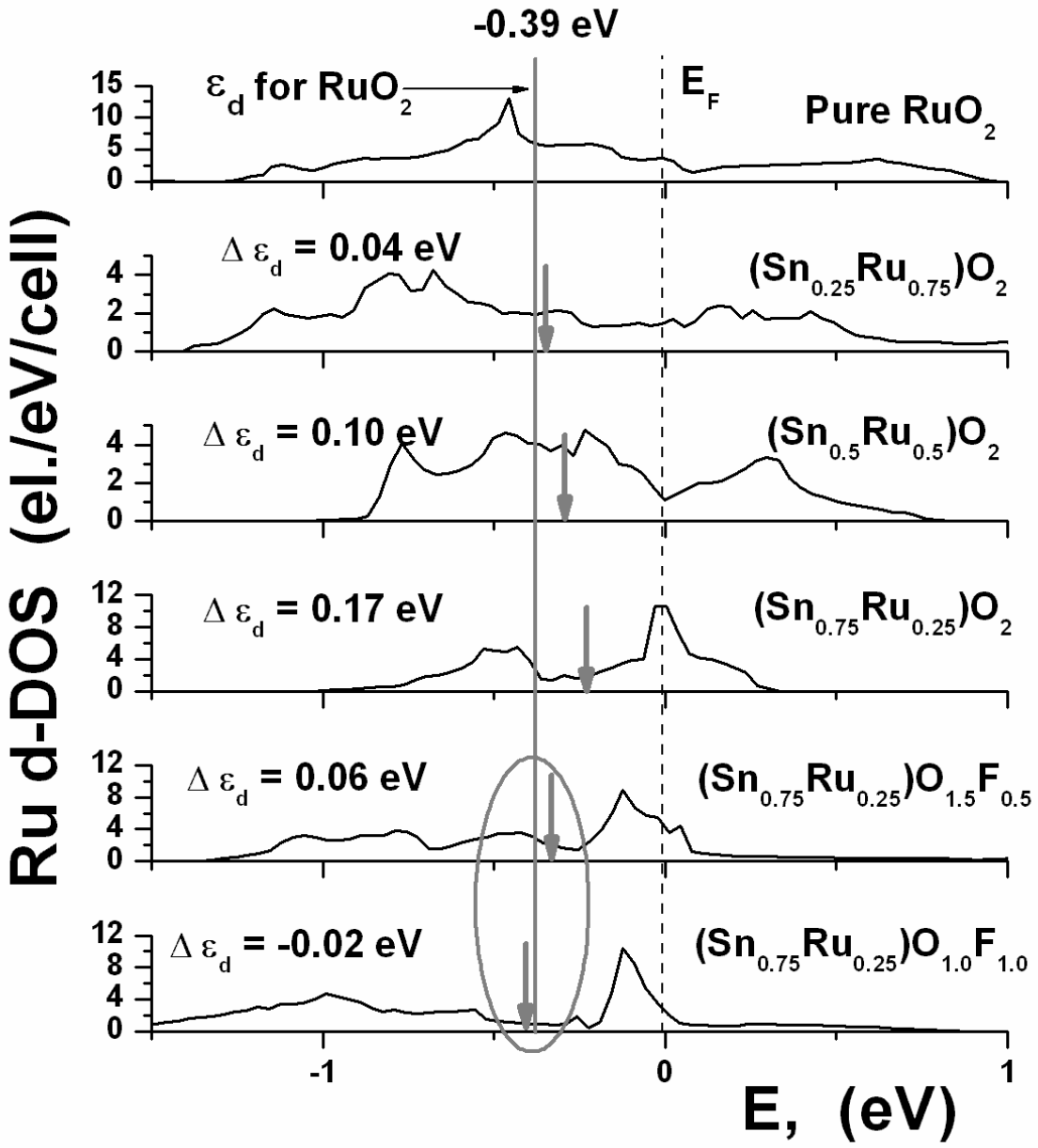

Figure 152. Ru d-band partial density of states for RuO_2, $(Ru,Sn)O_2$ and $(Ru,Sn)O_2$:F. The arrows denote positions of the d-band centers (ε_d)

Assuming that pure RuO_2 demonstrates an optimal catalytic activity corresponding to ε_d = - 0.39 eV, one can suggest a significant drop in the electrochemical activity observed

experimentally for $(Ru_{0.2}Sn_{0.8})O_2$ composition (**Figure 31**) could be most likely explained by a positive shift of the Ru d-band center deviating the catalytic activity from its optimal value. Such a behavior of the d-band center could be attributed to complex hybridization of the electronic Ru d-states and corresponding s and p states of Sn and O during formation of the binary oxide solid solution.

The effects of F doping on the catalytic activity of the materials can be considered from the electronic structure point of view and correspondingly, the d-band center shifting, in particular. Thus, it can be seen from **Figure 152** that for 6.4 wt.% F and 12.7 wt.% F, there is a gradual movement of the d band center resulting in ε_d almost matching that of pure RuO_2. **Figure 153** shows the total and partial density of states for $(Ru_{0.25}Sn_{0.75})O_{1.5}F_{0.5}$ composition. Introduction of fluorine manifests in an appearance of F 2p band mostly below - 5 eV with negligible amount of other states in a whole energy region. The higher the F content, the more pronounced these 2p states are and stronger is the effect of hybridization between F 2p and Ru 4d states. As a result, the Ru d-band center starts moving from - 0.22 eV for the undoped composition downward towards the position corresponding to pure RuO_2 (- 0.39 eV) with increase in the F content. It is seen that at 6.4 and 12.7 wt.% F, the d-band center passes - 0.33 eV and - 0.41 eV respectively, indicating an improvement in the catalytic activity with increase in F concentration. The optimal F concentration at which the d-center returns back to the position corresponding to pure RuO_2 is thus expected to be ~ 9 - 10 wt.% F which is in excellent agreement with the experimentally observed results (**Figure 33**).

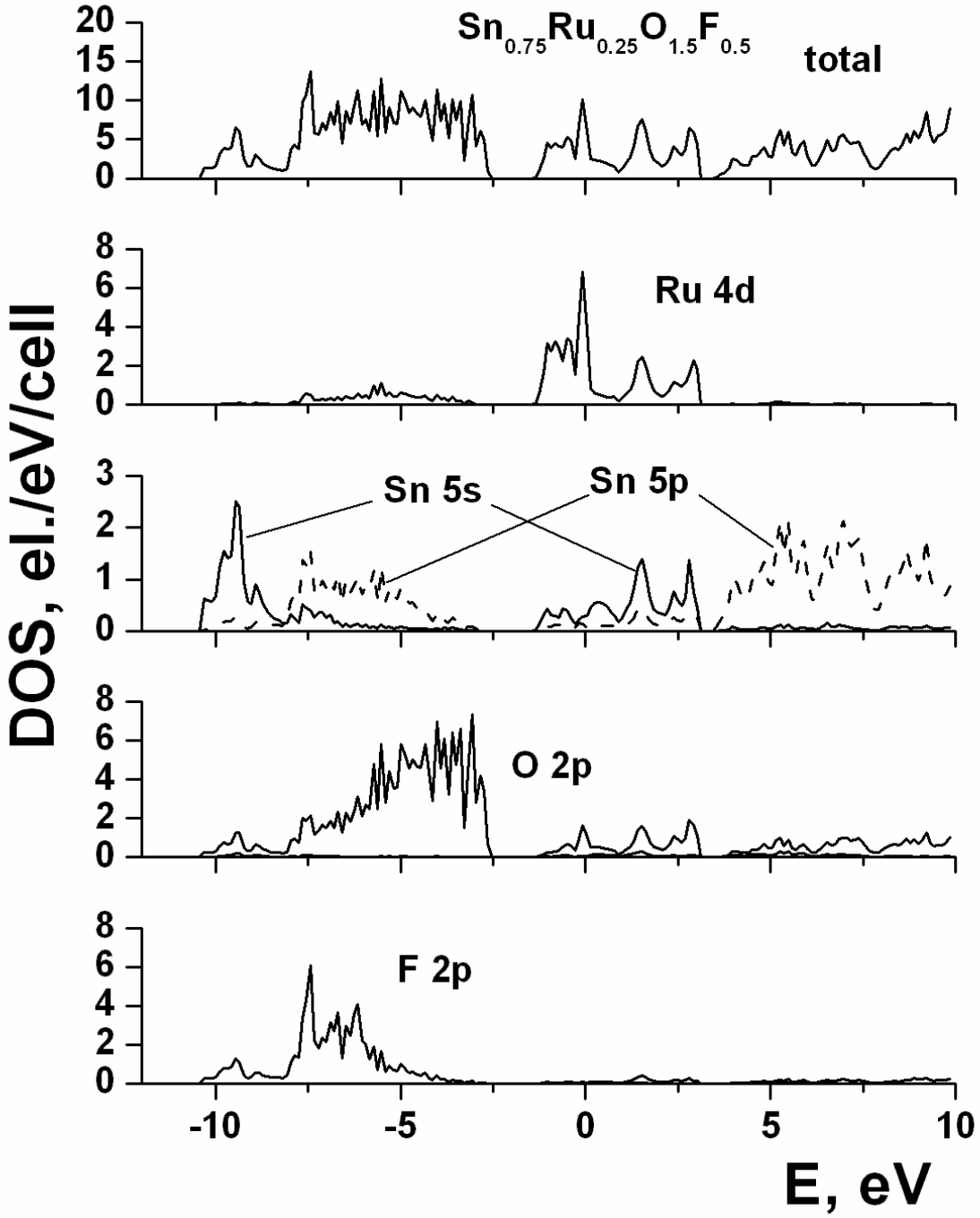

Figure 153. Total and partial density of states for $(Ru_{0.25}Sn_{0.75})O_{1.5}F_{0.5}$

Thus, the present theoretical study of the electronic structure peculiarities of the $(Ru,Sn)O_2$:F has demonstrated strong correlation between the d-band center position and the observed catalytic activity of the considered materials with the optimal composition corresponding to $(Ru_{0.25}Sn_{0.75})O_2$ doped with ~ 10 wt.% F rendering this material to demonstrate high electro-catalytic activity comparable to pure RuO_2.

6.4 F DOPED IRIDIUM - NIOBIUM OXIDE

6.4.1 Computational Methodology

The catalytic activity of virtually any electro-catalyst is expected to depend on the electronic structure as well as electronic conductivity, while the long term stability of the electrode is assumed to qualitatively depend on the cohesive energy of the system. The effect of compositions on the electronic and catalytic properties as well as on the structural stability of the material has been understood from the theoretical considerations. To obtain deeper insight into the intrinsic properties of undoped $(Ir_{0.25}Nb_{0.75})O_2$ as well as doped with ~ 9.4 wt.% F corresponding to the formula unit $(Ir_{0.25}Nb_{0.75})O_{1.25}F_{0.75}$, a series of ab-initio calculations of the electronic structure, equilibrium lattice parameters and cohesive energies of the above mentioned materials have been conducted using density functional theory (DFT) methodology implemented in the Vienna Ab-initio Simulation Package (VASP) [131-133]. The projector augmented wave (PAW) method with the generalized gradient approximation (GGA) for the exchange-correlation

energy functional in a form suggested by Perdew and Wang [130] has been applied in present study. The lattice parameters and internal positions of atoms were fully optimized employing the double relaxation procedure, where all atoms were allowed to relax with the residual force components on each atom to be lower than 0.01 eV/Å/atom, thus allowing for the accurate determination of the internal atomic positions and hence, the total energy of the whole system. The Monkhorst - Pack scheme was used to sample the Brillouin Zone (BZ) and generate the ***k*** point grid for the solids and the different isolated atoms used in the present study. A choice of the appropriate number of ***k*** points in the irreducible part of the BZ was based on convergence of the total energy to be 0.1 meV/atom. Standard PAW potentials were employed for the elemental constituents of all pure and doped compounds in the study.

As a model system, a 12 atom supercell containing two rutile type unit cells has been constructed to represent $(Ir_{0.25}Nb_{0.75})O_2$ and $(Ir_{0.25}Nb_{0.75})O_{1.25}F_{0.75}$ compositions. It should be noted that for $(Ir_{0.25}Nb_{0.75})O_{1.25}F_{0.75}$ composition, the corresponding atomic distributions are ambiguous and can be represented by different spatial configurations. There are 5 atoms of O and 3 atoms of F distributed randomly over 8 available oxygen sites in 12 atom super cell used for the calculations. To eliminate this uncertainty, several atomic configurations for this specific composition have been considered and a configuration corresponding to minimal total energy has been selected for further electronic structure and cohesive energy analysis. For calculation of the (1 1 0) surface electronic properties of the materials a two dimensional slab containing four oxygen and three metal layers repeated in (1 -1 0) direction with ~ 7 Å of thickness and a vacuum distance of ~ 14 Å between adjacent images of the slab was selected.

6.4.2 Theoretical Discussion

The main origins of enhanced electro-catalytic activity and the long-term structural stability of fluorine doped $Ir_{0.25}Nb_{0.75}O_2$ as seen in **Figure 136** and **Figure 139**, respectively can be understood from the electronic structure point of view. The total densities of electronic states calculated for pure IrO_2 as well as for undoped and F doped $Ir_{0.25}Nb_{0.75}O_2$ are shown in **Figure 154**. The band structure of IrO_2 consists of two main bands. One of them belongs to the oxygen 2s states located at around - 18 eV. Another band is the wide valence band around Fermi level and consisted of hybridized O 2p - Ir 5d states and provides a metallic type of electronic conductivity characteristic of IrO_2. Introduction of Nb and F into IrO_2 matrix changes the electronic structures of the compounds significantly with all major projected electronic states denoted with corresponding orbital numbers. However, all the materials remain metallic although with different electronic conductivity.

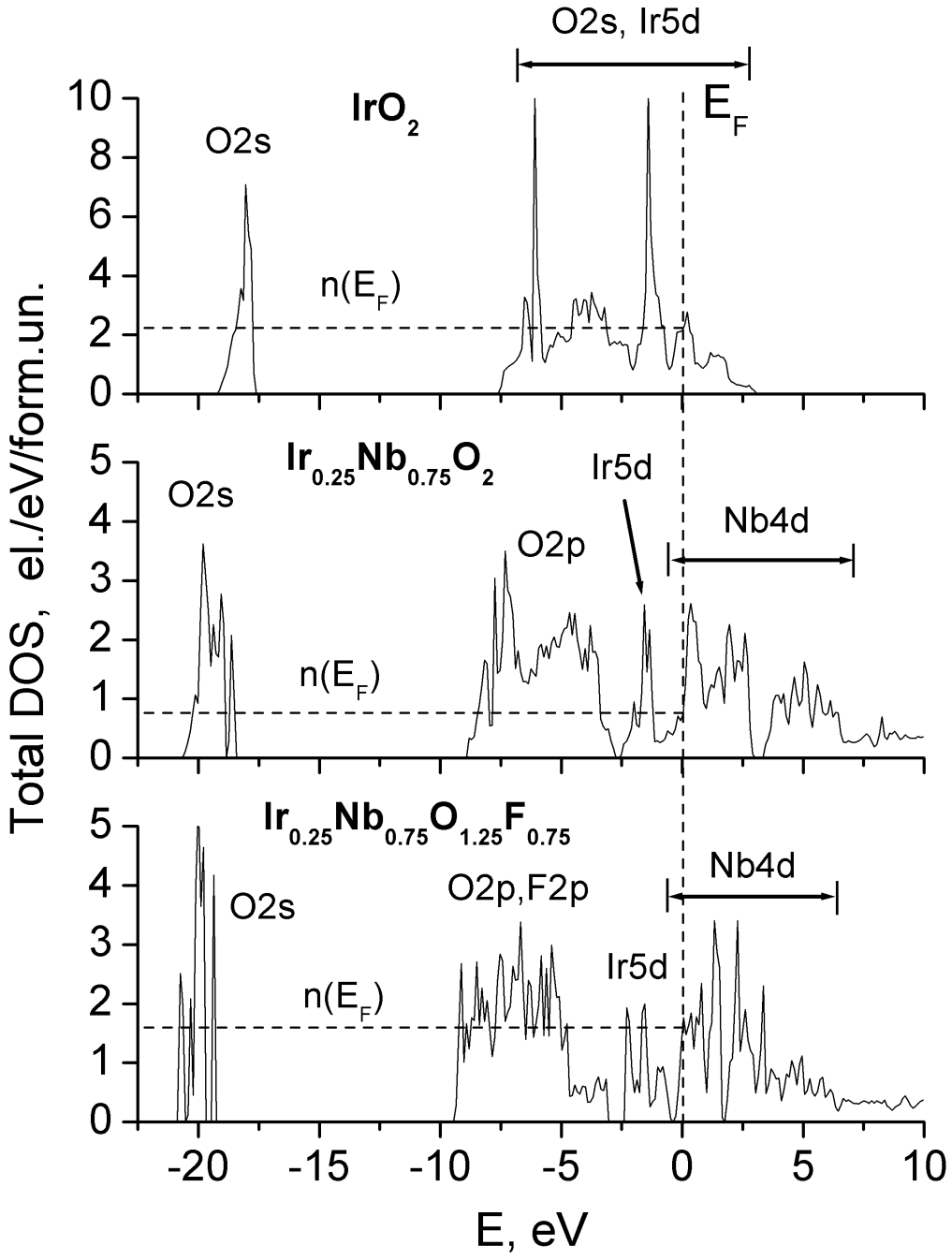

Figure 154. Total density of states for IrO_2, $(Ir_{0.25}Nb_{0.75})O_2$, and $(Ir_{0.25}Nb_{0.75})O_{1.25}F_{0.75}$

Since generally speaking, metallic conductivity is direct proportional to the density of states at Fermi level $n(E_F)$, a qualitative evaluation of the correlation between chemical compositions of the materials and their electronic conductivity becomes feasible and straightforward. **Table 11** collects the values of $n(E_F)$ corresponding to pure IrO_2, undoped and F doped $(Ir,Nb)O_2$. One can see that the $n(E_F)$ for pure IrO_2 is the highest among all the three compounds and can serve as a benchmark for the electronic conductivity of the other two materials. As expected, an introduction of a substantial amount of niobium oxide into IrO_2 results in a drastic decrease of the electronic conductivity, since Nb_2O_5 is a very poor electric conductor with a wide band gap of 3.9 eV [137]. Introduction of fluorine significantly improves the overall conductivity though not up to the value demonstrated for pure IrO_2. The role of fluorine doping into SnO_2 and $(Ir,Sn,Nb)O_2$ solid solutions has been discussed previously by us indicating significant improvement in the electronic conductivity of the compounds with an introduction of ~ 10 wt.% F due to an increase of the charge carrier concentration in the system [24, 56, 59]. Thus, such an increase in the conductivity of $Ir_{0.25}Nb_{0.75}O_2$:10 wt.% F may noticeably contribute to the high electro-catalytic activity of the compound.

Table 11. Calculated values of density of electronic states at Fermi level n(E_F), positions of the Ir d-band center ε_d, and the cohesive energy - E_{coh} for the catalysts.

	n(E_F) [el./eV/f.un.]	**ε_d (eV)**	**- E_{coh} [eV/f.un.]**
IrO_2	2.15	- 1.33	15.86
$Ir_{0.25}Nb_{0.75}O_2$	0.76	- 0.95	20.20
$Ir_{0.25}Nb_{0.75}O_{1.25}F_{0.75}$	1.62	- 1.41	18.81

Another aspect in the computational part of the present study relates to the qualitative evaluation of the electro-catalytic activity utilizing an inspiring concept proposed by Nørskov *et al.* [125, 126] regarding the existence of a simple descriptor for determining the catalytic activity of the surface. This descriptor has been defined as a gravity center of the noble metal d-band ε_d usually located in the vicinity of the Fermi level. An optimal position of ε_d thus provides an optimal highly favorable interaction between the catalytic surface and the various species participating in the elementary catalytic reactions during water electrolysis process. An appropriate control of the d-band center position with respect to the Fermi level may crucially contribute to the design of novel highly active and electrochemically stable electro-catalysts.

Since (1 1 0) is the most stable and hence, preferred surface for water electrolysis to occur, the corresponding electronic structure (1 1 0) surface calculations have been conducted to define Ir d-band center position and thus, to qualitatively evaluate the electro-catalytic activity of pure and F doped $Ir_{0.25}Nb_{0.75}O_2$ as compared to that of pure IrO_2 which is the gold standard OER

catalyst. Also, positions of corresponding Ir d-band centers have been obtained as a first moments of $n_d(E)$: $\varepsilon_d = \int n_d(E)E\mathrm{d}E / \int n_d(E)\mathrm{d}E$.

Figure 155 shows partial Ir d-band densities of states together with corresponding ε_d centers marked with vertical arrows on the plots. As mentioned above, ε_d for pure IrO_2 is - 1.33 eV below Fermi level that may serve as a reference point for the optimal position of the d-band center corresponding to the optimal catalytic activity of the compound [**Figure 155** (a)]. In case of $Ir_{0.25}Nb_{0.75}O_2$ [**Figure 155** (b)], an introduction of Nb leads to the noticeable shift of Ir d-band center up towards the Fermi level. It happens due to partial Ir 5d - Nb 4d hybridization, where Nb 4d electronic states locate above the Ir 5d states on the energy scale resulting in the position of ε_d at - 0.95 eV. This d-band shift explains the degradation of the overall catalytic activity (**Figure 136**). However, it is also observed that doping of $Ir_{0.25}Nb_{0.75}O_2$ compound by 10 wt.% F leads to an improvement in the catalytic activity as compared to fluorine free $Ir_{0.25}Nb_{0.75}O_2$.

Such an improvement could be expected from the Ir d-band center calculations of the model system $Ir_{0.25}Nb_{0.75}O_{1.25}F_{0.75}$ shown in **Figure 155** (c). It is seen that in presence of fluorine, ε_d moves back to almost the same (actually, slightly lower) position as that for pure IrO_2. This downward shift occurs because of the presence of lower energy fluorine 2p states located below Ir 5d electrons (not shown in the Figure). Thus, due to F 2p - Ir 5d hybridization, the Ir 5d band becomes wider as compared to the corresponding Ir 5d states in $Ir_{0.25}Nb_{0.75}O_2$; resulting in the movement of Ir d-band center lower on the energy scale. **Table 11** collects ε_d values calculated for all the three compositions.

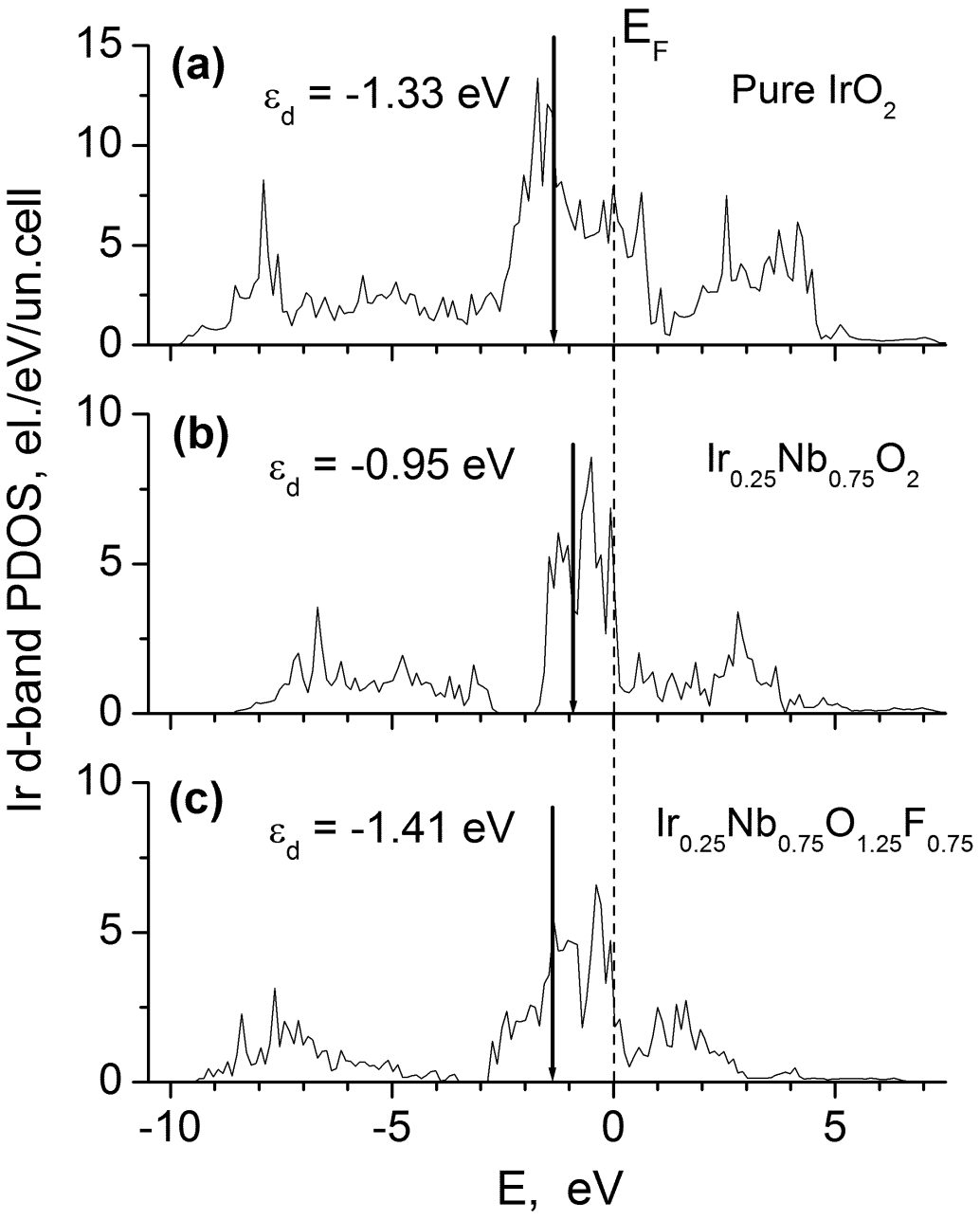

Figure 155. Ir d-band projected DOS for IrO_2 (a), $(Ir_{0.25}Nb_{0.75})O_2$ (b), and $(Ir_{0.25}Nb_{0.75})O_{1.25}F_{0.75}$ (c). The arrows denote positions of the d-band centers (ε_d)

The last aspect to be highlighted in the present study is the cohesive energy E_{coh}. In general, E_{coh} can be considered as a qualitative indicator of the structural and chemical stability of the system, thus the higher E_{coh} (the more negative value), the more stable and durable material is expected to be during long term electro-catalytic processes. It is observed (**Table 11**) that an introduction of Nb into IrO_2 oxide significantly improves the overall stability of $Ir_{0.25}Nb_{0.75}O_2$ due to presence of much stronger Nb - O bonds in comparison to Ir - O ones (calculated E_{coh} for pure NbO_2 is - 18.251 eV/f.un. *vs.* - 15.859 eV/f.un. for IrO_2). However, further F doping of $Ir_{0.25}Nb_{0.75}O_2$ compound results in relatively lower cohesive energy that occurs mainly due to lower ionic charge of F^- *vs.* O^{2-} and thus, significantly weakens the electrostatic component of Ir - F and Nb - F bonds than those of Ir - O and Nb - O ionic bonds. Nevertheless, even relatively less stable $Ir_{0.25}Nb_{0.75}O_2$:F compound is noticeably more stable than pure IrO_2, which is clearly indicated and confirmed by the chronoamperometry measurements shown in **Figure 139**.

6.5 IRIDIUM - TIN - NIOBIUM OXIDE

6.5.1 Computational Methodology

In this study, the thin film of $(Ir,Sn,Nb)O_2$ synthesized by thermal decomposition of chloride precursors on Ti substrate has been considered to exhibit the rutile structure with a tetragonal unit cell and space group P42/mnm following experimental validation. The rutile structure of

$(Ir,Sn,Nb)O_2$ thin film electrode has been confirmed experimentally from XRD analysis which has been presented in the results section (**Figure 43** and **Figure 44**). This unit cell has been chosen as the basis for construction of the different super cells corresponding to the specific Ir, Sn and Nb concentrations of the oxide solid solution. In particular, for IrO_2 and $(Sn_{0.5}Nb_{0.5})O_2$ the super cell has been chosen as the regular rutile unit cell with two metal and four oxygen atoms in the primitive unit cell. On the other hand, $(Ir_{1-2x}Sn_xNb_x)O_2$ with x = 0.125, 0.25 and 0.375 compositions were made to fit a fourfold super cell (1 x 1 x 4) comprising 8 metal and 16 oxygen atoms in the cell unit. For calculation of the (110) surface electronic properties of the materials, a two-dimensional slab repeated in (1 -1 0) direction with a vacuum distance ~ 15 Å between adjacent images of the slab was selected.

For calculating the total energies, electronic structure and density of electronic states the Vienna Ab-initio Simulation Package (VASP) was used within the projector-augmented wave (PAW) method [131-133] and the generalized gradient approximation (GGA) for the exchange correlation energy functional in a form suggested by Perdew and Wang [130]. This program calculates the electronic structure and *via* the Hellmann - Feynman theorem, the inter-atomic forces are determined from first principles. Standard PAW potentials were employed for the elemental constituents and the Ir, Sn, Nb, and O potentials thus contained nine, four, eleven and six valence electrons, respectively.

For all the materials considered the plane wave cutoff energy of 520 eV has been chosen to maintain a high accuracy of the total energy calculations. The lattice parameters and internal positions of atoms were fully optimized employing the double relaxation procedure, and consequently, the minima of the total energies with respect to the lattice parameters and internal ionic positions have been determined. This geometry optimization was obtained by minimizing

the Hellman - Feynman forces *via* a conjugate gradient method, so that the net forces applied on every ion in the lattice are close to zero. The total electronic energies were converged within 10 - 5 eV/un.cell resulting in the residual force components on each atom to be lower than 0.01 eV/Å/atom, thus allowing for the accurate determination of the internal structural parameters. The Monkhorst-Pack scheme was used to sample the Brillouin Zone (BZ) and generate the ***k*** point grid for the solids and the different isolated atoms used in the present study. A choice of the appropriate number of ***k*** points in the irreducible part of the BZ was based on convergence of the total energy to 0.1 meV/atom.

It should also be noted that for the ternary (Ir,Sn,Nb)O_2 compositions, the corresponding atomic distributions are ambiguous and can be represented by different spatial configurations. To eliminate this uncertainty several atomic configurations for each given composition have been constructed and only those configurations corresponding to minimal total energies have been selected for further numerical investigations of these specific compositions of the ternary oxides.

6.5.2 Theoretical Discussion

The computational component of the present study is an attempt to systematically investigate the electronic properties of the different solid solutions between IrO_2, SnO_2 and NbO_2. The compositions of the solid solutions chosen to model the compounds are pure IrO_2, $(Sn_{0.5}Nb_{0.5})O_2$, $(Ir_{0.75}Sn_{0.125}Nb_{0.125})O_2$, $(Ir_{0.50}Sn_{0.25}Nb_{0.25})O_2$ and $(Ir_{0.25}Sn_{0.375}Nb_{0.375})O_2$. The total energy, electronic and optimized crystal structures, total and projected densities of electronic states together with the cohesive energies for the different compositions of (Ir,Sn,Nb)O_2 have been calculated using the first principle approach within the density functional theory. An effect of

introduction of tin and niobium dioxides into IrO_2 on the electronic conductivity and structural stability of the compounds as well as a position of Ir d-band center with decrease of Ir-concentration in the material is discussed.

Although there are various published theoretical studies dedicated to pure IrO_2, and the electronic structure of the oxide [78, 79, 136], it is justifiably logical to describe the electronic structure of IrO_2 in the context of the present study. In addition, pure IrO2 corresponds to 0 at.% of tin and niobium oxides and thus represents a starting point for the current study employing a full range of Sn and Nb concentrations. **Table 12** summarizes the structural parameters calculated and experimentally obtained in the present study. It is seen that the calculated structural parameters are in a good agreement with experimental data (**Table 3**). Slight overestimations of calculated lattice parameters and molar volumes are expected for GGA approximation utilized in this study.

Table 12. Lattice parameters, cohesive energy and density of electronic states at Fermi level for IrO_2, SnO_2 and (Ir,Sn,Nb)O_2

Composition	a=b (nm)	c (nm)	V_m (cm^3/mol)	E_{coh} (eV/f.u.)	$n(E_f)$ el./eV/f.u.
IrO_2	0.4511	0.3235	19.82	-15.859	2.15
SnO_2	0.4772	0.3216	22.13	-15.237	0
$(Ir_{0.75}Sn_{0.125}Nb_{0.12.5})\ O_2$	0.4633	0.3182	20.57	-16.964	1.97
$(Ir_{0.50}Sn_{0.25}Nb_{0.25})O_2$	0.4722	0.3147	21.13	-17.315	1.23
$(Ir_{0.25}Sn_{0.375}Nb_{0.375})\ O_2$	0.4746	0.3203	21.72	-17.560	0.90
$(Sn_{0.5}Nb_{0.5})O_2$	0.4782	0.3206	22.07	-16.594	0.92

The total and projected densities of electronic states calculated for pure IrO_2 are shown in **Figure 147**. The main energy band structure of IrO_2 consists of two bands. The low energy band between - 19.2 eV and -17.5 eV is composed of the 2s states of oxygen and the wide valence band around Fermi level consists of hybridized O 2p - Ir 5d states with two prominent peaks corresponding to these O 2p and Ir 5d states and providing a metallic type of electronic conductivity characteristic of IrO_2. Introduction of Sn and Nb into IrO_2 matrix is supposed to change the electronic properties of the compound and thus, the electronic structure of bulk as well as the electronic structure of the most stable (1 1 0) surface has been calculated for the

ternary compositions of $(Ir_{1-2x}Sn_xNb_x)O_2$ with x = 0, 0.125, 0.25, 0.375 and 0.5 in the computational study. Total electronic densities of states for all these compositions are shown in **Figure 156**. It is observed that all the materials demonstrate metallic behavior, although to different extents. Since in general, the metallic conductivity is proportional to the density of states at Fermi level $n(E_F)$, it provides an opportunity to qualitatively evaluate the correlation between the residual amount of Ir in the ternary compounds and the electronic conductivity of the materials. **Figure 157** shows the variation of $n(E_F)$ with respect to various compositions of $(Ir,Sn,Nb)O_2$. For comparison, the values of $n(E_F)$ are normalized to electrons per one $(Ir_{1-2x}Sn_xNb_x)O_2$ formula unit. The graph shows that the conductivity decreases with decrease of Ir content up to 0.25 atoms per formula unit (x = 0.375) and then the conductivity value is maintained almost the same as zero content of Ir. Poor electronic conductivity is customarily expected to impair the overall catalytic activity of the material. However, reduction in the conductivity with decrease of IrO_2 concentration up to 50 mol.% most likely is not sufficient to significantly deteriorate the catalytic properties of the material as confirmed by the experimental results shown in **Figure 54**.

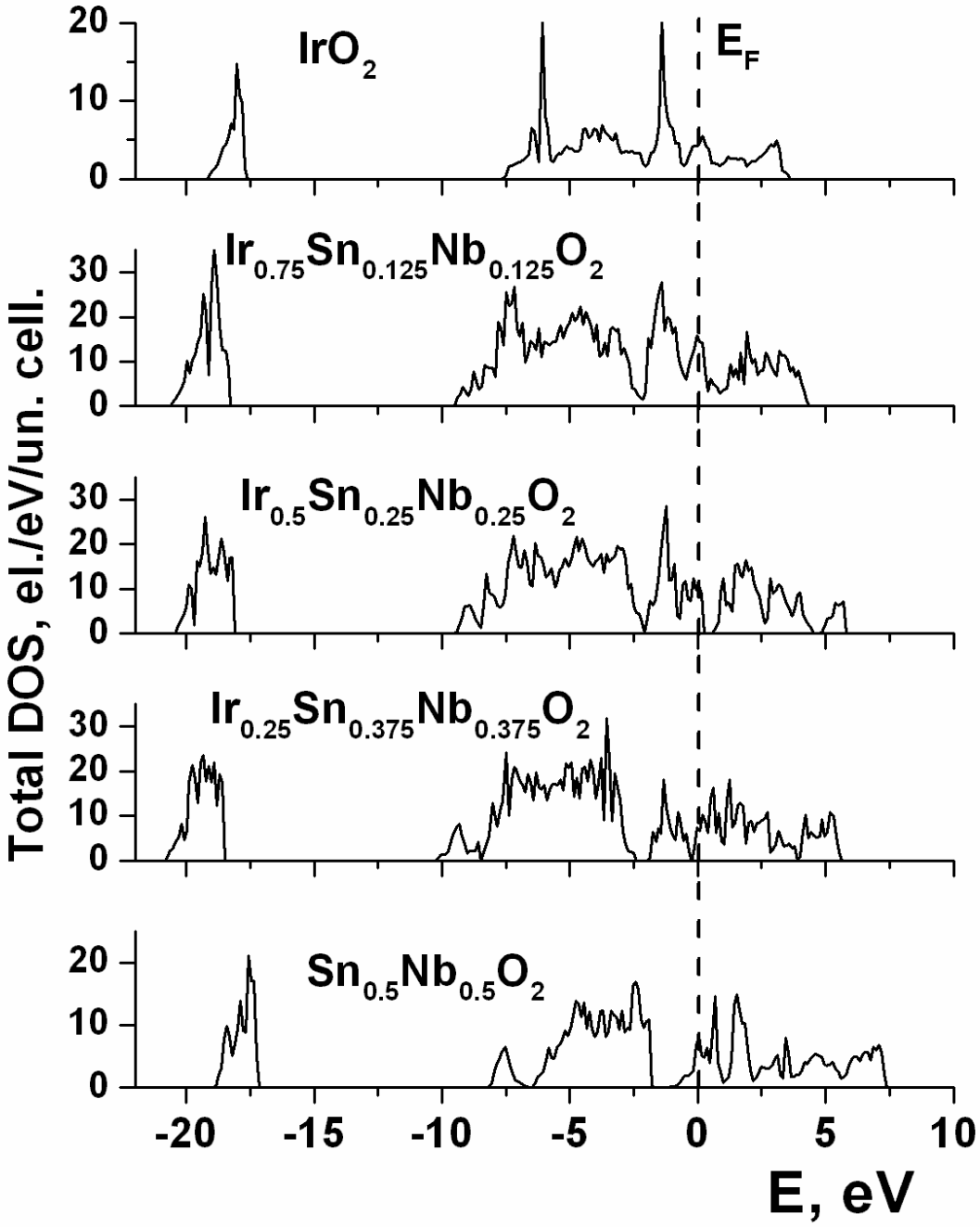

Figure 156. Total electronic density of states for (Ir,Sn,Nb)O_2

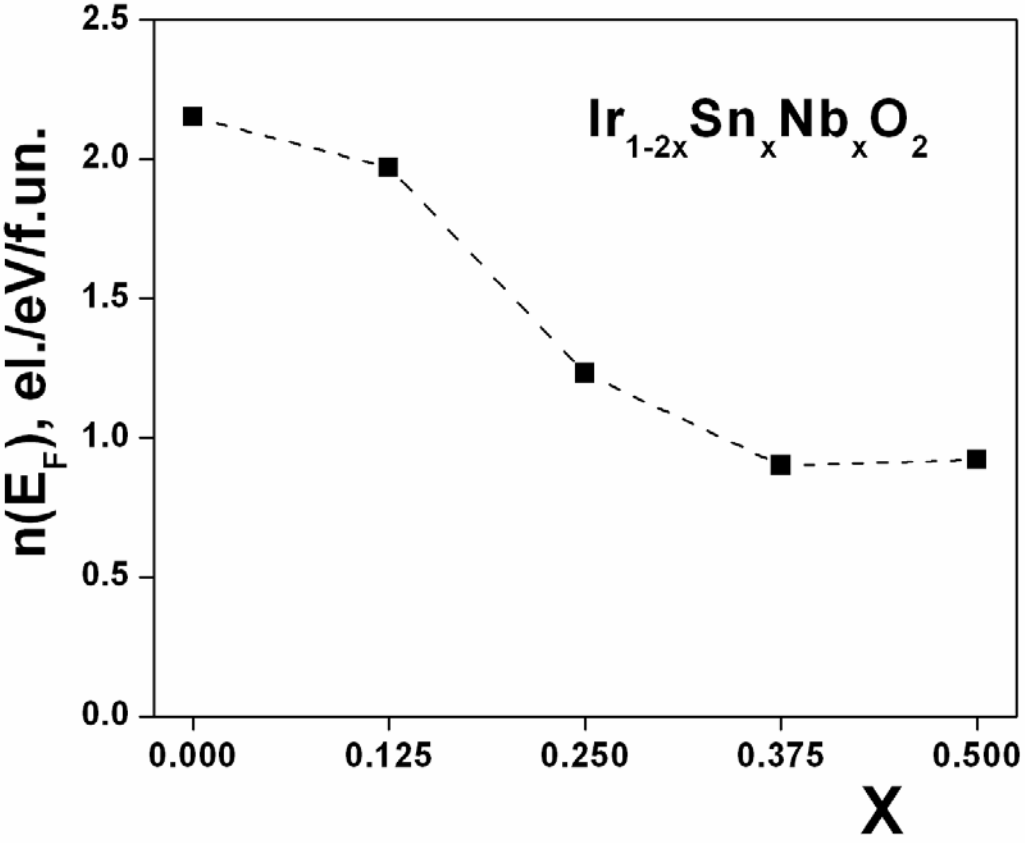

Figure 157. Density of states at Fermi level for different compositions of (Ir,Sn,Nb)O_2

In recent years, another aspect considered in the computational part relates to a wide spread concept proposed by Nørskov *et al.* [125, 126], that the catalytic activity of the surface could be qualitatively characterized by the simple descriptor obtained from the electronic structure of the material. This descriptor has been defined as a gravity center of d-band of the noble metal ε_d usually located in the vicinity of the Fermi level. An optimal position of the d-band center provides an optimal interaction between the catalytic surface and the various species participating in the catalytic reactions predominantly occurring at the surface. Since, such an interaction should be “just - right” implying resulting in a moderate effect allowing reagents and

products to adsorb at the surface and leave most efficiently. Thus, an adjustment of the d-band center position with respect to the Fermi level may play a critical role in designing novel catalyst materials.

Calculations have been done for the electronic structure of the stable (1 1 0) surfaces for all the mentioned (Ir,Sn,Nb)O_2 and the positions of corresponding d-band centers have been obtained as a first moment of $n_d(E)$: $\varepsilon_d = \int n_d(E)EdE / \int n_d(E)dE$, where $n_d(E)$ is a sum of projected densities of d-electrons of Ir, Sn and Nb.

Figure 158 shows partial Ir d-band densities of states together with corresponding centers of these zones marked with vertical arrows on the graphs. One can see that d-centers for Ir compositions from 100 at.% up to 50 at.% of IrO_2 locate virtually at the same position with respect to the Fermi level (- 1.31 eV to - 1.33 eV). However, further decrease in the Ir content causes a noticeable shift of the Ir d-band center upward and for 25 at.% IrO_2, ε_d reaches its position at - 0.49 eV indicating that an overall chemisorption reaction of different species reacting at the surface is noticeably stronger at this composition rather than at higher Ir content. Assuming that pure IrO_2 demonstrates an optimal catalytic activity corresponding to ε_d = - 1.33 eV, a significant drop in the activity is expected for IrO_2 content below 40 mol. % as seen experimentally in **Figure 53** which could be most likely due to a positive shift of the Ir d-band center deviating the catalytic activity from its optimal value. Such a behavior of the d-band center could be attributed to complex hybridization of electronic Ir d-states and corresponding d, s and p states of Sn, Nb and O during formation of the solid solution ternary oxide.

Another important aspect to be highlighted in the present study is the cohesive energy E_{coh} calculated for all the materials considered and collected in **Table 12**. It clearly shows that with a decrease in Ir concentration in the compound, there is an increase in the E_{coh} values (*i.e.*

more negative values). This would result in an overall improved structural and chemically stable (Ir,Sn,Nb)O_2. Such an improvement may be due to presence of much stronger Nb - O bonds in comparison with Ir - O ones since the calculated E_{coh} for pure NbO_2 is - 18.251 eV/f.un. *vs.* - 15.859 eV/f.un. for IrO_2. An increase in the cohesive energy of the iridium oxide doped with tin and niobium yields a robust and chemically stable ternary oxide (**Figure 55**) in comparison to the original pure IrO_2.

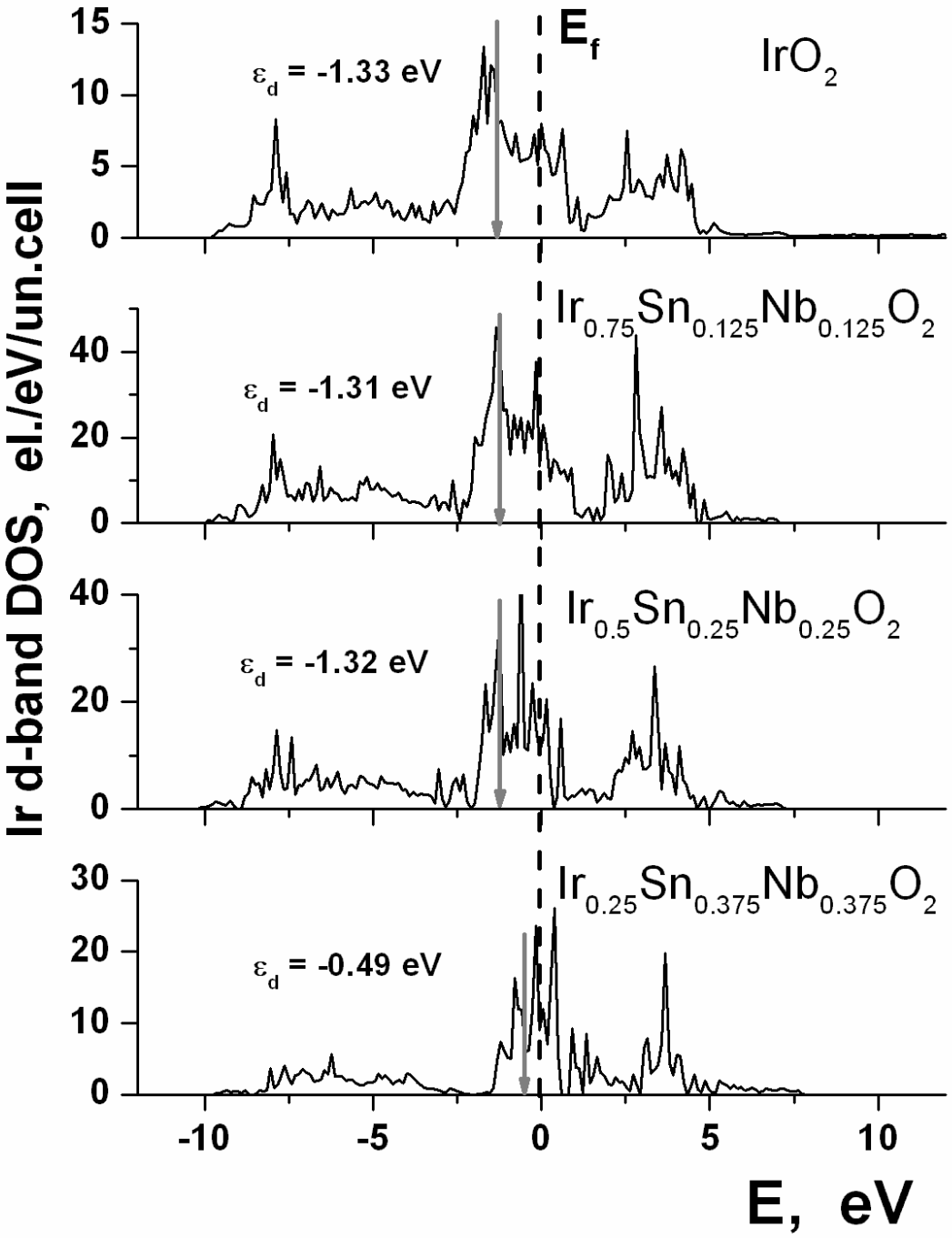

Figure 158. Ir d-band partial density of states for (Ir,Sn,Nb)O_2. The arrows denote positions of the d-band centers (ε_d)

6.6 F DOPED IRIDIUM - TIN - NIOBIUM OXIDE

6.6.1 Computational Methodology

The electrochemical activity of the (Ir,Sn,Nb)O_2:F electro-catalyst is expected to depend on the electronic structure and the electronic conductivity; and the cohesive energy of the system will qualitatively tell us more about the structural stability of the electrode materials. Theoretical calculations will help understand the effect of different (Ir,Sn,Nb)O_2:F compositions on the electronic conductivity, long term stability and the catalytic activity of the material. In the present study, the electronic properties of the solid solution between IrO_2, SnO_2 and NbO_2 with and without the incorporation of different amounts of F have been investigated to mimic the (Ir,Sn,Nb)O_2:F materials system. First principles approach has been used to calculate the total energy, electronic and optimized crystal structures; total and projected densities of electronic states along with the cohesive energies for pure IrO_2 and different compositions of (Ir,Sn,Nb)O_2:F using the density functional theory. Tin oxide, niobium dioxide and fluorine have been introduced with IrO_2 to study the electronic conductivity and structural stability of the compounds along with the electronic structure peculiarities related to the chemical compositions of the materials considered in the present study.

The bulk and (1 1 0) surface of (Ir,Sn,Nb)O_2 doped with different amount of F has been considered to exhibit rutile structure with a tetragonal unit cell and space group $P4_2/mnm$ following experimental validation. Based on this primitive rutile type unit cell there has been chosen a fourfold 2 x 2 x 1 super-cell with different atomic configurations corresponding to the specific Ir, Sn, Nb and F compositions of the oxide solid solutions. To facilitate convenient

calculations, the basic composition has been chosen as 25 at.% IrO_2 - 37.5 at.% SnO_2 - 37.5 at.% NbO_2 instead of 30/35/35 ratio used in the experiment. Such 25/37.5/37.5 composition, although slightly different from the experimental ratio, allows us to select smaller representative super-cells for all the calculation of bulk and surface electronic structures. Thus, the compositions of the solid solutions chosen to model the compounds considered in the experimental study are pure IrO_2 and $(Ir_{0.25}Sn_{0.375}Nb_{0.375})O_{2-x}F_x$, where x = 0, 0.5, 1.0 and 1.5 corresponding to 0, 4.5, 9.0 and 13.5 wt.% F, respectively. A two-dimensional slab repeated in (1 -1 0) direction with 36 atom unit cell and a vacuum distance ~ 12 Å between adjacent images of the slab was selected for calculating (1 1 0) surface electronic properties.

The Vienna Ab-initio Simulation Package (VASP) was used within the projector-augmented wave (PAW) method [131-133] and the generalized gradient approximation (GGA) for the exchange-correlation energy functional in a form suggested by Perdew and Wang [130] for calculating the total energies, electronic structure, and density of electronic states. It should be noted that for all the $(Ir,Sn,Nb)O_2$:F compositions, the corresponding atomic distributions are ambiguous and can be represented by different spatial configurations. Several atomic configurations have been constructed for each composition and only those configurations having the lowest total energies are considered for our calculations.

6.6.2 Theoretical Discussion

Figure 159 shows the total densities of electronic states calculated for pure IrO_2 and all solid solutions considered in the study. The IrO_2 band structure consists of two main bands. The 2s states of oxygen are in the low energy band between - 17.5 eV and - 19.2 eV. Around the Fermi

level, there is a wide valence band which has hybridized O 2p and Ir 5d states. O 2p and Ir 5d states have 2 prominent peaks that provide the metallic type of electronic conductivity to IrO_2. Tin, niobium and fluorine have been introduced into the IrO_2 matrix which noticeably changes the electronic structures of the compounds along with all major projected electronic states denoted with corresponding orbital numbers. It is observed (**Figure 159**) that all the materials remain metallic, although to different extent.

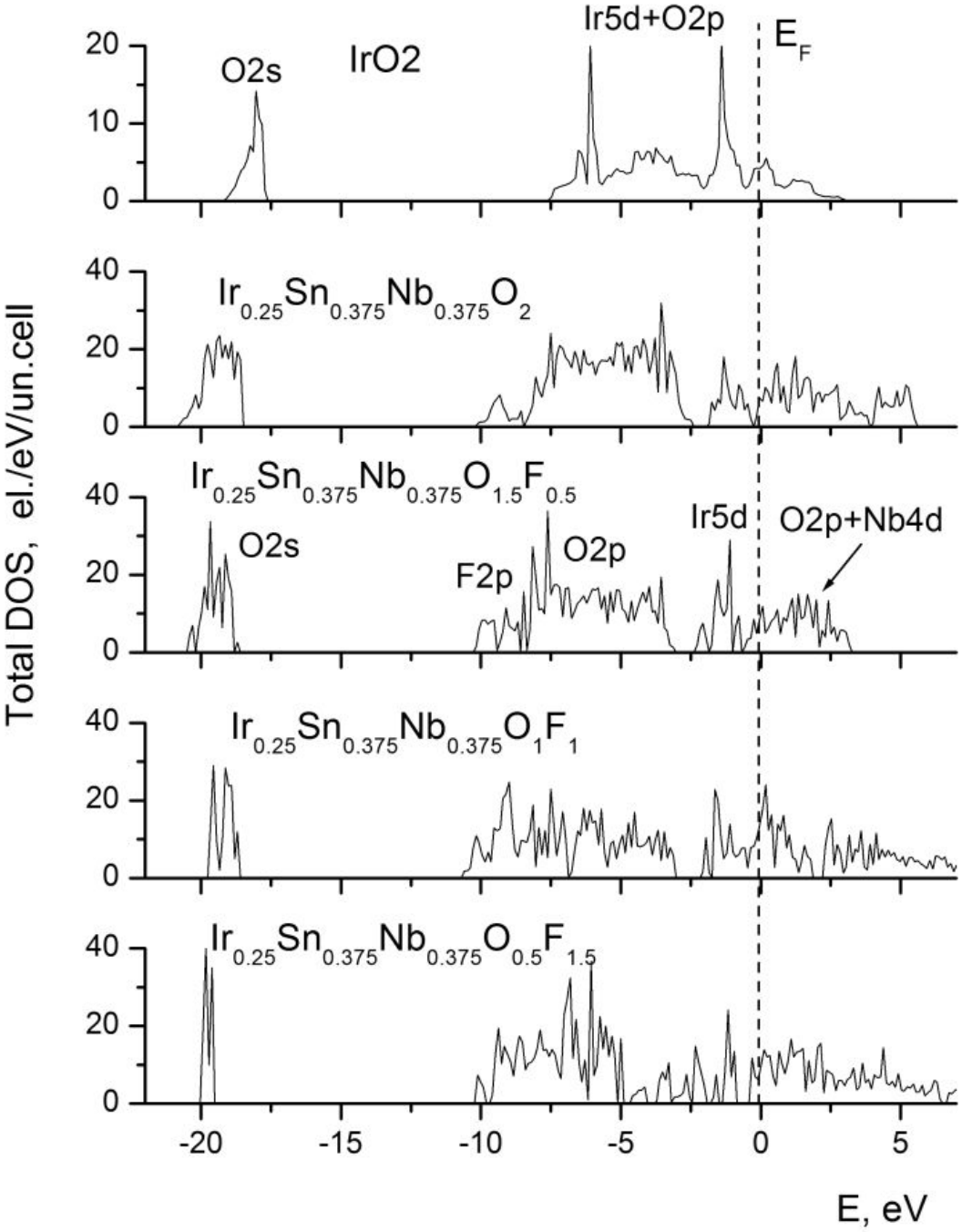

Figure 159. Total bulk density of electronic states for pure IrO_2 and $(Ir_{0.25}Sn_{0.375}Nb_{0.375})O_{2-x}F_x$ (x = 0, 0.5, 1, 1.5)

It is well known that the metallic conductivity of a material is proportional to the density of states at Fermi level $n(E_F)$. This would provide an opportunity for understanding and evaluating the correlation between chemical compositions of materials and their electronic conductivity. **Figure 160** shows the dependence of $n(E_F)$ *vs.* composition of $(Ir_{0.25}Sn_{0.375}Nb_{0.375})O_{2-x}F_x$. It is to be noted that the values of $n(E_F)$ have been normalized to electrons per one $(Ir_{0.25}Sn_{0.375}Nb_{0.375})O_{2-x}F_x$ formula unit for comparison. The value of $n(E_F)$ for pure IrO_2 is marked with a dash horizontal line as a benchmark of the electronic conductivity. It clearly shows that there is a drastic decrease in conductivity for 25 at.% IrO_2. Such a drop in the electronic conductivity is expected due to presence of substantial amount of SnO_2 known to be a very poor conductor with a high band gap of 3.6 eV [138]. Introduction of fluorine improves the overall conductivity reaching an optimal value at ~ 9 - 10 wt.% F. It agrees well with different theoretical studies and experimental validation for F doped tin oxide; wherein significant improvement in the electronic conductivity of SnO_2 is observed with introduction of ~ 10 wt.% F due to an increase of the charge carriers concentration in the system [24, 76, 139, 140]. Since a necessary condition for excellent catalytic activity of the system is high electronic conductivity, the dependence shown in **Figure 160** may shed light to some extent on the intrinsic reasons of high electro-catalytic activity of the $(Ir_{0.3}Sn_{0.35}Nb_{0.35})O_2$:10 wt.% F solid solution (**Figure 65**).

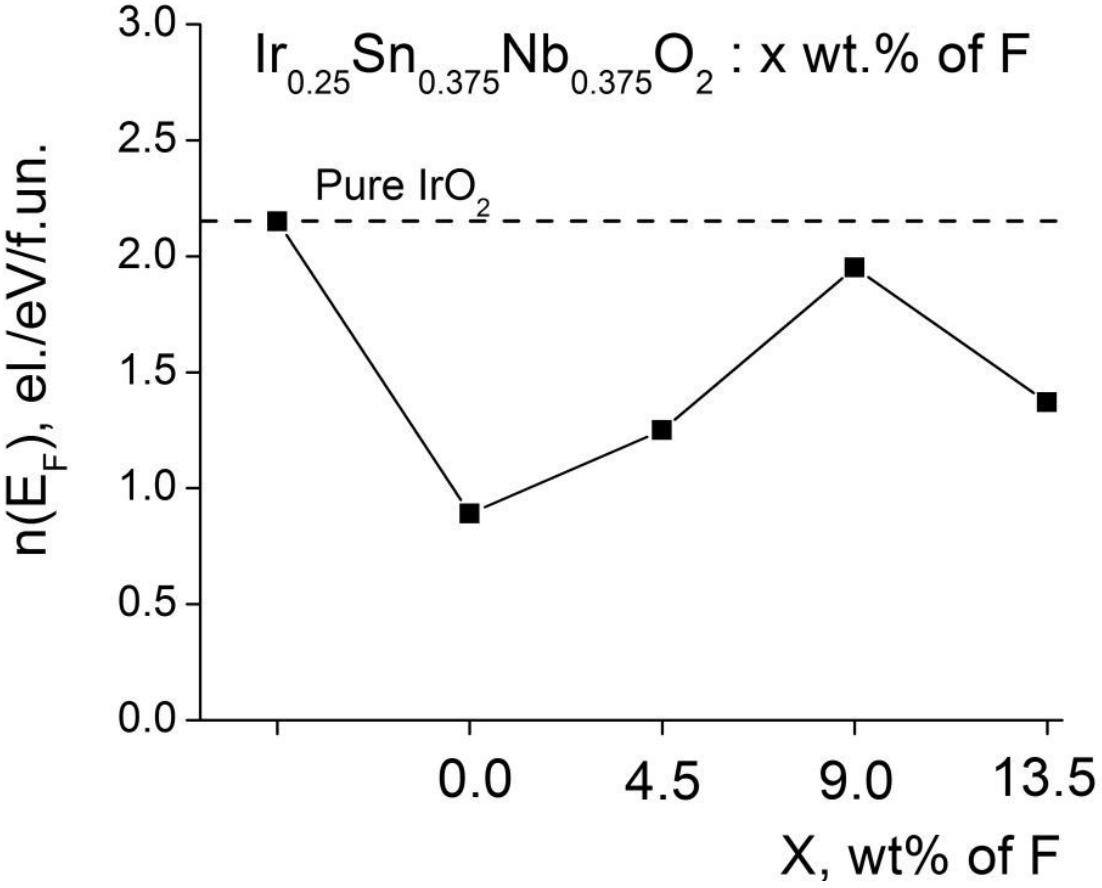

Figure 160. Total bulk density of states at Fermi level for IrO_2 and $(Ir,Sn,Nb)O_2$:F

Another aspect considered in the computational part of the present study relates to a wide spread concept proposed by Nørskov *et al.* [125, 126], that the catalytic activity of the surface could be qualitatively characterized by the simple descriptor obtained from the electronic structure of the material. Such a descriptor is determined as a position of a gravity center of d-band of the metal ε_d located usually in the vicinity of the Fermi level. The optimal position of the d-band center would provide, in turn, the optimal interaction between the surface and various species during catalytic water splitting on the surface leading to a maximum possible catalytic activity of the particular material. Hence, if an appropriate adjustment to the d-band center

position with respect to the Fermi level is done, it will very likely be critical in contribution to the design of novel highly active and electrochemically stable electro-catalysts discussed herein.

Calculations have been done for the electronic structure of the stable (1 1 0) surfaces for all the mentioned (Ir,Sn,Nb)O_2 and the positions of corresponding d-bands centers have been obtained as a first moment of $n_d(E)$: $\varepsilon_d = \int n_d(E)EdE / \int n_d(E)dE$, where $n_d(E)$ is a sum of projected densities of d-electrons of Ir, Sn and Nb. **Figure 161** shows the projected sums of Ir, Sn and Nb d-band densities of states with their corresponding centers. It is seen that the d-center for pure IrO_2 is located at ~ 1.33 eV below the Fermi level. This position was considered as a reference point for comparison of the catalytic activities of the other oxides in the present study. Substantial reduction of Ir content (up to 25 at.%) along with an introduction of Sn and Nb electronic states leads to a shift of the d-band center up to the position at - 0.09 eV below the Fermi level. This clearly indicates that an overall chemisorption reaction of various species at the surface is stronger for $(Ir_{0.25}Sn_{0.375}Nb_{0.375})O_2$ rather than for pure IrO_2.

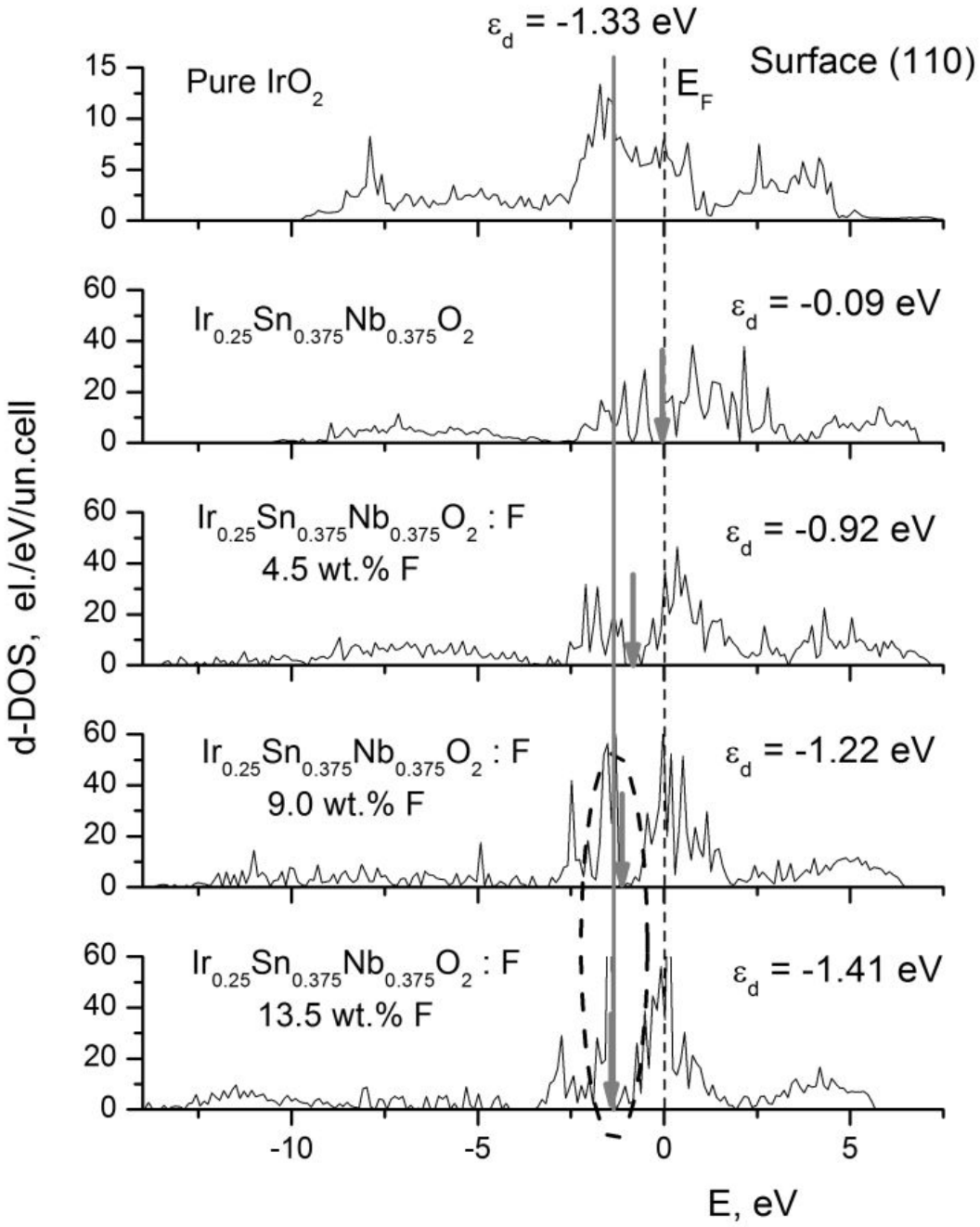

Figure 161. Projected d-band density of states for IrO_2 and (Ir,Sn,Nb)O_2:F. The arrows denote positions of the d-band centers (ε_d)

Assuming pure IrO_2 as the gold standard OER catalyst, it demonstrates optimal activity as a catalyst at ε_d = -1.33 eV. It can therefore be suggested that the decrease in electrochemical activity seen in $(Ir_{0.30}Sn_{0.35}Nb_{0.35})O_2$ electrode (**Figure 65**) might be due to the d-band center being at a more positive value and reducing the catalytic activity with respect to IrO_2. This shift in the d-band center could be attributed to an introduction of the additional Sn and Nb electronic states contributing to the total d-band of the system during formation of $(Ir,Sn,Nb)O_2$ solid solution. Further consideration of the effect of fluorine doping on the overall catalytic activity of the materials is conducted in terms of a change of the electronic structure of the compounds in general, and a shift in the position of the d-band center in particular.

Figure 162 and **Figure 163** shows the total and projected DOS of $(Ir_{0.25}Sn_{0.375}Nb_{0.375})O_2$ and $(Ir_{0.25}Sn_{0.375}Nb_{0.375})O_1F_1$, respectively. Introduction of F manifests in an appearance of the F 2p band around - 10 eV with negligible amount of other states in the entire energy domain. Increase in F content results in more pronounced 2p states leading to a stronger hybridization effect between F 2p, Ir 5d and Nb 4d states. As a result, the overall d-band center location moves from - 0.09 eV for the non-fluorine (undoped) composition downward towards the position corresponding to pure IrO_2 (- 1.33 eV) with increase in F content. It can therefore be perceived from **Figure 161** that at 4.5, 9.0 and 13.5 wt.% F, the d-band center passes accordingly through -0.92 eV, - 1.22 eV and -1.41 eV positions, respectively; indicating significant improvement in the overall catalytic activity with increase in F concentration. The optimal F concentration at which the d-center of $(Ir,Sn,Nb)O_2$:F returns back to the position corresponding to pure IrO_2 can therefore be expected to be around 10 - 12 wt.% F which is in excellent agreement with the experimental results (**Figure 65** and **Figure 67**).

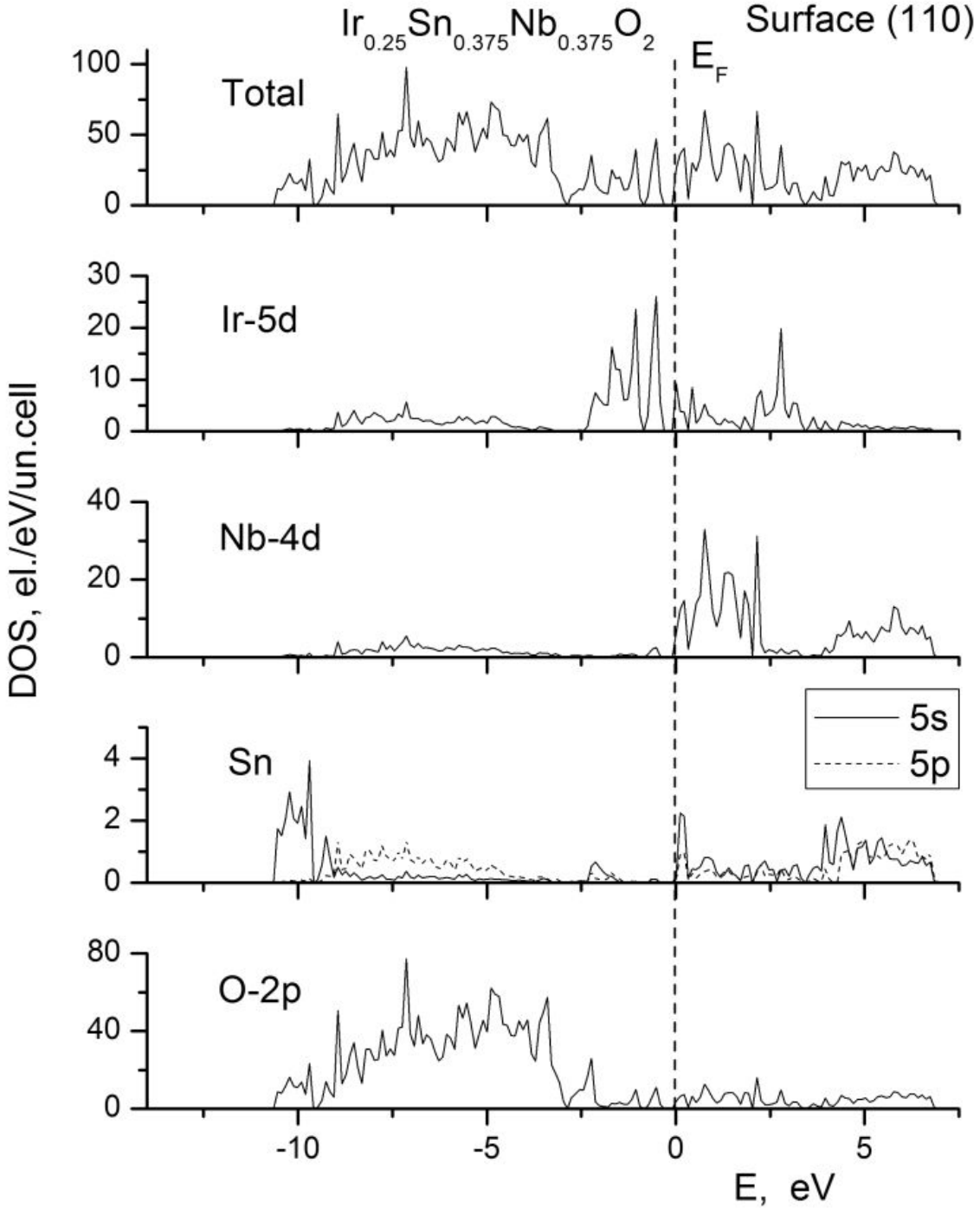

Figure 162. Total and projected density of states for $(Ir_{0.25}Sn_{0.375}Nb_{0.375})O_2$

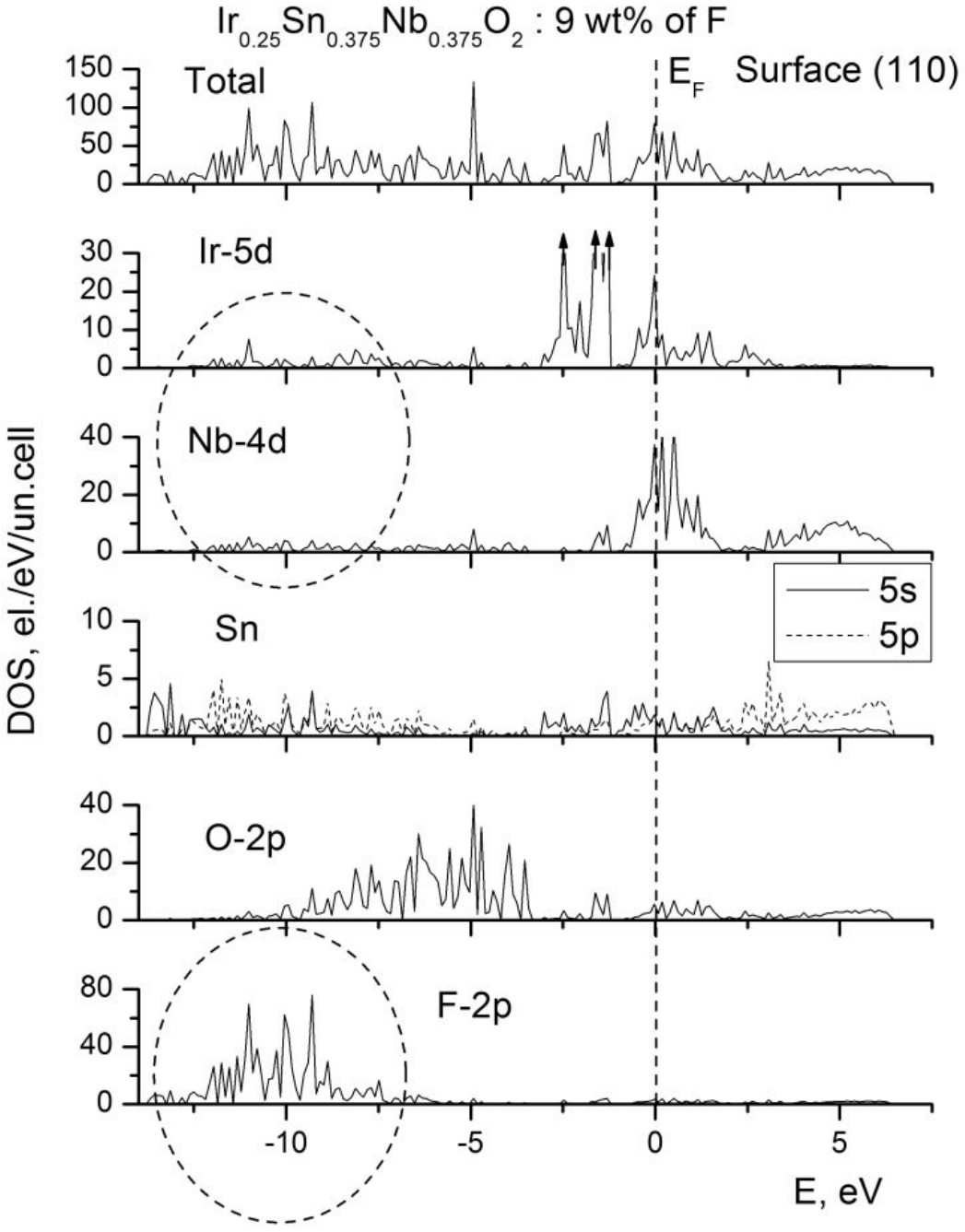

Figure 163. Total and projected density of states for $(Ir_{0.25}Sn_{0.375}Nb_{0.375})O_1F_1$

Hence, it is seen that with increase in F content, the d-band center shifts downward on the energy scale returning back to the position corresponding to pure IrO_2 at ~ 10 wt.% F rendering the system essentially mimicking the electronic and electro-catalytic properties of pure IrO_2. A combination of the improved metallic electronic conductivity and the d-band center position being optimal conceivably renders (Ir,Sn,Nb)O_2:F demonstrating high catalytic activity comparable to pure IrO_2. Additionally, for this composition it should be noted that the electronic structural change results in the entire oxide (not only Ir cations) becoming catalytically active mimicking the catalytic behavior of pure IrO_2.

Figure 164 shows the calculation of cohesive energy (E_{coh}) for the materials considered in this study. It is observed that reducing Ir concentration and simultaneous increase of Sn and Nb content in the catalyst material leads to a more negative value of E_{coh}. This can be attributed to the formation of Nb - O bonds which are more strong than Ir - O (calculated E_{coh} for pure NbO_2 is - 18.251 eV/f.un. *vs.* - 15.859 eV/f.un. for IrO_2). However, introduction of F leads to a gradual decrease in the cohesive energy (absolute value) due to weaker metal - F^- bonds in comparison with corresponding metal - O^{2-} ones (the lower negative charge of F^- leads to the weaker electrostatic metal - fluorine interaction). Nevertheless, such a negative effect of F doping does not significantly affect the overall stability of the material. As seen in **Figure 164**, E_{coh} of the F doped (Ir,Sn,Nb)O_2 becomes equal to that of pure IrO_2 approximately at ~ 7 wt.% F. Further increase in F content results in the material displaying less stability compared to pure IrO_2. Although the optimal composition of the oxide with ~ 10 wt.% F demonstrates slightly lower E_{coh} than the reference IrO_2, one can state that the overall stability of the material (qualitatively determined by the cohesive energy) is of the same order as pure IrO_2. This

conclusion also agrees well with the experimental results (**Figure 74**) obtained from the chronoamperometry curves.

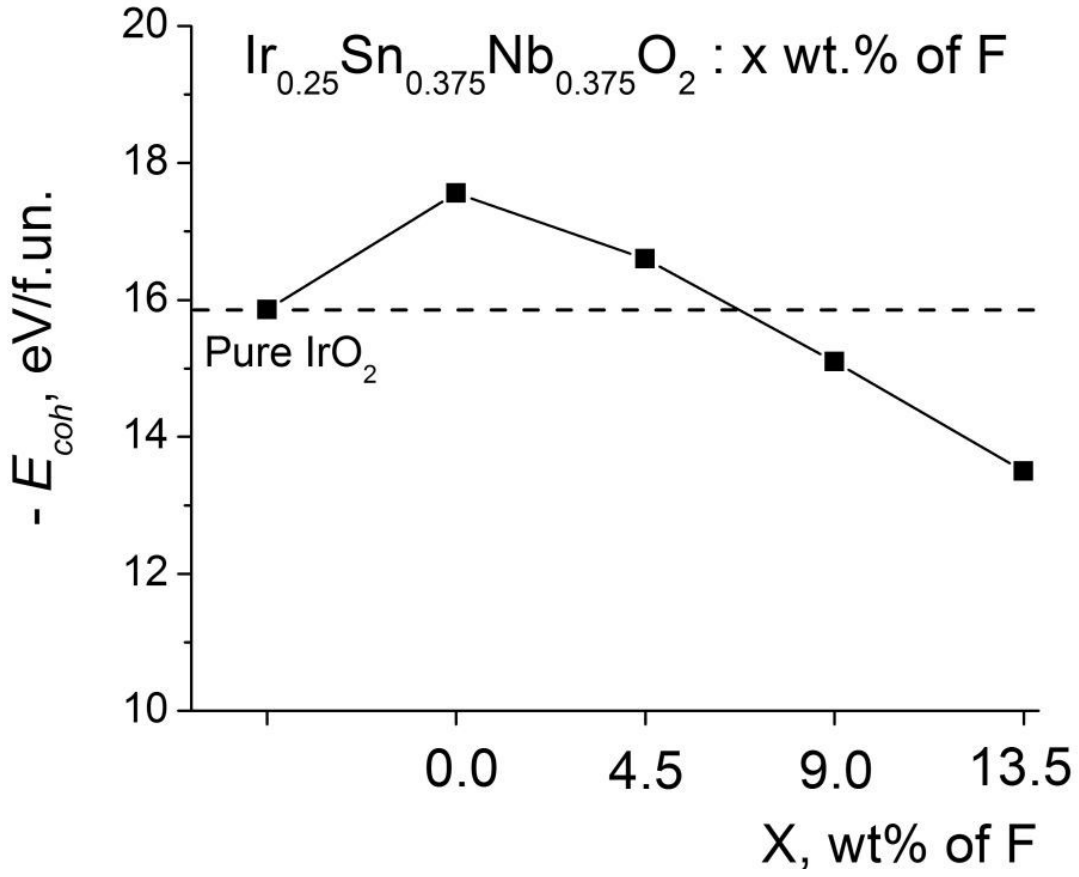

Figure 164. Cohesive energy of IrO_2 and $(Ir_{0.25}Sn_{0.375}Nb_{0.375})O_{2-x}F_x$

7.0 SUMMARY

Nanostructured robust mixed metal oxides with reduced noble metal content have been synthesized, characterized and developed for use as anode electro-catalysts in proton exchange membrane (PEM) based water electrolysis. The catalysts were developed in the form of thin films and nanostructured high specific surface area powders for the oxygen evolution reaction (OER). The experimental work in the thesis was primarily targeted towards accomplishment of better efficiency, durability and lower cost catalyst materials.

Electro-catalysts with significant decrease in the noble metal loading along with improved catalytic response using novel synthesis techniques were obtained. Strategies involved synthesizing less expensive and more durable high surface area nanostructured materials as supports or diluents for the expensive electro-catalyst, which would ultimately help in immensely lowering the overall costs. The electro-catalysts mentioned in the thesis thus portend to be potentially preferred for use as an anode OER material in PEM electrolyzers.

Different catalyst systems were chosen systematically in order to achieve excellent electrochemical activity without compromising the stability of the catalysts. Fluorine was used as the dopant not only with pure IrO_2, but also with the binary and ternary metal oxides which boosted the overall performance and electro-catalytic activity of the catalysts. Tin oxide and/or niobium oxide were chosen as supports with pure IrO_2 and RuO_2 in order to decrease the cost

due to the noble metal oxides. A reduction of up to ~ 80 at.% in the noble metal oxide content has been achieved for various electro-catalyst systems. The electro-catalysts in nano-crystalline form of 2D and 3D architectures with different morphology, microstructure and composition were prepared. Systematic structural and electrochemical characterization was carried out throughout the thesis to understand the relation between the catalyst structure and the electrochemical behavior.

7.1 THIN FILM CATALYSTS

The thin films have been synthesized by homogenizing the precursor solutions and heat treatment to 400°C. The synthesis technique resulted in formation of a complete solid solution for all the different catalyst systems. No phase separation or any extra peak was observed for the supports or dopant used in our studies. Detailed characterization and electrochemical studies were conducted to confirm the catalysts' potential as an OER anode for PEM electrolyzers.

The study of F doped IrO_2 which has been discussed in **Section 5.1.1** shows the viability of fluorine as a great dopant. It not only helps achieve greater electrochemical activity, but also does not comprise the stability of the resultant IrO_2:F electro-catalyst. These results gave the motivation for doping F in the various binary and ternary catalyst systems.

Consequently, F doped SnO_2 was used as a support with IrO_2 and RuO_2. SnO_2:F imparted stability to the overall structure and helped achieve comparable current density as the pure noble metal oxide counterpart even after reducing the expensive metal oxide content by ~ 80 at.%. Detailed results involving Tafel slope and Electrochemical Impedance Spectroscopy (EIS) have

been discussed in **Section 5.1.2** and **Section 5.1.3** for the binary thin film structures of $(Ir,Sn)O_2$:F and $(Ru,Sn)O_2$:F, respectively. Rotating disk electrode (RDE) studies were also conducted on the most optimized composition of $(Ir_{0.2}Sn_{0.8})O_2$:10 wt.% F to confirm the reaction mechanism and get the number of electrons getting transferred in the reaction.

Since niobium oxide is known to have greater cohesive energy than IrO_2 and SnO_2, a novel rutile structure of $(Ir,Sn,Nb)O_2$ was developed. The ternary compositions were all single phase confirming the formation of complete solid solution. They were characterized extensively *via* x-ray diffraction (XRD) and x-ray photoelectron spectroscopy (XPS). The $(Ir,Sn,Nb)O_2$ catalyst helped achieve similar electrochemical activity after decreasing IrO_2 by ~ 60 at.%. But, due to the incorporation of niobium oxide in the lattice, a much stable structure is achieved in comparison with pure IrO_2, the accepted gold standard anode in PEM based water electrolysis. This enabled the ternary catalyst materials to exhibit excellent resistance to corrosion and enhance chemical stability as discussed in **Section 5.1.4**. Fluorine doping to the ternary electro-catalysts has been discussed in **Section 5.1.5** which further decreased the noble metal oxide content without compromising the catalysts durability.

7.2 NANOPARTICULATE CATALYSTS

The electro-catalytic materials based on IrO_2:F, $(Ir,Sn)O_2$:F and $(Ir,Nb)O_2$:F in 3D architectures of nanoparticles were synthesized to achieve the compositional homogeneity at atomic and nanometer length scale. Synthesis of the nanostructured high surface area electro-catalyst architectures with manipulation of particle morphology and size was carried out to promote

cooperative, sequential reaction steps along different catalytic domains of the nanoscale structure.

F doped IrO_2 nanoparticles were synthesized by the modified Adams fusion approach giving us enormously high specific surface area catalysts. This resulted in enhance electro-chemical activity with no loss in stability. Detailed RDE experiments and kinetic studies, along with the long term structural stability tests and EIS studies were conducted as discussed in **Section 5.2.1**. The kinetic parameters obtained were most superior for IrO_2:10 wt.% F which was corroborated by other electrochemical tests like polarization, EIS and chronoamperometry (CA).

Nanoparticulate robust fluorine doped SnO_2 was used as a support with IrO_2. SnO_2:F was synthesized *via* a surfactant based approach to achieve high specific surface area supports. A single solid solution of IrO_2 with SnO_2:F resulted in reducing the IrO_2 content by ~ 70 at.% without compromising the electrochemical activity as compared to pure IrO_2. Enhanced corrosion resistance of the (Ir,Sn)O_2:F materials has been obtained and is discussed in **Section 5.2.2**. Significant characterization in the form of transmission electron microscopy (TEM), XRD and XPS was also carried out to complement the electrochemical results.

High surface area fluorine doped niobium oxides were developed as supports by a facile low temperature sol-gel technique. The electro-catalyst system of (Ir,Nb)O_2:F exhibited similar electrochemical activity as commercially used IrO_2 with reduction in noble metal by ~ 75 at.%. But, these binary electro-catalyst systems showed way better durability than the commercial IrO_2. Detailed structural characterization along with the electrochemical testing including extended time CA plots have been discussed in **Section 5.2.3**.

Identification of such non-noble metal based catalysts systems or electro-catalysts with significant reduction of expensive noble metal contents, yielding comparable or higher

electrochemical performance than the gold standards for PEM based water electrolysis; would result in reduction in the overall capital costs of PEM based water electrolyzers. This would thus help in the attainment of the targeted hydrogen production cost (< $ 3.0 / gallon gasoline equivalent delivered) comparable to conventional liquid fuels.

.

APPENDIX A

PEM WATER ELECTROLYSIS SUPPORTS

There is considerable demand for identification of non-noble metal based catalysts and catalyst supports for water electrolysis. Theoretical approaches provide an ideal framework for identifying such systems. In an attempt to identify new electrochemically stable catalyst supports for electrolysis of water, the electronic structures of $MgNb_2O_6$, $MgTa_2O_6$, $ZnNb_2O_6$, and $ZnTa_2O_6$ compounds doped with elements from 3A, 3B, 5B, 6A groups of the Periodic Table as well as F from group VII have been calculated using the Vienna ab-initio simulation package (VASP), within the projector augmented-wave (PAW) method in the general gradient approximation (GGA) for conducting the exchange-correlation corrections. The role of incorporating the additional elements in improving the electronic conductivity as well as the structural and chemical stability is discussed. Based on the calculated values of the cohesive energies for the materials and their type of electronic conductivity, we hypothesize that introduction of group 3A elements (Sc and Y) as well as F contribute drastically to the improvement of the electronic properties as well as the chemical stability of all four Mg and Zn tantalates/niobates based parent oxides. The study indicates that these doped compounds might serve as the most appropriate candidate catalyst supports for water electrolysis.

A.1 AB-INITIO STUDIES

A.1.1 Introduction

Advanced water electrolyzers using proton exchange membranes (PEM) generally utilize expensive noble metal electro-catalysts for the oxygen electrode such as platinum and platinum alloys [15] as well as the equally prohibitively expensive iridium oxide (IrO_2) and ruthenium oxide (RuO_2) catalysts. The tremendous cost associated with the use of noble metal oxides at the current loading levels could be substantially lowered by developing new non-noble metal based catalysts that exhibit comparable or improved catalytic activity as the parent noble metal counterparts or identification of electrochemically stable catalyst supports that can be economically synthesized in high surface area (HSA) forms allowing for reduced levels of catalyst loading without compromising the electro-catalytic activity. Thus, it is desirable that these catalyst supports exhibit high electronic conductivity comparable to the noble metals combined with excellent chemical and electrochemical stability at potentials of 1.8 V - 2.0 V *vs.* normal hydrogen electrode (NHE) wherein electrolysis of water is known to occur.

Very few materials are known to exhibit both the desired electrical conductivity and the much needed electrochemical stability in the desired potential window. In this regard, several researchers have proposed [71, 74, 141, 142] the use of IrO_2 combined with highly corrosive resistant tantalum oxide (Ta_2O_5), tin oxide (SnO_2), niobium oxide (Nb_2O_5), titanium oxide (TiO_2) and non-stoichiometric tungsten oxide (WO_x) for stabilizing the IrO_2 dimensionally stable anode electrode during the service life of the electrolyzer. However, there is a need to further improve

the electronic conductivity to enhance the electro-catalytic activity thus improving the catalyst efficiency and consequently minimizing the catalyst loading.

One approach to achieve this goal would be the introduction of solid solutions of transition metal oxides, such as Nb_2O_5 and Ta_2O_5, with tin oxide, which are known to exhibit the desired high chemical and electrochemical stability but are also well known insulators with poor electronic conductivity. Alloying of the oxides with SnO_2 can likely change their electronic structure, which in turn could positively influence the electronic conductivity. In our recently published first principles theoretical study of different ternary oxides, such as $SnTa_2O_6$, $SnNb_2O_6$, $Sn_2Ta_2O_7$, $Sn_2Nb_2O_7$, doped with small concentration of elements selected from groups 5B and 6A of the Periodic Table, including As, Sb, Bi as well as Cr, Mo, and W [143], it was postulated that $SnTa_2O_6$ doped with As, Sb, or Bi would be the most appropriate material for implementation as catalyst supports with respect to all other materials investigated in the study, both in terms of the electronic conductivity as well as structural / chemical stability.

Besides Sn-Nb/Ta-O oxides there is a large family of bivalent niobates and tantalates [144, 145] which remain largely unexplored for possible use as catalyst supports, however their structural and chemical stability is higher than the tin based oxides. For example, CaO, MgO, SrO oxides have higher formation enthalpy in comparison to SnO, thus one can suggest that tantalates and niobates of Ca, Mg or Sr can also be expected to demonstrate higher structural stability than the tin based systems. Recently, our group investigated a large family of calcium niobates and tantalates doped with small amount of different elements playing the role of donors of additional electrons for improving the electronic conductivity of the material [145]. The results showed that Sc, Y, and F are the best dopants that are able to drastically improve the

conductivity without compromising the structural and electrochemical stability under the aggressive pH and chemical reaction conditions prevalent during operation.

A.1.2 Magnesium and Zinc Tantalates and Niobates

The present study is an attempt to explore Mg- and Zn- based niobates and tantalates as potentially possible candidate materials for use as catalyst supports for water electrolysis and hydrogen fuel cells. We selected $MgNb_2O_6$, $MgTa_2O_6$, $ZnNb_2O_6$, and $ZnTa_2O_6$ compounds for our investigation since these materials are relatively inexpensive, demonstrating high structural and chemical stability and are also well known mostly as promising dielectrics for applications in microwave devices [146, 147] as well as photocatalysts for water splitting and producing hydrogen gas under light illumination [148-150].

Since all the four $MgNb_2O_6$, $MgTa_2O_6$, $ZnNb_2O_6$, and $ZnTa_2O_6$ are semiconductors it would be interesting to investigate the effect of different dopants selected particularly in light of improving the electronic conductivity necessary for achieving high performance of the potential catalyst supports. These elements would likely serve as donors of additional free electrons participating in the charge transfer and thus, increasing the electronic conductivity. Such elements substituting for divalent Mg^{2+} or Zn^{2+} at the corresponding sites in the crystal lattice could belong to 3A, 3B, 5B groups of the Periodic Table, while elements substituting Nb^{5+} and Ta^{5+} in the lattice might belong to 6A group. An additional likely pathway for donating free electrons into the system is to dope the oxides with a small amount of fluorine substituting the corresponding oxygen ions in the crystal structure. An effect of such F doping could be similar to

that observed in fluorine doped tin oxide (FTO) widely investigated experimentally and from first principles [56, 140, 151, 152].

First principles (or *ab-initio*) approaches by definition are based on fundamental laws of quantum mechanics without needs of experimental fitting data, which makes them very attractive for study various properties of materials computationally, without time and cost consuming experimental trials and errors. It makes it possible to rapidly evaluate the effect of compositional modifications of the oxides on their electronic conductivity and structural stability. Based on the above, *ab-initio* calculations of total energies, electronic and optimized crystal structures, and cohesive energies have been carried out in the present study [153] for the following oxides: $MgNb_2O_6$, $MgTa_2O_6$, $ZnNb_2O_6$, and $ZnTa_2O_6$ in both, pure and doped forms with the introduction of a small amount of elements from 3A group - Sc, Y, 3B group - B, Al, Ga, In, 6A group - Cr, Mo, W, 5B group - As, Sb, Bi, as well as F from group 7. The formula units of the doped materials can be written as: $[(Mg/Zn)_{1-x}(3A,\ 3B,\ 5B\ elements)_x](Nb/Ta)_2O_6$, $(Mg/Zn)[(Nb/Ta)_{1-y}(6A\text{-}elements)_y]_2O_6$, and $(Mg/Zn)(Nb/Ta)_2O_{6-x}F_x$, where x = 0.25 and y = 0.125.

A.2 COMPUTATIONAL DETAILS

The total energies, electronic structure and density of electronic states are calculated within density functional theory (DFT) using the generalized gradient approximation (GGA) for the exchange-correlation energy functional in a form suggested by Perdew and Wang [130]. We use the projector augmented wave (PAW) method and a plane wave basis set, as implemented in a

widely used the Vienna Ab initio Simulation Package (VASP) [131-133]. DFT calculations using the common density functionals give adequate values for ground state properties such as total energies and vibrational frequencies. However, excited state properties are not given accurately, for example, the electronic band gap is typically underestimated approximately by a half. Since otherwise DFT approaches are quite accurate and reliable yet faster than other traditional *ab-initio* techniques, such as Hartree - Fock theory and its derivations based on the complex many electron wavefronts, we have chosen VASP package as a main computational tool in present theoretical study.

The atomic positions and the cell parameters, including the cell volume, are optimized by minimizing the forces and stresses *via* the Hellmann - Feynman theorem. Standard PAW potentials were employed for the elemental constituents of all pure and doped compounds in the study. For all the materials considered the plane wave cutoff energy of 520 eV has been chosen to maintain high accuracy of the total energy calculations. The lattice parameters and internal positions of atoms were fully optimized during the double relaxation procedure employed; and consequently, the minima of the total energies with respect to the lattice parameters and internal ionic positions have been determined. This geometry optimization was obtained by minimizing the Hellman - Feynman forces *via* a conjugate gradient method, so that the net forces applied on every ion in the lattice is maintained close to zero. The total electronic energies were converged within 10^{-5} eV/un.cell resulting in the residual force components on each atom to be lower than 0.01 eV/Å/atom, thus allowing for the accurate determination of the internal structural parameters. Since the doped structures contain a small amount of additional elements, it is expected that the equilibrium volume of the basic unit cell is not substantially altered. Hence,

only internal atomic positions have been optimized during the calculations keeping the volumes of the unit cells identical to that of the corresponding undoped parent materials.

The Monkhorst - Pack scheme was used to sample the Brillouin Zone (BZ) and generate the ***k*** point grid for the solids and the different isolated atoms used in the present study. A choice of the appropriate number of ***k*** points in the irreducible part of the BZ was based on convergence of the total energy to be 0.1 meV/atom. For pure and doped forms of $MgNb_2O_6$, $MgTa_2O_6$, $ZnNb_2O_6$ and $ZnTa_2O_6$, the numbers of ***k*** points in the irreducible parts of BZ used were 84, 84, 110 and 110 points, respectively.

$MgNb_2O_6$ and $ZnNb_2O_6$ adopt the orthorhombic columbite crystal structures with Pbcn (#60) space group containing 36 atoms in the conventional unit cell (Z = 4) [154]. The crystal structure of $MgTa_2O_6$ on the other hand belongs to the tetragonal tri-rutile type with $P4_2/mnm$ (#136) space group containing 18 atoms in the unit cell (Z = 2), while $ZnTa_2O_6$ adopts an orthogonal tri-α-PbO_2 type structure with Pbcn (#60) space group containing 36 atoms in the unit cell. To maintain uniformity in all calculations we artificially doubled the 18 atom tri-rutile unit cell of $MgTa_2O_6$ up to 36 atoms per cell to be consistent with the other three parent oxides considered in the study.

A.3 RESULTS AND DISCUSSION

The electronic structures of orthorhombic $MgNb_2O_6$ and tetragonal $MgTa_2O_6$ are almost identical due to the isoelectronic similarity of Nb and Ta. It is also for this reason that orthorhombic $ZnNb_2O_6$ and tetragonal $ZnTa_2O_6$ exhibit similar characteristics. The structural

parameters of the oxides obtained experimentally and derived from the calculations are presented by Velikokhatnyi *et al.* [153]. One can see that the results of the calculations obtained from the structural optimization are in very good agreement with experimental measurements and are characterized by an error of less than 1.2 % for all the four compounds considered in the study. This margin of error is typical for state-of-the-art approximations to density functional theory.

Figure 165 and **Figure 166** show the total (DOS) and partial (PDOS) density of electronic states for all the four parent materials studied. The energy scale has been shifted in such a way that the zero corresponds to the Fermi energy. The occupied bands of $MgNb_2O_6$ and $MgTa_2O_6$ shown in **Figure 165** consist mainly of O 2s, O 2p and to some extent, d-orbitals of Nb or Ta. Mg 3s and Mg 2p states are observed in a very limited amount. The valence band consists primarily of O 2p states with small admixture of transition metal d-orbitals as well as 3s and 2p states of Mg. The conduction bands of the materials are composed of Nb 4d or Ta 5d orbitals hybridized with another part of O 2p states. Similar electronic structure is observed for $ZnNb_2O_6$ and $ZnTa_2O_6$ shown in **Figure 166**. The only difference between Mg- and Zn- based materials is that Mg 3s and 2p are replaced by Zn 3d orbitals hybridized with O 2p and Nb 4d / Ta 5d electronic states comprising the main portions of the valence band of the oxides. Otherwise, the electronic structures of all the four materials are qualitatively very similar. All of the materials demonstrate a forbidden energy gap between the valence and conduction bands. As it was mentioned before, the values of the band gaps (BG) calculated within the DFT methodology are usually underestimated; hence the calculated values of BGs should be taken into consideration only qualitatively.

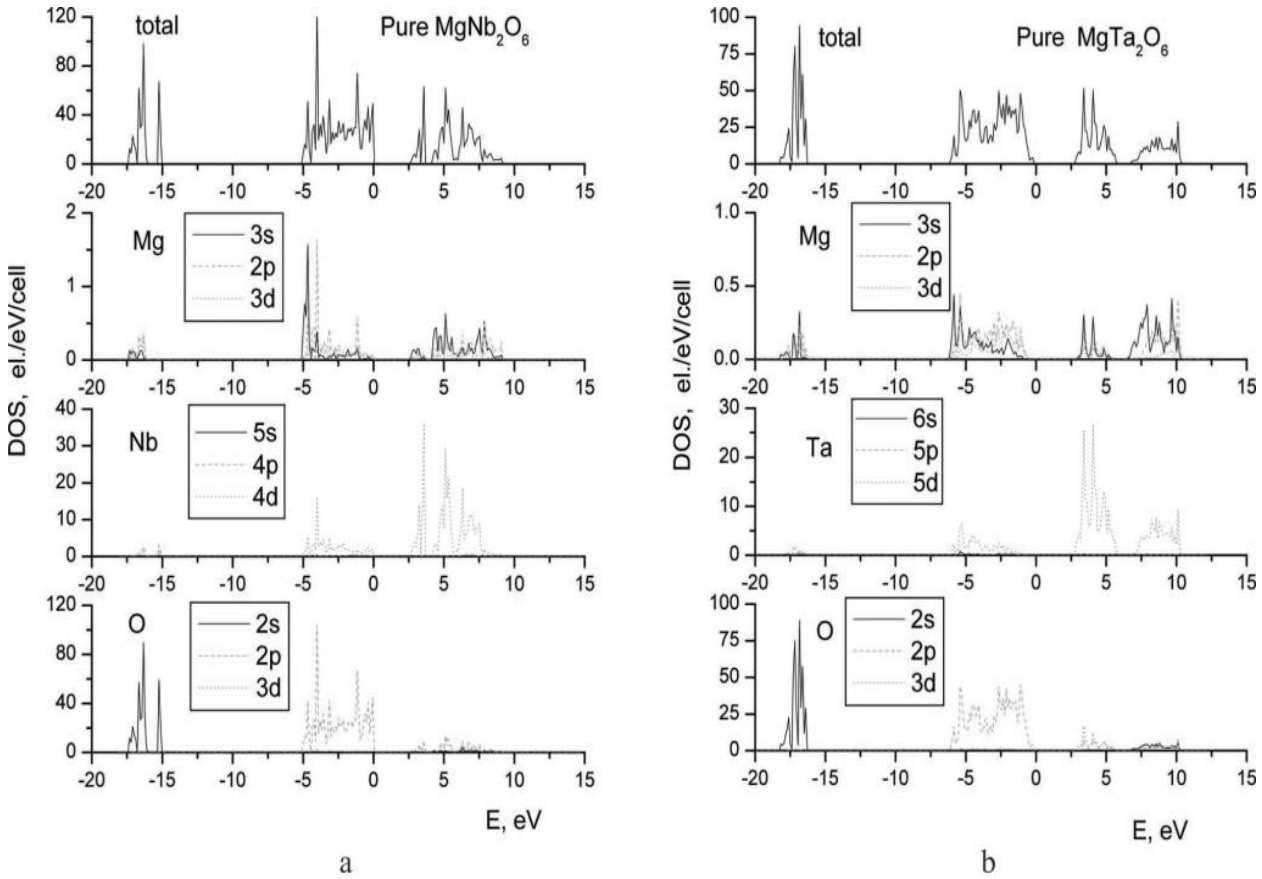

Figure 165. Electronic density of states for $MgNb_2O_6$ (a), and $MgTa_2O_6$ (b)

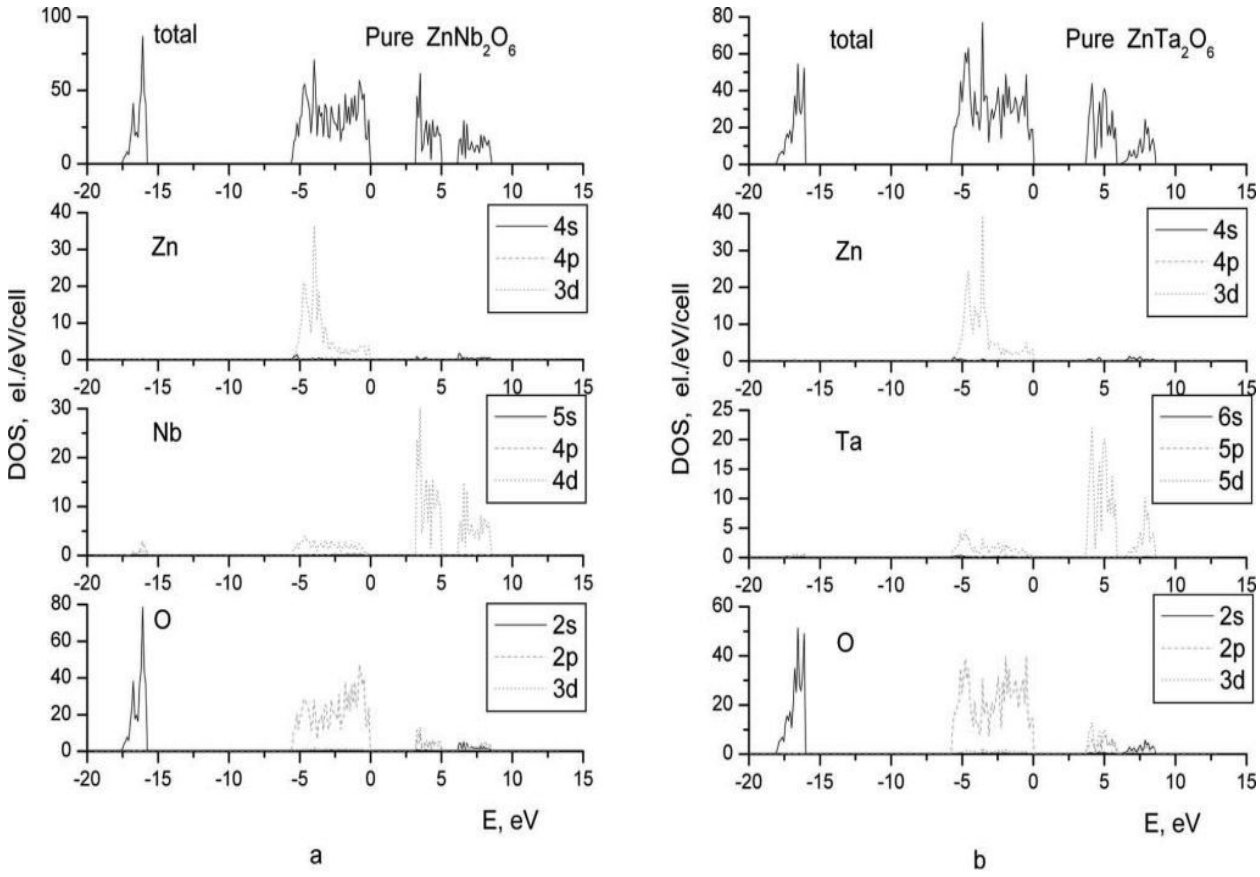

Figure 166. Electronic density of states for $ZnNb_2O_6$ (a), and $ZnTa_2O_6$ (b)

Since all the four oxides are semiconductors, their electronic conductivity is still inadequate for use as electrode materials for electrolysis and needs to be improved further to enhance the charge transfer characteristics critical for lowering the over potential and attaining good catalytic activity. The electronic conductivity could be improved by introducing a small amount of additional elements possessing more valence electrons than Mg / Zn or Nb / Ta. Hence these elements will be capable of serving as donors of free charge carriers, thus increasing the electronic conductivity.

Since the goal of the current study is to unravel the principal role of the introduction of small concentrations of dopants and their corresponding influence on the electronic conductivity

and chemical stability of the parent oxide, only one atom of each dopant has been placed into the elementary cell. Such a selection eliminates any uncertainty in the atomic configurations occurring due to the presence of multiple (two or more) dopant atoms in the unit cell. For example, the 36 atom unit cell of the orthorhombic columbites $(Mg/Zn)Nb_2O_6$ contains 4 Mg or Zn, 8 Nb, and 24 O ions; so that those elements substituting for Mg/Zn in the unit cell will replace one Mg / Zn atom out of the four available. Similarly, only one atom from the 6B group will be substituted for one atom of Nb out of the existing 8 sites and one atom of F will replace one out of 24 oxygen atoms available in the unit cell. The valence electronic configurations of Mg, Zn, Nb, Ta and O atoms are $3s^2 2p^6$, $3d^{10} 4s^2$, $4p^6 5s^1 4d^4$, $6s^2 5d^3$ and $2s^2 2p^4$, respectively. The electronic configurations for Sc and Y are $4s^2 3d^1$ and $4s^2 4p^6 5s^2 4d^1$, respectively; for B, Al, Ga and In are $2s^2 2p^1$, $3s^2 3p^1$, $3d^{10} 4s^2 4p^1$ and $4d^{10} 5s^2 5p^1$, respectively; for As, Sb and Bi are $4s^2 4p^3$, $5s^2 5p^3$ and $6s^2 6p^3$, respectively; for Cr, Mo and W are $3d^5 4s^1$, $4d^5 5s^1$ and $5d^4 6s^2$, respectively; and finally, for F is $2s^2 2p^5$.

Since the niobates and tantalates considered in the present study have similar electronic structures, the main discussion of the results primarily focuses on Mg and Zn niobates doped with the different elements. Moreover, most of the conclusions derived from the present study on doped Mg / Zn niobates can also be applied to the corresponding iso-electronic Mg / Zn tantalates, and hence the results obtained for doped $MgTa_2O_6$ and $ZnTa_2O_6$ will be shown primarily for illustration purposes.

A.3.1 3A and 3B group elements

Due to the isoelectronic nature of elements belonging to the same group of the Periodic Table, the changes in the electronic structure resulting from doping the parent oxides with such elements are qualitatively very similar. Hence we will discuss in detail only one or two representative dopants from each group and mention briefly the results for other members of the particular periodic group.

We chose Sc and Y from 3A group and B, Al, Ga and In from group 3B of the Periodic Table. All the elements have valence +3, and hence they could serve as donors of additional free electrons when they were used as substituents for divalent Mg^{2+} or Zn^{2+}. The total and partial electronic densities of states calculated for $Mg_{0.75}Sc_{0.25}Nb_2O_6$ are shown in **Figure 167** (a). Almost identical results have been obtained for Y doping due to the identical outer electronic configuration. One can therefore see that the doped system demonstrates very similar electronic structure as undoped $MgNb_2O_6$. The only prominent difference is that in the doped system the Fermi level is shifted towards the conduction band rendering this material metallically conductive. It occurs due to the strong hybridization of Sc 3d (or Y 4d) and Nb 4d zones forming the conduction band occupied with additional electrons being supplied to the system by the donor serving Sc- or Y- dopants. It is also worth mentioning that the band gap value between valence and conduction bands is practically not changed during doping and are 2.39 eV and 2.35 eV for Sc- and Y- doping, respectively. Sc- and Y- doping of $MgTa_2O_6$ demonstrate the same results as for $MgNb_2O_6$ discussed above with corresponding band gaps equal to 2.75 eV and 2.9 eV respectively.

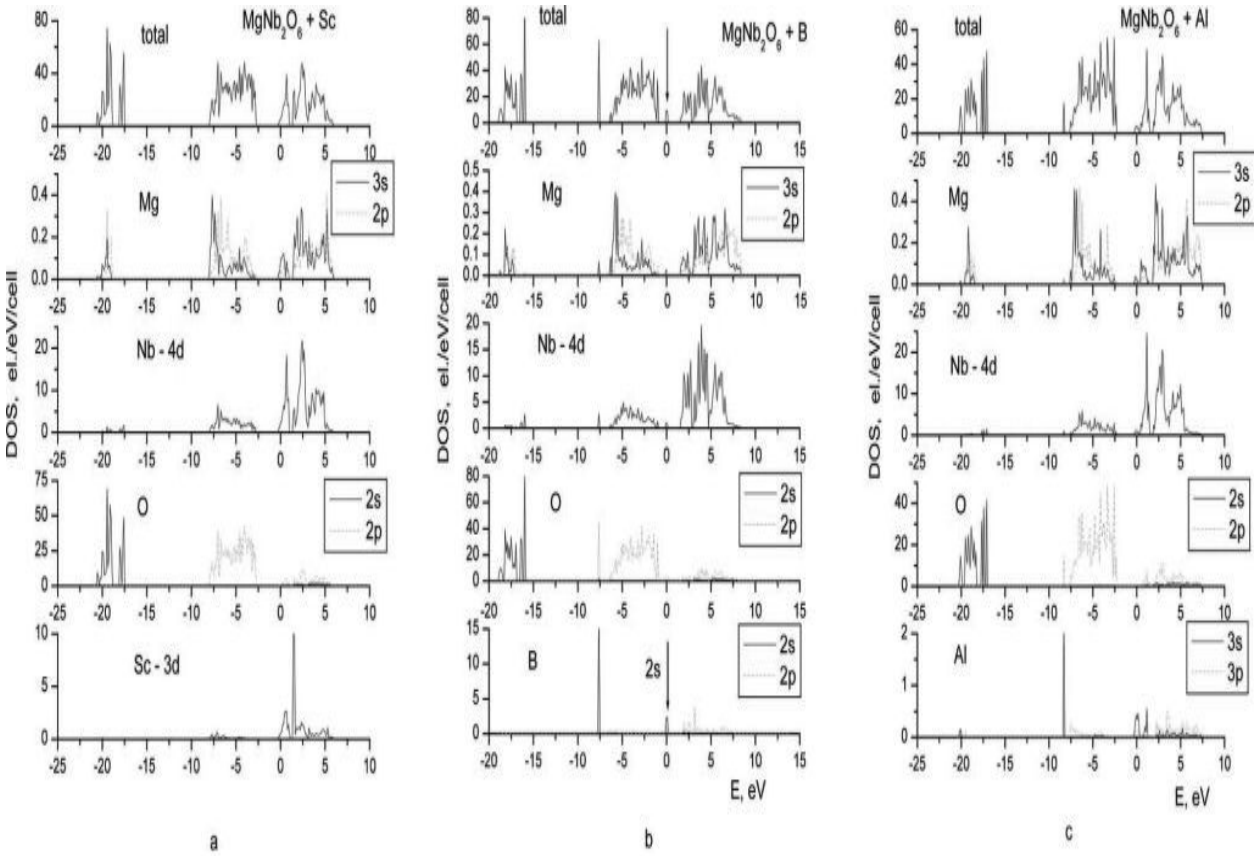

Figure 167. Electronic density of states for $MgNb_2O_6$ with Sc (a), B (b), and Al (c)

As for doping with 3B elements, the results are quite different from those seen for 3A dopants. The total and partial DOS for $MgNb_2O_6$ doped with B and Al are shown on **Figure 167** (b) and (c), respectively. Incorporation of boron introduces a new non-hybridized completely localized impurity zone which is its own valence s states located in the energy gap between the valence and conduction bands (see partial density of states of B denoted by an arrow). This impurity s-zone is separated from the main conduction band by an energy gap of 1.41 eV, which is the value of the activation energy, E_a for the electronic conductivity determined by electron transitions from these localized s-states to the conduction band. Quite similar situation is observed for Ga doped $MgNb_2O_6$ with corresponding E_a equal to 0.54 eV; however, in the case

of Ga doped $MgTa_2O_6$, the Ga 3s orbitals are shifted towards the conduction band, thus hybridizing with Ta 5d states and making the material electronically conductive. This case is very similar to those for Al- and In- doped $MgNb_2O_6$ and $MgTa_2O_6$. Both Al and In s-orbitals hybridize with Nb 4d or Ta 5d conduction bands making these materials also metallically conductive with the activated conductivity $E_a = 0$.

In regards to $ZnNb_2O_6$ and $ZnTa_2O_6$ doped with 3A and 3B elements, the results are very similar to those obtained for Mg niobates and tantalates. **Figure 168** shows the total and partials DOS for $ZnNb_2O_6$ doped with Sc, B and Al. Similar to the Mg niobates and tantalates, Sc and Al improves the electronic conductivity of the parent oxide converting it from the inherent semiconducting state to a metallic form. Similar effect is observed for both $ZnNb_2O_6$ and $ZnTa_2O_6$ doped with Y, Ga and In. Furthermore, B doping of $Zn(Nb/Ta)_2O_6$ demonstrates a similar effect for the electronic conductivity observed in the case of B doped $Mg(Nb/Ta)_2O_6$, wherein the conductivity is improved by significant reduction of the main band gap, while still retaining it in the semiconductor range of 0.8 eV and 1.1 eV for $ZnNb_2O_6$ and $ZnTa_2O_6$, respectively.

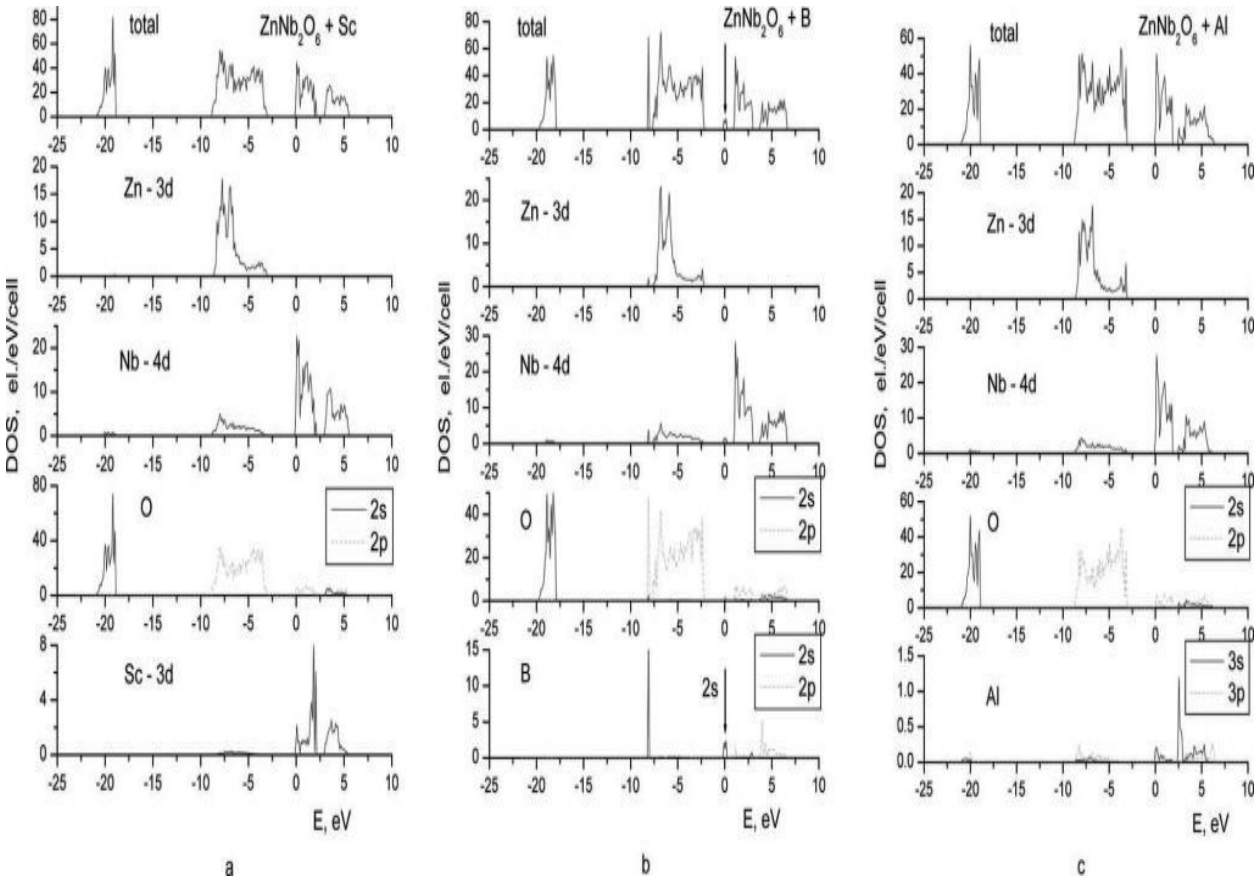

Figure 168. Electronic density of states for $ZnNb_2O_6$ with Sc (a), B (b), and Al (c)

A.3.2 5B and 6A group elements and Fluorine

The total and partial DOS calculated for $Mg_{0.75}As_{0.25}Nb_2O_6$, $Mg[Nb_{0.875}Cr_{0.125}]_2O_6$ and $Mg[Nb_{0.875}W_{0.125}]_2O_6$ are shown in **Figure 169**. In contrast to pure $MgNb_2O_6$, the electronic structures of the doped oxides display several features related to the substituted dopants. The main differences between pure $MgNb_2O_6$ and the structure doped with As, Sb or Bi are the appearance of the s-states of the dopants indicated by arrows hybridized with O 2p states located at the bottom of the valence band and separated from the upper portion of the valence band by an

energy gap of 2.1 eV - 3.0 eV [**Figure 169** (a)]. Also, similar to 3A dopants due to the additional free electrons introduced into the system, the Fermi level of the doped structures is also shifted towards the conduction band resulting in metallic conductivity of the material. The band gap between the valence and conduction bands is ~ 2.1 eV and does not change significantly with respect to that of the undoped oxide (2.4 eV); so that introduction of small amounts of 5B group elements does not noticeably affect the width of the forbidden zone. A similar result is observed for $MgTa_2O_6$ doped with identical 5B elements demonstrating that the values of the energy gap between the valence and conduction bands for all the three dopants are 2.9 eV, 3.0 eV and 2.8 eV for As, Sb and Bi, respectively, which correlates well with the calculated band gap for the pure $MgTa_2O_6$ of 2.75 eV.

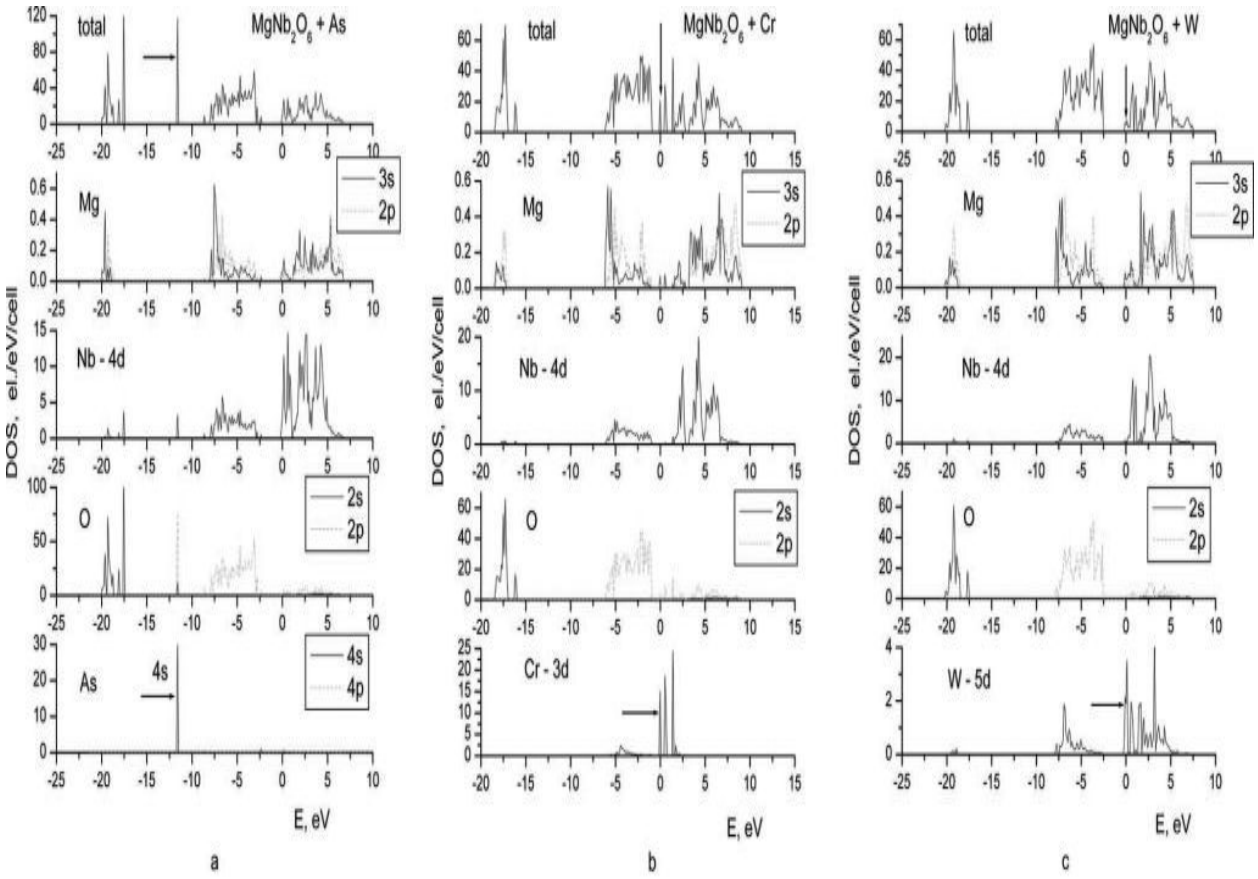

Figure 169. Electronic density of states for $MgNb_2O_6$ with As (a), Cr (b), and W (c)

Incorporation of 6A transition metal, such as Cr, Mo and W demonstrates similar features in the electronic structure as those resulting due to 3B doping. Incorporation of Cr, Mo and W as dopants introduce new states which are their own valence d-states located in the energy gap between valence and conduction bands and marked with arrows in **Figure 169**. In the case of $Mg[Nb_{0.875}Cr_{0.125}]_2O_6$, the partially occupied Cr 3d states are completely localized and separated from the main conduction band by an energy gap of ~ 0.6 eV. Quite a similar situation is observed for Mo doped $MgNb_2O_6$. There is also a partially occupied middle portion of Mo 4d states separated from the upper conduction band by a small energy gap of ~ 0.3 eV that facilitates electron transition to the conduction band and, thus improves the overall electronic

conductivity of the material. Finally, in the case of the W doped oxide, these corresponding W 5d states overlap with the Nb 5d conduction band thus resulting in the activation energy for the conductivity equal to zero. As regards to $MgTa_2O_6$ doped with Cr, Mo and W, all the three doped oxides remain semiconductors and there is no overlap between W 5d states and the Ta 5d conduction band.

Very similar results are obtained for the doping of Zn niobates and tantalates with corresponding dopants. **Figure 170** shows the total and partial DOS calculated for $Zn_{0.75}As_{0.25}Nb_2O_6$, $Zn[Nb_{0.875}Cr_{0.125}]_2O_6$ and $Zn[Nb_{0.875}W_{0.125}]_2O_6$. Apparently, it should be noted that the overall electronic structures of Zn based niobates are almost identical to those of Mg based oxides. The only qualitative difference is that observed in the case of W doped $MgTa_2O_6$ and $ZnTa_2O_6$.

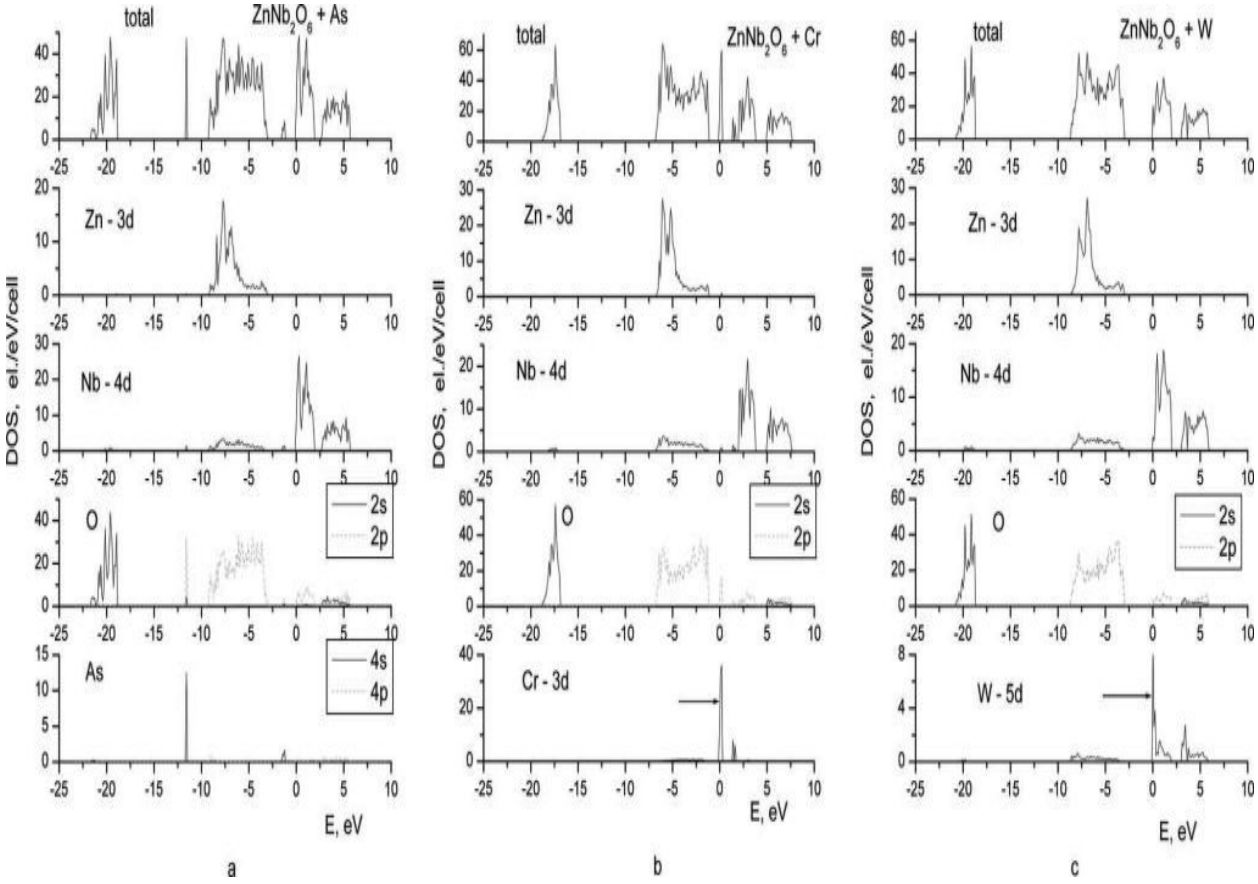

Figure 170. Electronic density of states for $ZnNb_2O_6$ with As (a), Cr (b), and W (c)

Figure 171 demonstrates the electronic DOS calculated for F doped $MgNb_2O_6$ and $ZnNb_2O_6$. As expected, F introduces its own local p-zone located ~ 1 - 2 eV below the main valence zone formed by 2p states of oxygen. Total density of states in the vicinity of the Fermi level is very similar to what one can see in the case of the structure doped with group 3A (Sc) and group 5B (As) elements. No impurity states appear within the band gap so that the Fermi level shifts towards the conduction band resulting in metallic conductivity of the material. Identical result is observed for F doped magnesium and zinc tantalates similar to that calculated for fluorine doped tin oxide (SnO_2:F) systematically investigated and reported by our group [56].

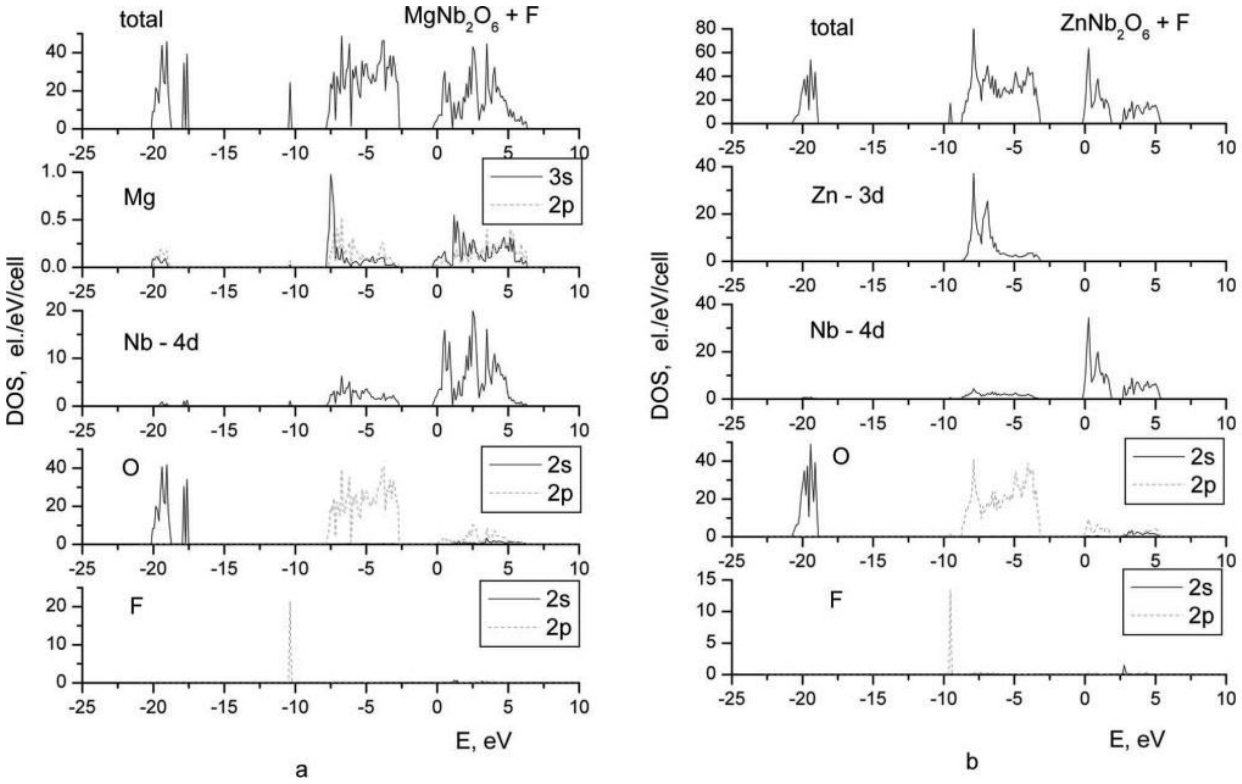

Figure 171. Electronic density of states for $MgNb_2O_6$ (a), and $ZnNb_2O_6$ (b) doped with F

Thus, based on the results obtained on the electronic structure peculiarities demonstrated due to introduction of the small amount of different elements from 3A, 3B, 5B, 6A and 7B periodic groups; one can make a conclusion that introduction of all the dopants do improve the electronic conductivity of doped magnesium and zinc niobates and tantalates, although to different extents. According to the energy values reported by Velikokhatnyi *et al.* [153], one can see that the presence of 3A, 3B (except boron and Ga in the case of $MgNb_2O_6$), 5B and 7B dopants help improve the electronic conductivity much better than those containing 6A. The compounds doped with Sc, Y, Al, Ga (except doped $MgNb_2O_6$), In, As, Sb, Bi, F and W (except doped $MgTa_2O_6$), demonstrate metallic conductivity, while B, Cr, Mo and Ga doped $MgNb_2O_6$ and W doped $MgTa_2O_6$ are characterized by the semiconductor behavior.

A.3.3 Structural and Chemical Stability

The present study is focused at identifying and hierarchically classifying materials in order of their electrochemical stability indicating their ability to withstand the harsh physical, chemical and electrochemical conditions prevalent during water electrolysis. Accordingly, the study is directed at identifying materials that are stable when exposed to acidic or other aggressive environments, and hence the chemical stability in the presence of an electric potential dictated by the cohesive energy is more relevant as opposed to the mechanical strength and is the main focus of the current work. The value of the cohesive energy E_{coh}, thus could serve as a qualitative criterion for comparing and selecting materials that would likely exhibit the most resistance to decomposition when exposed to chemically reactive environments of aggressive acids and bases prevalent during water electrolysis.

The calculated cohesive energies for pure and the doped oxide structures considered in the present study is shown in **Figure 172**. One can see that all the tantalate compounds have higher absolute values of cohesive energy than their corresponding niobium analogs and thus, can be considered to be more stable. This can be expected due to the stronger Ta - O interactions in comparison with the Nb - O bonds in the (Ta/Nb)-O_6 octahedra. Based on the calculated values of cohesive energy per atom in the unit cell, the structural stability of the materials increases as follows: $MgNb_2O_6$ (- 6.30eV/atom) < $ZnNb_2O_6$ (- 6.31 eV/atom) < $ZnTa_2O_6$ (- 6.82 eV/atom) < $MgTa_2O_6$ (- 7.21 eV/atom). Also, it can be seen that basically an introduction of almost all dopants renders the magnesium based compounds less stable than the parent oxides, although to different extents. The only exception is the doping of 3A group elements which renders both $MgNb_2O_6$ and $MgTa_2O_6$ even more stable. This directly relates with the Sc - O and

Y - O bonds which are stronger than the Mg - O bonds of the corresponding parent compounds. Bond dissociation energies of Sc - O, Y - O and Mg - O diatomic molecules are 671.4 kJ/mol, 714.1 kJ/mol and 358.2 kJ/mol respectively [155]. All other dopant elements either do not change or decrease the structural and chemical stability.

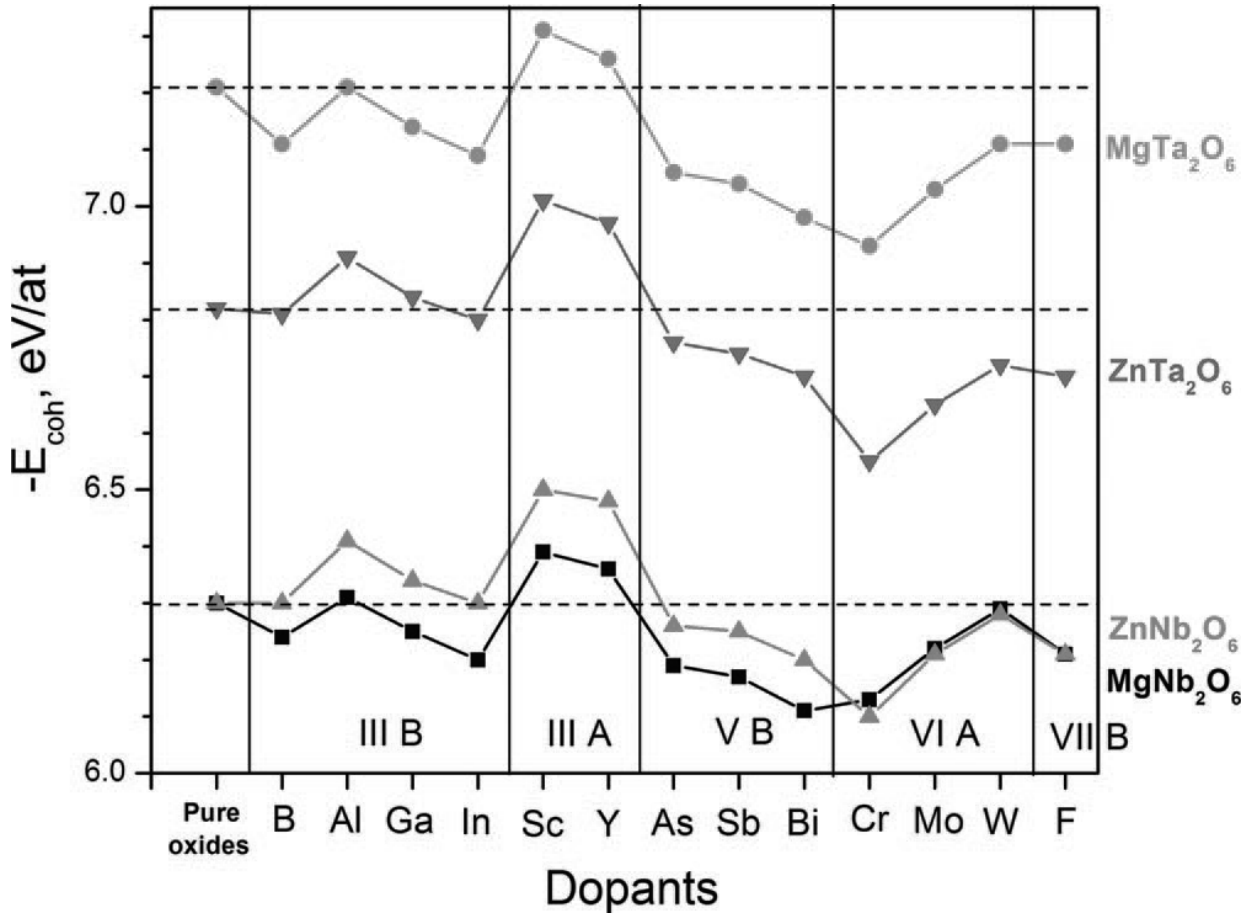

Figure 172. Cohesive energy for all materials studied in eV/at

As for doped $ZnNb_2O_6$ and $ZnTa_2O_6$, not only Sc and Y improve their stability similar to Mg based oxides, but Al and Ga also make these oxides more stable in comparison with the pure undoped parent oxides. Although a substantial amount of doped compounds are less stable in

comparison with the corresponding pure parent oxides, all the doped materials are more stable than pure SnO_2 or F doped SnO_2 that is commonly used as the catalyst support material for water electrolysis (calculated E_{coh} for pure SnO_2 is - 5.08 eV/at and for SnO_2 doped with ~ 6.2 wt.% F is - 4.74 eV/at).

This allows us to conclude that in terms of general stability, the tetragonal trirutile $MgTa_2O_6$ with a cohesive energy of - 7.21 eV/atom can be marked as the most stable compound among the entire four parent oxides considered in the present study. However, $MgTa_2O_6$ doped with Sc and Y render the oxide even more stable with E_{coh} = - 7.31 and -7.26 eV/at, respectively. It is also noteworthy to mention that among all the magnesium and zinc tantalates considered in the study, the least stable is $ZnTa_2O_6$ doped by Cr with E_{coh} = - 6.55 eV/at. However, it demonstrates higher stability in comparison to the most stable niobate $ZnNb_2O_6$ doped with Sc indicating a E_{coh} = - 6.50 eV/at. Hence it could be construed that the tantalite based compounds are more resistant to decomposition and cleavage of the primary bonds when exposed to harsh mechanical or chemical environments such as those likely experienced by these systems when used in highly corrosive acidic environments typically encountered in water electrolysis and the oxygen reduction reactions (ORR) in proton exchange membrane fuel cells.

To validate the theoretical calculations, we synthesized $ZnNb_2O_6$ doped with small amount of yttrium. For these purposes mixtures of powders of zinc oxide (ZnO, Alfa Aesar, 99.9%), niobium oxide (Nb_2O_5, Alfa Aesar, 99.95%) and yttrium oxide (Y_2O_3, Acros, 99.99%) of compositions with yttrium doping up to 1 at. % with a formula unit $(Zn_{0.9}Y_{0.1})Nb_2O_6$ were subjected to a mechano-chemical reaction in a high energy shaker mill (SPEX CertiPrep 8000M) for up to 15 minutes in a stainless steel (SS) vial using 20 SS balls of 2 mm diameter (~ 20 g) with a ball to powder weight ratio 10 : 1. The mechano-chemical miled powders obtained were

sintered in air at 1000°C for 12 hours. Pellets were prepared by compacting the powder using a uniaxial pressure of 7000 lb in a manual press (Carver Inc.).

In order to study the structural stability of the material, chronoamperometry (current signal *vs.* time) has been performed at ~ 1.75 V (*vs.* NHE) for ~ 3 hours using 1 N H_2SO_4 as an electrolyte. The H_2SO_4 solution is kept at a constant temperature of 40°C using a Fisher Scientific 910 Isotemp Refrigerator Circulator. The chronoamperometry (CA) signal was recorded using platinum as a counter electrode and Hg / Hg_2SO_4 as a reference electrode that has a potential of + 0.65V *vs.* NHE. The CA curve for $(Zn_{0.9}Y_{0.1})Nb_2O_6$ is shown in **Figure 173**. The CA curve shows a marked decay of current in the initial period of ~ 30 min with further stabilization of the current. Since this material itself is catalytically inactive (catalyst support only), the CA curve reflects a degree of corrosion occurring at the surface of the electrode. The faster the material degrades, the higher current signal versus time should be detected. It is seen that no increase of current is observed indicating high stability of zinc niobate doped with small amount of yttrium. It is worth to note that according to our calculations, $ZnNb_2O_6$ has lower cohesive energy than those of both zinc and magnesium tantalates (**Figure 172**), which means that $ZnTa_2O_6$ and $MgTa_2O_6$ are expected to demonstrate even higher electrochemical stability than $ZnNb_2O_6$ oxide, thus confirming our theoretical predictions.

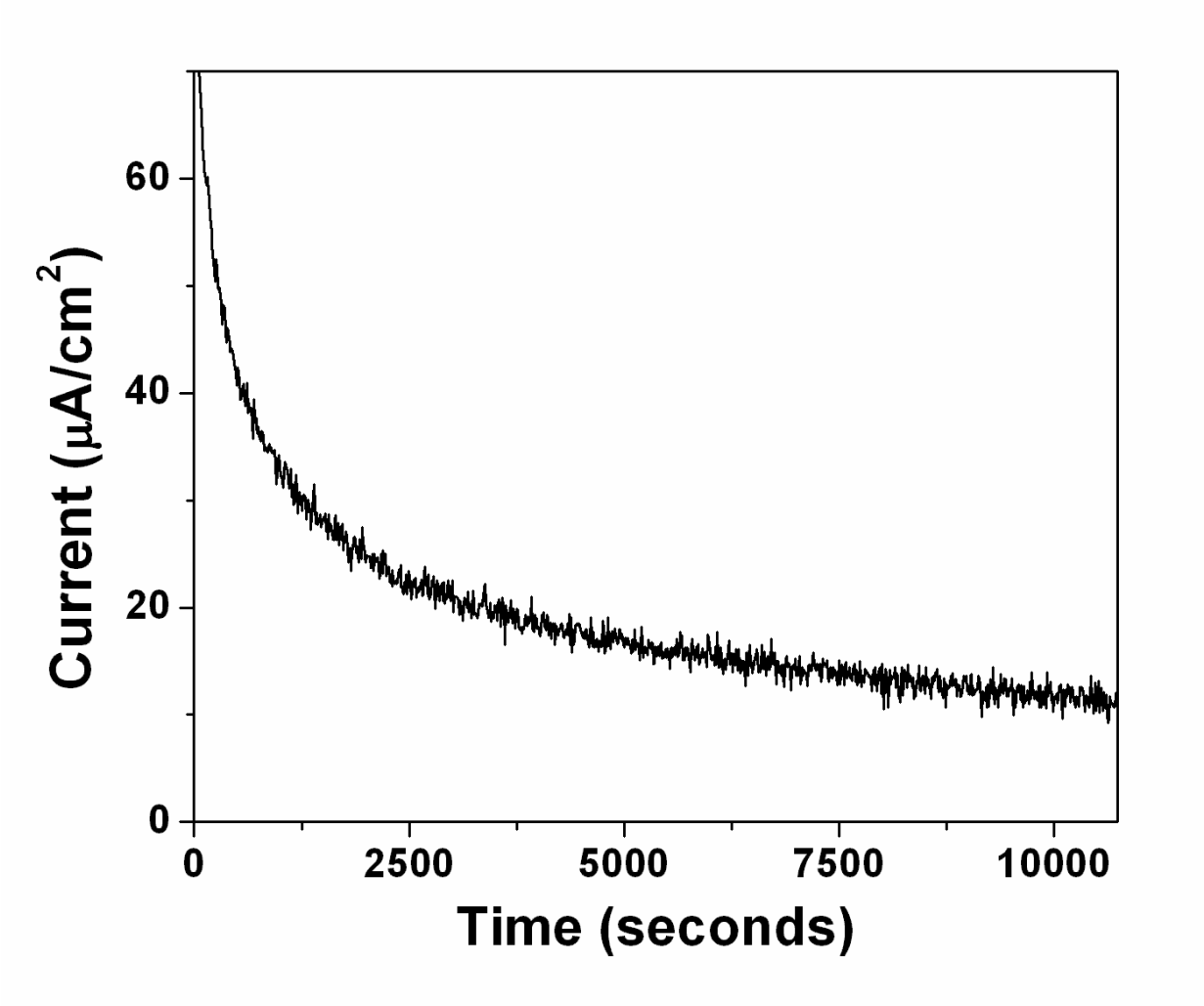

Figure 173. Variation of current vs. time in the chronoamperometry test performed on $(Zn_{0.9}Y_{0.1})Nb_2O_6$ in a 1 N H_2SO_4 solution at 1.75 V (*vs.* NHE)

A.4 CONCLUSION

An attempt to identify new electrochemically stable catalyst supports for PEM water electrolysis using *ab-initio* DFT approach has been undertaken in the present study. Magnesium and zinc

niobates, and magnesium and zinc tantalates, have been chosen for systematic investigation of the influence of small amounts of dopants selected from group 3A, 3B, 5B, 6A and 7B of the Periodic Table on the electronic conductivity and structural stability of the compounds. The study showed that small amounts of 3A, 5B, 7B and the most of 3B group elements noticeably improve the conductivity in comparison to the elements from group 6A of the Periodic Table.

Also, a comparison of the cohesive energies calculated for the pure and doped oxides displayed $MgTa_2O_6$ and Y doped $MgTa_2O_6$ to be the most stable compounds among all materials considered in the study. The study thus allows us to hypothesize based on electronic conductivity and cohesive energy considerations that among all the materials considered in the present study, $MgTa_2O_6$ doped with Sc and Y are the most appropriate candidates for use as a catalyst support in water electrolysis.

LIST OF PUBLICATIONS AND PATENTS

Peer reviewed publications

1. K. Kadakia, O.I. Velikokhatnyi, M.K. Datta, P. Jampani, S.J. Chung, S.K. Park, J.A. Poston, A. Manivannan, P.N. Kumta, "Fluorine doped (Nb,Ir)O_2 solid solution electro-catalyst powders for oxygen evolution reaction via PEM based water electrolysis", *RSC Advances*, Submitted (Oct 2014).
2. K. Kadakia, P. Jampani, O.I. Velikokhatnyi, S.K. Park, D.H. Hong, S.J. Chung, P.N. Kumta, "Nanostructured F doped IrO_2 electro-catalyst powders for PEM water electrolysis", *Journal of Power Sources*, 269 (2014) 855-865.
3. K. Kadakia, P. Jampani, M.K. Datta, S.J. Chung, J.A. Poston, A. Manivannan, P.N. Kumta, "Nanostructured (Ir,Sn)O_2:F - Oxygen evolution reaction anode electro-catalyst powders for PEM based water electrolysis", *Journal of the Electrochemical Society*, 161[9] (2014) F868-F875.
4. K. Kadakia, M.K. Datta, O.I. Velikokhatnyi, P. Jampani, P.N. Kumta, "Fluorine doped (Ir,Sn,Nb)O_2 anode electro-catalyst for oxygen evolution *via* PEM based water electrolysis", *International Journal of Hydrogen Energy*, 39 (2014) 664-674.
5. K. Kadakia, M.K. Datta, O.I. Velikokhatnyi, P. Jampani, S.K. Park, S.J. Chung, P.N. Kumta, "High performance fluorine doped (Sn,Ru)O_2 oxygen evolution reaction electro-

catalysts for proton exchange membrane based water electrolysis", *Journal of Power Sources*, 245 (2014) 362-370.

6. K. Kadakia, M.K. Datta, P. Jampani, S.K. Park, P.N. Kumta, "Novel F-doped IrO_2 oxygen evolution electrocatalyst for PEM based water electrolysis", *Journal of Power Sources*, 222 (2013) 313-317.
7. K. Kadakia, M.K. Datta, O.I. Velikokhatnyi, P. Jampani, S.K. Park, P. Saha, J.A. Poston, A. Manivannan, P.N. Kumta, "Novel (Ir,Sn,Nb)O_2 anode electrocatalysts with reduced noble metal content for PEM based water electrolysis", *International Journal of Hydrogen Energy*, 37 (2012) 3001-3013.
8. M.K. Datta, K. Kadakia, O.I. Velikokhatnyi, P. Jampani, S.J. Chung, J.A. Poston, A. Manivannan, P.N. Kumta, "High performance robust F-doped tin oxide oxygen evolution electro-catalysts for PEM based water electrolysis", *Journal of Materials Chemistry A*, 1 (2013) 4026-4037.
9. O.I. Velikokhatnyi, K. Kadakia, M.K. Datta, P.N. Kumta, "Fluorine-Doped IrO_2: A potential electrocatalyst for water electrolysis", *Journal of Physical Chemistry C*, 117 (2013) 20542-20547.
10. O.I. Velikokhatnyi, K. Kadakia, S.K. Park, P.N. Kumta, "Theoretical study of magnesium and zinc tantalates and niobates as prospective catalyst supports for water electrolysis", *Journal of the Electrochemical Society*, 159[10] (2012) F607-F616.
11. Velikokhatnyi, O. I.; Kadakia, K.; Park, S. K.; Kumta, P. N. "Theoretical study of magnesium and zinc tantalates and niobates as prospective catalyst supports for water electrolysis." *Journal of the Electrochemical Society* 2012, 159, F607-F616.

12. Velikokhatnyi, O. I.; Kumta, P. N. In *Ab-initio study of doped tin niobates and tantalates as prospective catalyst supports for water electrolysis,* ECS Transactions, 2010; pp 37-48.
13. Velikokhatnyi, O. I.; Kumta, P. N. Ab-initio study of fluorine-doped tin dioxide: A prospective catalyst support for water electrolysis. *Physica B: Condensed Matter* 2011, 406, 471-477.

Conference oral presentations

1. K. Kadakia, M.K. Datta, O.I. Velikokhatnyi, P.N. Kumta, "High performance fluorine doped oxygen evolution reaction electro-catalysts for PEM based water electrolysis", *American Institute of Chemical Engineers (AIChE) Annual Meeting,* San Francisco, CA, November 2013.
2. K. Kadakia, M.K. Datta, O.I. Velikokhatnyi, P.N. Kumta, "Fluorine doped (Sn,Ru)O_2 electro-catalysts for oxygen evolution reaction in PEM based water electrolysis", *Electrochemical Society (ECS) Annual Meeting,* San Francisco, CA, October 2013.
3. K. Kadakia, M.K. Datta, P. Jampani, P.N. Kumta, "Novel ternary and doped transition metal oxide based oxygen evolution electro-catalysts for hydrogen production via PEM based water electrolysis", *American Institute of Chemical Engineers (AIChE) Annual Meeting,* Pittsburgh, PA, November 2012.
4. K. Kadakia, M.K. Datta, O.I. Velikokhatnyi, P.N. Kumta, "Novel fluorine doped transition metal oxide ($Ru_xSn_{1-x}O_2$:F) oxygen evolution electro-catalysts for Hydrogen generation from PEM based water electrolysis", *Electrochemical Society (ECS) Annual Meeting,* Honolulu, HI, October 2012.

5. K. Kadakia, M.K. Datta, O.I. Velikokhatnyi, P.N. Kumta, "Novel transition metal oxide oxygen evolution electro-catalysts for hydrogen production via PEM based water electrolysis", *American Chemical Society (ACS) Fall Meeting,* Philadelphia, PA, August 2012.
6. K. Kadakia, M.K. Datta, A. Manivannan, P.N. Kumta, "(Ir,Sn,Nb)O_2 and (Ir,Sn)O_2:F thin film anode electro-catalysts with reduced noble metal content for PEM based water electrolysis", *Electrochemical Society (ECS) Spring Meeting,* Seattle, WA, May 2012.
7. K. Kadakia, M.K. Datta, P.N. Kumta, "High surface area anode electro-catalysts of fluorine doped $Ir_{1-x}Sn_xO_2$ and $Ir_{1-x}Nb_xO_2$ in proton exchange membrane based water electrolysis", *Electrochemical Society (ECS) Annual Meeting,* Boston, MA, October 2011.
8. K. Kadakia, M.K. Datta, A. Manivannan, P.N. Kumta, "$Ru_{1-x}Sn_xO_2$:F and $Ir_{1-x}Sn_xO_2$:F thin film anode electro-catalysts for PEM based water electrolysis", *Electrochemical Society (ECS) Spring Meeting,* Montreral, QC, May 2011.
9. M.K. Datta, K. Kadakia, P.N. Kumta, "Synthesis and electrochemical performance of IrO_2-SnO_2-Nb_2O_5 thin film anode electro-catalysts for PEM based water electrolysis", *Electrochemical Society (ECS) Annual Meeting,* Las Vegas, NV, October 2010.

Patent

1. K. Kadakia, M.K. Datta, O.I. Velikokhatnyi, P.N. Kumta, "Non-noble metal based electro-catalyst compositions for Proton Exchange Membrane based water electrolysis and Methods of Making", *U.S. Patent Application # 13/961,327,* August 2013.

Thesis

Kadakia, K. S. Fundamental Study of nanostructured electro-catalysts with reduced noble metal content for PEM based water electrolysis. University of Pittsburgh, 2014.

Personnel supported by the project annually

Dr. Karan S. Kadakia-Graduate researcher-100%

Dr. Oleg I. Velikokhatnyi-Research faculty-100%

Dr. Moni K. Datta-Research faculty-50%

Dr. Prashant N. Kumta – Principal Investigator – 25%

BIBLIOGRAPHY

[1] G.D. Berry, Hydrogen Production, in: J.C. Editor-in-Chief: Cutler (Ed.) Encyclopedia of Energy, Elsevier, New York, 2004, pp. 253-265.
[2] J. Suntivich, K.J. May, H.A. Gasteiger, J.B. Goodenough, Y. Shao-Horn, Science, 334 (2011) 1383-1385.
[3] K. Zeng, D.K. Zhang, Prog. Energy Combust. Sci., 36 (2010) 307-326.
[4] J.M. Ogden, Phys. Today, 55 (2002) 69.
[5] F. Barbir, Chapter 11 - 11. Fuel Cells and Hydrogen Economy, in: PEM Fuel Cells, Academic Press, Burlington, 2005, pp. 399-426.
[6] G.D. Berry, J. Martinez-Frias, F. Espinosa-Loza, S.M. Aceves, Hydrogen Storage and Transportation, in: J.C. Editor-in-Chief: Cutler (Ed.) Encyclopedia of Energy, Elsevier, New York, 2004, pp. 267-281.
[7] H. Wang, D.Y.C. Leung, J. Xuan, International Journal of Hydrogen Energy, 37 (2012) 10002-10009.
[8] M.F. Hordeski, Hydrogen & Fuel Cells: Advances in Transportation and Power, Fairmont Press, 2009.
[9] F. Barbir, Chapter Twelve - Future of Fuel Cells and Hydrogen, in: PEM Fuel Cells (Second Edition), Academic Press, Boston, 2013, pp. 469-508.
[10] B. Sørensen, Chapter 2 - Hydrogen, in: Hydrogen and Fuel Cells, Academic Press, Burlington, 2005, pp. 5-111.
[11] C. Schroeder, Chapter 8 - Hydrogen from Electrolysis, in: S. Daniel, S.C. James (Eds.) The Hydrogen Energy Transition, Academic Press, Burlington, 2004, pp. 121-133.
[12] C.J. Winter, International Journal of Hydrogen Energy, 34 (2009) S1-S52.
[13] M. Conte, F. Di Mario, A. Iacobazzi, A. Mattucci, A. Moreno, M. Ronchetti, Energies, 2 (2009) 150-179.
[14] K. Hedegaard, P. Meibom, Renewable Energy, 37 (2012) 318-324.
[15] F. Barbir, Sol. Energy, 78 (2005) 661-669.
[16] P. Millet, N. Mbemba, S.A. Grigoriev, V.N. Fateev, A. Aukauloo, C. Etievant, International Journal of Hydrogen Energy, 36 (2011) 4134-4142.
[17] M. Carmo, D.L. Fritz, J. Mergel, D. Stolten, International Journal of Hydrogen Energy, 38 (2013) 4901-4934.
[18] M.W. Kanan, D.G. Nocera, Science, 321 (2008) 1072-1075.
[19] R.E. Clarke, S. Giddey, S.P.S. Badwal, International Journal of Hydrogen Energy, 35 (2010) 928-935.

[20] G.W. Crabtree, M.S. Dresselhaus, M.V. Buchanan, Phys. Today, 57 (2004) 39-44.
[21] C.R. Bealing, W.J. Baumgardner, J.J. Choi, T. Hanrath, R.G. Hennig, ACS Nano, 6 (2012) 2118-2127.
[22] J.I. Levene, M.K. Mann, R.M. Margolis, A. Milbrandt, Sol. Energy, 81 (2007) 773-780.
[23] Y.H.P. Zhang, W.-D. Huang, Trends in Biotechnology, 30 (2012) 301-306.
[24] K. Kadakia, M.K. Datta, O.I. Velikokhatnyi, P. Jampani, S.K. Park, P. Saha, J.A. Poston, A. Manivannan, P.N. Kumta, International Journal of Hydrogen Energy, 37 (2012) 3001-3013.
[25] S. Pedrazzi, G. Zini, P. Tartarini, Renewable Energy, 46 (2012) 14-22.
[26] M.W. Kanan, Y. Surendranath, D.G. Nocera, Chem. Soc. Rev., 38 (2009) 109-114.
[27] Y.Y. Liang, Y.G. Li, H.L. Wang, J.G. Zhou, J. Wang, T. Regier, H.J. Dai, Nat. Mater., 10 (2011) 780-786.
[28] S. Malkhandi, B. Yang, A.K. Manohar, A. Manivannan, G.K.S. Prakash, S.R. Narayanan, J. Phys. Chem. Lett., 3 (2012) 967-972.
[29] C.P. De Pauli, S. Trasatti, Journal of Electroanalytical Chemistry, 538–539 (2002) 145-151.
[30] J.M. Hu, H.M. Meng, J.Q. Zhang, C.N. Cao, Corrosion Sci., 44 (2002) 1655-1668.
[31] A.T. Marshall, S. Sunde, M. Tsypkin, R. Tunold, International Journal of Hydrogen Energy, 32 (2007) 2320-2324.
[32] A. Marshall, B. Borresen, G. Hagen, M. Tsypkin, R. Tunold, Electrochimica Acta, 51 (2006) 3161-3167.
[33] S.D. Song, H.M. Zhang, X.P. Ma, Z.G. Shao, R.T. Baker, B.L. Yi, International Journal of Hydrogen Energy, 33 (2008) 4955-4961.
[34] K. Kadakia, M.K. Datta, P.H. Jampani, S.K. Park, P.N. Kumta, Journal of Power Sources, 222 (2013) 313-317.
[35] Y. Takasu, N. Yoshinaga, W. Sugimoto, Electrochem. Commun., 10 (2008) 668-672.
[36] X. Wu, K. Scott, International Journal of Hydrogen Energy, 36 (2011) 5806-5810.
[37] B. Sørensen, Chapter 2 - Hydrogen, in: Hydrogen and Fuel Cells (Second Edition), Academic Press, Boston, 2012, pp. 5-94.
[38] R.L. LeRoy, International Journal of Hydrogen Energy, 8 (1983) 401-417.
[39] P. Millet, S. Grigoriev, Chapter 2 - Water Electrolysis Technologies, in: L.M. Gandía, G. Arzamendi, P.M. Diéguez (Eds.) Renewable Hydrogen Technologies, Elsevier, Amsterdam, 2013, pp. 19-41.
[40] J.C. Ganley, International Journal of Hydrogen Energy, 34 (2009) 3604-3611.
[41] S. Marini, P. Salvi, P. Nelli, R. Pesenti, M. Villa, M. Berrettoni, G. Zangari, Y. Kiros, Electrochimica Acta, 82 (2012) 384-391.
[42] T. Smolinka, FUELS – HYDROGEN PRODUCTION | Water Electrolysis, in: J. Garche (Ed.) Encyclopedia of Electrochemical Power Sources, Elsevier, Amsterdam, 2009, pp. 394-413.
[43] S.-D. Kim, J.-H. Yu, D.-W. Seo, I.-S. Han, S.-K. Woo, International Journal of Hydrogen Energy, 37 (2012) 78-83.
[44] C. Yang, A. Coffin, F. Chen, International Journal of Hydrogen Energy, 35 (2010) 3221-3226.
[45] N. Li, M. Keane, M.K. Mahapatra, P. Singh, International Journal of Hydrogen Energy, 38 (2013) 6298-6303.
[46] S. Siracusano, V. Baglio, N. Briguglio, G. Brunaccini, A. Di Blasi, A. Stassi, R. Ornelas, E. Trifoni, V. Antonucci, A.S. Aricò, International Journal of Hydrogen Energy, 37 (2012) 1939-1946.

[47] F.I. Mattos-Costa, P. de Lima-Neto, S.A.S. Machado, L.A. Avaca, Electrochimica Acta, 44 (1998) 1515-1523.
[48] E. Rasten, G. Hagen, R. Tunold, Electrochimica Acta, 48 (2003) 3945-3952.
[49] A. Damjanovic, A. Dey, J.O.M. Bockris, Journal of The Electrochemical Society, 113 (1966) 739-746.
[50] R.L. LeRoy, C.T. Bowen, D.J. LeRoy, Journal of The Electrochemical Society, 127 (1980) 1954-1962.
[51] N. Krstajic, S. Trasatti, Journal of Applied Electrochemistry, 28 (1998) 1291-1297.
[52] A. Minguzzi, F.-R.F. Fan, A. Vertova, S. Rondinini, A.J. Bard, Chemical Science, 3 (2012) 217-229.
[53] J. Rossmeisl, Z.W. Qu, H. Zhu, G.J. Kroes, J.K. Norskov, Journal of Electroanalytical Chemistry, 607 (2007) 83-89.
[54] J. Rossmeisl, A. Logadottir, J.K. Nørskov, Chemical Physics, 319 (2005) 178-184.
[55] O.I. Velikokhatnyi, K. Kadakia, M.K. Datta, P.N. Kumta, The Journal of Physical Chemistry C, 117 (2013) 20542-20547.
[56] O.I. Velikokhatnyi, P.N. Kumta, Physica B: Condensed Matter, 406 (2011) 471-477.
[57] M.K. Datta, K. Kadakia, O.I. Velikokhatnyi, P.H. Jampani, S.J. Chung, J.A. Poston, A. Manivannan, P.N. Kumta, Journal of Materials Chemistry A, 1 (2013) 4026-4037.
[58] K. Kadakia, M.K. Datta, O.I. Velikokhatnyi, P. Jampani, S.K. Park, S.J. Chung, P.N. Kumta, Journal of Power Sources, 245 (2014) 362-370.
[59] K. Kadakia, M.K. Datta, O.I. Velikokhatnyi, P.H. Jampani, P.N. Kumta, International Journal of Hydrogen Energy, 39 (2014) 664-674.
[60] A. Marshall, B. Borresen, G. Hagen, M. Tsypkin, R. Tunold, Materials Chemistry and Physics, 94 (2005) 226-232.
[61] S.A. Grigoriev, V.I. Porembsky, V.N. Fateev, International Journal of Hydrogen Energy, 31 (2006) 171-175.
[62] K.M. Papazisi, A. Siokou, S. Balomenou, D. Tsiplakides, International Journal of Hydrogen Energy, 37 (2012) 16642-16648.
[63] G.H. Chen, X.M. Chen, P.L. Yue, Journal of Physical Chemistry B, 106 (2002) 4364-4369.
[64] G.Y. Chen, C.C. Waraksa, H.G. Cho, D.D. Macdonald, T.E. Mallouk, Journal of the Electrochemical Society, 150 (2003) E423-E428.
[65] S. Ardizzone, C.L. Bianchi, G. Cappelletti, M. Ionita, A. Minguzzi, S. Rondinini, A. Vertova, Journal of Electroanalytical Chemistry, 589 (2006) 160-166.
[66] C.P. Depauli, S. Trasatti, Journal of Electroanalytical Chemistry, 396 (1995) 161-168.
[67] E. Mayousse, F. Maillard, F. Fouda-Onana, O. Sicardy, N. Guillet, International Journal of Hydrogen Energy, 36 (2011) 10474-10481.
[68] M. Morimitsu, R. Otogawa, M. Matsunaga, Electrochimica Acta, 46 (2000) 401-406.
[69] A.V. Nikiforov, A.L.T. Garcia, I.M. Petrushina, E. Christensen, N.J. Bjerrum, International Journal of Hydrogen Energy, 36 (2011) 5797-5805.
[70] F.M. Sapountzi, S.C. Divane, E.I. Papaioannou, S. Souentie, C.G. Vayenas, Journal of Electroanalytical Chemistry, 662 (2011) 116-122.
[71] A.J. Terezo, J. Bisquert, E.C. Pereira, G. Garcia-Belmonte, Journal of Electroanalytical Chemistry, 508 (2001) 59-69.
[72] A.J. Terezo, E.C. Pereira, Electrochimica Acta, 44 (1999) 4507-4513.
[73] A.J. Terezo, E.C. Pereira, Electrochimica Acta, 45 (2000) 4351-4358.

[74] G.P. Vercesi, J.Y. Salamin, C. Comninellis, Electrochimica Acta, 36 (1991) 991-998.
[75] E. Elangovan, K. Ramamurthi, Thin Solid Films, 476 (2005) 231-236.
[76] H. Kim, R.C.Y. Auyeung, A. Piqué, Thin Solid Films, 516 (2008) 5052-5056.
[77] E. Shanthi, A. Banerjee, V. Dutta, K.L. Chopra, Journal of Applied Physics, 53 (1982) 1615-1621.
[78] W.S. Choi, S.S.A. Seo, K.W. Kim, T.W. Noh, M.Y. Kim, S. Shin, Physical Review B, 74 (2006).
[79] J.S. de Almeida, R. Ahuja, Physical Review B, 73 (2006).
[80] M.A. Aegerter, Solar Energy Materials and Solar Cells, 68 (2001) 401-422.
[81] N. Özer, T. Barreto, T. Büyüklimanli, C.M. Lampert, Solar Energy Materials and Solar Cells, 36 (1995) 433-443.
[82] M.H.P. Santana, L.A. De Faria, J.F.C. Boodts, Electrochimica Acta, 49 (2004) 1925-1935.
[83] R. Kötz, S. Stucki, Electrochimica Acta, 31 (1986) 1311-1316.
[84] R. Adams, R.L. Shriner, Journal of the American Chemical Society, 45 (1923) 2171-2179.
[85] J. Cheng, H. Zhang, G. Chen, Y. Zhang, Electrochimica Acta, 54 (2009) 6250-6256.
[86] Y. Wang, C. Ma, X. Sun, H. Li, Journal of Colloid and Interface Science, 286 (2005) 627-631.
[87] N. Uekawa, T. Kudo, F. Mori, Y.J. Wu, K. Kakegawa, Journal of Colloid and Interface Science, 264 (2003) 378-384.
[88] T.H. de Keijser, J.I. Langford, E.J. Mittemeijer, A.B.P. Vogels, Journal of Applied Crystallography, 15 (1982) 308-314.
[89] R. Jiang, D. Chu, Electrochimica Acta, 45 (2000) 4025-4030.
[90] K.J.J. Mayrhofer, D. Strmcnik, B.B. Blizanac, V. Stamenkovic, M. Arenz, N.M. Markovic, Electrochimica Acta, 53 (2008) 3181-3188.
[91] T.J. Schmidt, H.A. Gasteiger, G.D. Stäb, P.M. Urban, D.M. Kolb, R.J. Behm, Journal of The Electrochemical Society, 145 (1998) 2354-2358.
[92] S. Gottesfeld, I.D. Raistrick, S. Srinivasan, Journal of The Electrochemical Society, 134 (1987) 1455-1462.
[93] K.E. Gubbins, R.D. Walker, Journal of The Electrochemical Society, 112 (1965) 469-471.
[94] R.N. Itoe, G.D. Wesson, E.E. Kalu, Journal of The Electrochemical Society, 147 (2000) 2445-2450.
[95] E. Lust, E. Härk, J. Nerut, K. Vaarmets, Electrochimica Acta, 101 (2013) 130-141.
[96] J.L. Cohen, D.J. Volpe, H.D. Abruna, Physical Chemistry Chemical Physics, 9 (2007) 49-77.
[97] L.M. Da Silva, D.V. Franco, L.A. De Faria, J.F.C. Boodts, Electrochimica Acta, 49 (2004) 3977-3988.
[98] E.M. Garcia, H.A. Tarôco, T. Matencio, R.Z. Domingues, J.A.F. dos Santos, International Journal of Hydrogen Energy, 37 (2012) 6400-6406.
[99] M.M. Hefny, S. Abdel-Wanees, Electrochimica Acta, 41 (1996) 1419-1422.
[100] A.A. Shaltout, H.H. Afify, S.A. Ali, Journal of Electron Spectroscopy and Related Phenomena, 185 (2012) 140-145.
[101] J.-M. Hu, J.-Q. Zhang, C.-N. Cao, International Journal of Hydrogen Energy, 29 (2004) 791-797.
[102] A. Damjanovic, Journal of Electroanalytical Chemistry, 355 (1993) 57-77.

[103] R. Jiang, F.C. Anson, Journal of Electroanalytical Chemistry and Interfacial Electrochemistry, 305 (1991) 171-184.
[104] L.M. Da Silva, L.A. De Faria, J.F.C. Boodts, Electrochimica Acta, 48 (2003) 699-709.
[105] A. Mills, H.L. Davies, Electrochimica Acta, 37 (1992) 1217-1225.
[106] S. Siracusano, V. Baglio, A. Di Blasi, N. Briguglio, A. Stassi, R. Ornelas, E. Trifoni, V. Antonucci, A.S. Aricò, International Journal of Hydrogen Energy, 35 (2010) 5558-5568.
[107] S. Ardizzone, M. Falciola, S. Trasatti, Journal of The Electrochemical Society, 136 (1989) 1545-1550.
[108] H. Tamura, C. Iwakura, International Journal of Hydrogen Energy, 7 (1982) 857-865.
[109] J. Ribeiro, M. Moats, A. Andrade, Journal of Applied Electrochemistry, 38 (2008) 767-775.
[110] M. Ito, Y. Murakami, H. Kaji, K. Yahikozawa, Y. Takasu, Journal of The Electrochemical Society, 143 (1996) 32-36.
[111] C. Iwakura, K. Hirao, H. Tamura, Electrochimica Acta, 22 (1977) 329-334.
[112] I.T. Weber, R. Andrade, E.R. Leite, E. Longo, Sensors and Actuators B: Chemical, 72 (2001) 180-183.
[113] B.S. Murty, M.K. Datta, S.K. Pabi, Sadhana-Academy Proceedings in Engineering Sciences, 28 (2003) 23-45.
[114] E.J.W. Whittaker, R. Muntus, Geochimica et Cosmochimica Acta, 34 (1970) 945-956.
[115] N. Todorova, T. Giannakopoulou, G. Romanos, T. Vaimakis, J. Yu, C. Trapalis, International Journal of Photoenergy, 2008 (2008).
[116] C. Papadopoulou, A. Lycourghiotis, P. Grange, B. Delmon, Applied Catalysis, 38 (1988) 255-271.
[117] A.K. Ghosh, R.A. Kydd, Catalysis Reviews, 27 (1985) 539-589.
[118] J. Ramirez, R. Cuevas, A.L. Agudo, S. Mendioroz, J.L.G. Fierro, Applied Catalysis, 57 (1990) 223-240.
[119] A.A. Bolzan, C. Fong, B.J. Kennedy, C.J. Howard, Acta Crystallographica Section B: Structural Science, 53 (1997) 373-380.
[120] J.C. Cruz, S. Rivas, D. Beltran, Y. Meas, R. Ornelas, G. Osorio-Monreal, L. Ortiz-Frade, J. Ledesma-García, L.G. Arriaga, International Journal of Hydrogen Energy, 37 (2012) 13522-13528.
[121] V. Natarajan, S. Basu, K. Scott, International Journal of Hydrogen Energy, 38 (2013) 16623-16630.
[122] Z.B. Zhou, R.Q. Cui, G.M. Hadi, W.Y. Li, Z.M. Ding, Journal of Materials Science: Materials in Electronics, 12 (2001) 417-421.
[123] T.H. Dekeijser, J.I. Langford, E.J. Mittemeijer, A.B.P. Vogels, Journal of Applied Crystallography, 15 (1982) 308-314.
[124] F.M. Amanullah, K.J. Pratap, V. Hari Babu, Materials Science and Engineering: B, 52 (1998) 93-98.
[125] B. Hammer, J.K. Nørskov, Theoretical surface science and catalysis—calculations and concepts, in: H.K. Bruce C. Gates (Ed.) Advances in Catalysis, Academic Press, 2000, pp. 71-129.
[126] T. Bligaard, J.K. Nørskov, Electrochimica Acta, 52 (2007) 5512-5516.
[127] H. Dau, C. Limberg, T. Reier, M. Risch, S. Roggan, P. Strasser, ChemCatChem, 2 (2010) 724-761.

[128] S. Kandoi, A. Gokhale, L. Grabow, J. Dumesic, M. Mavrikakis, Catalysis Letters, 93 (2004) 93-100.
[129] P. Atkins, J. de Paula, Physical Chemistry, W. H. Freeman, 2006.
[130] J.P. Perdew, W. Yue, Physical Review B, 33 (1986) 8800-8802.
[131] G. Kresse, J. Furthmüller, Physical Review B, 54 (1996) 11169-11186.
[132] G. Kresse, J. Furthmüller, Computational Materials Science, 6 (1996) 15-50.
[133] G. Kresse, D. Joubert, Physical Review B, 59 (1999) 1758-1775.
[134] G. Henkelman, A. Arnaldsson, H. Jónsson, Computational Materials Science, 36 (2006) 354-360.
[135] A.J. Bard, R. Parsons, J. Jordan, Standard Potentials in Aqueous Solution, Taylor & Francis, 1985.
[136] B. Hamad, The European Physical Journal B, 70 (2009) 163-169.
[137] N.D. Landolt-Bornstein, Group, 3 (1982) 12.
[138] J.E. Dominguez, X.Q. Pan, L. Fu, P.A. Van Rompay, Z. Zhang, J.A. Nees, P.P. Pronko, Journal of Applied Physics, 91 (2002) 1060.
[139] B. Gottlieb, R. Koropecki, R. Arce, R. Crisalle, J. Ferron, Thin Solid Films, 199 (1991) 13-21.
[140] D. Zaouk, R. al Asmar, J. Podlecki, Y. Zaatar, A. Khoury, A. Foucaran, Microelectronics Journal, 38 (2007) 884-887.
[141] S. Trasatti, Electrochimica Acta, 36 (1991) 225-241.
[142] S. Trasatti, Electrochimica Acta, 45 (2000) 2377-2385.
[143] O.I. Velikokhatnyi, P.N. Kumta, Physica B: Condensed Matter, 404 (2009) 1737-1745.
[144] D.R. Lide, H.V. Kehiaian, CRC Handbook of Thermophysical and Thermochemical Data, Taylor & Francis, 1994.
[145] O.I. Velikokhatnyi, P.N. Kumta, Journal of Power Sources, 202 (2012) 190-199.
[146] R.C. Pullar, Journal of the American Ceramic Society, 92 (2009) 563-577.
[147] W.-S. Xia, L.-X. Li, P. Zhang, P.-F. Ning, Materials Letters, 65 (2011) 3317-3319.
[148] Z. Ding, W. Wu, S. Liang, H. Zheng, L. Wu, Materials Letters, 65 (2011) 1598-1600.
[149] S.M. Ji, S.H. Choi, J.S. Jang, E.S. Kim, J.S. Lee, J. Phys. Chem. C, 113 (2009) 17824-17830.
[150] H. Kato, A. Kudo, Chem. Phys. Lett., 295 (1998) 487-492.
[151] A.V. Moholkar, S.M. Pawar, K.Y. Rajpure, C.H. Bhosale, J.H. Kim, Applied Surface Science, 255 (2009) 9358-9364.
[152] J. Xu, S. Huang, Z. Wang, Solid State Communications, 149 (2009) 527-531.
[153] O.I. Velikokhatnyi, K. Kadakia, S.K. Park, P.N. Kumta, Journal of The Electrochemical Society, 159 (2012) F607-F616.
[154] M. Waburg, H. Mullerbuschbaum, Zeitschrift Fur Anorganische Und Allgemeine Chemie, 508 (1984) 55-60.
[155] D.R. Lide, CRC Handbook of Chemistry and Physics, 85th Edition, Taylor & Francis, 2004.

Peer-reviewed publications

1. K. Kadakia, O.I. Velikokhatnyi, M.K. Datta, P. Jampani, S.J. Chung, S.K. Park, J.A. Poston, A. Manivannan, P.N. Kumta, "Fluorine doped (Nb,Ir)O_2 solid solution electro-catalyst powders for oxygen evolution reaction via PEM based water electrolysis", *RSC Advances*, Submitted (Oct 2014).
2. K. Kadakia, P. Jampani, O.I. Velikokhatnyi, S.K. Park, D.H. Hong, S.J. Chung, P.N. Kumta, "Nanostructured F doped IrO_2 electro-catalyst powders for PEM water electrolysis", *Journal of Power Sources*, 269 (2014) 855-865.
3. K. Kadakia, P. Jampani, M.K. Datta, S.J. Chung, J.A. Poston, A. Manivannan, P.N. Kumta, "Nanostructured (Ir,Sn)O_2:F - Oxygen evolution reaction anode electro-catalyst powders for PEM based water electrolysis", *Journal of the Electrochemical Society*, 161[9] (2014) F868-F875.
4. K. Kadakia, M.K. Datta, O.I. Velikokhatnyi, P. Jampani, P.N. Kumta, "Fluorine doped (Ir,Sn,Nb)O_2 anode electro-catalyst for oxygen evolution *via* PEM based water electrolysis", *International Journal of Hydrogen Energy*, 39 (2014) 664-674.
5. K. Kadakia, M.K. Datta, O.I. Velikokhatnyi, P. Jampani, S.K. Park, S.J. Chung, P.N. Kumta, "High performance fluorine doped (Sn,Ru)O_2 oxygen evolution reaction electro-catalysts for proton exchange membrane based water electrolysis", *Journal of Power Sources*, 245 (2014) 362-370.
6. K. Kadakia, M.K. Datta, P. Jampani, S.K. Park, P.N. Kumta, "Novel F-doped IrO_2 oxygen evolution electrocatalyst for PEM based water electrolysis", *Journal of Power Sources*, 222 (2013) 313-317.
7. K. Kadakia, M.K. Datta, O.I. Velikokhatnyi, P. Jampani, S.K. Park, P. Saha, J.A. Poston, A. Manivannan, P.N. Kumta, "Novel (Ir,Sn,Nb)O_2 anode electrocatalysts with reduced noble metal content for PEM based water electrolysis", *International Journal of Hydrogen Energy*, 37 (2012) 3001-3013.
8. M.K. Datta, K. Kadakia, O.I. Velikokhatnyi, P. Jampani, S.J. Chung, J.A. Poston, A. Manivannan, P.N. Kumta, "High performance robust F-doped tin oxide oxygen evolution electro-catalysts for PEM based water electrolysis", *Journal of Materials Chemistry A*, 1 (2013) 4026-4037.
9. O.I. Velikokhatnyi, K. Kadakia, M.K. Datta, P.N. Kumta, "Fluorine-Doped IrO_2: A potential electrocatalyst for water electrolysis", *Journal of Physical Chemistry C*, 117 (2013) 20542-20547.
10. O.I. Velikokhatnyi, K. Kadakia, S.K. Park, P.N. Kumta, "Theoretical study of magnesium and zinc tantalates and niobates as prospective catalyst supports for water electrolysis", *Journal of the Electrochemical Society*, 159[10] (2012) F607-F616.
11. Velikokhatnyi, O. I.; Kadakia, K.; Park, S. K.; Kumta, P. N. "Theoretical study of magnesium and zinc tantalates and niobates as prospective catalyst supports for water electrolysis." *Journal of the Electrochemical Society* 2012, 159, F607-F616.
12. Velikokhatnyi, O. I.; Kumta, P. N. In *Ab-initio study of doped tin niobates and tantalates as prospective catalyst supports for water electrolysis*, ECS Transactions, 2010; pp 37-48.

13. Velikokhatnyi, O. I.; Kumta, P. N. Ab-initio study of fluorine-doped tin dioxide: A prospective catalyst support for water electrolysis. *Physica B: Condensed Matter* 2011, 406, 471-477.

Conference oral presentations

1. K. Kadakia, M.K. Datta, O.I. Velikokhatnyi, P.N. Kumta, "High performance fluorine doped oxygen evolution reaction electro-catalysts for PEM based water electrolysis", *American Institute of Chemical Engineers (AIChE) Annual Meeting,* San Francisco, CA, November 2013.
2. K. Kadakia, M.K. Datta, O.I. Velikokhatnyi, P.N. Kumta, "Fluorine doped (Sn,Ru)O_2 electro-catalysts for oxygen evolution reaction in PEM based water electrolysis", *Electrochemical Society (ECS) Annual Meeting,* San Francisco, CA, October 2013.
3. K. Kadakia, M.K. Datta, P. Jampani, P.N. Kumta, "Novel ternary and doped transition metal oxide based oxygen evolution electro-catalysts for hydrogen production via PEM based water electrolysis", *American Institute of Chemical Engineers (AIChE) Annual Meeting,* Pittsburgh, PA, November 2012.
4. K. Kadakia, M.K. Datta, O.I. Velikokhatnyi, P.N. Kumta, "Novel fluorine doped transition metal oxide ($Ru_xSn_{1-x}O_2$:F) oxygen evolution electro-catalysts for Hydrogen generation from PEM based water electrolysis", *Electrochemical Society (ECS) Annual Meeting,* Honolulu, HI, October 2012.
5. K. Kadakia, M.K. Datta, O.I. Velikokhatnyi, P.N. Kumta, "Novel transition metal oxide oxygen evolution electro-catalysts for hydrogen production via PEM based water electrolysis", *American Chemical Society (ACS) Fall Meeting,* Philadelphia, PA, August 2012.
6. K. Kadakia, M.K. Datta, A. Manivannan, P.N. Kumta, "(Ir,Sn,Nb)O_2 and (Ir,Sn)O_2:F thin film anode electro-catalysts with reduced noble metal content for PEM based water electrolysis", *Electrochemical Society (ECS) Spring Meeting,* Seattle, WA, May 2012.
7. K. Kadakia, M.K. Datta, P.N. Kumta, "High surface area anode electro-catalysts of fluorine doped $Ir_{1-x}Sn_xO_2$ and $Ir_{1-x}Nb_xO_2$ in proton exchange membrane based water electrolysis", *Electrochemical Society (ECS) Annual Meeting,* Boston, MA, October 2011.
8. K. Kadakia, M.K. Datta, A. Manivannan, P.N. Kumta, "$Ru_{1-x}Sn_xO_2$:F and $Ir_{1-x}Sn_xO_2$:F thin film anode electro-catalysts for PEM based water electrolysis", *Electrochemical Society (ECS) Spring Meeting,* Montreral, QC, May 2011.
9. M.K. Datta, K. Kadakia, P.N. Kumta, "Synthesis and electrochemical performance of IrO_2-SnO_2-Nb_2O_5 thin film anode electro-catalysts for PEM based water electrolysis", *Electrochemical Society (ECS) Annual Meeting,* Las Vegas, NV, October 2010.

Patent

1. K. Kadakia, M.K. Datta, O.I. Velikokhatnyi, P.N. Kumta, "Non-noble metal based electro-catalyst compositions for Proton Exchange Membrane based water electrolysis and Methods of Making", *U.S. Patent Application # 13/961,327,* August 2013.

Thesis

Kadakia, K. S. Fundamental Study of nanostructured electro-catalysts with reduced noble metal content for PEM based water electrolysis. University of Pittsburgh, 2014.

Personnel supported by the project annually

Dr. Karan S. Kadakia-Graduate researcher-100%

Dr. Oleg I. Velikokhatnyi-Research faculty-100%

Dr. Moni K. Datta-Research faculty-50%

Dr. Prashant N. Kumta – Principal Investigator – 25%